



**HAL**  
open science

# Microwave susceptibility of thin ferromagnetic films: metrology and insight into magnetization dynamics

Claus Bilzer

► **To cite this version:**

Claus Bilzer. Microwave susceptibility of thin ferromagnetic films: metrology and insight into magnetization dynamics. Condensed Matter [cond-mat]. Université Paris Sud - Paris XI, 2007. English. NNT: . tel-00202827

**HAL Id: tel-00202827**

**<https://theses.hal.science/tel-00202827>**

Submitted on 8 Jan 2008

**HAL** is a multi-disciplinary open access archive for the deposit and dissemination of scientific research documents, whether they are published or not. The documents may come from teaching and research institutions in France or abroad, or from public or private research centers.

L'archive ouverte pluridisciplinaire **HAL**, est destinée au dépôt et à la diffusion de documents scientifiques de niveau recherche, publiés ou non, émanant des établissements d'enseignement et de recherche français ou étrangers, des laboratoires publics ou privés.

**THÈSE DE DOCTORAT**

**SPECIALITE : PHYSIQUE**

*Ecole Doctorale << Sciences et Technologies de l'Information des  
Télécommunications et des Systèmes >>*

Présentée par :

Claus BILZER

Sujet :

**Microwave susceptibility of thin ferromagnetic films:  
metrology and insight into magnetization dynamics**

**( Susceptibilité micro-ondes de couches minces ferromagnétiques :  
métrologie et analyse de la dynamique de l'aimantation )**

Soutenue le 30 novembre 2007 devant les membres du jury :

M. Matthieu BAILLEUL	Invité
M. Claude CHAPPERT	Examinateur
M. Thibaut DEVOLDER	Directeur de thèse
M. Jürgen FASSBENDER	Rapporteur
M. André THIAVILLE	Président du jury
M. Jan VOGEL	Rapporteur



# Contents

<b>0</b>	<b>Résumé en français</b>	<b>1</b>
0.1	Introduction . . . . .	1
0.2	Résumé . . . . .	3
0.3	Conclusion . . . . .	8
	<b>Introduction</b>	<b>13</b>
	Structure of the thesis . . . . .	15
<b>1</b>	<b>Basic theory of magnetization dynamics</b>	<b>17</b>
1.1	Energetics in Ferromagnets . . . . .	17
1.2	Magnetization Dynamics . . . . .	21
1.3	Dynamic Susceptibility . . . . .	22
1.4	Smit & Beljers resonance formula . . . . .	27
1.5	Magnetization Damping . . . . .	30
1.5.1	Scattering with itinerant conduction electrons . . . . .	31
1.5.2	Eddy currents . . . . .	33
1.5.3	Two-magnon scattering . . . . .	34
1.5.4	Spin-pumping . . . . .	35
1.6	Spin waves . . . . .	37
1.6.1	Magnetostatic Waves . . . . .	37
1.6.2	Exchange dominated (in-plane) spin waves . . . . .	40
1.6.3	Perpendicular Standing Spin Waves (PSSW) . . . . .	41
<b>2</b>	<b>Experimental Basics</b>	<b>43</b>
2.1	Measurement techniques in magnetization dynamics . . . . .	43
2.1.1	Ferromagnetic Resonance . . . . .	43
2.1.2	Inductive Permeameter . . . . .	44
2.1.3	Pulsed Inductive Microwave Magnetometer . . . . .	46
2.1.4	Propagating Spin Wave Spectroscopy . . . . .	47
2.1.5	Magneto-resistive measurements . . . . .	47
2.1.6	Brillouin Light Scattering . . . . .	48
2.1.7	Time Resolved Magneto Optical Kerr Effect . . . . .	49
2.1.8	Ferromagnetic Resonance Force Microscopy . . . . .	49
2.1.9	Comparison . . . . .	50
2.2	High-frequency Basics . . . . .	51
2.2.1	Derivation of the Telegrapher's Equations . . . . .	51
2.2.2	Guided Electromagnetic propagation . . . . .	54
2.2.3	Scattering parameters . . . . .	57
2.2.4	Vector Network Analyzer . . . . .	59

2.2.5	Error Correction . . . . .	60
2.3	Vector Network Analyzer Ferromagnetic Resonance . . . . .	62
2.3.1	Experimental Setup . . . . .	62
2.3.2	Characterization without sample . . . . .	64
2.3.3	Measurement of a ferromagnetic thin film . . . . .	67
<b>3</b>	<b>Two port VNA-FMR data analysis</b>	<b>75</b>
3.1	Introduction . . . . .	75
3.2	Full 2-Port data evaluation . . . . .	76
3.2.1	Raw data: S-parameters . . . . .	76
3.2.2	Correction of sample position . . . . .	78
3.2.3	Deembedding . . . . .	79
3.2.4	Extraction of $\Gamma$ and $\gamma$ . . . . .	79
3.2.5	Calculation of $\tilde{\epsilon}_r$ and $\tilde{\mu}_r$ . . . . .	80
3.2.6	Summary . . . . .	82
3.3	Other evaluation models . . . . .	82
3.3.1	Neglecting reflections, using $S_{21}$ only . . . . .	83
3.3.2	Absolute value of $S_{21}$ . . . . .	83
3.4	Comparison of evaluation models . . . . .	83
3.5	Summary . . . . .	86
<b>4</b>	<b>One port Open-reflection measurements</b>	<b>87</b>
4.1	Motivation . . . . .	87
4.2	Open-circuit one port measurement . . . . .	88
4.2.1	The measurement geometry . . . . .	88
4.2.2	The single measured scattering parameter $S_{11}^R$ . . . . .	89
4.2.3	Introducing an effective medium . . . . .	90
4.2.4	Simplifying $S_{11}^R$ . . . . .	91
4.2.5	Open one port data evaluation . . . . .	94
4.3	Comparison with two port measurement . . . . .	95
4.4	Conclusion . . . . .	97
<b>5</b>	<b>Fe/Au multilayers - Smoothing by irradiation</b>	<b>99</b>
5.1	Pre-growth substrate cleaning . . . . .	99
5.1.1	Removing substrate carbon contamination . . . . .	99
5.1.2	Studied samples . . . . .	100
5.1.3	Ferromagnetic resonance measurements . . . . .	102
5.1.4	Measurements using Perpendicular Magneto-Optical Kerr Effect (PMOKE) . . . . .	106
5.1.5	X-Ray characterization . . . . .	107
5.2	Post-growth irradiation . . . . .	109
5.2.1	Phase diagram of Fe-Au . . . . .	109
5.2.2	Low-energy ion irradiation . . . . .	110
5.2.3	Irradiated samples . . . . .	113
5.2.4	Ferromagnetic resonance measurements . . . . .	114
5.2.5	Perpendicular Magneto-Optical Kerr Effect . . . . .	118
5.2.6	X-Ray characterization . . . . .	118
5.3	Conclusion on smoothing . . . . .	120

<b>6</b>	<b>Dynamics of exchange biased films</b>	<b>121</b>
6.1	Brief overview of exchange bias . . . . .	121
6.2	Sample fabrication . . . . .	124
6.2.1	Basic characterization . . . . .	125
6.3	Hysteretic dynamics of ferromagnetic single layers . . . . .	126
6.3.1	The effective magnetization and anisotropy . . . . .	126
6.3.2	Dynamic bistability . . . . .	127
6.4	Hysteretic dynamics of exchange biased samples . . . . .	129
6.4.1	Effective magnetization, anisotropy and exchange bias . . . . .	129
6.4.2	Dynamic bistability with exchange bias . . . . .	131
6.4.3	Conclusion . . . . .	137
<b>7</b>	<b>High-frequency magnetization dynamics of CoFeB alloys</b>	<b>139</b>
7.1	Interest in CoFeB alloys . . . . .	139
7.2	Examined samples . . . . .	140
7.3	Ferromagnetic resonance measurements . . . . .	141
7.3.1	Results on the resonance frequency $f_{\text{res}}$ . . . . .	142
7.3.2	Results on the linewidth $\Delta f$ . . . . .	143
7.4	Expected consequences of our results on spin-torque magnetization switching . . . . .	146
7.5	Exchange stiffness constant of CoFeB . . . . .	147
7.6	Summary . . . . .	148
	<b>Conclusion</b>	<b>151</b>
	Summary . . . . .	151
	Outlook . . . . .	153
<b>A</b>	<b>Application Note</b>	<b>155</b>
A.1	Full two port measurement . . . . .	155
A.2	One port Open reflection measurement . . . . .	156
	<b>Bibliography</b>	<b>159</b>
	<b>Publications</b>	<b>177</b>
	<b>Acknowledgements</b>	<b>181</b>



# Chapter 0

## Résumé en français

### 0.1 Introduction

Les composants électroniques conventionnels sont basés sur la manipulation de la charge électrique de l'électron. Une autre propriété de l'électron, le spin, n'est habituellement pas exploitée. La mécanique quantique nous indique que cette propriété a le caractère d'un moment cinétique. Avec le moment cinétique orbital, il est responsable du moment magnétique de l'électron, et ainsi du phénomène macroscopique du magnétisme.

Le magnétisme est un sujet majeur dans la recherche d'aujourd'hui du fait que ce phénomène quantique très compliqué et fascinant n'est toujours pas entièrement compris et aucune théorie universelle n'existe. Cependant, les phénomènes magnétiques ne sont pas seulement intéressants pour la recherche fondamentale, mais également d'une grande importance pour les applications. Les matériaux ferromagnétiques sont notamment déjà employés dans la haute technologie, leur utilisation pour le stockage de données dans des disques durs est bien établie. Tandis que la part de marché de certaines applications diminue, comme par exemple l'enregistrement magnéto-optique, d'autres émergent : la logique magnétique offre la possibilité impressionnante d'être reprogrammable presque instantanément [1]. Un autre produit phare est la mémoire magnétique à accès aléatoire (MRAM pour Magnetoresistive Random Access Memory en anglais). Un effort de recherche considérable est dirigé vers l'exploration des différentes réalisations possibles de MRAM, entre autres la commutation de l'aimantation par l'application d'un champ magnétique [2], la commutation de l'aimantation thermiquement assisté [3] et l'utilisation du transfert de moment cinétique angulaire de spin [4]. Ce type de mémoire offre des propriétés avantageuses, notamment la non-volatilité et sa résistance au rayonnement, la prédestinant à une variété de nouveaux dispositifs.

L'utilisation du magnétisme dans la technologie de l'information a été rendu possible par la recherche fondamentale sur les couches minces magnétiques, devenue accessible grâce aux améliorations en technologie de dépôt de films minces.

Le confinement dans, au moins, une dimension a mené à une série de découvertes dans les 20 dernières années, comme le couplage d'échange intercouches [5] ou la magnétorésistance géante [6] et tunnel [7]. Ces effets sont exploités dans les processus de transport dépendant du spin en combinaison avec l'électronique conventionnelle menant aux nouvelles applications. Ce nouveau champ de recherches, appelé électronique de spin, (parfois 'spintronics' ou 'magnetoelectronics') fait progresser à l'heure actuelle les recherches dans le magnétisme.



Afin d’avoir une meilleure compréhension des processus physiques régissant les effets découverts, une caractérisation précise des couches minces (ferro-) magnétiques est nécessaire. Pendant plus de 50 ans, la technique expérimentale de la résonance ferromagnétique (FMR) [8] a constitué un moyen fiable pour caractériser précisément les propriétés des échantillons magnétiques, et, en particulier, des couches minces magnétiques [9, 10]. La FMR possède un aspect intéressant supplémentaire : l’évaluation du comportement de l’aimantation à haute fréquence. Comme le débit de données ne cesse d’augmenter, il existe un intérêt élevé pour la dynamique à grande vitesse dans les couches minces magnétiques.

Une version moderne de la FMR est la résonance ferromagnétique à l’aide d’un analyseur de réseau vectoriel (VNA-FMR), qui s’est avérée être un excellent outil pour la caractérisation à haute fréquence, particulièrement approprié pour l’examen des échantillons sous forme de couche mince. Cet instrument du type perméamètre inductif offre la possibilité d’examiner des aspects de la dynamique de l’aimantation, qui ne sont pas accessibles en utilisant la FMR classique : au lieu d’employer une cavité résonante limitée à une seule fréquence de résonance, on utilise un guide d’ondes coplanaire (CPW) pour créer un petit champ oscillatoire qui excite la précession de l’aimantation. Puisque le CPW est adapté sur une large bande de fréquences, il est possible d’acquérir des données résolues en fréquences au lieu de balayer le champ magnétique. Le balayage de la fréquence à un champ fixe conserve l’état de l’aimantation de l’échantillon, ce qui est avantageux pour l’étude de certains effets, comme, par exemple, le phénomène de l’anisotropie magnétique d’échange.

La capacité de changer indépendamment le champ magnétique et la fréquence est également une condition requise pour une étude quantitative du paramètre d’amortissement de l’aimantation, qui peut être calculé à partir de la largeur de la raie de résonance. L’amortissement de l’aimantation est toujours un sujet de recherche fondamentale : le paramètre d’amortissement est introduit phénoménologiquement et la possibilité de le manipuler serait avantageuse dans une variété des dispositifs. Les mesures de la largeur de raie à large bande sont nécessaires pour séparer l’amortissement “intrinsèque” des contributions extrinsèques [11, 12].

Une détermination précise de l’amortissement est également intéressante pour un nouvel effet utilisé par l’électronique de spin : le couple de transfert de spin [13, 14]. Cet effet ouvre les portes à des applications différentes, comme la commutation de la direction de l’aimantation [15] ou les oscillations de l’aimantation auto-entretenues par application d’un courant électrique [16, 17, 18]. Dans les deux cas, les courants de seuil, qui s’appellent le courant critique et le courant d’instabilité, dépendent de la valeur du paramètre d’amortissement.

Ce travail de thèse est consacré au développement de la résonance ferromagnétique à l’aide d’un analyseur de réseau vectoriel, et à son utilisation pour la compréhension de la dynamique de l’aimantation de couches minces magnétiques typiques. Bien que cette technique soit une approche prometteuse pour la métrologie de la dynamique de l’aimantation dans les couches minces, elle n’est apparue que récemment et sa standardisation n’est pas encore accomplie. Nous avons ainsi établi un traitement des données approprié pour une géométrie de transmission d’ondes, où une analyse rigoureuse est possible. En utilisant cette méthode comme standard de qualité, nous avons comparé plusieurs simplifications de l’expérience, en particulier aussi l’exploitation d’une réflexion à l’extrémité du guide d’ondes, permettant un dispositif expérimental plus compact et plus sensible.

En utilisant notre montage expérimental, nous avons étudié plusieurs couches

minces type, y compris des multicouches, des systèmes avec une anisotropie magnétique d'échange et des alliages amorphes. Deux traitements de bombardement d'ions ont été examinés pour améliorer les propriétés des multicouches Fe/Au. En combinaison avec des caractérisations structurales, la technique VNA-FMR s'est montrée adéquate, donnant des preuves claires des améliorations induites par le bombardement ionique : une rugosité d'interface réduite et une largeur de la raie de résonance ferromagnétique mieux définie. Nous avons également étudié le phénomène de l'anisotropie magnétique d'échange dans des systèmes IrMn/NiFe et IrMn/CoFeB, où les caractérisations conventionnelles peuvent assigner seulement une valeur unique au champ d'échange par boucle d'hystérésis. En utilisant la technique de VNA-FMR, nous avons pu déduire le champ d'échange agissant sur l'aimantation de la couche ferromagnétique à chaque point de la boucle d'hystérésis. Nous avons démontré comment il évolue avec l'histoire du champ appliqué, donnant une meilleure compréhension de l'évolution de l'état micromagnétique de l'antiferromagnétique. Enfin, nous avons étudié des alliages de CoFeB, afin de mettre en valeur leur paramètre d'amortissement effectif et leur constante de la raideur d'échange. Nous avons montré que le recuit thermique et la cristallisation suivante pouvaient déclencher une augmentation du paramètre d'amortissement. Un lien peut être établi entre nos résultats et l'augmentation du courant critique dans des expériences de commutation avec le couple de transfert de spin dans les jonctions tunnel magnétiques à base de CoFeB.

## 0.2 Résumé

Les chapitres 1 et 2 sont conçus pour introduire les notions de base théoriques et expérimentales.

Dans le **chapitre 1** nous présentons les concepts théoriques nécessaires à une bonne compréhension des expériences de résonance ferromagnétique effectuées. D'abord nous décrivons les différentes expressions des énergies qui entrent en jeu dans la description du comportement statique ou dynamique de l'aimantation dans un échantillon ferromagnétique en couche mince. Ensuite, nous introduisons l'équation du mouvement régissant la dynamique de l'aimantation. À l'aide de cette dernière, nous dérivons analytiquement la susceptibilité dynamique complexe qui est la quantité que nous avons l'intention de mesurer. La susceptibilité dynamique permet notamment de déterminer la relation entre les propriétés du matériau examiné, comme l'aimantation effective et la constante d'anisotropie, et la fréquence de résonance ainsi que la largeur de raie. En outre, une manière alternative de dériver la fréquence de résonance est exposée, suivant l'Ansatz de Smit et de Beljers.

La largeur de la raie de résonance est liée au paramètre d'amortissement. Nous analysons les mécanismes qui sont derrière l'amortissement du mouvement de l'aimantation dans les échantillons ferromagnétiques métalliques en couche mince. En conclusion, nous adressons les ondes de spin qui dépendent de la géométrie de l'échantillon.

Le **chapitre 2** traite les aspects de base expérimentaux. D'abord nous donnons une vue d'ensemble des techniques généralement répandues dans le domaine de la dynamique de l'aimantation. Parmi ces dernières, figure également un type d'instrument inductif appelé perméamètre. Le montage expérimental principalement utilisé au cours de cette thèse appartient à cette catégorie.

Ensuite, nous rappelons les connaissances de l'ingénierie micro-ondes qui sont indispensables pour l'analyse du processus de mesure. Puis, nous donnons une description détaillée de la technique de caractérisation, que nous avons utilisée principalement au cours de cette thèse, et sa réalisation expérimentale : la résonance ferromagnétique à l'aide d'un analyseur de réseau vectoriel (VNA-FMR).

Les chapitres 3 et 4 concernent l'interprétation des données brutes et du traitement de données.

Le **chapitre 3** est consacré à l'analyse des données brutes obtenues pour une mesure d'un réseau électrique à deux ports en utilisant une structure de guide d'ondes coplanaire. Le calcul présenté permet d'accéder à des valeurs proportionnelles à la perméabilité et la permittivité de l'échantillon. Nous décrivons analytiquement toutes les étapes nécessaires afin d'obtenir les données prévues : la susceptibilité dynamique complexe et sa dépendance au champ magnétique ainsi qu'à la fréquence. Une façon simple de corriger un alignement imprécis dans le centre du guide d'ondes est introduite. Comme autre avantage, cette correction rend la détermination exacte de la position de l'échantillon superflue. Au cours de cette thèse, ce traitement de données était implémenté dans un programme sous le langage LabView. Les instructions pour l'utilisation de ce programme se trouve en appendice A.

À part le traitement de données démontré, nous abordons deux méthodes approximatives trouvées dans la littérature. Ces dernières sont basées sur un seul paramètre  $S$  en transmission et nous analysons l'impact de cette simplification. Nous faisons une évaluation de leur validité en les appliquant aux mêmes données brutes et en procédant à une comparaison des résultats. Pour cela, nous avons mesuré la matrice  $S$  complète de deux échantillons modèles jusqu'à 15 GHz. Nous avons discuté la différence des données évaluées par rapport au traitement de données présenté dans cette thèse, qui seul prend en compte les paramètres de réflexion. Pour les fréquences de la résonance ferromagnétique, nous trouvons un bon accord entre les différentes méthodes. L'erreur relative reste en dessous de 1%. Mais pour la largeur de raie, les méthodes approximatives montrent une divergence qui peut atteindre 10% par rapport à l'utilisation des quatre paramètres  $S$ . L'exploitation d'un seul paramètre complexe mène nécessairement à une caractérisation réduite de l'échantillon. La plus grande partie du contenu de ce chapitre est publiée dans [19].

Dans le **chapitre 4** nous évaluons la possibilité de simplifier le montage expérimental en enlevant une sonde à haute fréquence tout en conservant le même guide d'ondes. À la place d'une mesure de la matrice  $S$  complète dans le cas présenté dans le chapitre précédent, nous n'obtenons qu'un seul paramètre. Nous discutons les inconvénients et les avantages d'une expérience à un port électrique, en particulier pour notre approche qui n'est pas basée sur un guide d'ondes court-circuité à une extrémité, comme les montages à un port décrits dans la littérature. Contrairement à ces derniers, l'extrémité déconnectée se comporte dans notre cas comme un circuit ouvert qui provoque une réflexion de l'onde électromagnétique.

Nous analysons les changements exercés sur les données brutes mesurées (paramètre de réflexion  $S_{11}^R$ ). Nous présentons un traitement de données adapté en reliant  $S_{11}^R$  et les quatre paramètres de la matrice  $S$ . À l'aide d'une approximation, il est possible de calculer une valeur complexe correspondant à la susceptibilité dynamique de l'échantillon. Afin d'évaluer la validité de l'approximation, nous faisons une comparaison avec les expériences à deux ports en utilisant des données brutes, comme

dans le chapitre précédent.

Les fréquences et la largeur de raie de la résonance ferromagnétique sont examinées pour deux échantillons modèles. La différence pour les fréquences de résonance entre l'expérience à un port et à deux ports est petite. Un ajustement de données pour l'obtention des propriétés magnétiques a montré une divergence entièrement négligeable. Il est évident dans la comparaison de la largeur de raie que les différences mesurées sont exclusivement liées au bruit et ne sont pas systématiques. L'accord est alors aussi excellent.

Nous concluons que l'expérience à un port électrique représente une véritable alternative à l'expérience à deux ports. Dans certains cas, elle est même avantageuse, par exemple si des contraintes spatiales empêchent l'utilisation des deux sondes à haute fréquence. Bien que nos résultats aient été corrects, la validité des approximations utilisées doit être vérifiée pour chaque montage expérimental individuel.

Les chapitres 5, 6 et 7 rapportent les résultats sur plusieurs sujets récents dans le domaine du magnétisme, qui ont été obtenus en particulier à l'aide des expériences de résonance ferromagnétique.

L'objet du **chapitre 5** est l'amélioration des interfaces des multicouches Fe/Au qui sont déposées par épitaxie par jet moléculaire sur des substrats monocristallins de MgO. Afin de réduire la rugosité de surface et d'interfaces, nous utilisons des bombardements par faisceau ionique. Deux traitements différents sont examinés : une irradiation avec des atomes d'oxygène avant la croissance afin d'optimiser l'état du substrat avant le dépôt de l'échantillon, et un bombardement après la croissance avec des ions  $\text{He}^+$ , qui mène à un démélange aux interfaces.

La première irradiation consiste en une exposition à un faisceau d'atomes d'oxygène chimiquement actifs à 60 eV pendant deux minutes. Elle résulte en un nettoyage du substrat en enlevant entièrement la contamination avec du carbone, qui est généralement observée sur les substrats MgO disponibles dans le commerce. Les expériences FMR donnent des critères pour l'efficacité du traitement : une réduction de l'élargissement inhomogène de la largeur de raie de la résonance pour l'échantillon déposé sur un substrat traité est reliée aux interfaces plus lisses. Des caractérisations structurales additionnelles sont fournies : Des mesures de la rugosité de la surface supérieure en Au à l'aide d'un microscope à force atomique ainsi que des expériences de diffractométrie aux rayons X ont permis d'obtenir des données quantitatives, qui ont validé les résultats des expériences de résonance ferromagnétique.

Le deuxième traitement consiste en un bombardement de l'échantillon après son dépôt avec des ions  $\text{He}^+$  d'une énergie de 30 keV. Les collisions d'ions fournissent la mobilité atomique qui est nécessaire pour activer un démélange du Fe et Au aux interfaces. Une interface plus lisse, qui correspond à une zone de contact réduite, est thermodynamiquement favorisée, car les deux éléments sont immiscibles. Simultanément, l'énergie relativement basse des ions empêche une amorphisation ou la création de défauts. Le lissage d'interfaces est mis en évidence par la diminution de la contribution inhomogène à la largeur de raie de la résonance ferromagnétique après le bombardement ionique. L'élargissement inhomogène devient d'autant plus petit que la fluence de l'irradiation est augmentée. Ceci est illustré dans la figure 1. Des expériences de diffractométrie aux rayons X fournissent une confirmation additionnelle et quantitative de l'effet de l'irradiation.

En conclusion, nous établissons l'efficacité des deux procédés de réduction de la rugosité interfacique par traitement ionique et, en plus, nous démontrons la possi-

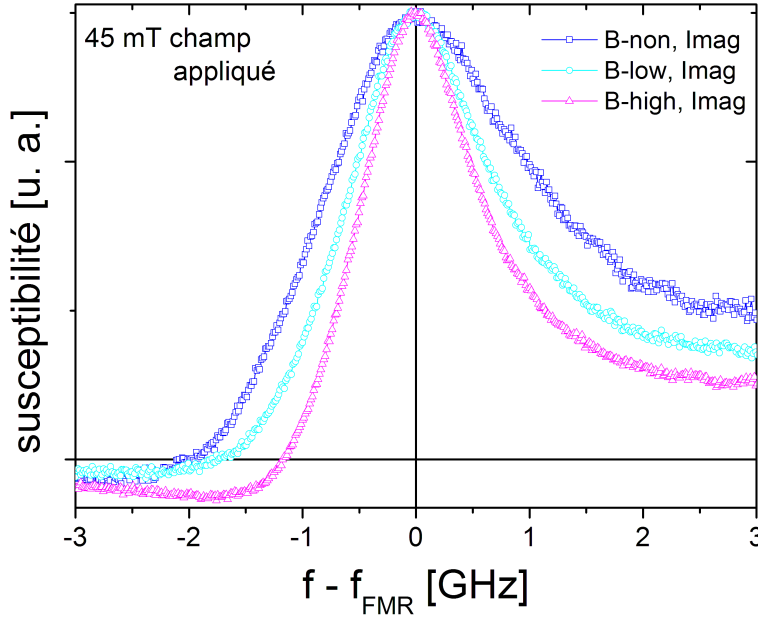


Figure 1: La partie imaginaire de la susceptibilité des trois échantillons B sous un champ appliqué de 45 mT. Les échantillons ont été soumis à une fluence croissante dans l'ordre B-non, B-low, B-high. L'élargissement inhomogène de la largeur de raie décroît dans le même ordre.

bilité de combiner leurs effets.

Le **chapitre 6** analyse l'influence d'une couche antiferromagnétique introduisant une anisotropie magnétique d'échange sur la résonance d'un échantillon ferromagnétique en couche mince. D'après la définition généralement utilisée, l'anisotropie magnétique d'échange est caractérisée par le champ  $H_{eb}$  qui est le champ au centre de deux coercivités dans une boucle d'hystérésis. En comparant les résultats des mesures des échantillons avec et sans une couche antiferromagnétique, en particulier leur comportement dans une boucle d'hystérésis, nous avons constaté qu'il est difficile d'attribuer une valeur précise suivant cette définition. Déterminer précisément  $H_{eb}$  est rendu difficile par l'existence de domaines dans l'antiferromagnétique, qui contribuent normalement à l'anisotropie d'échange, mais qui peuvent être renversés par une activation thermique, une fois que l'aimantation du ferromagnétique est renversée par un champ extérieur. Par conséquent, le champ  $H_{eb}$  effectivement observé est diminué, quand l'aimantation du ferromagnétique est inversé par rapport à la direction de l'anisotropie d'échange pendant un temps suffisamment long. Le même phénomène est valable pour les champs coercitifs. Il est également difficile de donner des valeurs précises pour  $H_c$ , car, par exemple, une boucle d'hystérésis d'un AGM ne fournit pas d'informations sur l'amplitude de  $H_{eb}$ , en passant un champ coercitif ou l'autre. Pour une basse vitesse de mesure, les champs coercitifs seront nécessairement influencés par une amplitude changeante du champ de l'anisotropie d'échange. Nous pouvons donc conclure que chaque amplitude extraite d'une expérience pour caractériser le champ de l'anisotropie d'échange ou les coercivités d'un échantillon avec une couche antiferromagnétique devrait toujours être accompagnée d'une description détaillée des conditions de mesure.

Nous remarquons que le phénomène observé apparait évidemment indépendamment de la technique de mesure. Cependant, il ne peut pas toujours être observé

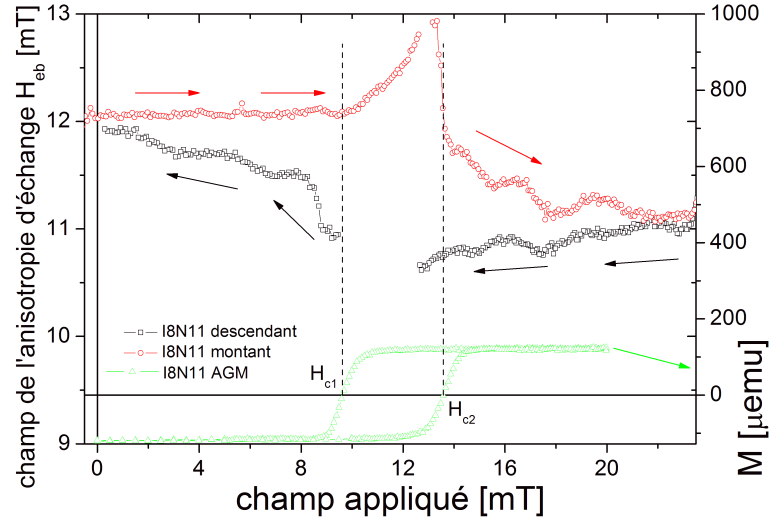


Figure 2: La gamme d'amplitudes du champ de l'anisotropie d'échange pendant une boucle d'hystérésis pour l'échantillon I8N11. Une boucle mesurée à l'aide d'un AGM est aussi montrée.  $H_{eb}$  ne pouvait pas être résolu correctement entre les champs coercitifs.

directement : Les boucles d'hystérésis mesurés à l'aide d'un magnétomètre conventionnel, comme un AGM et un Moke, indiquent seulement des informations sur les moments magnétiques des couches ferromagnétiques. Il n'y a aucune évidence si le champ de l'anisotropie d'échange effectif lors de la mesure d'une des deux coercivités est le même que celui agissant sur le ferromagnétique lors de la mesure de l'autre coercivité. En choisissant bien les conditions de l'expérience, il est néanmoins possible à l'aide de la magnétométrie conventionnelle d'améliorer la compréhension sur les processus fondamentaux, comme montré dans [20] et [21]. Les mesures VNA-FMR, par contre, ont également permis de tirer des conclusions directes : elles dépendent non seulement de l'alignement des moments magnétiques dans le ferromagnétique, mais aussi de l'énergie totale du système examiné. Par conséquent, il est possible d'extraire des informations sur l'état de l'antiferromagnétique, même lorsque le ferromagnétique est déjà saturé. A partir de chaque fréquence de résonance ferromagnétique le champ  $H_{eb}$  instantané peut être calculé, et il devient possible de donner une gamme d'amplitudes que le champ de l'anisotropie d'échange adopte pendant une boucle d'hystérésis. Ceci est illustré dans la figure 2.

Dans le **chapitre 7** nous présentons les propriétés magnétiques dynamiques des alliages de CoFeB. Puisque l'utilisation de ce matériau n'est devenue répandue que récemment, les données numériques le caractérisant n'étaient pas disponibles. Les expériences de résonance ferromagnétique fournissent les valeurs de l'aimantation effective et du paramètre phénoménologique de l'amortissement d'après Gilbert. Tous les deux sont examinés au moyen de la résonance ferromagnétique pour les échantillons  $\text{Co}_{72}\text{Fe}_{18}\text{B}_{10}$  déposés par un faisceau ionique en fonction de l'épaisseur de couche et du recuit thermique. Comme montré par d'autres études, sans traitement thermique les couches sont dans un état amorphe. Leurs largeurs de raie sont très fines correspondant à une constante d'amortissement très basse ( $\alpha_{app} = 0.006$ ). Pour les gammes d'épaisseurs des échantillons examinés (5 - 40 nm), la valeur de la constante était indépendante de l'épaisseur.

Nous avons aussi mesuré un échantillon de référence en  $\text{Co}_{80}\text{Fe}_{20}$  sans contenu de bore. Cet échantillon, qui est dans un état cristallin immédiatement après le dépôt, a montré un amortissement deux fois plus élevé ( $\alpha_{\text{app}} = 0.013$ ). Nous insistons sur le fait que la valeur obtenue pour les échantillons  $\text{Co}_{72}\text{Fe}_{18}\text{B}_{10}$  amorphes est même au-dessous de celle habituellement observée pour des échantillons en Permalloy de haute qualité. En conséquence, les alliages de CoFeB sont prédestinés à l'utilisation dans les applications à haute vitesse. A cause du manque des données explicites de la constante de l'amortissement pour CoFeB dans la littérature avant notre contribution, plusieurs observations expérimentales ont été expliqués à l'aide des valeurs que nous avons mesurées [22, 23].

Il a été démontré que le recuit thermique à  $280^\circ\text{C}$  déclenche un changement de phase dans le  $\text{Co}_{72}\text{Fe}_{18}\text{B}_{10}$  amorphe. Dans les expériences FMR, ce processus de cristallisation a eu pour conséquence une augmentation de l'aimantation effective ainsi qu'une augmentation dramatique de l'amortissement, atteignant un facteur de 5 pour le film d'une épaisseur de 40 nm. Pour les épaisseurs inférieures, l'augmentation de la constante d'amortissement après le recuit était moins prononcée. Ceci est illustré dans la figure 3.

La dépendance de l'amortissement au recuit thermique peut expliquer les évolutions étonnantes récemment observées dans des jonctions tunnel magnétiques consistant de CoFeB/MgO/CoFeB : La commutation de l'aimantation a été réalisée par transfert de spin par l'application d'un courant, et le courant critique  $J_c$ , qui représente le seuil nécessaire pour commuter, a été déterminé. Après recuit de leur échantillon, la valeur de  $J_c$  a augmenté, malgré une augmentation de la polarisation en spin qui devrait être accompagnée d'une diminution de  $J_c$ . Ce fait pourrait être expliqué par nos résultats, car  $J_c$  est proportionnel à  $\alpha$  et à l'aimantation effective, qui tous les deux ont augmentés après le recuit.

En plus des caractérisations précédentes, la constante de raideur d'échange a pu être extraite quantitativement à partir d'un mode de résonance dominée par l'échange. Pour l'échantillon  $\text{Co}_{72}\text{Fe}_{18}\text{B}_{10}$  amorphe nous avons déduit une valeur de  $A = 28.4 \cdot 10^{-12}$  J/m. Cette valeur est proche des valeurs publiées pour le Co. Puisqu'il n'y avait pas de données pour la raideur d'échange de  $\text{Co}_{72}\text{Fe}_{18}\text{B}_{10}$  dans la littérature, les valeurs déterminées peuvent se révéler utiles par exemple pour des simulations micromagnétiques, qui nécessitent la raideur d'échange comme paramètre d'entrée.

### 0.3 Conclusion

Au cours de cette thèse, nous avons employé la résonance ferromagnétique à l'aide d'un analyseur de réseau vectoriel pour améliorer la compréhension de plusieurs sujets d'étude du nanomagnétisme moderne. La technique elle-même étant une nouveauté, des efforts ont été dirigés vers l'amélioration de son mode de fonctionnement. Pour des expériences en géométrie deux ports sur une structure de guide d'ondes coplanaire, réalisation la plus commune de ce type de mesure pour des échantillons en couche mince, une meilleure description des données brutes obtenues a été réalisée. à cette fin, une représentation analytique précise des paramètres de répartition mesurés a été développée en utilisant des éléments de la théorie de circuit micro-ondes. Cette analyse a eu comme conséquence un procédé de traitement de données permettant de calculer une valeur directement proportionnelle à

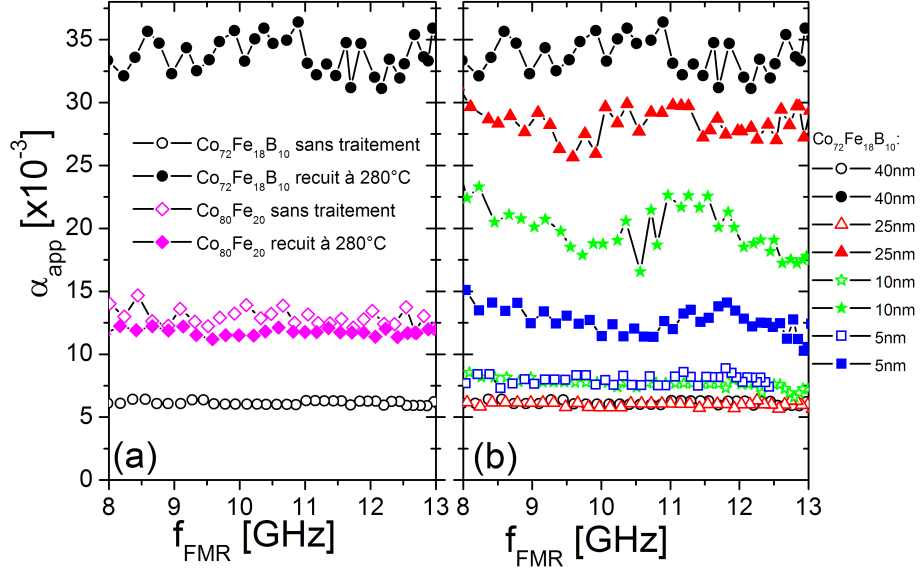


Figure 3: L'amortissement apparent  $\alpha_{app}$  en fonction de la fréquence de résonance ferromagnétique. Les symboles ouverts représentent les échantillons sans traitement, tandis que les symboles pleins représentent ceux recuits à 280°C. (a) 40 nm  $Co_{80}Fe_{20}$  (diamant) et 40 nm  $Co_{72}Fe_{18}B_{10}$  (cercle);  $\alpha_{app}$  est particulièrement bas pour  $Co_{72}Fe_{18}B_{10}$  sans traitement ( $\circ$ ). (b) 5 (rectangle), 10 (étoile), 25 (triangle) and 40 nm (cercle)  $Co_{72}Fe_{18}B_{10}$ , sans traitement et recuit.

la susceptibilité dynamique du dispositif à l'essai. Nous avons comparé ce nouveau procédé à des solutions approximatives trouvées dans la littérature. Alors que les résultats des procédés approximatifs conviennent plutôt bien pour quelques aspects (détermination de la fréquence de résonance), il y a une plus grande différence entre les résultats pour d'autres aspects (largeurs de raie). Par conséquent, nous recommandons l'utilisation du traitement de données présenté dans cette thèse pour des expériences en géométrie deux ports, car il s'agit de la seule méthode parmi celles examinées prenant en compte les paramètres de réflexion de la matrice de répartition.

Tandis que nous obtenions une description solide de l'expérience dans une géométrie à deux ports, plusieurs groupes de recherche effectuèrent leurs mesures en utilisant seulement une sonde à haute fréquence dans une géométrie à un port. Ceci peut offrir plusieurs avantages comme un calibrage simplifié, une plus haute rapidité de mesure ainsi qu'un signal plus élevé. Habituellement, la deuxième extrémité du guide d'ondes est court-circuitée. Par contre, nous avons examiné ici une réalisation alternative où le guide d'ondes est inchangé par rapport à la géométrie deux ports et la deuxième extrémité reste simplement déconnectée, fonctionnant comme un circuit ouvert. Bien que ceci permette un changement facile entre une mesure à deux ports et une mesure à un port en débranchant simplement la deuxième sonde haute fréquence, l'utilisation d'un circuit ouvert au lieu d'un court-circuit n'a pas été adressée jusqu'ici. Comme pour la géométrie à deux ports, nous avons établi un modèle analytique que nous avons résolu aussi loin que possible. En raison de la complexité additionnelle qui est ajoutée par la réflexion à l'extrémité ouverte, nous avons analysé la possibilité de simplifier le modèle. En utilisant une approximation appropriée, nous avons développé un traitement de données permettant de calculer la susceptibilité de l'échantillon. Faisant une comparaison avec des données de mesure



brutes, nous confirmons une bonne concordance avec des expériences en géométrie deux ports.

La largeur des raies de résonance, qui est extraite de la susceptibilité mesurée par VNA-FMR, contient une contribution due à l'inhomogénéité des propriétés magnétiques de l'échantillon. Cet élargissement inhomogène peut être séparé de la largeur de raie intrinsèque, si la largeur de raie est mesurée en fonction du champ appliqué dans le domaine fréquentiel. Nous avons exploité ce critère pour qualifier les changements infligés par irradiation ionique sur des multicouches Fe/Au. Un nettoyage du substrat MgO avant le dépôt de l'échantillon par un bombardement avec des atomes d'oxygène chimiquement actifs a entraîné une décroissance de l'élargissement inhomogène par rapport à un échantillon nominalelement équivalent déposé sur un substrat non nettoyé. Ce traitement enlève la contamination surfacique du substrat avec du carbone améliorant les conditions de croissance pour les couches déposées. La réduction de l'élargissement inhomogène a été corrélée avec une rugosité d'interface réduite par des caractérisations structurales. Une irradiation avec des ions  $\text{He}^+$  a été appliquée sur les échantillons après la croissance avec des fluences différentes. Le Fe et l'Au ne sont pas miscibles, mais un démélange aux interfaces des multicouches est cinétiquement interdit à température ambiante. En utilisant des simulations, les ions  $\text{He}^+$  à 30 keV ont été déterminés comme étant les candidats idéaux pour un traitement par faisceau ionique, où les collisions d'ions fournissent la mobilité atomique nécessaire pour réaliser le démélange. En effet, l'élargissement inhomogène de la largeur de raie est réduit de plus en plus avec une fluence d'irradiation plus haute. La réflectivité de rayons X a confirmé une réduction coïncidente de la rugosité interfaciale. Les effets des deux traitements d'irradiation peuvent être cumulés.

Les expériences FMR sont réputées pour leur détermination précise des propriétés magnétiques des matériaux ferromagnétiques. Nous avons examiné les informations accessibles par FMR sur une couche antiferromagnétique couplée à un ferromagnétique. La métrologie magnétique conventionnelle n'est sensible qu'à l'aimantation de la couche ferromagnétique et les propriétés de l'antiferromagnétique sont dérivées indirectement, par exemple le champ d'anisotropie magnétique d'échange est défini comme la moyenne arithmétique des deux coercivités qui marquent la commutation du ferromagnétique. En revanche, des expériences FMR permettent de tirer également des conclusions directes sur l'état de l'antiferromagnétique, car elles sont sensibles à l'énergie totale du système. En particulier, à partir des mesures dans le domaine fréquentiel le champ d'échange instantané a été déterminé à tous les champs appliqués d'une boucle d'hystérésis. Pendant le balayage du champ appliqué, la valeur du champ d'échange a changé. Ceci peut être expliqué par le renversement thermiquement activé de l'aimantation des grains de l'antiferromagnétique polycristallin. En principe ce recuit par champ magnétique est prévisible à température finie, mais il est difficile à analyser en utilisant des techniques standard. En raison de la dépendance du champ d'échange à l'histoire du champ appliqué et au temps de mesure, que nous avons découverte, nous recommandons d'accompagner toujours les résultats caractérisant un antiferromagnétique par une description précise des conditions de mesure. Sinon, la non-ambiguïté des résultats n'est pas garantie.

En raison de leurs propriétés avantageuses, l'utilisation des alliages de CoFeB est devenue très répandue dans les jonctions tunnel magnétiques. Tandis que des caractérisations statiques peuvent être trouvées facilement dans la littérature, les données d'expériences de résonance ferromagnétique n'étaient pas disponibles. Nous

avons mesuré une série d'échantillons de  $\text{Co}_{72}\text{Fe}_{18}\text{B}_{10}$  ayant des épaisseurs différentes et soit dans l'état immédiatement après la déposition soit après un recuit thermique. L'aimantation effective des couches sans traitement thermique a montré une dépendance avec l'épaisseur comme prévue pour une anisotropie surfacique. Il est connu que le recuit thermique provoque une cristallisation des couches autrement amorphes. Ceci a été démontré par des plus grandes valeurs de l'aimantation effective pour toutes les épaisseurs après le recuit. L'amortissement de l'aimantation, qui n'avait pas été caractérisé précédemment, s'est avéré très bas pour les films sans traitement thermique. Les valeurs obtenues sont bien comparables au Permalloy de haute qualité. Nous avons observé une forte augmentation inattendue de l'amortissement après le recuit thermique, qui peut être attribuée à la transition de phase déclenchée. La dépendance de l'amortissement des échantillons recuits avec l'épaisseur peut être associée à une cristallisation seulement partielle. En plus, nous avons observé des résonances appelées "perpendicular standing spinwave" (PSSW), qui permettent une détermination quantitative de la constante de raideur d'échange. Sa valeur pour l'alliage  $\text{Co}_{72}\text{Fe}_{18}\text{B}_{10}$  s'est avérée proche de la valeur publiée du Co.



# Introduction

Conventional electronic components are based on the manipulation of the electrical charge of the electron. Another property of the electron, the spin, is usually not used. This property has the character of a purely quantum mechanical angular momentum. Together with the orbital angular momentum, it is responsible for the magnetic moment of the electron, and thus for the macroscopic solid state phenomenon of magnetism.

One reason for the presence of magnetism as a top research topic today is certainly that this very complicated and fascinating quantum phenomenon is still not fully understood and no universal theory exists. But, magnetic phenomena are not only interesting for fundamental research, but also relevant for applications. Especially ferromagnetic materials are used nowadays in high technology, for example their utilization in data storage in hard disk drives is firmly established. While the market share of some areas of application, as e.g. magneto-optical recording, diminishes, new application scenarios are emerging at the same time: magnetic logic components for example offers the exciting possibility of being reprogrammable on the fly [1]. Another major product is the Magnetic Random Access Memory (MRAM). A strong research effort is directed at the possible implementations, among others field induced magnetic switching MRAM [2], thermally assisted magnetization switching MRAM [3] and spin-transfer torque MRAM [4]. This type of memory offers advantageous properties, notably non-volatility and radiation hardness, making it suitable for a variety of new devices.

The application of magnetism in information technology was enabled by the basic research in thin film magnetism, which was made possible thanks to considerable improvements in film deposition technology. The confinement in (at least) one dimension led to a series of discoveries in the last 20 years, as e.g. the interlayer coupling [5] or the giant [6] and tunnel magnetoresistance [7]. These effects are exploited in spin-dependent transport processes in combination with conventional electronics leading to novel applications. This new research field called spintronics (sometimes spin electronics or magnetoelectronics) is driving the progress in magnetism today [24].

In order to achieve a better understanding of the physical processes governing the discovered effects, a precise characterization of (ferro-) magnetic thin films is necessary. Since more than 50 years the well established experimental technique of FerroMagnetic Resonance (FMR) [8] provided a reliable means of characterizing accurately the properties of magnetic samples, in particular also magnetic thin films [9, 10]. FMR has an additional beneficial aspect: the evaluation of the magnetization behavior at high frequencies. Since data rates ever increase, there is a high interest in the high speed dynamics in magnetic thin films.

A modern version of FMR is Vector Network Analyzer FerroMagnetic Resonance

(VNA-FMR), which has proven to be an excellent tool for high frequency characterization, particularly adapted for the examination of thin film samples. This inductive permeameter type of instrument allows to gain insight into aspects of magnetization dynamics, which are impossible to assess using classical FMR: instead of using a microwave cavity limited to a single resonance frequency, a coplanar waveguide (CPW) is employed to create the oscillating field which excites magnetization precession. As the CPW is adapted over a wide frequency range, it allows to acquire frequency-resolved data, instead of sweeping the magnetic field. Sweeping the frequency at a fixed field conserves the magnetization state of the sample, which is advantageous for the study of certain effects, as e.g. the exchange bias phenomenon.

Being able to vary independently the magnetic field and the frequency is also beneficial for a quantitative study of the damping parameter, which can be calculated from the linewidth of the measured resonance. Magnetization damping is still a subject of fundamental research: the damping parameter is introduced phenomenologically and its engineering would be desirable in a variety of application devices. Broad-band measurements of the linewidth are imperatively necessary to separate the “intrinsic” damping from extrinsic contributions [11, 12].

A precise determination of damping is also of interest for a novel effect in magnetoelectronics, namely the spin-transfer torque [13, 14]. This effect leads to different applications, as the switching of the magnetization direction [15] or self-sustained magnetization oscillations [16, 17, 18] by the application of an electrical current. In both cases, the threshold currents, which are called critical current and instability current, depend on the value of the damping parameter.

This work is devoted to the development of VNA-FMR, and to its use for the understanding of the magnetization dynamics of model thin film. While this technique is a promising approach for the metrology of magnetization dynamics in thin films, it only appeared recently and its standardization was not yet completed. We thus established the appropriate data analysis in a wave transmission geometry, where a rigorous analysis is possible. Using the former method as a quality standard, we have compared several simplifications of the measurement method, with a special focus on the use of an open-end reflection at the end of the waveguide, allowing a more compact and more sensitive set-up.

Using our set-up, we have investigated several model thin films, including multilayers, exchange biased systems and amorphous alloys. Two ion bombardment treatments were tested to tailor the properties of Fe/Au multilayer. In combination with structural measurements, VNA-FMR proved as an adequate technique, giving clear evidence on the ion-induced ameliorations of the magnetic layers, both in terms of lower interface roughness and better defined ferromagnetic resonance linewidth. We have also studied the exchange bias phenomenon in IrMn/NiFe and IrMn/CoFeB systems, where conventional methods of investigation can only assign a sole exchange bias field value per hysteresis loop. Using VNA-FMR, we could deduce the exchange bias field acting on the magnetization at each point along an hysteresis loop. We could evidence how it evolves continuously with field history, giving thus insight into the micromagnetic state of the antiferromagnet. Finally, we have investigated CoFeB alloys, with an emphasis on their effective damping parameter and exchange stiffness constant. It was shown that the thermal annealing and the subsequent recrystallization could trigger a small to drastic increase of the effective damping parameter. Our findings correlate with the increase of the spin-transfer torque critical switching current in magnetic tunnel junctions of CoFeB,

that could formerly not be understood.

## Structure of the thesis

The thesis is organized as follows:

In **Chapter 1** we introduce the theoretical concepts necessary for the understanding of the performed ferromagnetic resonance measurements. These concepts include the energetics in ferromagnets, which allow in combination with the equation of motion to analytically represent the dynamic susceptibility, the quantity to be measured. Furthermore, we analyze the mechanisms which are behind the damping of magnetization motion and the concept of spin waves.

**Chapter 2** is concerned with the basic experimental aspects. We first give an overview of techniques commonly encountered in magnetization dynamics. Among these figure also the inductive permeameter type of instruments, to which the mainly used measurement setup belongs. Afterwards, we remind some important basics of microwave engineering indispensable for the analysis of the measurement process. Finally, we give a detailed description of the main characterization technique we employed and its experimental realization.

**Chapter 3** is dedicated to the analysis of the raw data obtained from a two port measurement using a coplanar waveguide structure. We describe analytically all steps necessary in order to obtain the intended data: the dynamic susceptibility and the magnetic field and frequency dependence thereof. Apart from the demonstrated data evaluation method, we address two approximate methods found in the literature. We give an estimation of their validity by applying them to the same raw data and proceeding with a comparison of the results.

In **Chapter 4** we assess the possibility of simplifying the measurement setup by removing one high-frequency probe while keeping the same microwave guide. We discuss the disadvantages and advantages of this one port technique, which exploits the reflection at the open end, and analyze the changes in the measured raw data. We present an adapted data analysis procedure and give a comparison to two port measurements as described in the previous chapter.

The improvement of the interfaces of Fe/Au multilayers by the use of ion-beam bombardments is the topic of **Chapter 5**. Two different treatments are examined: a pre-growth irradiation with oxygen atoms in order to optimize the condition of the substrate before the sample deposition, and a post-growth bombardment with He<sup>+</sup> ions, which leads to demixing at the interfaces. The FMR measurements give a criteria for the efficiency of the treatments, namely the inhomogeneous broadening in the resonance linewidth. Additional structural characterizations are provided.

**Chapter 6** analyzes the influence of an antiferromagnetic exchange biasing layer on the ferromagnetic resonance of a thin film sample. After giving a short introduction into the exchange bias phenomenon, we compare the measurements between samples with and without an added antiferromagnetic layer, in particular their hysteretic behavior. Differences to conventional magnetometry measurements are pointed out, especially the possibility to deduce from the resonance frequency the instantaneously acting exchange bias.

The dynamic magnetic properties of CoFeB alloys are presented in **Chapter 7**. Numerical data was still missing as this material gained widespread use only recently. Ferromagnetic resonance measurements provide characterization of the ef-

fective magnetization and the phenomenological Gilbert damping parameter. Both are examined for  $\text{Co}_{72}\text{Fe}_{18}\text{B}_{10}$  samples with respect to the layer thickness and thermal annealing. Additionally, the exchange stiffness constant could be extracted quantitatively from a higher-order exchange-dominated thickness mode.

Finally, we give a conclusion, containing a summary of the most important results and an outlook on interesting aspects for future studies. The subsequent appendix explains the use of the computer programs implemented to automate data acquisition and analysis.

# Chapter 1

## Basic theory of magnetization dynamics

In this chapter we first introduce the different energy terms which come into play when describing the static or dynamic behaviour of the magnetization in a ferromagnetic thin film sample (§1.1). In the following section we describe the equation of motion governing the magnetization dynamics (§1.2), from which we derive the complex dynamic susceptibility which is the quantity we intend to measure (§1.3). An alternative way to derive the resonance frequency is exposed, following the Ansatz of Smit and Beljers (§1.4). Finally, we discuss the origin of magnetization damping (§1.5) and we address the different spin waves in thin films (§1.6).

### 1.1 Energetics in Ferromagnets

The interplay between multiple interactions determines the domain structure in ferromagnets. Knowing the energy landscape created by these interactions is likewise indispensable in order to describe the dynamics. In the following we outline these interactions and give the corresponding energy terms which we will employ in the subsequent sections. We formulate the energies in the continuum model where the magnetization  $\mathbf{M}$  is given by the total of the magnetic moments divided by the enclosing volume.

- **Exchange Energy**

The exchange interaction is based on the Coulomb interaction in combination with the quantum mechanical Pauli exclusion principle, which declares that two fermions cannot be in the same state. The consequence for two atoms with the spins  $\mathbf{S}_i$  and  $\mathbf{S}_j$  is a difference in energy for parallel and antiparallel alignment of their spins. This is applied to solids in the Heisenberg model coupling  $N$  atoms, resulting in the following contribution to the total energy [25]

$$E_{\text{ex}} = - \sum_{i,j}^N J_{ij}(\mathbf{S}_i \cdot \mathbf{S}_j) = -2 \sum_{i<j}^N J_{ij}(\mathbf{S}_i \cdot \mathbf{S}_j), \quad (1.1)$$

where  $J_{ij}$  is the exchange integral. In the case of ferromagnetic ordering the sign of  $J_{ij}$  is positive, leading to a lower energy for parallel alignment of the spins.



In Eq. 1.1 the summation is sometimes limited to nearest neighbors only, as this interaction falls off rapidly with increasing distance [26]. This is justified by the fact that only the wavefunctions of nearest neighbors overlap and give a sizable contribution to the energy. Despite this limited range, the exchange interaction is at the origin of spontaneous long range ordering in ferromagnets due to its magnitude. It leads to the so-called exchange splitting between the spin-up and spin-down bands on the order of 1 eV [27].

At a mesoscopic level we make the transition to a (classical) continuum representation which is valid as long as the lengthscale is much bigger than the interatomic distance. The exchange energy density is given by [28]

$$\varepsilon_{\text{ex}} = \frac{A}{V} \int dV (\nabla \mathbf{m})^2, \quad (1.2)$$

where  $\mathbf{m} = \mathbf{M}/M_s$  is the normalized magnetization,  $\mathbf{M}$  being the magnetization vector and  $M_s$  being the saturation magnetization.  $A$  is the exchange stiffness constant, which has the dimension [energy/length] and is related to  $J$  by  $A = nJS^2/a$ , where  $a$  is the lattice constant,  $S$  is the magnitude of the spin and  $n$  is a factor depending on the crystal structure [29]. To give general guidelines, we give literature values:  $A(\text{Co}) = 28.5 \times 10^{-12}$  J/m [30],  $A(\text{Py}) \approx 10 \times 10^{-12}$  J/m [31],  $A(\text{Fe}) \approx 20 \times 10^{-12}$  J/m [32],  $A(\text{Ni}) \approx 8 \times 10^{-12}$  J/m [33]. In general, the exchange stiffness constant is on the order of  $10^{-11}$  J/m ( $1 \text{ J/m} = 10^{+5} \text{ erg/cm}$ ) [32, 28]. We will give numerical values for  $A$  extracted from our measurements in section 7.5 which we deduced from perpendicular standing spin waves introduced in section 1.6.3.

- **Zeeman Energy**

The interaction of the magnetization  $\mathbf{M}$  with an external magnetic field  $\mathbf{H}_{\text{ext}}$  is described by the energy density that follows [28]

$$\varepsilon_{\text{zee}} = -\frac{\mu_0}{V} \int dV \mathbf{M} \cdot \mathbf{H}_{\text{ext}}. \quad (1.3)$$

This energy is minimized by aligning the magnetization in the direction of the external field.

- **Demagnetizing Field Energy**

The dipolar interaction between the magnetic moments is very long ranged. It gives rise to a non-local energy contribution, as every magnetic moment interacts with the dipolar field of every other magnetic moment. This energy called demagnetizing field energy is described by [28]

$$\varepsilon_{\text{dem}} = -\frac{\mu_0}{2V} \int_{\text{sample}} dV \mathbf{M} \cdot \mathbf{H}_{\text{dem}}. \quad (1.4)$$

The demagnetizing field  $\mathbf{H}_{\text{dem}}$  created by the magnetic body itself, can be found starting from Maxwell's equation

$$\nabla \cdot \mathbf{B} = \mu_0 \nabla \cdot (\mathbf{H}_{\text{dem}} + \mathbf{M}) = 0 \quad \Rightarrow \quad \nabla \cdot \mathbf{H}_{\text{dem}} = -\nabla \cdot \mathbf{M} \quad (1.5)$$

$\mathbf{H}_{\text{dem}}$  is the field generated by the divergence of the magnetization, i.e. the presence of magnetic poles.

While the calculation of  $\mathbf{H}_{\text{dem}}$  is complicated in the general case, it is simple in the case of a uniformly magnetized ellipsoid [25]:

$$\mathbf{H}_{\text{dem}} = -\bar{\bar{N}}\mathbf{M}, \quad (1.6)$$

the demagnetizing field being a linear function of the magnetization with the location-independent demagnetizing tensor  $\bar{\bar{N}}$ . Eq. 1.4 can be expressed in a simpler form as

$$\varepsilon_{\text{dem}} = \frac{\mu_0}{2}\mathbf{M}\bar{\bar{N}}\mathbf{M}. \quad (1.7)$$

When orienting the coordinate system along the principles axes of the ellipsoid,  $\bar{\bar{N}}$  is diagonal and expressed as

$$\bar{\bar{N}} = \begin{pmatrix} N_x & 0 & 0 \\ 0 & N_y & 0 \\ 0 & 0 & N_z \end{pmatrix}. \quad (1.8)$$

The trace of the dimensionless demagnetizing tensor complies with  $N_x + N_y + N_z = 1$ . For a general ellipsoid with the axes  $(a, b, c)$ , the  $N_i$  can be calculated numerically [28]. Explicite analytical formulas for the  $N_i$  can be found for rotation ellipsoids with axes  $(a = b)$  [28].

Of particular importance within this thesis is the limit case of an oblate (disc-shaped) ellipsoid: for an infinitely extended thin film with the  $z$ -axis pointing perpendicular to the film plane one obtains  $N_x = N_y = 0$  and  $N_z = 1$ . The demagnetizing field and the corresponding energy density are expressed by

$$\mathbf{H}_{\text{dem}} = -\mathbf{e}_z(\mathbf{e}_z \cdot \mathbf{M}) \quad ; \quad \varepsilon_{\text{dem}} = \frac{\mu_0}{2}(\mathbf{e}_z \cdot \mathbf{M})^2, \quad (1.9)$$

where  $\mathbf{e}_z$  is the unit vector normal to the film plane.

- **Anisotropy Energy**

In general the energy of a magnetic sample is dependent on the direction of the magnetization. One explanation can be found in the shape anisotropy which is due to the dipolar energy. However, even in the case of an infinitely extended homogeneous sample without borders, the energy is not isotropic. This phenomenon is explained by the spin-orbit interaction: the spins are coupled to the orbital angular momentum, whose energy is connected to its orientation with respect to the crystal lattice. Through the spin-orbit coupling, the energy of the spins is also linked to the symmetry of the crystal lattice. While it is approximately 10 - 100 smaller than the exchange interaction [27], it is of considerable importance as it breaks the spatial isotropy. For cubic crystals the energy density of this so-called magnetocrystalline anisotropy is given by [28]

$$\varepsilon_{\text{ani}} = K_1(m_x^2m_y^2 + m_y^2m_z^2 + m_z^2m_x^2) + K_2m_x^2m_y^2m_z^2, \quad (1.10)$$

where  $m_i$  are the components of the normalized magnetization  $\mathbf{m}$  referring to the cubic axes of the lattice. Often this energy is written using the direction cosines of the normalized magnetization  $\alpha_i$ , which is simply the same as  $\alpha_i = \mathbf{e}_i \cdot \mathbf{m} = m_i$ .  $K_1$  assumes values in the range of  $\pm 10^4$  J/m<sup>3</sup> for different materials [28]. Literature values are often still in cgs units: [ergs/cm<sup>3</sup>] can

be simply converted to  $[\text{J}/\text{m}^3]$  by dividing by 10, e.g. the bulk anisotropy of Fe is  $4.7 \times 10^5 \text{ ergs}/\text{cm}^3 = 4.7 \times 10^4 \text{ J}/\text{m}^3$  [34]. This gives an anisotropy field  $\mu_0 H_1 = \frac{2K_1}{M_s} = 60 \text{ mT}$ , which is the quantity we measure, introduced in section 1.3.

$K_1$  and  $K_2$  are the anisotropy constants of first and second order. Third or higher order terms are negligibly small [28].

A uniaxial magnetocrystalline anisotropy is often observed. Its energy density is described by

$$\varepsilon_{\text{uni}} = -K_u m_x^2, \quad (1.11)$$

where  $K_u$  is the uniaxial anisotropy constant. For  $K_u > 0$  the x-axis becomes a so-called easy axis, i.e. the energy is minimal when the magnetization is aligned in parallel. For  $K_u < 0$  the x-axis is a hard axis and the magnetization tends to align in the plane perpendicular to it. Uniaxial anisotropies can be very strong, reaching  $10^7 \text{ J}/\text{m}^3$  for rare earth transition metal permanent magnets [28]. For commonly employed materials they are often deliberately minimized, e.g. for evaporated Permalloy films  $K_u \approx 10^2 \text{ J}/\text{m}^3$ , expressed as an anisotropy field  $\mu_0 H_u = \frac{2K_u}{M_s} = 0.2 \text{ mT}$ .

Apart from the volume anisotropies described above, in thin films surface anisotropies become important. This effect which is negligible in bulk samples is attributed to the reduced symmetry of the atomic environment of surface atoms. It is described using a phenomenological uniaxial perpendicular anisotropy parameter  $K_\perp$  as

$$\varepsilon_{\text{sur}} = -\frac{K_\perp}{d} m_z^2, \quad (1.12)$$

where  $d$  is the film thickness.  $K_\perp$  is also often given in cgs-units: to convert from  $[\text{ergs}/\text{cm}^2]$  to  $[\text{J}/\text{m}^2]$  one has to divide by 1000. An example for Fe in an Fe/Au multilayer is  $0.38 \text{ mJ}/\text{m}^2$  [35]. For very thin layers ( $< 1 \text{ nm}$ ) this can even dominate the demagnetization energy and lead to a stabilization of a perpendicular magnetization direction.

Summing up the different contributions, we can now calculate the total energy density as

$$\varepsilon_{\text{tot}} = \varepsilon_{\text{ex}} + \varepsilon_{\text{zee}} + \varepsilon_{\text{dem}} + \varepsilon_{\text{ani}} + \varepsilon_{\text{uni}} + \varepsilon_{\text{sur}}. \quad (1.13)$$

We will choose the contributing energies depending on the examined sample. We remind that finding the minima in Eq. 1.13 permits to determine the different static equilibrium configurations of the magnetization.

The total energy density allows us to introduce the total effective magnetic field  $\mathbf{H}_{\text{eff}}$  [36]: it is defined as the functional derivative of  $\varepsilon_{\text{tot}}$  with respect to the magnetization  $\mathbf{M}$  as

$$\mathbf{H}_{\text{eff}} = -\frac{1}{\mu_0} \nabla_{\mathbf{M}} \varepsilon_{\text{tot}} \quad (1.14)$$

We will see in the following section that  $\mathbf{H}_{\text{eff}}$  represents the instantaneous axis of magnetization precession.

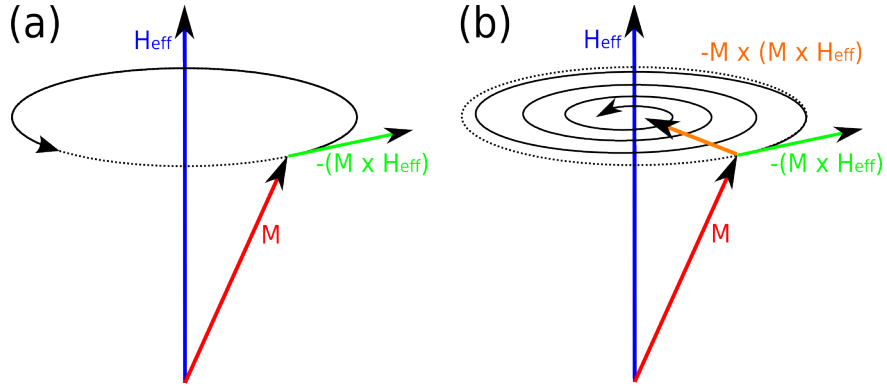


Figure 1.1: (Color online) (a) The magnetization  $\mathbf{M}$  (red) precesses counterclockwise around the effective field  $\mathbf{H}_{\text{eff}}$  (blue) following the Landau-Lifshitz equation (green, Eq. 1.15). (b) Adding the phenomenological damping term (orange) causes the magnetization motion to relax in the direction of  $\mathbf{H}_{\text{eff}}$ .

## 1.2 Magnetization Dynamics

Having introduced in the last section the effective magnetic field  $\mathbf{H}_{\text{eff}}$  which determines the static equilibrium orientation, we now introduce the dynamical model proposed by Landau and Lifshitz (LL) in 1935:

$$\frac{d\mathbf{M}}{dt} = -\gamma\mu_0\mathbf{M} \times \mathbf{H}_{\text{eff}}, \quad (1.15)$$

with the gyromagnetic ratio  $\gamma = g|e|/(2m_e)$ , choosing the convention of a positive  $\gamma$ .  $g$  is the g-factor,  $e$  the electron charge and  $m_e$  the electron mass. To give an example, assuming  $g = 2.1$  we find  $\gamma = 184.7 \times 10^9 \text{ rad}/(\text{sT})$ .

According to the LL model the total magnetic moment is connected to a total angular momentum which is subject to a torque, resulting in a precessional motion. However, the behavior predicted by Eq. 1.15 in the case of a misalignment of the magnetization with respect to  $\mathbf{H}_{\text{eff}}$  does not correspond to experimental observation: An undamped precession with a constant cone angle is anticipated, but in practice the magnetization aligns after a finite time with the direction of minimal energy (see Fig. 1.1). Landau and Lifshitz amended this inconsistency by adding a phenomenological dissipation term [37]:

$$\frac{d\mathbf{M}}{dt} = -\gamma\mu_0\mathbf{M} \times \mathbf{H}_{\text{eff}} - \frac{\lambda}{M_s^2}\mathbf{M} \times (\mathbf{M} \times \mathbf{H}_{\text{eff}}), \quad (1.16)$$

with the phenomenological damping constant  $\lambda > 0$  having the dimension of a frequency. We point out that Eq. 1.16 conserves the magnitude of the magnetization according to the micromagnetic constraint  $|\mathbf{M}| = M_s$ .

While Eq. 1.16 can account for experimental observations, the most often employed equation of motion is the so-called Landau-Lifshitz-Gilbert (LLG) equation. It consists of the same precessional term as in the LL equation (Eq. 1.15) but combined with a different damping term. This phenomenological dissipation term after Gilbert (1955) models a 'viscous' damping, depending on the time derivative of the magnetization. The LLG equation [38] is given by

$$\frac{d\mathbf{M}}{dt} = -\gamma\mu_0\mathbf{M} \times \mathbf{H}_{\text{eff}} + \frac{\alpha}{M_s} \left( \mathbf{M} \times \frac{d\mathbf{M}}{dt} \right), \quad (1.17)$$

with the phenomenological dimensionless Gilbert damping parameter  $\alpha$ . As already for the LL model, the magnitude of the magnetization is conserved by the LLG equation.

The LLG equation (Eq. 1.17) can be transformed into a form similar to the LL equation (Eq. 1.16) [27]:

$$\frac{d\mathbf{M}}{dt} = -\frac{\gamma\mu_0}{1+\alpha^2}\mathbf{M} \times \mathbf{H}_{\text{eff}} - \frac{\gamma\mu_0\alpha}{M_s(1+\alpha^2)}\mathbf{M} \times (\mathbf{M} \times \mathbf{H}_{\text{eff}}). \quad (1.18)$$

One can see the mathematical equivalence between Eq. 1.18 and Eq. 1.16 when assuming

$$\gamma_{\text{LL}} = \frac{\gamma_{\text{Gilb}}}{1+\alpha^2} \quad ; \quad \lambda = \frac{\alpha\gamma_{\text{Gilb}}\mu_0 M_s}{1+\alpha^2}. \quad (1.19)$$

While mathematically equivalent, the two equations do not lead to the same magnetization dynamics for infinitely high damping: The LLG equation results in  $(d\mathbf{M})/(dt) \rightarrow 0$  for  $\alpha \rightarrow \infty$ . In contrast, the LL equation results in  $(d\mathbf{M})/(dt) \rightarrow \infty$  for  $\lambda \rightarrow \infty$ . As only the behavior predicted by the LLG equation is physical for large damping, we will use it exclusively in the following.

We insist on the fact that the damping term is phenomenological, i.e. it was specifically introduced to imitate in the best conceivable manner the experimental observation. However, the processes of energy dissipation in ferromagnets are numerous and complicated and can be only approximately described by a single damping parameter. In section 1.5 we will give an overview of contributions to energy dissipation and thus to  $\alpha$ .

As one of the processes analyzed in that section does not conserve the magnitude of the magnetization, we introduce the equation of motion after Bloch-Bloembergen (BB), which is better suited to describe such behavior. The BB equation reads [39]

$$\frac{d\mathbf{M}}{dt} = -\gamma\mu_0\mathbf{M} \times \mathbf{H}_{\text{eff}} - \frac{(\mathbf{e}_x \cdot \mathbf{M})}{T_2}\mathbf{e}_x - \frac{(\mathbf{e}_y \cdot \mathbf{M})}{T_2}\mathbf{e}_y - \frac{(\mathbf{e}_z \cdot \mathbf{M} - M_s)}{T_1}\mathbf{e}_z, \quad (1.20)$$

where the z-axis is aligned with the equilibrium direction of the magnetization. Instead of a single relaxation parameter, two independent relaxation times are used: The *transverse relaxation time*  $T_2$ , which describes the relaxation of the magnetization in the equilibrium direction and which reduces the magnitude of  $\mathbf{M}$ , and the *longitudinal relaxation time*  $T_1$  describing the relaxation along the equilibrium direction towards the full magnitude of the magnetization ( $M_s$ ). Only for the special case of small angle excitations and  $T_1 = T_2/2$  the magnitude of the magnetization is conserved by the BB equation. We will come back to a more precise interpretation of this equation in section 1.5.3.

### 1.3 Dynamic Susceptibility

Finding an analytical solution for the LLG differential equation (Eq. 1.17) is not feasible in a general form. Therefore, we resolve it for the special case under the following assumptions:

- Our sample is an (infinitely extended) thin film in the x-y plane. We can use the demagnetizing factors  $N_x = N_y = 0$  and  $N_z = 1$  and resort to Eq. 1.9.

- We assume a uniform uniaxial in-plane magnetocrystalline anisotropy with an easy axis along x, where the anisotropy field  $H_{\text{uni}} \ll M_s$  (see Eq. 1.24).
- A uniaxial perpendicular anisotropy caused by the two surfaces is also present. We assume that it is not so high as to outweigh the demagnetizing field, i.e. the effective magnetization remains positive in Eq. 1.24.
- Under the influence of a homogenous magnetic field  $\mathbf{H}_{\text{ext}}$  which we apply in the plane along the x-axis, the magnetization is uniformly pointing in that direction.
- The magnetization is treated in the macrospin model, i.e. a model in which no spatial variation of the magnetization is allowed [40].
- Corresponding to our experimental situation, we assume a small uniform excitation field  $\mathbf{h}$  pointing along the y-axis, i.e. perpendicular to  $\mathbf{H}_{\text{ext}}$ .

As  $\mathbf{h} \ll \mathbf{H}_{\text{ext}}$ , we expect the excitation field to sustain a precession with a very small angle around the x-axis. This allows us to decompose the magnetization into a static and a dynamic part as follows

$$\mathbf{M} = M_s \mathbf{m} \approx M_s \mathbf{e}_x + m_y \mathbf{e}_y + m_z \mathbf{e}_z, \quad (1.21)$$

where  $M_s$  is the saturation magnetization and  $m_y$  and  $m_z$  are the oscillating high frequency components of the magnetization. In order to prevent misunderstanding, we emphasize that  $m_y$ ,  $m_z$  and  $h$  are not used as dimensionless variables, but all have the dimension of a magnetic field strength [A/m]. We can now combine the Eqs. 1.3, 1.9, 1.11, 1.12 to the total energy density, which is

$$\varepsilon_{\text{tot}} = -\mu_0 \mathbf{M} \cdot \mathbf{H}_{\text{ext}} + \frac{\mu_0}{2} (\mathbf{e}_z \cdot \mathbf{M})^2 - \frac{K_{\perp}}{d} (\mathbf{e}_z \cdot \mathbf{m})^2 - K_u (\mathbf{e}_x \cdot \mathbf{m})^2. \quad (1.22)$$

Including the small excitation field, we find after Eq. 1.14:

$$\mathbf{H}_{\text{eff}} = \mathbf{H}_{\text{ext}} + \mathbf{h} - \mathbf{e}_z (\mathbf{e}_z \cdot \mathbf{M}) + \frac{2K_{\perp}}{d\mu_0 M_s} \mathbf{e}_z (\mathbf{e}_z \cdot \mathbf{m}) + \frac{2K_u}{\mu_0 M_s} \mathbf{e}_x (\mathbf{e}_x \cdot \mathbf{m}). \quad (1.23)$$

We introduce the anisotropy field  $H_{\text{uni}}$  containing the uniaxial anisotropy and we contract the demagnetizing and perpendicular anisotropy contributions by introducing the effective magnetization  $M_{\text{eff}}$  (as they show the same symmetry):

$$H_{\text{uni}} = \frac{2K_u}{\mu_0 M_s} \quad ; \quad M_{\text{eff}} = M_s - \frac{2K_{\perp}}{d\mu_0 M_s}. \quad (1.24)$$

Introducing Eq. 1.21 and Eq. 1.24 in Eq. 1.23 we obtain

$$\mathbf{H}_{\text{eff}} = (H_{\text{ext}} + H_{\text{uni}}) \mathbf{e}_x + h \mathbf{e}_y - \frac{M_{\text{eff}}}{M_s} m_z \mathbf{e}_z. \quad (1.25)$$

Inserted into Eq. 1.17, we find

$$0 = -\gamma \mu_0 \left( -m_y \frac{M_{\text{eff}}}{M_s} m_z - m_z h \right) + \frac{\alpha}{M_s} \left( m_y \frac{dm_z}{dt} - m_z \frac{dm_y}{dt} \right) \quad (1.26)$$

$$\frac{dm_y}{dt} = -\gamma \mu_0 (m_z (H_{\text{ext}} + H_{\text{uni}}) + M_{\text{eff}} m_z) - \alpha \frac{dm_z}{dt} \quad (1.27)$$

$$\frac{dm_z}{dt} = -\gamma \mu_0 (M_s h - m_y (H_{\text{ext}} + H_{\text{uni}})) + \alpha \frac{dm_y}{dt}. \quad (1.28)$$

We linearize this set of equations in  $h$  and  $m_i$  by dropping terms which contain products of these quantities. Next we introduce the time dependence of the expected oscillating motion as  $m_i = \text{Re}(\tilde{m}_i e^{i\omega t})$ , according to the excitation field as  $h = \text{Re}(\tilde{h} e^{i\omega t})$ . While  $\tilde{h}$  is real, the  $\tilde{m}_i$  are complex values, where  $\text{Re}(\tilde{m}_i)$  is in phase with  $\tilde{h}$  and  $\text{Im}(\tilde{m}_i)$  is in quadrature. We use the exponential notation to eliminate the time dependence. The remaining two equations are:

$$0 = \tilde{m}_y(i\omega) + \tilde{m}_z(\omega_H + \omega_{\text{eff}} + i\omega\alpha) \quad (1.29)$$

$$\omega_M \tilde{h} = \tilde{m}_y(i\omega\alpha + \omega_H) + \tilde{m}_z(-i\omega), \quad (1.30)$$

with the following convenient abbreviations

$$\omega_H = \gamma\mu_0(H_{\text{ext}} + H_{\text{uni}}) \quad ; \quad \omega_M = \gamma\mu_0 M_s \quad ; \quad \omega_{\text{eff}} = \gamma\mu_0 M_{\text{eff}}. \quad (1.31)$$

We can rewrite the equations as a relation between  $\mathbf{h} = (\tilde{h}, 0)$  and  $\mathbf{m} = (\tilde{m}_y, \tilde{m}_z)$  as follows

$$\begin{pmatrix} \tilde{h} \\ 0 \end{pmatrix} \omega_M = \begin{bmatrix} \omega_H + i\omega\alpha & -i\omega \\ i\omega & \omega_H + \omega_{\text{eff}} + i\omega\alpha \end{bmatrix} \begin{pmatrix} \tilde{m}_y \\ \tilde{m}_z \end{pmatrix}. \quad (1.32)$$

To extract the susceptibility tensor  $\bar{\chi}$  after Polder[41], we now only need to invert the matrix in order to find

$$\begin{pmatrix} \tilde{m}_y \\ \tilde{m}_z \end{pmatrix} = \mathbf{m} = \bar{\chi} \mathbf{h} = \begin{bmatrix} \chi_{yy} & \chi_{yz} \\ \chi_{zy} & \chi_{zz} \end{bmatrix} \begin{pmatrix} \tilde{h} \\ 0 \end{pmatrix}, \quad (1.33)$$

where we find

$$\begin{pmatrix} \tilde{m}_y \\ \tilde{m}_z \end{pmatrix} = \frac{\omega_M}{\omega_H(\omega_{\text{eff}} + \omega_H) - \omega^2 + i\omega\alpha(2\omega_H + \omega_{\text{eff}})} \begin{bmatrix} \omega_H + \omega_{\text{eff}} + i\omega\alpha & i\omega \\ -i\omega & \omega_H + i\omega\alpha \end{bmatrix} \begin{pmatrix} \tilde{h} \\ 0 \end{pmatrix}. \quad (1.34)$$

As we suppose that  $\alpha \ll 1$ , we simplify during the calculation using  $1 + \alpha^2 \approx 1$ . We measure the component  $\chi_{yy}$  of the susceptibility tensor. The real and the imaginary parts  $\chi'_{yy} - i\chi''_{yy}$  (negative sign following common usage) are

$$\chi'_{yy} = \frac{\omega_M(\omega_H + \omega_{\text{eff}})(\omega_{\text{res}}^2 - \omega^2)}{(\omega_{\text{res}}^2 - \omega^2)^2 + \alpha^2\omega^2(2\omega_H + \omega_{\text{eff}})^2} \quad (1.35)$$

$$\chi''_{yy} = \frac{\alpha\omega\omega_M[\omega^2 + (\omega_H + \omega_{\text{eff}})^2]}{(\omega_{\text{res}}^2 - \omega^2)^2 + \alpha^2\omega^2(2\omega_H + \omega_{\text{eff}})^2}, \quad (1.36)$$

where we introduced the resonance frequency  $\omega_{\text{res}}$  defined by

$$\omega_{\text{res}}^2 = \omega_H(\omega_{\text{eff}} + \omega_H). \quad (1.37)$$

The real part  $\chi'_{yy}$  expresses the component of  $\tilde{m}_y$  which is in phase with  $\tilde{h}$ , while  $\chi''_{yy}$  expresses its component which is delayed by a phase angle of  $90^\circ$  from  $\tilde{h}$ . Hence,  $\omega_{\text{res}}$  marks the frequency where  $\tilde{m}_y$  and  $\tilde{h}$  are out-of-phase by  $90^\circ$ , as  $\chi'_{yy}(\omega_{\text{res}}) = 0$ . In the absence of losses,  $\chi_{yy} = \chi'_{yy}$ . The presence of the component  $\chi''_{yy}$  requires a supply of energy to maintain the alternating magnetization [29].

For completeness, we also list the other components of the susceptibility tensor:

$$\chi'_{yz} = -\chi'_{zy} = \frac{\alpha\omega\omega_M(2\omega_H + \omega_{\text{eff}})}{(\omega_{\text{res}}^2 - \omega^2)^2 + \alpha^2\omega^2(2\omega_H + \omega_{\text{eff}})^2} \quad (1.38)$$

$$\chi''_{yz} = -\chi''_{zy} = \frac{\omega(\omega_{\text{res}}^2 - \omega^2)}{(\omega_{\text{res}}^2 - \omega^2)^2 + \alpha^2\omega^2(2\omega_H + \omega_{\text{eff}})^2} \quad (1.39)$$

$$\chi'_{zz} = \frac{\omega_M\omega_H(\omega_{\text{res}}^2 - \omega^2)}{(\omega_{\text{res}}^2 - \omega^2)^2 + \alpha^2\omega^2(2\omega_H + \omega_{\text{eff}})^2} \quad (1.40)$$

$$\chi''_{zz} = \frac{\alpha\omega\omega_M[\omega^2 + \omega_H^2]}{(\omega_{\text{res}}^2 - \omega^2)^2 + \alpha^2\omega^2(2\omega_H + \omega_{\text{eff}})^2}. \quad (1.41)$$

This also allows us to examine the ellipticity of the forced precession. We compare the maxima of  $m_y$  and  $m_z$  reached at any moment in time, which corresponds to the following ratio:

$$\frac{\max(m_y)}{\max(m_z)} = \frac{\max(\text{Re}(\tilde{m}_y e^{i\omega t}))}{\max(\text{Re}(\tilde{m}_z e^{i\omega t}))} = \frac{|\tilde{m}_y|}{|\tilde{m}_z|} = \frac{|\chi_{yy}|}{|\chi_{zy}|} \approx \sqrt{\frac{(\omega_H + \omega_{\text{eff}})^2}{\omega^2}} = \frac{\omega_H + \omega_{\text{eff}}}{\omega}. \quad (1.42)$$

The magnetization component out of the film plane increases with increasing excitation frequency, but is much smaller than the in-plane component for usual frequencies, e.g. at resonance we find

$$\frac{\max(m_y)}{\max(m_z)} \approx \sqrt{\frac{(\omega_H + \omega_{\text{eff}})^2}{\omega_{\text{res}}^2}} = \sqrt{\frac{\omega_H + \omega_{\text{eff}}}{\omega_H}}. \quad (1.43)$$

A calculated example of  $\chi_{yy}$  is presented in Fig.1.2. In order to make sure that  $\alpha \ll 1$  leads to a good approximation, we also calculated  $\omega_{\text{res}}$  without neglecting the corresponding terms, which leads to

$$\omega_{\text{res}}^2 = \frac{\omega_H(\omega_{\text{eff}} + \omega_H)^2}{\omega_{\text{eff}} + \omega_H - \alpha^2\omega_H}. \quad (1.44)$$

This is obviously equivalent to Eq. 1.37 in the case of  $\alpha$  being small. For usual material parameters and an external magnetic field leading to resonance frequencies of several GigaHz, the corrections don't exceed some tens of kiloHz and are far below the contributions from  $H_{\text{ext}}$ ,  $H_{\text{uni}}$  and  $M_{\text{eff}}$ .

The imaginary part of the susceptibility  $\chi''_{yy}$  represents the absorption of the electromagnetic energy provided by the small excitation field  $h$ .  $\chi''_{yy}$  has a Lorentzian line shape and reaches a maximum for the ferromagnetic resonance frequency  $\omega_{\text{res}}$ , which is given by

$$\text{Max}(\chi''_{yy}) = \frac{\omega_M}{\alpha} \frac{\sqrt{\omega_{\text{eff}} + \omega_H}}{(\omega_{\text{eff}} + 2\omega_H)\sqrt{\omega_H}} \approx \frac{\omega_M}{\alpha\omega_{\text{res}}}. \quad (1.45)$$

The real part  $\chi'_{yy}$  represents the dispersion and is antisymmetric around  $\omega_{\text{res}}$  reaching 0 at this particular frequency. It has been shown that the saturation magnetization is related to the imaginary part of the susceptibility by an integral criteria: In the thin film case with an uniaxial in-plane anisotropy, the following integral of the frequency-weighted  $\chi''_{yy}$  is valid independently of the external applied field and the anisotropy field [42]:

$$I = \int_0^{+\infty} f\chi''_{yy} df \approx \frac{\pi}{2} \left( \frac{\gamma\mu_0}{2\pi} M_s \right)^2. \quad (1.46)$$



As this equation is also applicable to measurements having a limited frequency range, it can be used to check the accuracy of susceptibility measurements [42, 43].

It is also of interest to observe the low frequency limit: while the imaginary part tends to 0, the real part tends to

$$\chi_{\text{stat}} = \chi'_{\text{stat}} = \frac{\omega_M}{\omega_H} = \frac{M_s}{H_{\text{ext}} + H_{\text{uni}}}, \quad (1.47)$$

which is well known from static susceptibility measurements.

Another important frequency is the antiresonance frequency  $\omega_{\text{antires}}$ . At this frequency the real part of the high-frequency permeability is equal to 0, corresponding to  $\chi'_{yy} = -1$ . At the same frequency  $\chi''_{yy}$  is small, while in contrast it passes through a maximum at the resonance frequency. The condition for antiresonance is

$$\omega_{\text{antires}} = \sqrt{(\omega_{\text{eff}} + \omega_H)(\omega_M + \omega_H)} \approx \omega_{\text{eff}} + \omega_H. \quad (1.48)$$

We cannot measure at these high frequencies, as e.g. for Fe:  $\omega_{\text{antires}}/(2\pi) \geq 60$  GHz. Nevertheless, it still is theoretically interesting, as the skin depth is increased appreciably at  $\omega_{\text{antires}}$  [44]. Indeed, only because of the presence of damping the skin depth remains finite, as without damping  $\chi_{yy}$  would be purely real and the skin depth would diverge, making the magnetic sample completely transparent for the microwaves. Therefore, it is assured that Eddy currents, which we will introduce in section 1.5.2, don't interfere with the measurement of the intrinsic damping and measuring the antiresonance allows for a precise determination of  $\alpha$  [33].

The obtained solution for the resonance frequency is a special case of the well-known Kittel formula [8] determining the resonance frequency in an ellipsoidal sample:

$$\omega_{\text{res}}^2 = (\omega_H + (N_z - N_x)\omega_M)(\omega_H + (N_y - N_x)\omega_M). \quad (1.49)$$

The transition is achieved by going to the thin film geometry ( $N_z = 1$ ) with an additional surface anisotropy ( $\omega_M \rightarrow \omega_{\text{eff}}$ ).

The frequency linewidth  $\Delta\omega$ , which is defined as the Full Width at Half Maximum (FWHM) of the imaginary part of the susceptibility, is described by

$$\Delta\omega = \alpha(2\omega_H + \omega_{\text{eff}}). \quad (1.50)$$

One has to bear in mind that  $\chi''_{yy}$  is not precisely symmetric around  $\omega_{\text{res}}$  and therefore, this is a slight approximation.

$\Delta\omega$  can also be obtained by calculating the difference of the frequencies of the maximum and the minimum in the real part  $\chi'_{yy}$  as a peak-to-peak linewidth  $\Delta\omega_{\text{pp}}$ . This seems a convenient alternative, as it is easier to extract the frequencies of the two extrema than to implement a fit using Eq. 1.36. Their positions can be easily obtained from the roots of the derivative of  $\chi'_{yy}$ . We find

$$\omega_{\text{Max}} = \omega_{\text{res}} \sqrt{1 - \frac{\alpha(2\omega_H + \omega_{\text{eff}})}{\omega_{\text{res}}}} \quad (1.51)$$

$$\omega_{\text{Min}} = \omega_{\text{res}} \sqrt{1 + \frac{\alpha(2\omega_H + \omega_{\text{eff}})}{\omega_{\text{res}}}}, \quad (1.52)$$

where  $\omega_{\text{res}}$  was defined in Eq. 1.37.  $\Delta\omega_{\text{pp}} = \omega_{\text{Min}} - \omega_{\text{Max}}$  converges to  $\Delta\omega$  as defined in Eq. 1.50 when  $\Delta\omega \ll \omega_{\text{res}}$ . For usual material parameters,  $\Delta\omega_{\text{pp}} - \Delta\omega$  becomes

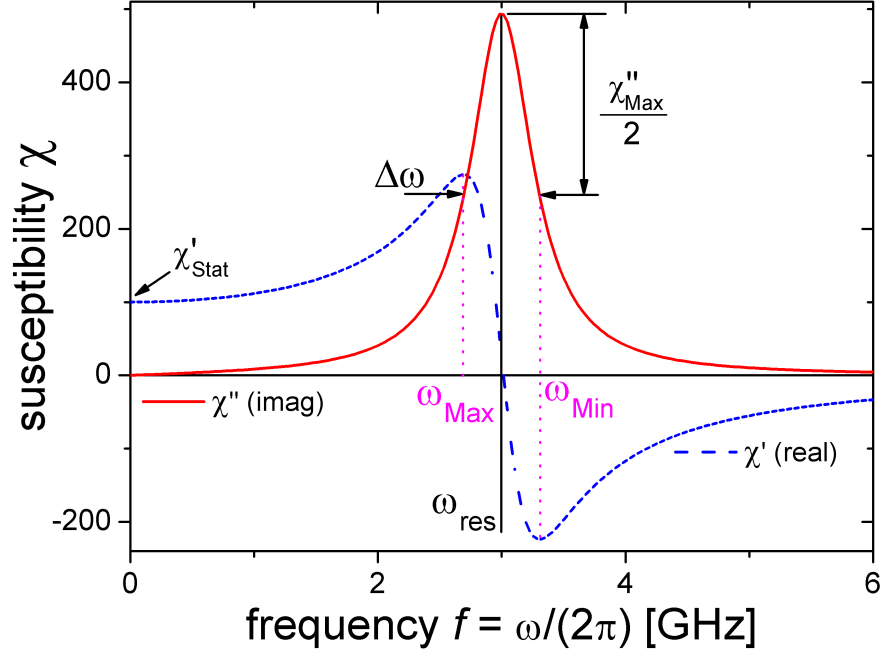


Figure 1.2: (Color online) The real (dashed blue line) and imaginary (plain red line) parts of the transverse complex susceptibility  $\chi_{yy}$  (see Eqs. 1.35, 1.36). We used  $\gamma/(2\pi) = 30$  GHz/T,  $\mu_0 M_S = 1$  T  $\approx \mu_0 M_{\text{eff}}$ ,  $\mu_0(H_{\text{ext}} + H_{\text{uni}}) = 0.01$  T and  $\alpha = 0.02$ .

negligible for a resonance frequency greater than a few hundred MegaHz. Nevertheless, this has to be kept in mind when evaluating linewidth data at very low frequencies, where a fit of  $\chi$  is preferable to simply calculating  $\Delta\omega_{\text{pp}}$  from the real part in order to determine the frequency linewidth.

To find further information on the calculation of the susceptibility under different conditions, in different materials and in the field as well as in the frequency domain, we refer the reader to [33]. As we refer to it later, we still introduce the (full width at half maximum) field linewidth  $\Delta H$ , which is related to  $\alpha$  as [45]

$$\mu_0 \Delta H = 2 \frac{\alpha}{\gamma} \omega_{\text{res}}. \quad (1.53)$$

$\Delta H$  is measured by sweeping the external field instead of the frequency, while keeping the frequency at a constant value. This can be done using an experimental setup similar to the one used here (see e.g. [46]), and  $\Delta H$  is also the linewidth measured in classical FMR (see section 2.1.1).

## 1.4 Smit & Beljers resonance formula

In the last section we derived the resonance frequency  $\omega_{\text{res}}$  after calculating the dynamic susceptibility. It is also possible to deduce it directly from the total energy density  $\varepsilon_{\text{tot}}$  by using the Ansatz after Smit and Beljers [47], which we will derive in the following. It was found simultaneously and independently by Suhl [48] and by Gilbert [38].

We first introduce spherical coordinates (see Fig. 1.3). The unit vectors of this

orthogonal coordinate system which moves with the magnetization is given by

$$\mathbf{e}_\rho = \begin{pmatrix} \sin \theta \cos \phi \\ \sin \theta \sin \phi \\ \cos \theta \end{pmatrix} ; \quad \mathbf{e}_\theta = \begin{pmatrix} \cos \theta \cos \phi \\ \cos \theta \sin \phi \\ -\sin \theta \end{pmatrix} ; \quad \mathbf{e}_\phi = \begin{pmatrix} -\sin \phi \\ \cos \phi \\ 0 \end{pmatrix}. \quad (1.54)$$

Under the condition  $M_s = \text{const.}$ , the magnetization is conveniently expressed as

$$\mathbf{M} = M_s \mathbf{m} = M_s (m_x \mathbf{e}_x + m_y \mathbf{e}_y + m_z \mathbf{e}_z) \quad (1.55)$$

$$= M_s (\sin \theta \cos \phi \mathbf{e}_x + \sin \theta \sin \phi \mathbf{e}_y + \cos \theta \mathbf{e}_z) \quad (1.56)$$

$$= M_s \mathbf{e}_\rho + 0 \mathbf{e}_\theta + 0 \mathbf{e}_\phi. \quad (1.57)$$

In order to express the Landau-Lifshitz equation in the mobile coordinate system, we remind the time derivatives of the unit vectors:

$$\frac{\partial \mathbf{e}_\rho}{\partial t} = \dot{\mathbf{e}}_\rho = \sin \theta \dot{\phi} \mathbf{e}_\phi + \dot{\theta} \mathbf{e}_\theta \quad (1.58)$$

$$\frac{\partial \mathbf{e}_\theta}{\partial t} = \dot{\mathbf{e}}_\theta = -\dot{\theta} \mathbf{e}_\rho + \cos \theta \dot{\phi} \mathbf{e}_\phi \quad (1.59)$$

$$\frac{\partial \mathbf{e}_\phi}{\partial t} = \dot{\mathbf{e}}_\phi = -\dot{\phi} (\sin \theta \mathbf{e}_\rho + \cos \theta \mathbf{e}_\theta). \quad (1.60)$$

When writing the effective magnetic field which we introduced in Eq. 1.14 in spherical coordinates

$$\mathbf{H}_{\text{eff}} = H_\rho \mathbf{e}_\rho + H_\theta \mathbf{e}_\theta + H_\phi \mathbf{e}_\phi, \quad (1.61)$$

we can finally write the Landau-Lifshitz equation (Eq. 1.15) in  $(\mathbf{e}_\rho, \mathbf{e}_\theta, \mathbf{e}_\phi)$ :

$$\frac{d\mathbf{M}}{dt} = \begin{pmatrix} 0 \\ \dot{\theta} M_s \\ \dot{\phi} \sin \theta M_s \end{pmatrix} = \begin{pmatrix} 0 \\ \gamma \mu_0 H_\phi M_s \\ -\gamma \mu_0 H_\theta M_s \end{pmatrix} = -\gamma \mu_0 \mathbf{M} \times \mathbf{H}_{\text{eff}}. \quad (1.62)$$

In thermal equilibrium the total energy density is minimal. Hence, we can find the equilibrium orientation of the magnetization  $(\theta_0, \phi_0)$  as

$$\varepsilon_\theta = \left. \frac{\partial \varepsilon_{\text{tot}}}{\partial \theta} \right|_{\theta=\theta_0} = 0 \quad \text{and} \quad \varepsilon_\phi = \left. \frac{\partial \varepsilon_{\text{tot}}}{\partial \phi} \right|_{\phi=\phi_0} = 0. \quad (1.63)$$

However, we are in a non-equilibrium state, as we excite the magnetization to a small angle oscillation, which is described by

$$\theta = \theta_0 + \delta\theta ; \quad \delta\theta \ll \theta_0 \quad (1.64)$$

$$\phi = \phi_0 + \delta\phi ; \quad \delta\phi \ll \phi_0. \quad (1.65)$$

Eq. 1.63 is no longer valid, but as we imposed a small deflection, we can use a linear development:

$$\varepsilon_\theta = \varepsilon_{\theta\theta} \delta\theta + \varepsilon_{\theta\phi} \delta\phi \quad (1.66)$$

$$\varepsilon_\phi = \varepsilon_{\phi\theta} \delta\theta + \varepsilon_{\phi\phi} \delta\phi, \quad (1.67)$$

where  $\varepsilon_{ij}$  are the second partial derivatives of  $\varepsilon_{\text{tot}}$  after  $i$  and  $j$ .

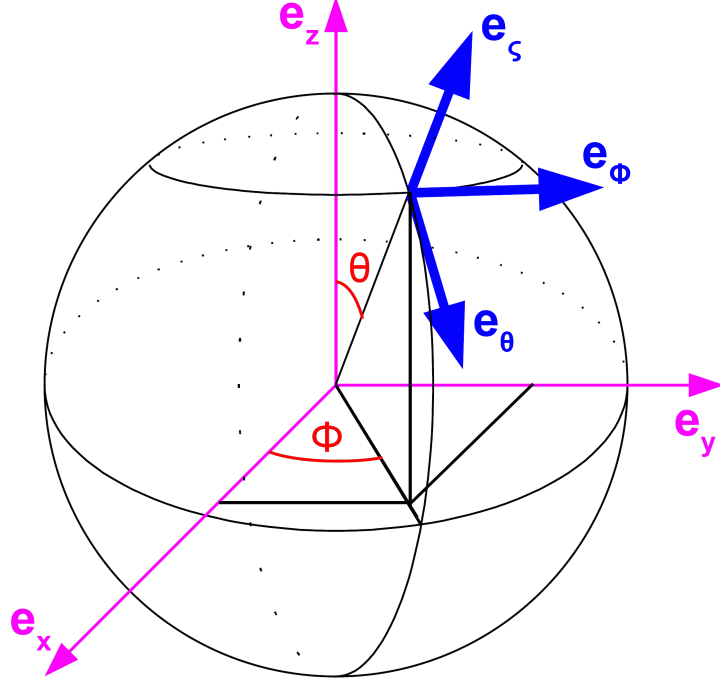


Figure 1.3: (Color online) Spherical coordinates used during the derivation of the Smit and Beljers resonance formula.  $\mathbf{M}$  is pointing along  $\mathbf{e}_\rho$ .

When writing the del operator  $\nabla$  in spherical coordinates

$$\nabla f = \frac{\partial f}{\partial \rho} \mathbf{e}_\rho + \frac{1}{\rho} \frac{\partial f}{\partial \theta} \mathbf{e}_\theta + \frac{1}{\rho \sin \theta} \frac{\partial f}{\partial \phi} \mathbf{e}_\phi, \quad (1.68)$$

we can express the effective field (Eq. 1.14) using the derivatives of  $\varepsilon_{\text{tot}}$ , which gives

$$H_\theta = -\frac{\varepsilon_\theta}{\mu_0 M_s} \quad \text{and} \quad H_\phi = -\frac{\varepsilon_\phi}{\mu_0 M_s \sin \theta}. \quad (1.69)$$

We combine Eqs. 1.62 with the subsequent equations to find

$$\frac{M_s}{\gamma} \sin \theta_0 \frac{\partial \theta}{\partial t} = \varepsilon_{\phi\theta} \delta\theta + \varepsilon_{\phi\phi} \delta\phi \quad (1.70)$$

$$-\frac{M_s}{\gamma} \sin \theta_0 \frac{\partial \phi}{\partial t} = \varepsilon_{\theta\theta} \delta\theta + \varepsilon_{\theta\phi} \delta\phi, \quad (1.71)$$

where we used

$$\sin(\theta_0 + \delta\theta) = \sin \theta_0 \cos \delta\theta + \cos \theta_0 \sin \delta\theta \approx \sin \theta_0 + \cos \theta_0 \delta\theta \approx \sin \theta_0. \quad (1.72)$$

As we suppose an harmonic excitation of the magnetization motion, we are searching now for periodic solutions in the form  $\delta\theta = \text{Re}(\delta\tilde{\theta}e^{i\omega t})$  and  $\delta\phi = \text{Re}(\delta\tilde{\phi}e^{i\omega t})$ . Therefore,  $\delta\dot{\theta} = i\omega\delta\tilde{\theta}$  and  $\delta\dot{\phi} = i\omega\delta\tilde{\phi}$ . We now write the homogenous system of equations in matrix form:

$$0 = \begin{bmatrix} \varepsilon_{\phi\theta} - i\omega \frac{M_s \sin \theta_0}{\gamma} & \varepsilon_{\phi\phi} \\ \varepsilon_{\theta\theta} & \varepsilon_{\theta\phi} + i\omega \frac{M_s \sin \theta_0}{\gamma} \end{bmatrix} \begin{pmatrix} \delta\tilde{\theta} \\ \delta\tilde{\phi} \end{pmatrix}. \quad (1.73)$$

We find nontrivial solutions if the determinant is equal to 0, which is fulfilled under the following condition:

$$\omega_{\text{res}} = \frac{\gamma}{M_s \sin \theta_0} \sqrt{\frac{\partial^2 \varepsilon_{\text{tot}}}{\partial \phi^2} \frac{\partial^2 \varepsilon_{\text{tot}}}{\partial \theta^2} - \left( \frac{\partial^2 \varepsilon_{\text{tot}}}{\partial \phi \partial \theta} \right)^2} \Bigg|_{\theta=\theta_0, \phi=\phi_0}. \quad (1.74)$$

This general expression, which is called the Smit and Beljers formula, relates the resonance frequency to the curvature of the total energy at its minimum. It has evolved to the standard method in ferromagnetic resonance to determine the precessional frequency. In comparison with the derivation of  $\omega_{\text{res}}$  in the last section, it offers the possibility to easily integrate different directions of the applied field and the magnetization. We will show this in an example, expressing the total energy density given in Eq. 1.22 in spherical coordinates:

$$\varepsilon_{\text{tot}} = -\mu_0 M_s |H_{\text{ext}}| \sin \theta \cos \phi + \frac{\mu_0}{2} M_{\text{eff}} M_s \cos^2 \theta - H_{\text{uni}} \frac{\mu_0 M_s}{2} \cos^2(\phi - \beta) \sin^2 \theta. \quad (1.75)$$

While we still assumed  $\mathbf{H}$  pointing along the x-axis being sufficiently high to align the magnetization  $\mathbf{M}$  in parallel, we now allowed the easy axis of the in-plane anisotropy to be at an arbitrary angle  $\beta$ . The solution we find using Eq. 1.74 resembles Eq. 1.37, except that now the influence of the anisotropy direction is revealed:

$$\omega_{\text{res}}^2 = \gamma^2 \mu_0^2 [H_{\text{ext}} + H_{\text{uni}} \cos(2\beta)] [M_{\text{eff}} + H_{\text{ext}} + H_{\text{uni}} \cos^2(\beta)]. \quad (1.76)$$

Of course, it is also possible to determine the resonance frequency using this formula when the magnetization is not aligned with the external magnetic field direction (when  $\mathbf{H}_{\text{ext}}$  is pointing out of the plane or is dominated by the anisotropy field). Then the magnetization angle  $(\theta_0, \phi_0)$ , which we simply provided in the example, needs to be calculated first by minimizing  $\varepsilon_{\text{tot}}$ .

We want to note that the Smit and Beljers approach is based on the Landau-Lifshitz equation without the phenomenological damping term. While thus the influence of the damping parameter is neglected, we already demonstrated with Eq. 1.44 that the resonance frequency shift related to  $\alpha$  is generally negligible.

As a final remark, we state that due to the choice of parameters Eq. 1.74 has a singular point when the magnetization is directed normal to the sample ( $\theta = 0$ ). While throughout this thesis the magnetic field was always applied in the sample plane, we direct the interested reader to Ref. [49], which provides a possibility to circumvent this problem.

## 1.5 Magnetization Damping

In section 1.2 we introduced the phenomenological Gilbert damping parameter  $\alpha$  in the term modeling the viscous relaxation of the magnetization motion. In reality this single parameter contains contributions from a variety of processes, which lead to a coupling of the uniform and non-uniform precession modes and other thermal baths of the magnetically ordered substance, and therefore to dissipation of energy to non-magnetic degrees of freedom (see Fig. 1.4). In most cases the energy is transferred finally to the lattice resulting in heating it (i.e. the creation of phonons) [33]. To clarify the different damping processes, a lot of work was directed in the

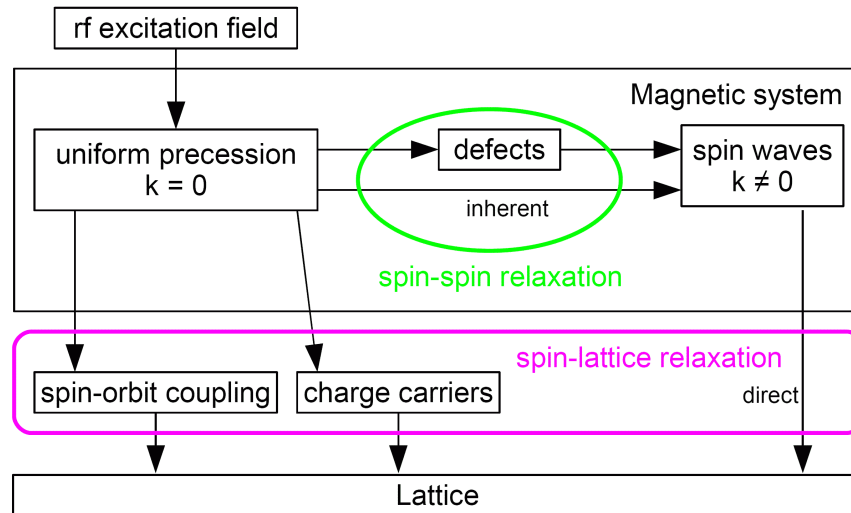


Figure 1.4: (Color online) Nonexhaustive schematization of the involved relaxation mechanisms (see [33]). The spin-spin processes redistribute the energy between the different modes of the magnetic system. The spin-lattice processes transfer energy to the lattice.

past towards the study of ferromagnetic insulators [50], in particular yttrium iron garnet (YIG). In the metallic thin films which are the subject of this thesis several processes come into play. They are related to the presence of itinerant conduction electrons and lead to a considerably faster relaxation [51].

In the following we outline the most important processes. They can be cast into intrinsic unavoidable processes, e.g. direct coupling to the lattice mediated by the spin-orbit coupling, and extrinsic processes, for example the two-magnon scattering which is linked to the presence of defects breaking the translational invariance.

### 1.5.1 Scattering with itinerant conduction electrons

The most important contribution to the Gilbert damping in metals is caused by incoherent scattering of itinerant conduction electrons by phonons and magnons [52]: Two processes can contribute to damping.

(i) In a three particle scattering process, a magnon with the energy  $\hbar\omega_{\mathbf{q}}$  collides with an itinerant electron with the energy  $\varepsilon_{\mathbf{k},s}$ , where  $s$  denotes the spin state. The magnon is annihilated and the electron-hole pair has the energy  $\varepsilon_{\mathbf{k}+\mathbf{q},s'}$  after the scattering process. As the s-d exchange interaction conserves the total angular momentum, the electron spin  $s'$  is flipped [44]. A second three particle scattering event leads to the emission of a magnon. In the case of no intermediate interaction, the emitted magnon corresponds to the initial magnon and no damping is mediated (see Fig. 1.5).

Conversely, if the itinerant electron is subject to a scattering process changing its spin state with a thermally excited phonon or magnon between the annihilation and the recreation of the magnon, the emitted magnon no longer corresponds to the initial magnon. Therefore, it is lost for the precession motion.

This is only possible due to the spin-orbit interaction, which creates a non-zero scattering probability between the two spin states [53]. The rate of spin-flip is pro-

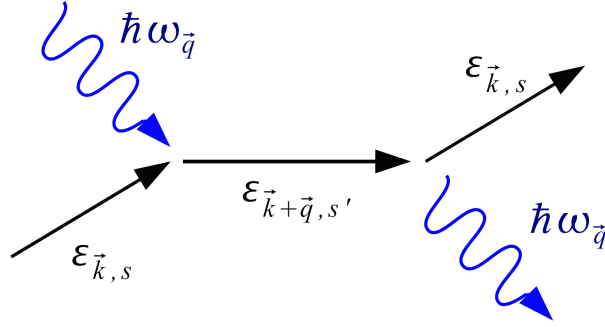


Figure 1.5: (Color online) Coherent scattering process between a magnon with energy  $\hbar\omega_{\mathbf{q}}$  and an itinerant electron with energy  $\epsilon_{\mathbf{k},s}$ . In the case of this graph, the emitted magnon corresponds to the initial magnon.

portional to the inverse of  $\tau_{\text{flip}} = \tau_{\text{orb}}/(g-2)^2$ , where  $\tau_{\text{orb}}$  is the orbital relaxation time and  $g$  is the g-factor [54]. The contribution to the Gilbert damping is proportional to the rate of spin-flip and therefore to  $1/\tau_{\text{flip}}$ . This shows the importance of the spin-orbit coupling for damping in metals, as the g-factor depends on the ratio of the spin and the orbital momentum [55]. We add that this proportionality to the inverse orbital relaxation time corresponds to a direct proportionality to the resistivity. Therefore, we expect the intrinsic damping to increase with increasing temperature. This was observed in [56].

(ii) In ferromagnetic metals the shape of the Fermi surface changes when the magnetization direction is changed [53]. Hence, the uniform precession results in a periodical variation of the Fermi surface due to spin-orbit coupling (often called breathing Fermi surface) [57]. The adaptation of the itinerant electrons to the changed Fermi surface is a dissipative process, as it introduces a dephasing between the magnetization precession and the periodical variation. Thus the repopulation of the Fermi surface leads to relaxation for the scattered itinerant electron. As mentioned, this Gilbert-like contribution to the damping also depends on the spin-orbit coupling and is proportional to  $\tau_{\text{orb}}(g-2)^2$  [53]. In contrary to (i), which is proportional to the resistivity, the proportionality to  $\tau_{\text{orb}}$  corresponds to a proportionality to the conductivity.

This effect has been shown to give an appreciable contribution in pure Ni and Co at low temperature, while it is not observed in pure Fe or in alloys [58]. The contribution is higher at lower temperature as the conductivity increases. The non-appearance of this effect for alloys is explained by their reduced mean free path. For Fe its non-appearance is linked to the absence of a special feature of the band structure, which is present in Ni and Co: Near the Fermi energy band-crossing degeneracies exist, which are lifted by the spin-orbit interaction and which contribute strongly to the damping [58].

In summary, the two processes (i) and (ii) both lead to a Gilbert-like damping term, i.e. to an  $\alpha$  which is constant with resonance frequency. However, depending on temperature (i) and (ii) do not necessarily contribute equally to the relaxation, as (i) is proportional to the resistivity, while (ii) is proportional to the conductivity. This is demonstrated in [56], where the temperature dependence of the relaxation is examined, as the orbital relaxation time  $\tau_{\text{orb}}$  is temperature-dependent. A more detailed discussion can be found in [44].

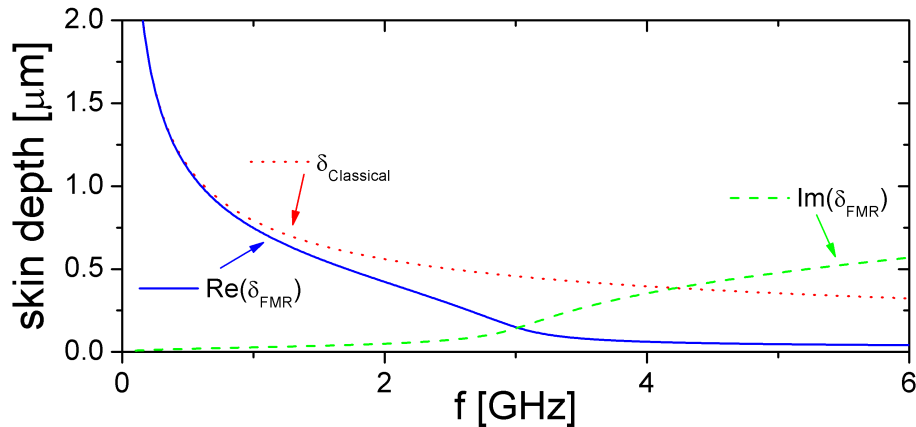


Figure 1.6: (Color online) The classical skin depth (dotted red line) as well as the real (plain blue line) and imaginary (dashed green line) parts of the FMR skin depth using the same parameters as for Fig. 1.2:  $\gamma/(2\pi) = 30$  GHz/T,  $\mu_0 M_S = 1$  T  $\approx \mu_0 M_{\text{eff}}$ ,  $\mu_0(H_{\text{ext}} + H_{\text{uni}}) = 0.01$  T and  $\alpha = 0.02$ . Additionally, we assumed the resistivity of Permalloy:  $\rho = 25 \times 10^{-8}$   $\Omega\text{m}$  [60].

### 1.5.2 Eddy currents

Eddy currents, i.e. the screening of the electromagnetic microwave field by the conduction electrons, lead to another contribution to the relaxation. Eddy currents are characterized by the skin depth  $\delta$ , which is defined as the depth below the surface of the conductor at which the current density decays to  $1/e$  of the current density at the surface. It is given by

$$\delta = \sqrt{\frac{2}{\omega\sigma\mu_r\mu_0}}, \quad (1.77)$$

where  $\sigma$  is the conductivity and  $\mu_r$  is the relative permeability with  $\mu_r = \mu/\mu_0 = 1 + \chi$ . The conductivity  $\sigma$  is the inverse of the resistivity  $\rho$ , which can be found tabulated e.g. in [59]:  $\rho(\text{Fe}) = 9.61 \times 10^{-8}$   $\Omega\text{m}$ ,  $\rho(\text{Au}) = 2.21 \times 10^{-8}$   $\Omega\text{m}$ ,  $\rho(\text{Ag}) = 1.59 \times 10^{-8}$   $\Omega\text{m}$ , all at 20°C. Eddy currents become important when the film thickness is comparable to or greater than the skin depth: for typical transition metals the classical skin depth at 10 GHz is in the range of one micron [45]. But, it has to be taken into account that the permeability  $\mu$  can increase drastically at frequencies around the ferromagnetic resonance (see Fig. 1.2), reducing the skin depth.

A calculated example of the skin depth is shown in Fig. 1.6: The classical skin depth is calculated using the static relative permeability which is invariant with frequency:  $\mu_r = 1 + \chi_{\text{stat}} = 1 + \omega_M/\omega_H$ , according to Eq. 1.47. This is a simplification only valid for low frequencies. The FMR skin depth is calculated using  $\mu_r = 1 + \chi_{yy} = 1 + \chi'_{yy} - i\chi''_{yy}$  [61], where  $\chi_{yy}$  is defined by Eqs. 1.35 and 1.36. Note that the FMR skin depth is a complex number.

For thick magnetic films Ament and Rado showed that the eddy currents lead to a finite FMR linewidth even in the absence of damping, this effect being called exchange conductivity mechanism [62]. The designation is chosen as this linewidth broadening is proportional to  $\sqrt{A\sigma}$ , where  $A$  is the exchange stiffness constant. This contribution can be rather high for thick films, e.g. for an Fe film of 200 nm a 7 fold increase with respect to intrinsic damping is observed [44]. The additional damping decreases rapidly with the thickness  $d$ , as it is proportional to  $d^2$ . For films



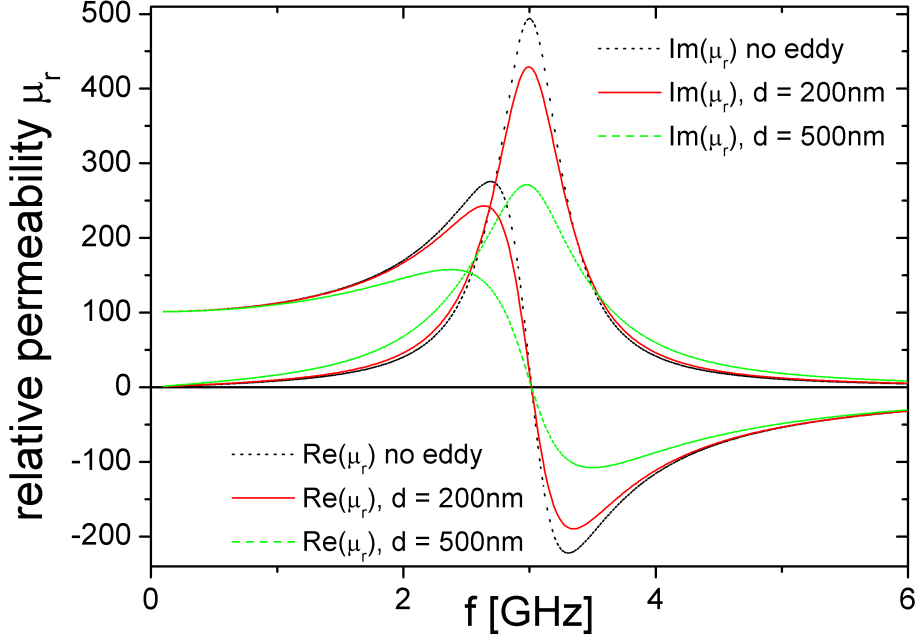


Figure 1.7: (Color online) The black dotted line marks the real and imaginary part of the permeability without taking eddy currents into account. The red plain and the green dashed lines were calculated after Eq. 1.78 including eddy currents for a 200 nm and a 500 nm layer. The parameters are the same as for Fig. 1.6 and 1.2.

with thicknesses below  $\delta$ , this contribution is negligible, e.g. after [44] it becomes important for Fe films of 25 nm or permalloy films of 100 nm.

In order to take eddy currents into account, a full derivation of the complex frequency-dependent permeability with eddy currents can be found in [61]: To derive the effect of the eddy currents, the screening of the excitation field in an infinite plate of finite thickness is calculated by solving the Maxwell equations with appropriate boundary conditions. This gives the field as a function of the penetration depth. Integrating over the thickness, the average effective permeability is obtained as

$$\mu_r^{\text{Eddy}} = \mu_r \frac{(1-j) e^{(1+j)d/\delta} - 1}{d/\delta e^{(1+j)d/\delta} + 1}, \quad (1.78)$$

where  $j$  is the imaginary unit,  $\mu_r = 1 + \chi_{yy}$ ,  $\delta$  is the FMR skin depth and  $d$  the total thickness of all metallic layers. We insist on the fact that also non-magnetic metallic layer (as e.g. cover layers) add to the total thickness. Fig. 1.7 picks up the relative permeability corresponding to the susceptibility shown in Fig. 1.2, where additionally two relative permeabilities for a 200 nm and a 500 nm layer with a resistivity  $\rho = 25 \times 10^{-8} \Omega\text{m}$  are calculated after Eq. 1.78. In particular for the thicker layer the linewidth broadening is obvious. Experiments with the measured layers being so thick that it was necessary to take eddy currents into account can be found in [63, 60].

### 1.5.3 Two-magnon scattering

Several decades ago two-magnon scattering was already examined in detail as an extrinsic contribution to the linewidth for ferromagnetic insulators [50]. Recently, a

considerable amount of research was directed on the effect of this linewidth broadening in different samples: in metallic thin films (see e.g. [11, 12, 64, 34, 65]). In the two-magnon process a uniform precession magnon (wave vector  $k = 0$ ) is annihilated and a  $k \neq 0$  magnon is created. As this is a spin-spin process (see Fig. 1.4), the total number of magnons is unchanged. However, as for a  $k \neq 0$  magnon the spins are not parallel to one another, the excitation of such a magnon reduces the length of the magnetization. This is why this process can be modeled better with the equation of motion after Bloch-Bloembergen (BB) (see Eq. 1.20) than with the LLG-equation which conserves the magnetization. This spin de-phasing mechanism is described by the transverse relaxation time  $T_2$ . In the long run, the  $k \neq 0$  magnons relax to the lattice, leading to an independent relaxation time  $T_1$ .

In [11] Arias and Mills develop this magnon scattering mediated by surface and interface defects for in-plane magnetized thin films. In Fig. 1.10 we will see that in this situation a spin wave with a non-zero wave vector but the same energy as the uniform precession magnon exists. It is important to realize that the possible spin wave modes depend upon the orientation of the magnetic field and that for out-of-plane magnetization there is no spin wave mode degenerate with the uniform precession mode. Hence, two magnon scattering is inoperative in this field configuration [44].

The two-magnon contribution to damping is not Gilbert-like, i.e. it is not proportional to the resonance frequency in the field linewidth (as introduced in Eq. 1.53). It can be easily confused with a finite zero-frequency linewidth, which is usually introduced to account for sample inhomogeneities as [10]

$$\mu_0 \Delta H = \mu_0 \Delta H_{\text{inhomo}} + 2 \frac{\alpha}{\gamma} \omega_{\text{res}}. \quad (1.79)$$

In [12] the frequency linewidth is measured over a large range up to 225 GHz and the conclusion was: “Clearly, a limited set of low frequency experimental data can always be fitted with a linear frequency dependence and a constant inhomogeneous term.” As in older publication on the linewidth in metallic thin films (e.g. [66]) this contribution was not always taken into account, the conclusions on inhomogeneous broadening need to be considered with care.

#### 1.5.4 Spin-pumping

Mizukami observed that the ferromagnetic resonance linewidth, and therefore the damping, of a permalloy layer in a sandwich between two metallic non-magnetic layers depends on the material of these cladding layers [67, 68, 69]. Materials with a stronger spin-orbit coupling, e.g. Pt and Pd, which results in a higher spin-flip scattering, caused a broadening of the linewidth. This is explained by the injection of spins into the adjacent normal metal by a ferromagnet with moving magnetization. This spin current ‘pumped’ by the precessing magnetization is subject to spin-flip scattering in the normal metal, adding to the damping. It is important that this spin current is not accompanied by an electrical charge current. For the inverse effect, the so-called spin-transfer torque, a spin polarized current is creating magnetization precession, see [70].

Spin-pumping was originally proposed by Berger [14] and the theory was further elaborated in [71, 72, 73]. The spin-pumping term has exactly the same form as the Gilbert damping [70]. According to [71] the spin current emitted into the normal

metal is

$$\mathbf{I}_S^{\text{pump}} = \frac{\hbar}{4\pi} g_{\uparrow\downarrow} \left( \mathbf{m} \times \frac{d\mathbf{m}}{dt} \right), \quad (1.80)$$

where  $g_{\uparrow\downarrow}$  is the dimensionless interfacial spin-mixing component in the spin-conductance tensor.  $g_{\uparrow\downarrow}$  determines the spin current emitted into the normal metal, when the ferromagnet is thicker than the ferromagnetic coherence length (a few Å in transition metals such as Co, Ni or Fe) [71]. In a simplified picture assuming a spherical Fermi surface,  $g_{\uparrow\downarrow}$  can be expressed as  $g_{\uparrow\downarrow} \cong 0.85n^{2/3}$ , where  $n$  is the density of conduction electrons per spin [74].

Adding this torque to the LLG equation the Gilbert damping is increased  $\alpha \rightarrow \alpha + \alpha'$ , where  $\alpha'$  is the spin-pumping contribution. As it is also constant with frequency  $\omega$ , it is difficult to separate it from the intrinsic damping. The additional damping can be calculated as [75]

$$\alpha' = g_{\uparrow\downarrow} \frac{\gamma \hbar}{AM_s d_{\text{FM}}}, \quad (1.81)$$

where  $A$  is the total surface area of the interface,  $d_{\text{FM}}$  the thickness of the ferromagnetic layer,  $\gamma$  the gyromagnetic ratio and  $\hbar$  is the Planck constant. Here, we neglected the angular momentum which diffuses back into the ferromagnet due to spin accumulation in the normal metal.

This increase in damping was also observed in magnetic double layer structures separated by a normal metal spacer [76]: the FMR field linewidth of two different samples is compared: a single layer sample GaAs/Fe(16)/Au(20) and a double layer sample GaAs/Fe(16)/Au(40)/Fe(40)/Au(20), where all thicknesses are given in monolayers (ML). The magnetic properties of the nominally identical 16 ML Fe layer deduced from the FMR frequency are found to be identical in both samples. Therefore, no exchange coupling between the two magnetic layers is present in the double layer sample. However, the field linewidth for the thin Fe layer is higher in the double layer sample than in the single layer sample. The observed linewidth in the single layer sample and the additional linewidth in the double layer sample are plotted as a function of resonance frequency  $f_{\text{res}}$  in Fig. 1.8. We remind that the field linewidth is directly proportional to  $\alpha f_{\text{res}}$  (see Eq. 1.53). Consequently, the observed damping  $\alpha$  is higher for the thin Fe layer in the double layer sample.

This can be explained in a descriptive manner using the quantum mechanical picture given in Fig. 1.5: In the thin Fe layer a uniform precession magnon is annihilated and its energy  $\hbar\omega_{\mathbf{q}}$  transferred to a conduction electron [77]. This electron traverses the Au spacer. As the spacer layer thickness is far below the electron mean free path of Au (38 nm [44]), the spin transport is considered as purely ballistic. As the second thicker Fe layer has a different interface anisotropy, its resonance frequency is different from the one of the thin Fe layer for the same external magnetic field. Thus, if the initial magnon with energy  $\hbar\omega_{\mathbf{q}}$  is emitted again by the excited conduction electron inside the thicker Fe layer, it will not contribute to its resonance due to its differing frequency  $\omega_{\mathbf{q}}$ . It is lost for the precession motion in the thin Fe layer and is perceived as an additional damping.

Indeed, for the 16 ML Fe film in the single layer the damping was determined to  $\alpha = 0.0044$ , the observed damping  $\alpha + \alpha'$  was twice that value in a magnetic double layer. In continuative work, it was found that the resonance frequencies can coincide for a specific angle and strength of the applied field exploiting the different anisotropies in the thin and thick Fe layers [78, 79]. In this special geometry

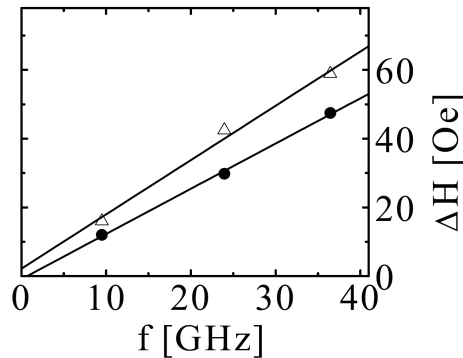


Figure 1.8: The FMR field linewidth  $\Delta H$  as a function of resonance frequency, after [76]. The triangles correspond to the 16 ML Fe film in the single layer structure. The filled dots show the additional linewidth measured for the 16 ML Fe film in the double layer sample.

the magnon transferred from one magnetic layer to the other and vice versa can contribute to the uniform precession in the other layer, and the experiment confirmed that the linewidth, and therefore the observed damping, was decreased for both layers in this specific situation.

For more extensive informations on this effect, we refer the reader to [73].

## 1.6 Spin waves

In the preceding sections we addressed only uniform magnetization motion, i.e. the exchange interaction is so strong as to keep all magnetic moments aligned perfectly in parallel. Coherent magnetization precession occurs at the same frequency and phase. This uniform precession can be described as a wave with infinite wavelength. In realistic systems different conditions such as a finite temperature  $T \neq 0$ , a non-uniform excitation field or defects in the sample lead to the excitation of spin waves with finite wavelength, also called magnons.

We discuss in the following the different types of spin waves occurring in ultrathin film samples. Short wavelength spin waves are dominated by the exchange interaction: usually when speaking about *spin waves*, exchange dominated spin waves are addressed. For long wavelengths the exchange interaction is falling off rapidly and is dominated by the magnetic dipolar interaction: corresponding waves are termed *magnetostatic waves* [80]. Finally, we will address *perpendicular standing spin waves*, which are related to the two dimensional confinement in the magnetic thin film. These thickness modes are exchange dominated.

### 1.6.1 Magnetostatic Waves

The basic equation for magnetostatic waves is found by starting from the Maxwell equations in the magnetostatic limit in the absence of currents [81], which read:

$$\nabla \times \mathbf{H} = 0 \quad ; \quad \nabla \cdot \mathbf{B} = 0 \quad ; \quad \nabla \times \mathbf{E} = -\dot{\mathbf{B}}. \quad (1.82)$$

We use the definition of the magnetic induction

$$\mathbf{B} = \mu_0(1 + \bar{\chi})\mathbf{H}, \quad (1.83)$$

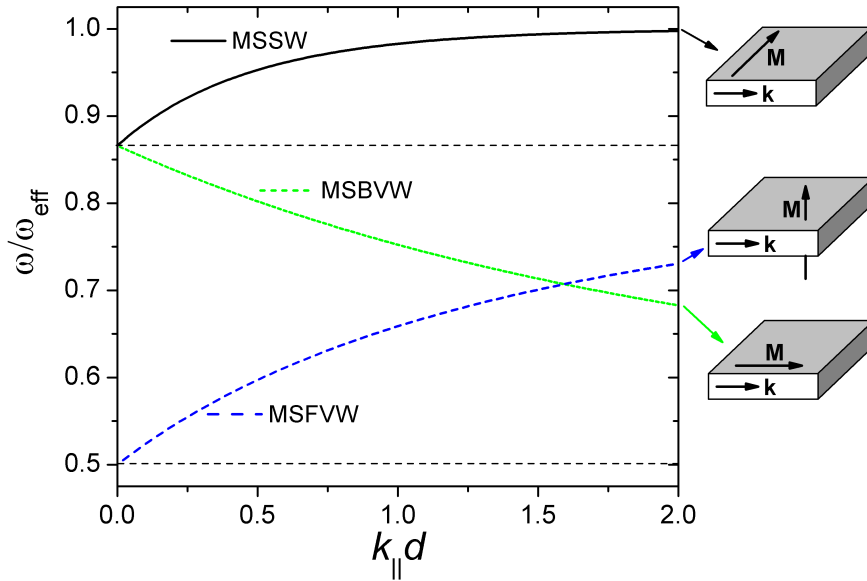


Figure 1.9: (Color online) The dispersion relation and geometry for the three magnetostatic modes described in the text (see Eqs. 1.87, 1.88 and 1.89). The frequency axis was normalized to  $1/\omega_{\text{eff}}$ , where we chose  $\omega_H = \omega_{\text{eff}}/2$ . The magnetization is aligned by an external field as sketched on the right hand side. In the case of in-plane magnetization the uniform resonance frequency is found at 0.866.

where  $\bar{\chi}$  is the high-frequency susceptibility derived from the Landau-Lifshitz equation without loss in a similar manner as in section 1.3. We introduce the magnetostatic scalar potential  $\psi$  using  $\mathbf{H} = -\nabla\psi$ , which allows us to deduce Walkers's equation:

$$(1 + \chi) \left[ \frac{\partial^2 \psi}{\partial x^2} + \frac{\partial^2 \psi}{\partial y^2} \right] + \frac{\partial^2 \psi}{\partial z^2} = 0. \quad (1.84)$$

This equation is the basic equation for magnetostatic waves in homogeneous media. In order to find the dispersion relation, an assumption is made for  $\psi$ , e.g. for a uniform plane wave propagation:  $\psi \propto \exp(ik \cdot \mathbf{r})$ . This yields

$$(1 + \chi)(k_x^2 + k_y^2) + k_z^2 = 0, \quad (1.85)$$

which relates the wave vector with the frequency (contained in  $\chi$ ). The different magnetostatic modes are obtained by imposing specific relations for the different components of  $\mathbf{k}$  taking into account the boundary conditions. The original work giving full details can be found in [82] (note that the geometry is defined differently than in section 1.3).

In the following we present the different magnetostatic modes in the case of a thin film geometry, where we neglect anisotropy and the exchange interaction and where the direction of the magnetization is determined by an external magnetic field. The modes are primarily distinguished by the angle between the magnetization direction and the in-plane wave vector ( $k_{\parallel}$ ) as well as the direction of the magnetization with respect to the film plane.

Part of their naming is related to the dispersion relation of the modes, i.e. the frequency  $\omega$  as a function of the wave vector  $k$ . The group- and phase velocity are

defined depending on the dispersion relation as

$$v_{\text{group}} = \frac{\partial \omega}{\partial k} \quad ; \quad v_{\text{phase}} = \frac{\omega}{k}. \quad (1.86)$$

Modes that show positive (negative) dispersion, i.e. modes with  $v_{\text{group}}$  and  $v_{\text{phase}}$  having the same (opposite) direction, are called *forward (backward) waves*. The different dispersion relations in the magnetostatic limit are illustrated in Fig. 1.9.

- **MagnetoStatic Surface Waves (MSSW):**

These waves are also called Damon Eshbach modes, as they were first described by Damon and Eshbach [83]. They are observed when the magnetization is in the sample plane and the in-plane wave vector  $\mathbf{k}_{\parallel}$  is perpendicular to  $\mathbf{M}$ . They show positive dispersion and are therefore forward waves. The dispersion relation is given by [81]

$$\omega_{\text{MSSW}}^2 = \omega_H(\omega_H + \omega_{\text{eff}}) + \frac{\omega_{\text{eff}}^2}{4}(1 - e^{-2k_{\parallel}d}) \quad (1.87)$$

We note that in the limit case  $k_{\parallel} \rightarrow 0$ , this corresponds to Eq. 1.37.

The amplitude of this type of wave decays exponentially from the surfaces of the film. Hence, the designation of this mode [84]. Depending on the propagation direction it is located next to one of the two film surfaces.

- **MagnetoStatic Backward Volume Waves (MSBVW):**

The MSBVW are the modes with the in-plane wave vector being collinear to the magnetization which is in-plane, too. While the MSSW are located at the sample surface, the amplitude of backward volume waves is distributed uniformly through the volume of the film. As mentioned before, they are called backward waves as they show negative dispersion. An approximation of the dispersion relation derived in [85] states

$$\omega_{\text{MSBVW}}^2 = \omega_H \left[ \omega_H + \omega_{\text{eff}} \left( \frac{1 - e^{-k_{\parallel}d}}{k_{\parallel}d} \right) \right]. \quad (1.88)$$

As for Eq. 1.87, for  $k_{\parallel} \rightarrow 0$  we find the uniform in-plane precession frequency (Eq. 1.37).

- **MagnetoStatic Forward Volume Waves (MSFVW):**

These modes occur when the magnetization is aligned perpendicular to the plane. While this experimental situation is never met within this thesis, we will mention it for the sake of completeness. Kalinikos derived an approximate solution of the dispersion relation, which is found in [81]:

$$\omega_{\text{MSFVW}}^2 = \omega_H \left[ \omega_H + \omega_{\text{eff}} \left( 1 - \frac{1 - e^{-k_{\parallel}d}}{k_{\parallel}d} \right) \right]. \quad (1.89)$$

It is of interest to note that the wave propagation does not depend on the direction of the in-plane wave vector (in the absence of magnetocrystalline anisotropy). This mode is called a volume wave because the amplitude is uniformly distributed through the volume of the film as in the case of MSBVW. In contrast, this mode is a forward wave, as the group and the phase velocity point in the same direction.

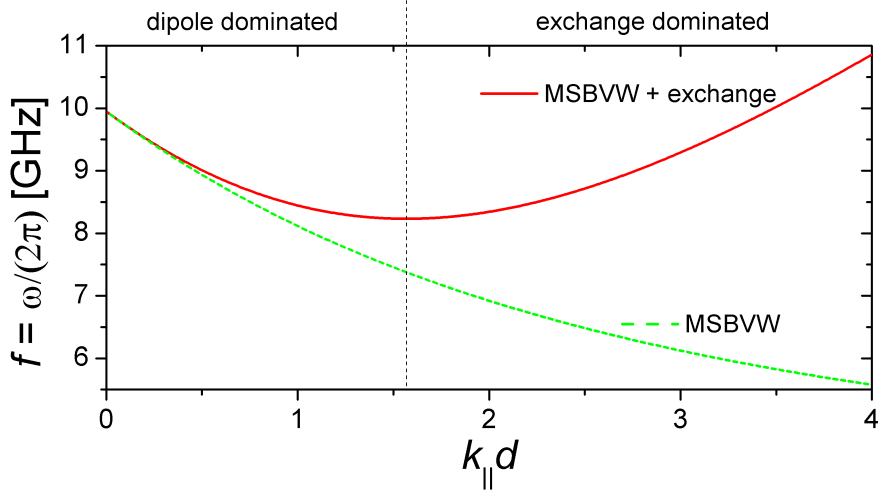


Figure 1.10: (Color online) The dispersion relation of the magnetostatic backward volume wave (Eq. 1.88) without taking the exchange interaction into account (green dashed line) and with adding  $\omega_{\text{ex}}^2$  following Eq. 1.91 (red plain line). The vertical dashed line separates the long wavelength dipolar dominated from the exchange dominated wave vectors. The following parameters were assumed:  $\gamma/(2\pi) = 30$  GHz/T,  $\mu_0 M_{\text{eff}} = 1$  T,  $A = 2 \times 10^{-11}$  J/m,  $d = 100$  nm,  $\mu_0 H_{\text{ext}} = 0.1$  T.

### 1.6.2 Exchange dominated (in-plane) spin waves

The formulas describing the magnetostatic modes are only valid up to a certain wave vector. For short wave length the exchange interaction becomes important and can no longer be ignored. It increases the resonance frequency, as it costs energy to misalign spins which are close by. An approximate formula for the dispersion relation of in-plane spin waves in the ultrathin film limit taking into account exchange was derived by Arias and Mills [11]:

$$\omega_{\text{in-plane}}^2 = \omega_H(\omega_H + \omega_{\text{eff}}) - \frac{\omega_{\text{eff}}}{2}(\omega_H - [\omega_H + \omega_{\text{eff}}] \sin^2 \phi_k) k_{\parallel} d + (2\omega_H + \omega_{\text{eff}}) \gamma \frac{2A}{M_s} k_{\parallel}^2, \quad (1.90)$$

where  $A$  is the exchange stiffness constant and  $\phi_k$  is the angle between  $\mathbf{M}$  and  $k_{\parallel}$ , which are both in-plane. It is easy to check, that Eq. 1.87 and Eq. 1.88 are approximated by Eq. 1.90 when neglecting the last (exchange) term and expanding the exponential function.

The exchange contribution is included as

$$\omega_{\text{ex}}^2 = (2\omega_H + \omega_{\text{eff}}) \gamma \frac{2A}{M_s} k_{\parallel}^2. \quad (1.91)$$

We note that  $\omega_{\text{ex}}^2$  is isotropic, as the exchange interaction is isotropic. Fig. 1.10 demonstrates the effect of the exchange interaction on the dispersion relation of magnetostatic backward volume waves: with increasing wave vector the exchange interaction dominates the dipolar interaction. In particular for the MSBVW, this changes the curvature and allows an exchange dominated spin wave at the same resonance frequency as the uniform mode ( $\approx 10$  GHz), but at a non zero wave vector. We referred to these modes in section 1.5, when analyzing 2-magnon scattering.

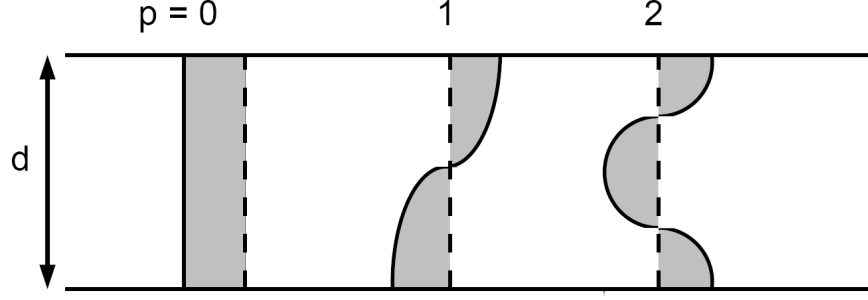


Figure 1.11: Schematization of the lowest order perpendicular standing spin waves where multiples of half the wavelength fit into the film thickness (see Eq. 1.92). Here we assumed no surface pinning, which could influence the precession of the spins near the surface due to different anisotropy fields (see [88]).

### 1.6.3 Perpendicular Standing Spin Waves (PSSW)

Previously we only allowed for wave vectors lying inside the sample plane, i.e. the phase was always uniform through the film thickness for the magnetization aligned in the plane by an external magnetic field. As we assumed an infinite thin film, the wave length could be chosen continuously. This is not the case for the out-of-plane wave vector  $\mathbf{k}_\perp$  because of the different boundary conditions: only wavelengths  $\lambda$  with half the wavelength fitting into the film thickness in whole numbers are allowed due to the confinement (see Fig. 1.11). With  $\mathbf{k}_\perp = \pi p/\lambda$ , an approximation of the dispersion relation is given by [86]:

$$\omega_{\text{PSSW}}^2 = \left[ \omega_H + \omega_{\text{eff}} + \gamma \frac{2A}{M_s} \left( \frac{\pi p}{d} \right)^2 \right] \left[ \omega_H + \gamma \frac{2A}{M_s} \left( \frac{\pi p}{d} \right)^2 \right]. \quad (1.92)$$

When expanding this equation and separating the exchange contribution from the uniform resonance formula, one finds a term being similar to Eq. 1.91. However, in Eq. 1.91 we expect  $\gamma 2A k_\parallel^2 / M_s < \omega_H$ , while in Eq. 1.92 typically  $\gamma 2A k_\perp^2 / M_s > \omega_H$  is found. This is due to the comparatively higher out-of-plane wave vectors and leads to a shift to considerably higher frequencies. More on the observation of PSSW can be found in [87]. In chapter 7 we present data on the observation of the thickness mode of the order  $p = 1$  for 40 nm thick samples and extract the exchange stiffness constants  $A$  for the sample material.





# Chapter 2

## Experimental Basics

To introduce magnetization dynamics, we begin this chapter by briefly presenting some of the most important measurement techniques in this field (§2.1). In a following section we describe in more detail the technique of Vector Network Analyzer Ferromagnetic Resonance (VNA-FMR), which was the mainly employed technique for sample characterization throughout this thesis (§2.3). But, before explaining its mode of operation, we remind the most important concepts of microwave engineering necessary for a complete understanding (§2.2).

### 2.1 Measurement techniques in magnetization dynamics

In this section several measurement techniques are presented. They can be classified by their mode of detecting the magnetization: The first five use an electrical detection. The following sections describe optical techniques, while the last described technique (section 2.1.8) relies on mechanical detection. This section is concluded by a tentative comparison between the different techniques.

#### 2.1.1 Ferromagnetic Resonance

The Ferromagnetic Resonance (FMR) technique is one of the oldest [8] and most well understood techniques to study and characterize the (small angle) dynamics of magnetization motion (see Fig. 2.1(a)). The sample is placed in a resonant microwave cavity. A Klystron or a Gunn diode provides microwave radiation with a fixed frequency (typically 1 – 80 GHz), which is coupled into the cavity creating a standing microwave field. Depending on the type of cavity used, there can be several sample positions allowing to realize different pumping geometries [89] (see Fig. 2.1(b)). An electromagnet provides an external magnetic field which is swept while the power reflected by the cavity is monitored. When the ferromagnetic resonance condition deduced in the previous chapter is met, there is a strong increase in the absorbed power. This is measured by the reduction of the reflected power, given by

$$\Delta P_{\text{refl}} \propto < \chi''_{\xi\xi} > h^2 \eta, \quad (2.1)$$

where  $\xi$  is the direction of the microwave excitation field  $h$  at the sample position.  $\eta$  is the filling factor depending on the ratio of the cavity to the sample volume.

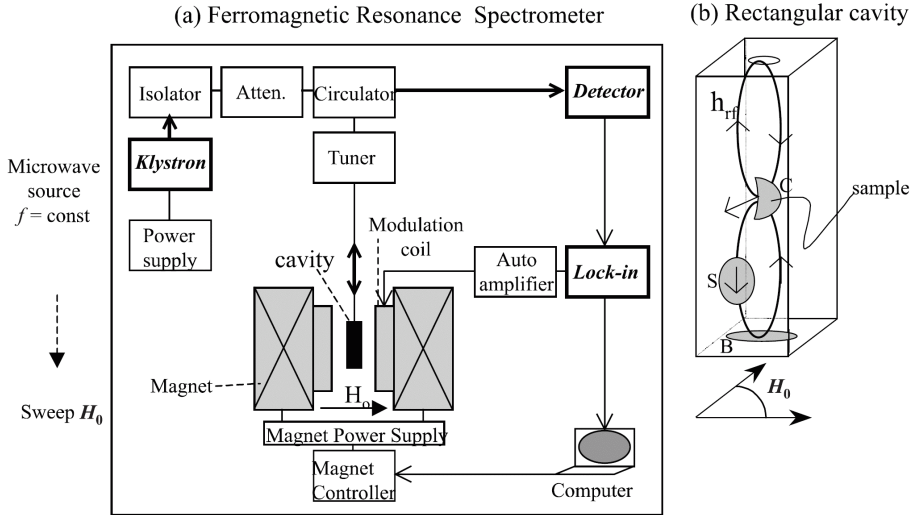


Figure 2.1: (a) Basic layout of a typical FMR spectrometer and (b) rectangular microwave cavity with multiple different pumping geometries at the positions B, S and C, after [89].

$\langle \chi'' \rangle$  is the imaginary part of the hf-susceptibility averaged over the sample volume.

In order to enhance the signal to noise ratio, in practice the external magnetic field is modulated. Typical modulation frequencies are in the range of 100 – 200 Hz. This allows for the use of lock-in amplifier detection. For further details on the measurement setup we refer the reader to [9], for its application on ultrathin metallic layers to [10].

While this technique has the disadvantage of being limited to a specific frequency by the microwave cavity, it has a very high sensitivity enabling the detection of  $9.4 \times 10^{12} \mu_B$  [90]. This is due to the high quality factors of the resonance cavities, which compensate for the low filling factor and easily permit the study of extended thin films.

Whenever we speak in the following about ferromagnetic resonance measurements using a resonant cavity and sweeping the magnetic field, we will use the terms of conventional or classical FMR for this well-established technique.

### 2.1.2 Inductive Permeameter

While in classical FMR the resonance frequency is fixed by the cavity, the inductive permeameter technique enables broadband resonance measurements: The sample is coupled to a non-resonant microwave device. In a simplified picture, the device reacts to the magnetic flux change caused by the moving magnetization of the sample due to the application of a high-frequency field. This response is detected with a (phase-sensitive) vector network analyzer. Different geometries have been implemented:

In an early implementation in [91] the excitation and detection is still distributed to two components: the sinusoidal excitation field is created by a stripline waveguide, while a nonresonant butterfly-coil pickup loop detects the stray field signal. The sample is located in a plane parallel to the ground plane above the signal sheet of the strip-line. The flat pickup loop is in the same plane having the shape of

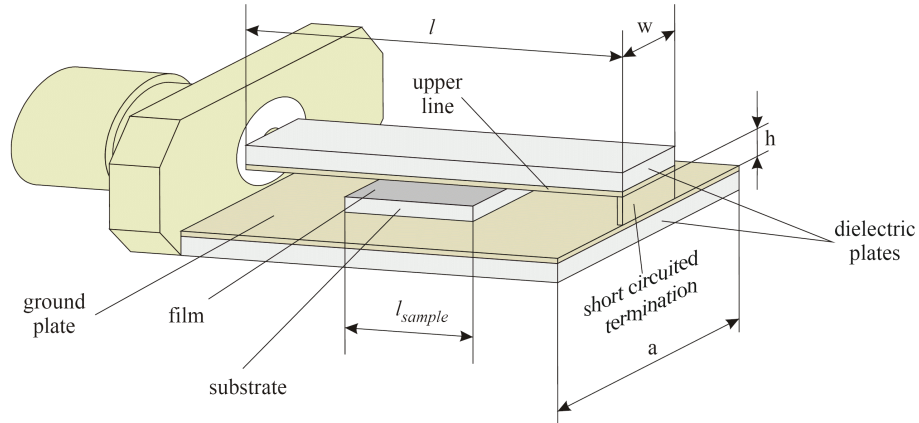


Figure 2.2: A single coil geometry realized using a short circuited microstrip line with the magnetic film placed between the conducting plates, after [92].

a double eight figure. As the loop is in this plane, it is sensitive to the stray field perpendicular to the latter, generated by the oscillating magnetization. The permeability is calculated from the induced voltage. It was found that the upper operating frequencies were limited to a few hundred MegaHertz due to the formation of standing waves in the coil. It can be extended to a few GigaHertz by reducing the size of the coil.

Recent implementations of inductive permeameters often use only one component performing the excitation and the detection at the same time. Ferromagnetic thin films or microwires were measured in a coaxial geometry: The magnetic material has to be conformed into a torus on the outside of the inner conductor of the coaxial line or on the inside of the outer conductor [93]. While this imposes a constraint, as nonflexible magnetic material has to be deposited on a toroidal substrate already during manufacturing, measurements of the microwave permeability up to 18 GHz were demonstrated. As the coaxial geometry is well suited for hf measurements, this method has the potential to be extended to higher frequencies using a different coaxial standard than the employed APC-7 limited to the mentioned frequency. However, the sample needs to be flexible or elaborately prepared.

For rigid thin film samples a different geometry has to be adapted. Transmission lines are suitable for this approach (see Fig. 2.2). A short circuited microstrip line was used as the equivalent of a single turn coil [94]. Here, the thin film sample is placed between the strip line and the ground plane [95], and the excitation and detection are both mediated by the strip line. In the cited reference the usable frequency range was limited to 6 GHz in order to prevent the appearance of higher order electromagnetic field modes when the microstrip line length is equal to a quarter of the wavelength.

Transmission lines in a coplanar geometry are well suited for the study of thin film samples, as these can be placed directly on top of them. As in the latter example, the coplanar waveguide acts at the same time as a driving and pickup coil [96]. From the changes in the transmission and reflection of the electromagnetic waves induced by the sample the permeability can be calculated. As this geometry is used throughout this thesis, we will give a description in greater detail in section 2.3.

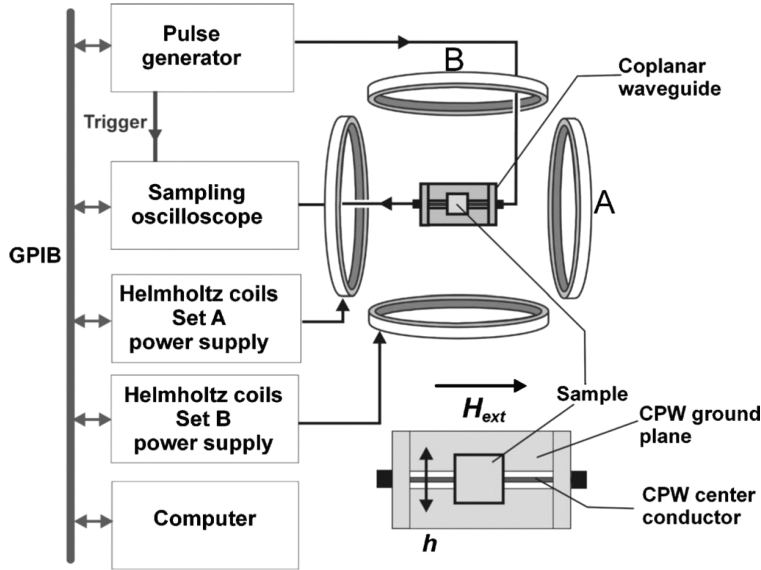


Figure 2.3: Schematic diagram of a pulsed inductive microwave magnetometer setup, after [97]. The sample is placed on the coplanar waveguide as indicated on the lower right hand side, where the static applied field  $H_{\text{ext}}$  is perpendicular to the excitation pulse field  $h$ .

### 2.1.3 Pulsed Inductive Microwave Magnetometer

The geometry of a pulsed inductive microwave magnetometer (PIMM) corresponds to the last one mentioned in the previous section (see Fig. 2.3): The thin film sample is placed on a coplanar waveguide [98]. Instead of a sinusoidal excitation field at a single frequency as employed in classical FMR and in the inductive permeameters, a voltage step applied to the central conductor creates a current pulse. The changing current creates a magnetic excitation pulse transverse to the coplanar waveguide (CPW). This excitation pulse causes the magnetization, which was aligned parallel to the CPW by an external magnetic field, to be rotated in the transverse direction [99]. The magnetization then relaxes in the direction of the external field parallel to the waveguide. The moving magnetization causes a changing flux, which induces a voltage in the CPW which can be detected using a fast oscilloscope. While the previously discussed techniques observe forced oscillations, here, decaying free oscillations are monitored. Another difference is that the former measurement techniques probe the magnetization response in the frequency domain, the PIMM probes the response in the time domain. The acquired data can be transformed into the frequency domain by applying a Fourier transformation. In [100] the precision was compared between such a Fourier transformed frequency response and a direct measurement in the frequency domain and the latter method was found preferable. This is not astonishing as the Fourier transform is applied to a limited time window. It was also pointed out in [90] that the signal to noise ratio (SNR) is considerably worse for PIMM measurements: For the same number of spins ( $1.5 \times 10^{14} \mu_B$ ) the SNR for the PIMM was determined to smaller than 10, for VNA-FMR a value of  $\approx 40$  was found. This can easily be understood, as excitations with a single frequency allow using lock-in detection. While therefore the evaluated frequency band of the PIMM is on the order of  $\Delta\nu = 10$  GHz, for FMR it is limited to  $\Delta\nu = 10$  Hz. The

Johnson-Nyquist thermal noise is proportional to  $\sqrt{\Delta\nu}$  being considerably higher for the PIMM.

It is also important to consider the magnetic excitation pulse, which is commonly higher than the sinusoidally oscillating field in FMR. This is necessary to be able to still follow the free oscillations despite the smaller SNR as described above. Then, it has to be reevaluated if the excitation is still in the linear regime.

In principle, the frequency range measurable by PIMM is not limited. However, in practice the pulse generator needs to be capable to produce a pulse shape containing a corresponding high frequency component. Additionally, the high frequency component is weakly represented in the pulse, leading to a low pumping efficiency for the respective frequency.

A detailed description of the experimental setup of a PIMM can be found in [101].

#### 2.1.4 Propagating Spin Wave Spectroscopy

Propagating Spin Wave Spectroscopy (PSWS) allows to measure the magnetostatic wave modes of a sample. The experimental setup consists of the ferromagnetic thin film with two microwave antennae which are realized as shorted coplanar transmission lines. These are both connected to a vector network analyzer. In contrast to classical FMR and the permeameters, modes having a non-zero wavevector are excited by the excitation field created by the first antenna working as a transducer. These propagate to the second antenna employed as a receiver where their detection allows to draw conclusions on the relaxation of the magnetostatic modes [102].

The experimental requirements are different to the previously mentioned techniques, e.g. the microwave field created by the antenna is deliberately nonuniform in order to couple to spin waves with nonzero wave vectors.

In the past, PSWS was only applied to insulating ferromagnetic films [103]. Bailleul et al. achieved such a measurement for the first time in metallic thin films [104]. In metallic films it is more difficult due to the increased damping, which results in faster wave attenuation, and therefore a shorter propagation distance of the magnetostatic waves: While in the original experiment in yttrium iron garnet insulating films the propagation distance was on the order of mm, the attenuation length (decrease of the amplitude by a factor  $e$ ) was  $26 \mu\text{m}$  in the employed permalloy films [105].

For full details we advise the reading of [105].

#### 2.1.5 Magnetoresistive measurements

Magnetoresistive effects, as the Giant Magneto Resistance (GMR) and the Tunnel Magneto Resistance (TMR), are frequently employed in the observation of magnetization dynamics. We will not discuss the physical origin of the different effects (see e.g. [6] for GMR and [7] for TMR). In this context, their property of practical interest is to introduce a relation between the orientation of the magnetization and the resistance of the sample. Different implementations are used, but the most commonly designed structures are called spin valve for the GMR and Magnetic Tunnel Junction (MTJ) for the TMR. Essentially, they consist of three layers: a reference layer, which is a magnetic layer having its magnetization fixed in a defined direction. A non-magnetic barrier, which is metallic for spin valves and insulating for MTJs.

And a so-called free layer, which is a magnetic layer having most often a uniaxial anisotropy with the easy axis following the preferential direction of the reference layer. We remark that this kind of structure having two equilibrium states with different resistance is at the basis of Magnetic Random Access Memory (MRAM), as it is ideally suited to represent binary information [106].

In a good approximation the change in resistance is directly proportional to the cosine of the angle between the magnetization in the free and the reference layer. As the angle is fixed in the reference layer, the measured resistance allows to calculate the average magnetization component of the free layer along this direction. The average component is observed, as the magnetic moments of the sample are not necessarily aligned in parallel.

Usually the devices are designed lithographically with an integrated high-frequency transmission line necessary for the excitation of the free layer magnetization [107]. The transmission line can either be fed with continuous wave power to obtain frequency domain data, or it can be used to create a field pulse while acquiring time domain data. Recently, the latter type of experiment has been intensely studied when applying the field pulse perpendicularly to the easy axis of the free layer, as this can be used to switch rapidly the magnetization direction, the so-called precessional switching [108].

Electrical measurements offer some advantages [109]: individual structures well below 100 nm can be measured being not easily accessible by other techniques. Due to a high magnetoresistance, single-shot response can be measured without the need for averaging. The current “record” for the TMR effect is situated at 1010% at 5 K and 500% at room temperature [110]. Another benefit of magnetoresistive measurements is that they enable the observation of the magnetization dynamics in complicated multilayer stacks, like they are employed in actual applications.

A review on magnetization dynamics observed by magnetoresistive measurements can be found in [109].

### 2.1.6 Brillouin Light Scattering

Brillouin Light Scattering (BLS) denominates the scattering of visible light from low frequency excitations ( $f < 100$  GHz). Laser light is shone onto the magnetic thin film sample, often using an Argon ion laser at a frequency  $f_0 = 5.83 \times 10^{14}$  Hz [32] ( $\lambda = 514.5$  nm). The angle of incidence is  $45^\circ$  in the standard geometry and only the light back-scattered in the incidence direction is evaluated, while the specularly reflected beam is ignored. The highest intensity in the back-scattered light is found at the frequency of the incident light  $f_0$  and is caused by dust particles or sample irregularities. Additionally, components at shifted frequencies  $f_0 \pm f_{ex}$  are observed, where  $f_{ex}$  is the frequency of an excitation in the film: a phonon (a mechanical oscillation) or a magnon. The magnons are excited thermally. In metals the interaction is taking place close to the surface. The light which was scattered by a spin wave can be selected using a polarization analyzer, as it is polarized at  $90^\circ$  to the incident light polarization, while the polarization is not changed by a scattering process with a phonon. The frequency spectrum around  $f_0$  is analyzed using a multi-pass Fabry-Perot interferometer [111], before being detected by a photomultiplier. Using two interferometers with differing distances between the reflecting surfaces allows to reach a higher selectivity of the transmitted wave lengths, as for only one interferometer the resonance condition is fulfilled for several wave lengths. This allows to

reach the high contrast necessary to detect the weak inelastic excitations. The frequency is typically analyzed over the broad range of 5 – 100 GHz, but the precision is limited to only  $\sim 0.1$  GHz [32] in the best cases.

By changing the angle of incidence, spin waves with different wave vectors can be probed, e.g. in [112] between 0 and  $25 \mu\text{m}^{-1}$  corresponding to wave lengths between  $\infty$  and 250 nm. At the same time the applied in-plane magnetic field can be varied. This allows to probe the dispersion relation of the spin waves.

It is also possible to perform these measurements spatially resolved. The high lateral resolution is defined by the size of the laser beam focus, which is 1 – 2  $\mu\text{m}$  [87].

For further reading, we refer the reader to [32], for recent results to [87].

### 2.1.7 Time Resolved Magneto Optical Kerr Effect

In the Time Resolved Magneto Optical Kerr Effect (TR-MOKE) the magnetization at the surface of the sample is probed using laser light. Most often the polar magneto-optical Kerr effect is employed, which is sensitive to the out-of-plane component of the magnetization [28]. In principle, the in-plane components can also be probed, allowing for a vectorial resolution of the magnetization.

The time resolution is achieved by using ultrafast laser pulses, e.g. by an amplified Ti:Sapphire laser system at 840 nm with 170 fs pulse duration [113]. In the pump-probe measurement geometry two pulses are used to reconstruct the magnetization dynamics in a stroboscopical way: The first pulse called pump pulse creates a small magnetic field pulse deflecting the magnetization from its equilibrium direction. This can be either achieved using a Schottky Barrier or by creating an electrical field pulse using a photo-switch which traverses a microcoil or a micro strip line [114]. The second pulse called probe pulse is then directed at the sample probing the magnetization state via the change of the polarization due to the Kerr effect [115]. To monitor the time evolution of the magnetization the experiment is repeated and the time delay between the pump and the probe pulse is varied. Several measurements with the same delay time are additionally accumulated in order to increase the signal to noise ratio. We note that this is not exactly time resolved as the time evolution is reconstructed from independent measurements.

Additionally, this technique can be adapted to resolve spatially the response of the magnetization: The sample is scanned under the probe beam using a piezo stage. The resolution is limited by the used wavelength. Therefore, the probe beam is frequency doubled [113]. This mode of operation is usually called Time Resolved Scanning Kerr Microscopy (TR-SKEM). While here the magnetization motion is monitored in the time domain, recently a modification of the excitation source allows its use in the frequency domain: In Ferromagnetic Resonance Scanning Kerr Microscopy (FMR-SKEM), the strip line generating the excitation field is connected to a network analyzer providing a continuous wave current creating a sinusoidal high-frequency field [116].

Further details on stroboscopic microscopy can be found in [117, 118].

### 2.1.8 Ferromagnetic Resonance Force Microscopy

A Ferromagnetic Resonance Force Microscope (FMRFM) uses the force exerted on a cantilever as in a magnetic force microscope to detect the magnetization dynamics.



Table 2.1: Comparison between several techniques used in magnetization dynamics.

Technique	Domain	Resolution	Usual geometry
FMR (§2.1.1)	Frequency	No	Thin film
Permeameter (§2.1.2)	Frequency	No	Thin film (patterned [123])
PIMM (§2.1.3)	Time	No	Thin film
PSWS (§2.1.4)	Frequency/Time	No	Thin film (patterned [104])
GMR/TMR (§2.1.5)	Frequency/Time	No	Nanostructures
BLS (§2.1.6)	Frequency	Yes (1 $\mu\text{m}$ )	Surface (patterned [111])
TRMOKE (§2.1.7)	Equivalent Time	Yes (0.3 $\mu\text{m}$ )	Surface (patterned [124])
FMRFM (§2.1.8)	Frequency	Yes (5 $\mu\text{m}$ )	Thin film (patterned [119])

The cantilever with the magnetic tip placed on top of the sample is sensitive to the out-of-plane component of the magnetization. In [119] for example the magnetization is aligned in that direction by an external magnetic field normal to the sample (z-direction). As for the inductive permeameters a strip line situated underneath the sample creates a small transverse excitation field leading to precession of the magnetization. In principle, it is possible to detect the precession by simply measuring the static deformation of the cantilever [120]: When assuming conservation of the magnetization magnitude (as for Gilbert damping) a precession around the z-axis reduces the component of the magnetization along that direction, when the excitation can no longer be linearized. Detecting this reduction  $\Delta M_z = M_s - M_z$  is equivalent to detecting the in-plane component of the magnetization (for conserved magnitude).

However, in practice the detection is achieved by modulating the external field or the amplitude of the excitation field with the resonance frequency of the cantilever. This allows to use the resonating cantilever as an amplifier, considerably increasing the sensitivity. The resonance amplitude of the cantilever is then detected either optically or using piezoresistive detection [121].

FMRFM allows spatially resolved detection of FMR as the magnetic tip is scanned over the sample. A lateral resolution of 5  $\mu\text{m}$  was demonstrated detecting spatially modulated exchange bias [121]. According to [122] FMRFM even has the prospect to provide insights at submicrometer dimensions.

Further reading can be found in [122] and references therein. Many details on a practical implementation can be found in [120].

### 2.1.9 Comparison

Tab. 2.1 shows an overview of the presented techniques. It summarizes some of the most important criteria at a glance: if the mode of operation is in the time or frequency domain. The possibility to achieve a lateral resolution and, if possible, demonstrated values. Finally, the possible sample geometries are mentioned, where we examine the applicability on (patterned) thin films.

An exhaustive comparison seems impossible, as too many different operating scenarios exist. For more details we refer to the previous sections and the references given therein.

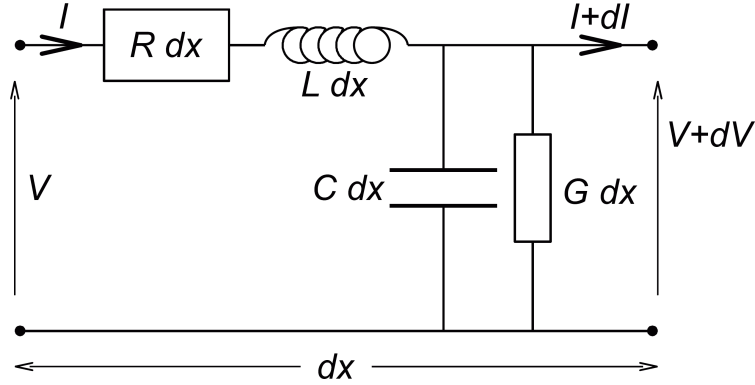


Figure 2.4: Representation of a small line section of length  $dx$  characterized by the four fundamental parameters  $R$ ,  $L$ ,  $G$  and  $C$ .

## 2.2 High-frequency Basics

In order to understand the measurement process in inductive techniques, we introduce in the following some basic concepts of microwave circuits. Readers who are familiar with the basic notions of microwave engineering (microwave propagation, S-parameters, vector network analyzer) can skip this section and continue directly with section 2.3.

### 2.2.1 Derivation of the Telegrapher's Equations

In the following we will use the example of a two-conductor transmission line to derive the elementary equations of electromagnetic propagation in microwave circuits. The line is characterized by four fundamental electrical parameters: The series resistance  $R$  and the series inductance  $L$ , which represent the active and reactive energy loss in the conductors, as well as the shunt conductance  $G$  and the shunt capacitance  $C$ , which represent the active and reactive energy loss in the dielectric. The four parameters are here expressed as quantities per unit length. Other constants, as e.g. a shunt inductance or a series capacitance exist, but can be shown negligible [125]. We have to note that these concepts are only applicable without difficulty in the case of Transversal Electric and Magnetic fields (TEM) wave propagation, because only in this case current and voltage are defined. Coaxial cables are good examples, where this is valid and the electric and magnetic field are both perpendicular to the center conductor, which is pointing in the direction of the wave propagation.

We break down the line into a series of lumped components of length  $dx$  as shown in Fig. 2.4, where  $dx$  is small compared to the wavelength  $\lambda$ . In each line section the current  $I$  and voltage  $V$  are decreased, according to

$$dV = -(R dx I + L dx \frac{\partial I}{\partial t}) \quad (2.2)$$

$$dI = -(G dx V + C dx \frac{\partial V}{\partial t}). \quad (2.3)$$

This transforms into two coupled differential equations for an infinitely small  $dx$ :

$$\frac{\partial V}{\partial x} = -(RI + L \frac{\partial I}{\partial t}) \quad (2.4)$$

$$\frac{\partial I}{\partial x} = -(GV + C \frac{\partial V}{\partial t}). \quad (2.5)$$

We suppose a sinusoidal time dependence as

$$V(x, t) = \text{Re}(\tilde{V}(x)e^{j\omega t}) \quad ; \quad I(x, t) = \text{Re}(\tilde{I}(x)e^{j\omega t}), \quad (2.6)$$

where we use a complex notation, which allows to separate the space and time dependence. We can now eliminate  $t$  from our equations as

$$\frac{\partial \tilde{V}}{\partial x} = -(R + j\omega L)\tilde{I} \quad (2.7)$$

$$\frac{\partial \tilde{I}}{\partial x} = -(G + j\omega C)\tilde{V}. \quad (2.8)$$

Combining the two equations, we find

$$\frac{\partial^2 \tilde{V}}{\partial x^2} = \gamma^2 \tilde{V} \quad ; \quad \frac{\partial^2 \tilde{I}}{\partial x^2} = \gamma^2 \tilde{I}, \quad (2.9)$$

where we introduced the propagation constant  $\gamma$  having the dimension of a wave vector (1/m), which is defined by

$$\gamma = \sqrt{(R + j\omega L)(G + j\omega C)}. \quad (2.10)$$

The Eqs. 2.9 are commonly referred to as the telegrapher's equations as they were first developed in connection with long-distance telegraphy over cables [125]. Their solutions have the following form:

$$\tilde{V}(x) = \tilde{V}^+ e^{-\gamma x} + \tilde{V}^- e^{\gamma x} \quad (2.11)$$

$$\tilde{I}(x) = \tilde{I}^+ e^{-\gamma x} + \tilde{I}^- e^{\gamma x}, \quad (2.12)$$

where  $\tilde{V}^+$ ,  $\tilde{I}^+$ ,  $\tilde{V}^-$ ,  $\tilde{I}^-$  are integration constants. The solutions are linear combinations of waves traveling along the line in opposite directions. The integration constants are linked according to equations 2.7 and 2.8, as follows

$$Z_c = \frac{\tilde{V}^+}{\tilde{I}^+} = -\frac{\tilde{V}^-}{\tilde{I}^-} = \sqrt{\frac{(R + j\omega L)}{(G + j\omega C)}}. \quad (2.13)$$

This ratio is called the characteristic impedance  $Z_c$  of the line and is the high-frequency counterpart to the impedance linking a static voltage to the current. While not treated here, we remark that the characteristic impedance (as well as the propagation constant) are also defined in the case of non-TEM mode propagation, where voltage and current are not defined. In that case, they relate the components of the electric field  $E$  and of the the magnetic field  $H$  [126].

It is important to realize that generally both  $\gamma$  and  $Z_c$  are complex values.  $\gamma$  is usually split in the real part  $\alpha$  called attenuation constant and the imaginary part  $\beta$  called phase constant:

$$\gamma = \alpha + j\beta = \sqrt{(R + j\omega L)(G + j\omega C)}. \quad (2.14)$$

This can easily be understood when writing one of the two voltage wave solutions using Eqs. 2.6 and 2.11:

$$V(x, t) = \tilde{V}^+ e^{-\alpha x} e^{j(\omega t - \beta x)}. \quad (2.15)$$

$\alpha$  describes the dissipation reducing the wave amplitude, while  $\beta$  describes the phase rotation per unit length of propagation and allows for the calculation of the phase velocity:

$$v_{\text{Phase}} = \frac{\omega}{\beta}. \quad (2.16)$$

For low-loss lines where  $R$  is small compared with  $\omega L$  and  $G$  is small compared with  $\omega C$ , an approximate solution can be found for  $\alpha$  and  $\beta$  [126]:

$$\alpha \approx \frac{R}{2} \sqrt{\frac{C}{L}} + \frac{G}{2} \sqrt{\frac{L}{C}} \quad ; \quad \beta \approx \omega \sqrt{LC}. \quad (2.17)$$

The characteristic impedance is approximated by

$$Z_c = \sqrt{\frac{L}{C}} \sqrt{1 + j \frac{G}{\omega C} - j \frac{R}{\omega L}}. \quad (2.18)$$

If additionally the losses in the dielectric are small compared to the losses in the conductor,  $\alpha$  and  $Z_c$  can be simplified further by neglecting terms containing  $G$ .

An important consequence of Eq. 2.17 for low-loss cables is that the phase velocity becomes independent of the frequency:

$$v = \frac{\omega}{\beta} = \frac{1}{\sqrt{LC}}. \quad (2.19)$$

For radio transmission lines this means, that the group velocity is equal to the phase velocity, and signals are not distorted (while still being attenuated). The wavelength can then be deduced and is simply inversely proportional to the frequency:

$$v = f\lambda \quad \Rightarrow \quad \lambda = \frac{v}{f} = \frac{2\pi}{\beta}. \quad (2.20)$$

The characteristic impedance tends towards a constant value for high frequencies ( $\omega L \gg R$ ):

$$Z_c = \sqrt{\frac{L}{C}}. \quad (2.21)$$

When speaking about 50  $\Omega$  adapted cables (or 75  $\Omega$ , as used for television signals), always this high-frequency impedance is addressed. The 50  $\Omega$  are not related to the resistance of the cable. The series inductance  $L$  and shunt capacitance  $C$  are chosen such, that  $\sqrt{L/C} = 50 \Omega$ . Indeed, the finite resistance of the cable leads to a bad adaptation for low frequencies, as according to Eq. 2.18  $Z_c$  will deviate from 50  $\Omega$ .

We analyze this using as an example the parameters of the coplanar waveguide which we will employ later: Using the phase velocity which we will determine in section 2.3.2 to  $v = 128650$  km/s for the empty coplanar waveguide and assuming  $Z_c = 50 \Omega$ , we find a series inductance  $L = 3.89 \times 10^{-7}$  H/m and a shunt capacitance  $C = 1.55 \times 10^{-10}$  F/m, after Eqs. 2.19 and 2.21.

The characteristic impedance  $Z_c$  is calculated after Eq. 2.18 neglecting the shunt conductance  $G$ . For very low frequencies the series resistance  $R$  of the coplanar

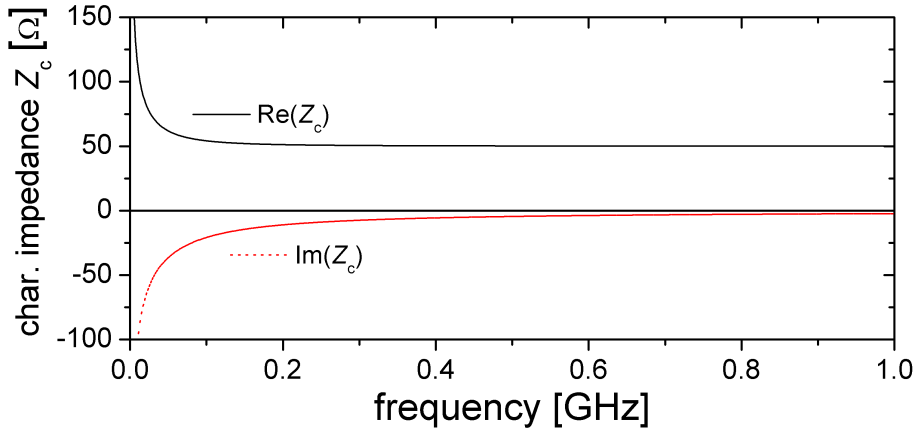


Figure 2.5: (Color online) The real and imaginary part of the characteristic impedance  $Z_c$  taking into account the finite conductivity. With increasing frequency of the microwave current it converges to the purely real  $50 \Omega$ .

waveguide can no longer be neglected, as the inequality  $\omega L \gg R$  is no longer fulfilled and  $Z_c$  deviates from its ideal value.

If we use  $R = 220 \Omega/\text{m}$  assuming the conductivity of gold to  $\sigma = 45 \times 10^6 \text{ S/m}$ , we find the frequency dependence of  $Z_c$  as shown in Fig. 2.5: At frequencies below 500 MHz the CPW deviates from its ideal value. This impedance mismatch entails reflection at connections to other  $50 \Omega$  components. While this can have an influence on the extraction of the susceptibility, even a small anisotropy field with no applied field leads to resonance frequencies lying above this frequency. Therefore, while in principle detrimental to the measurement, we can ignore this effect.

## 2.2.2 Guided Electromagnetic propagation

In the last section we derived the basic equations of TEM wave propagation. This type of propagation is observed in coaxial lines, which we analyze first. Afterwards we apply this concept to a special type of microstrip structure: the coplanar waveguide.

### Coaxial line

The coaxial line is schematically represented in Fig. 2.6: The line consists of a round conducting wire (of radius  $r_1$ ), which is separated from an outer metallic cylinder (of radius  $r_2$ ) by an insulating spacer characterized by its relative dielectric constant  $\epsilon_r = \epsilon/\epsilon_0$ . As the dominant mode of propagation is TEM, both the magnetic and electric field are transverse, i.e.  $E_z = 0$  and  $H_z = 0$  [127]. From symmetry considerations it is deduced that the electric field is oriented radially following  $\vec{u}_r$ , while the magnetic field lines run in circles between the two conductors (following  $\vec{u}_\theta$ ). Integrating the Maxwell equations for this geometry, leads to an equivalent result as in the last section: When the series inductance  $L$  and the shunt capacitance  $C$  are known, basic characteristics of a low-loss line can be calculated. Therefore, we give an estimation of the two quantities.

Using Ampere's law, the magnetic induction on a circle with radius  $r$  between

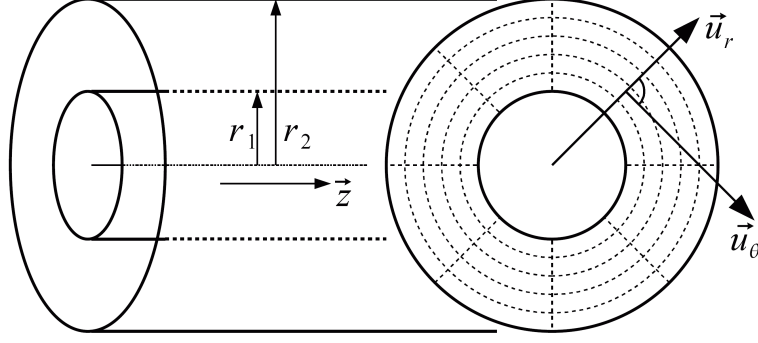


Figure 2.6: Sketch of a coaxial cable consisting of two cylindrical conductors with radii  $r_1$  and  $r_2$  symmetrically aligned around the  $z$ -axis. In the cross section the electric (radial dashed lines) and magnetic field lines (concentric dashed circles) are shown.

the two conductors is given by

$$\vec{B} = \mu_0 \frac{I}{2\pi r} \vec{u}_\theta, \quad (2.22)$$

where  $I$  is the current running through the center conductor. The magnetic flux through a small surface of length  $dz$  parallel to the axis of the coaxial line is therefore expressed by

$$\phi = \mu_0 \frac{I dz}{2\pi} \int_{r_1}^{r_2} \frac{dr}{r} = \mu_0 \frac{I dz}{2\pi} \ln \left( \frac{r_2}{r_1} \right). \quad (2.23)$$

The inductance per unit length is found as

$$L = \frac{\phi}{I dz} = \mu_0 \frac{\ln \left( \frac{r_2}{r_1} \right)}{2\pi}. \quad (2.24)$$

Using Gauss's law, the electric field on a circle with radius  $r$  between the two conductors is given by

$$\vec{E} = \frac{Q}{2\pi r \varepsilon} \vec{u}_r, \quad (2.25)$$

where  $Q$  is the electric charge per unit length on the central wire. The voltage between the two conductors is then

$$V = \frac{Q}{2\pi \varepsilon} \int_{r_1}^{r_2} \frac{dr}{r} = \frac{Q}{2\pi \varepsilon} \ln \left( \frac{r_2}{r_1} \right). \quad (2.26)$$

The capacitance per unit length is therefore given by

$$C = \frac{Q}{V} = \varepsilon \frac{2\pi}{\ln \left( \frac{r_2}{r_1} \right)}. \quad (2.27)$$

Knowing  $L$  and  $C$ , we find for the phase velocity after Eq. 2.19:

$$v = \frac{1}{\sqrt{LC}} = \frac{1}{\sqrt{\varepsilon \mu_0}}. \quad (2.28)$$

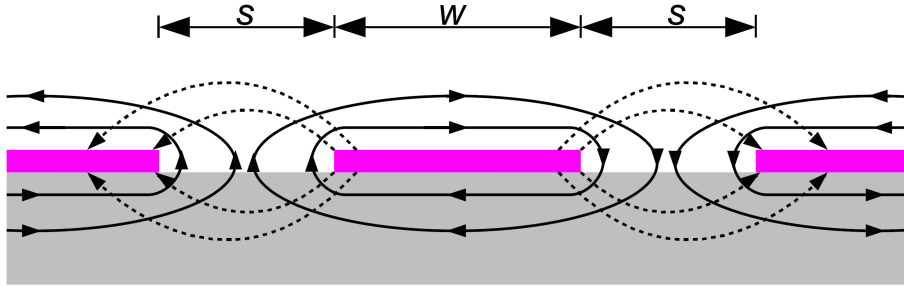


Figure 2.7: Cross section of a coplanar waveguide consisting of the central signal line of width  $w$  with two ground planes separated by  $s$ . The magnetic field  $\vec{H}$  is indicated by the plain lines, the electric field  $\vec{E}$  by the dashed lines.

$v$  is equal to the propagation speed of light in a media of dielectric constant  $\varepsilon$  and is independent of the radii. This is different for the hf characteristic impedance, which we find after Eq. 2.21:

$$Z_c = \sqrt{\frac{L}{C}} = \frac{1}{2\pi} \sqrt{\frac{\mu_0}{\varepsilon}} \ln \left( \frac{r_2}{r_1} \right). \quad (2.29)$$

A combination of the inner and outer radius is chosen on the basis of different criteria: For  $r_2/r_1 = e = 2.718\dots$  the dielectric strength is maximized, i.e. it leads to the highest voltage required for breakdown [125]. Choosing  $r_2/r_1 = 3.6$  minimizes the attenuation in the coaxial cable [125]. In practice, the most commonly used standard is  $Z_c = 50 \Omega$ . This characteristic impedance represents a compromise between a low attenuation, a high breakdown voltage and a high power handling, but is also linked by historical reasons to formerly available dielectrics ( $\varepsilon_r(\text{polyethylene}) \approx 2.25$ ). For reference, we give the impedance of free space, which is  $Z_0 = \sqrt{\mu_0/\varepsilon_0} = 376.73 \Omega$  (often approximated by  $120\pi$ ). Hence, we find  $Z_0/(2\pi) \approx 60 \Omega$ , explaining the usual choice of the magnitude of the hf impedance.

Up till here we did not include magnetic materials. However, a magnetic property of the insulating material can be easily included by making the transition  $\mu_0 \rightarrow \mu_r \mu_0$ . This leaves the shunt capacitance  $C$  unmodified, while changing the series inductance  $L$ , which accordingly leads to a change of the propagation velocity  $v$  and the characteristic impedance  $Z_c$ . Measuring  $v$  and  $Z_c$  as a function of frequency allows then to calculate the frequency-dependent permeability. Applying an external magnetic field, the ferromagnetic resonance is observed in the permeability [93].

### Coplanar waveguide

For the coplanar waveguide (CPW), we can find relations resembling those for the coaxial line. The configuration of this type of transmission line is shown in Fig. 2.7 in the cross section: The center strip conductor of width  $w$  on a substrate with dielectric constant  $\varepsilon$  is accompanied by two coplanar ground planes separated by a distance  $s$ . The CPW is easier to fabricate than other transmission lines as all conductors lie in a single plane, e.g. in contrast to the microstrip line, which has metallic layers in different planes and requires more processing steps. As the wave propagation takes place in different dielectric media, the substrate below and air above the metallic planes, the propagation mode is not precisely TEM, but is well

approximated as quasi-TEM in the quasi-static regime. Only at higher frequencies, the mode of propagation in the CPW becomes non-TEM because a longitudinal component of the magnetic field exists [128]. As for the coaxial line,  $L$  and  $C$  can be used to calculate  $Z_c$  and  $v$ . After [129],  $L$  and  $C$  are given by

$$L = \frac{\mu_0}{4} f(s, w) \quad ; \quad C = 4\tilde{\varepsilon} \frac{1}{f(s, w)}, \quad (2.30)$$

where  $f(s, w)$  is a complicated function depending on  $s$  and  $w$ , i.e. solely on the geometry.  $\tilde{\varepsilon}$  is the effective permittivity, which depends on the dielectric constant of the substrate  $\varepsilon_r \varepsilon_0$  and of air (simply  $\varepsilon_0$ ), as well as on  $s$  and  $w$ . In practice, the substrate thickness is generally much bigger than  $s$  and  $w$  and the effective permittivity is well approximated by the following limit case [130]:

$$\tilde{\varepsilon} = \varepsilon_0 \frac{\varepsilon_r + 1}{2}. \quad (2.31)$$

We now find for the phase velocity after Eq. 2.19:

$$v = \frac{1}{\sqrt{LC}} = \frac{1}{\sqrt{\tilde{\varepsilon}\mu_0}}, \quad (2.32)$$

which is similar to the coaxial line except that the effective dielectric constant is used. The hf characteristic impedance is calculated after Eq. 2.21 to:

$$Z_c = \sqrt{\frac{L}{C}} = \frac{1}{4} \sqrt{\frac{\mu_0}{\tilde{\varepsilon}}} f(s, w). \quad (2.33)$$

By choosing a proper geometry, i.e. suitable values of  $s$  and  $w$ ,  $Z_c$  can be set to  $50 \Omega$ . The parameters for the CPW employed in our measurement setup are  $w = 50 \mu\text{m}$ ,  $s = 20 \mu\text{m}$  and  $\varepsilon_r = 9.9$  (Alumina), resulting in  $L = 0.39 \text{ nH/mm}$  and  $C = 0.16 \text{ pF/mm}$ . This gives  $v = 128417 \text{ km/s}$  and  $Z_c = 50 \Omega$ . Detailed information on the practical implementation of CPWs can be found in [128].

In Fig. 2.7 the electric and magnetic field lines are sketched. As for the coaxial line the magnetic field runs around the center conductor. Due to its rectangular shape, they are flattened close by the surface. Directly on top of the conductor, they run parallel to the surface.

### 2.2.3 Scattering parameters

In waveguides supporting non-TEM propagation, voltages and currents cannot be specified uniquely. For these systems it is advantageous to introduce the scattering parameters, also called S-parameters, which relate incident and reflected electromagnetic waves. Even if we always stay in the quasi-TEM approximation, S-parameters allow to avoid measurements of total voltage and current, which become difficult at high frequencies [131]. As we will see later, S-parameters are also the values measured by the vector network analyzer.

In a microwave network, every access line to a component consisting of a pair of terminals is called port. It is possible to define the scattering matrix for a  $n$ -port device, but here we will only deal with two-port devices. The complex normalized waves  $a_i$  and  $b_i$  at a port  $i$  are defined by

$$a_i = \frac{V_i + Z_{ci} I_i}{2\sqrt{Z_{ci}}} \quad ; \quad b_i = \frac{V_i - Z_{ci} I_i}{2\sqrt{Z_{ci}}}, \quad (2.34)$$



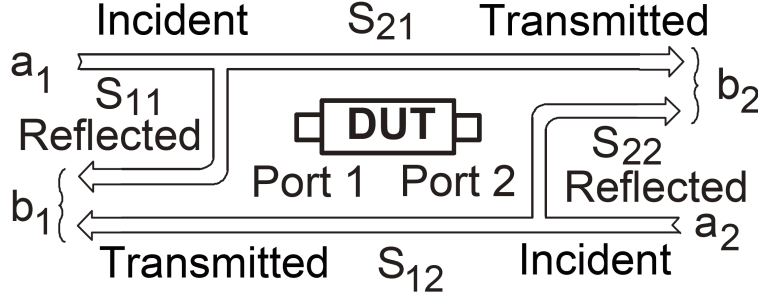


Figure 2.8: Schematization of the relation between the S-parameters of the two-port device under test and the complex normalized waves  $a_i$  and  $b_i$ , after [131].

where  $Z_{ci}$  is the characteristic impedance of the transmission line at port  $i$ . The voltage  $V_i$  and the current  $I_i$  at port  $i$  can then be calculated as

$$V_i = \sqrt{Z_{ci}}(a_i + b_i) \quad (2.35)$$

$$I_i = \frac{a_i - b_i}{\sqrt{Z_{ci}}}. \quad (2.36)$$

When introducing Eqs. 2.11 and 2.12 into Eq. 2.34, it becomes obvious that  $a_i$  characterizes the incident wave, while  $b_i$  is the outgoing wave:

$$a_i = \frac{V_i^+}{Z_{ci}} e^{-\gamma x} \quad ; \quad b_i = \frac{V_i^-}{Z_{ci}} e^{\gamma x}. \quad (2.37)$$

The relation between  $a_{1,2}$  and  $b_{1,2}$  and the S-parameters is schematized in Fig. 2.8: For a  $n$ -port device  $n^2$  S-parameters are necessary. Therefore, in our case there are four, which describe the two-port network by

$$\begin{pmatrix} b_1 \\ b_2 \end{pmatrix} = \bar{\bar{S}} \begin{pmatrix} a_1 \\ a_2 \end{pmatrix} = \begin{bmatrix} S_{11} & S_{12} \\ S_{21} & S_{22} \end{bmatrix} \begin{pmatrix} a_1 \\ a_2 \end{pmatrix}, \quad (2.38)$$

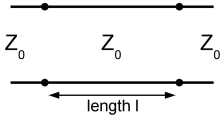
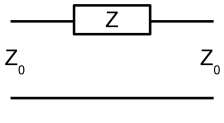
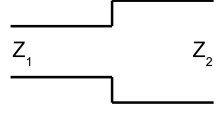
where  $\bar{\bar{S}}$  is the scattering matrix. Each  $S_{ij}$  parameter is the ratio of the outgoing wave  $b_i$  at port  $i$  to the incident wave  $a_j$  at port  $j$  when no signal is fed at any other port  $k \neq j$  (i.e., when the other ports are terminated into nonreflecting matched loads) [127].

The reflected wave  $b_i$  at any port is described as a linear combination of the incident waves at all ports. A full set of S-parameters completely characterizes any linear device under test (DUT).

Apart from linearity another important property of the DUT is reciprocity: The transfer function of the device does not depend on the direction of propagation, which is expressed by  $S_{12} = S_{21}$ . Most passive devices made from non ferromagnetic dielectric and nonferromagnetic metal satisfy this condition [127], however, it is not satisfied in devices containing magnetized ferrites due to the presence of magnetostatic surface waves (MSSW, see Sec. 1.6.1). This is exploited in isolators and circulators, but can be neglected here due to the low thickness of the examined films [100].

An additional qualifier for the DUT is their symmetry: A device is called symmetric if the condition  $S_{11} = S_{22}$  is fulfilled.

Table 2.2: S and T matrices of several circuit components [133, 134].

	S matrix	T matrix	
Line section, length $l$ , matched char. Impedance $Z_0$	$\begin{bmatrix} 0 & e^{-\gamma l} \\ e^{-\gamma l} & 0 \end{bmatrix}$	$\begin{bmatrix} e^{-\gamma l} & 0 \\ 0 & e^{\gamma l} \end{bmatrix}$	
Lumped serial impedance $Z$ on a line with char. impedance $Z_0$	$\begin{bmatrix} \frac{Z}{Z+2Z_0} & \frac{2Z_0}{Z+2Z_0} \\ \frac{2Z_0}{Z+2Z_0} & \frac{Z}{Z+2Z_0} \end{bmatrix}$	$\begin{bmatrix} \frac{2Z_0-Z}{2Z_0} & \frac{Z}{2Z_0} \\ \frac{-Z}{2Z_0} & \frac{2Z_0+Z}{2Z_0} \end{bmatrix}$	
Change of char. impedance: port1: $Z_1$ , port2: $Z_2$	$\begin{bmatrix} \frac{Z_2-Z_1}{Z_2+Z_1} & \frac{2\sqrt{Z_1Z_2}}{Z_2+Z_1} \\ \frac{2\sqrt{Z_1Z_2}}{Z_2+Z_1} & \frac{Z_1-Z_2}{Z_2+Z_1} \end{bmatrix}$	$\begin{bmatrix} \frac{Z_1+Z_2}{2\sqrt{Z_1Z_2}} & \frac{Z_2-Z_1}{2\sqrt{Z_1Z_2}} \\ \frac{Z_2-Z_1}{2\sqrt{Z_1Z_2}} & \frac{Z_1+Z_2}{2\sqrt{Z_1Z_2}} \end{bmatrix}$	

Later on we will encounter the necessity of cascading several two-port networks. This can be realized in a straightforward manner by introducing the transmission coefficients  $T_{ij}$ . The transmission matrix  $\bar{T}$  relates the  $a_i$  and  $b_i$  as follows

$$\begin{pmatrix} b_1 \\ a_1 \end{pmatrix} = \bar{T} \begin{pmatrix} a_2 \\ b_2 \end{pmatrix} = \begin{bmatrix} T_{11} & T_{12} \\ T_{21} & T_{22} \end{bmatrix} \begin{pmatrix} a_2 \\ b_2 \end{pmatrix}. \quad (2.39)$$

The transmission coefficients offer the considerable advantage, that chaining several two-port devices is equivalent to multiplying their T matrices. Transforming an S matrix into the corresponding T matrix and vice versa, is a simple mathematical operation [132]:

$$\begin{bmatrix} S_{11} & S_{12} \\ S_{21} & S_{22} \end{bmatrix} = \begin{bmatrix} \frac{T_{12}}{T_{22}} & \frac{T_{11}T_{22}-T_{12}T_{21}}{T_{22}} \\ \frac{1}{T_{22}} & -\frac{T_{12}}{T_{22}} \end{bmatrix} \quad (2.40)$$

$$\begin{bmatrix} T_{11} & T_{12} \\ T_{21} & T_{22} \end{bmatrix} = \begin{bmatrix} \frac{S_{12}S_{21}-S_{11}S_{22}}{S_{21}} & \frac{S_{11}}{S_{21}} \\ -\frac{S_{22}}{S_{21}} & \frac{1}{S_{21}} \end{bmatrix} \quad (2.41)$$

$$(2.42)$$

In Tab. 2.2 we list several important matrices to which we will resort later.

## 2.2.4 Vector Network Analyzer

The Vector Network Analyzer (VNA) allows the measurement of all four S-parameters of the DUT over a broad frequency range. We used a HP8510C, which allowed for frequencies between 45 MHz and 50 GHz. A simplified schematization of a transmission/reflection test set is depicted in Fig. 2.9.

A synthesized hf source provides the signal at the intended measurement frequency  $f$ . The signal is split into two branches: the reference signal and the signal connected to the device under test at port 1. The reference signal is used to lock a local oscillator with the frequency  $f + \Delta f$  to the hf source. The directional coupler is used to collect the signal reflected by the DUT. The tuned receiver then mixes the signal of the local oscillator with either the reflected or transmitted signal, so as to transpose the signal to a low intermediate frequency  $\Delta f$ . The signals are

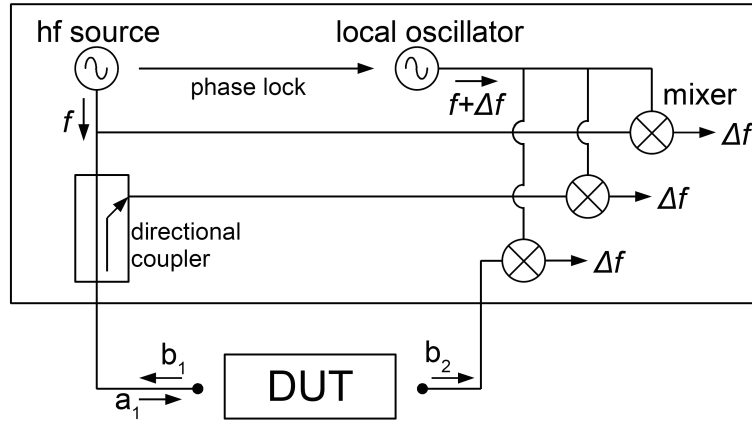


Figure 2.9: Simplified schematization of a Vector Network Analyzer: Here, a transmission/reflection test set is shown, which measures only  $S_{11}$  and  $S_{21}$  and does not allow for a full two-port calibration [135].

then bandpass filtered and as they were brought to low frequency (e.g.  $\Delta f \approx 3$  kHz [135]), their magnitude and phase can be analyzed.

The simplified architecture in Fig. 2.9 only allows for the measurement of  $S_{11}$  and  $S_{21}$ . In order to measure all four S-parameters a transfer switch has to be added which allows to apply power on both ports and a second directional coupler at port 2 allows a symmetrical detection. As introduced in the previous section, each  $S_{ij}$  parameter is the ratio of the output signal  $b_i$  at port  $i$  to the input signal  $a_j$  at port  $j$  when no signal is fed at any other port  $k \neq j$  (i.e., when the other ports are terminated into nonreflecting matched loads) [127]. Therefore, in order to measure a single S-parameter it is in principle sufficient to apply a signal to only one of the two ports while monitoring  $b_1$  and  $b_2$ . We will see in the next section, why in practice it is not that simple.

Finally, we insist on the term “vector” in the name of the VNA, as the detection is phase sensitive and the measured S-parameters are complex. This is an important difference to spectrum analyzer or scalar network analyzer measurements, which only provide scalar quantities. We will see that the measurement of the phase enables the calculation of both the real and the imaginary part of the susceptibility. Whenever we speak about a network analyzer in the following, we refer to a VNA.

### 2.2.5 Error Correction

The calibration procedure serves two purposes: firstly, it removes contributions from the high-frequency probes and cables connecting the VNA to the DUT. The frequency-dependent signal attenuation and the contact discontinuities are then taken into account. Therefore, the reference planes of the high-frequency measurements are at the tips of the microwave probes, and the measured S-parameters only depend on the microwave circuit in-between.

The second purpose is linked to the non ideal measurement: Unfortunately, the hardware used in the network analyzer is not perfect, e.g. couplers are not perfectly directive and signals leak across channels [127]. Signal reflections at discontinuities (connections) contribute as well. These systematic errors are repeatable and assuming that they are time invariant, they can be corrected using a calibration process:

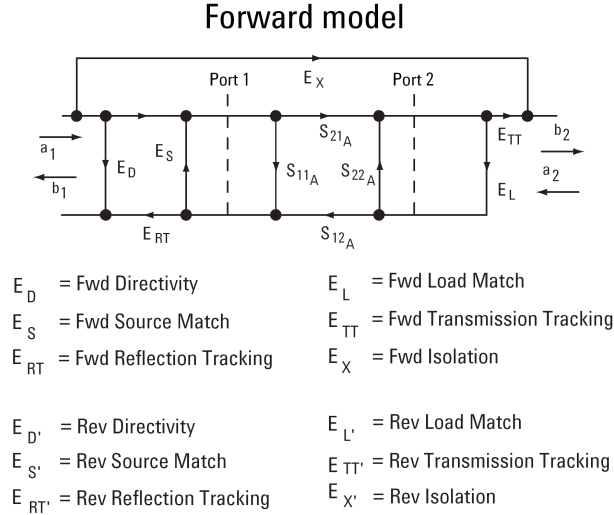


Figure 2.10: The forward model of the two-port error correction containing 6 of the 12 error terms, after [136]. The calibration is completed by the reverse model, where power is applied at the port 2.

An error model, part of which is shown in Fig. 2.10, is defined.

For a two port measurement, this model contains 12 error terms. They are determined by connecting the VNA to a so-called calibration kit, which contains several well-known standards allowing to calculate back to the imperfections of the hardware. We used a calibration standard which is commonly termed SOLT, abbreviating Short, Open, Load and Through. The employed impedance standard from Cascade Microtech contained correspondingly the following standards implemented in coplanar geometry, as to allow connections of high-frequency probes: A short-circuit, an open-circuit, a precise  $50\ \Omega$  impedance and a short section of a coplanar waveguide of defined length. Each standard has to be connected with both ports and measured for each anticipated frequency in both directions. When performing measurements using the calibration, each actual S-parameter is a complicated function of all four measured S-parameters and the 12 error terms. So, to correct any one S-parameter, the network analyzer must first have measured all four of them in order to calculate the intended one [135].

We want to insist on the importance of a precise calibration in order to attain the highest sensibility. Therefore, the calibration is typically repeated successively multiple times to improve the error terms (as it is e.g. easily possible to have a bad contact when measuring one of the calibration standards). While it is not possible to completely suppress any error, criteria which determine a satisfactory error correction are available: Values which should be equal to 0, as e.g. the reflection at a port connected to the  $50\ \Omega$  matched sample, should be below  $-50\ \text{dB}$ . Values which should in principle be 1, for example  $S_{12}$  when both ports are connected with the Through sample, should lie between  $-0.01\ \text{dB}$  and  $+0.01\ \text{dB}$ .

The calibration typically degrades with time, as the system performance changes after a calibration has been done. These drift errors can be primarily attributed to temperature variations [135]. They are removed by repeating the calibration sequence, but minimized in the first place by providing a stable ambient temperature. This has to be taken into account as the measurement setup can heat up considerably

(power supplies, electromagnet). In the absence of air conditioning, we repeated the calibration at least twice a day.

For more on error correction, we advise [135, 136], which also treat one-port calibration, which we will employ in chapter 4.

## 2.3 Vector Network Analyzer Ferromagnetic Resonance

Vector network analyzer VNA-FMR has been used extensively during this thesis. In this section, we first describe the experimental realization of the measurement. Then we present raw data as provided by the VNA for the CPW without a sample. As the calculation of the susceptibility from the raw measurement data of a two-port measurement (the scattering parameters) was not treated uniformly in the literature, we will dedicate the next chapter exclusively to this matter. There, we will give a comparison between commonly employed calculations and we will show a complete high-frequency analysis of the problem. Here, we still show using a simple argument how the excited magnetization oscillation is detected. Finally, we give an example of the extraction and analysis of the ferromagnetic resonance frequency and the resonance linewidth from the evaluated measurement data.

### 2.3.1 Experimental Setup

The main components of the experimental setup are sketched in Fig. 2.11: The VNA is connected to a coplanar waveguide (CPW) having a characteristic impedance of  $50 \Omega$  using coaxial cables and microwave probes. For such radio frequency connections often coaxial cables with teflon insulation and SMA (SubMiniature version A) connectors are employed. They are comparably low priced and offer a bandwidth of typically 18 GHz. Instead of SMA type cables, we employed air-spaced coaxial cables with so-called K-connectors. Using air as the dielectric allows to further improve their microwave characteristics. The distance between the inner and outer conductors has to be maintained by a series of insulating washers at regular intervals. The K-connectors mate with SMA connectors and while being more expensive, the bandwidth of this type of cables is specified to 40 GHz. This renders measurements at higher frequencies possible and increases the precision at lower frequency respectively. The used cables did not have a metallic reinforcement. It was found previously [100], that the reinforcement can contain nickel making the cables sensitive to an applied magnetic field causing mechanical strain. Additionally, the cables need to be protected from moving or bending: Already a slight contact can change their physical length, having a negative effect on the measurement.

The coaxial geometry now needs to be connected to the coplanar geometry. This was achieved using microwave probes of the brand Picoprobe [137]. These microwave probes accomplish the transition from a female K connector to three individually spring loaded tips in a Ground-Signal-Ground geometry with the use of a miniature  $50 \Omega$  coaxial cable, leading to a low insertion loss. Similar to the K-type cables, these probes offer a bandwidth of 40 GHz or higher. However, we found that a set of two small adjustment screws present on some models was ferromagnetic and had to be replaced by non-magnetic ones available on request. We insist that in general most of the commercial microwave equipment is not free from magnetic materials

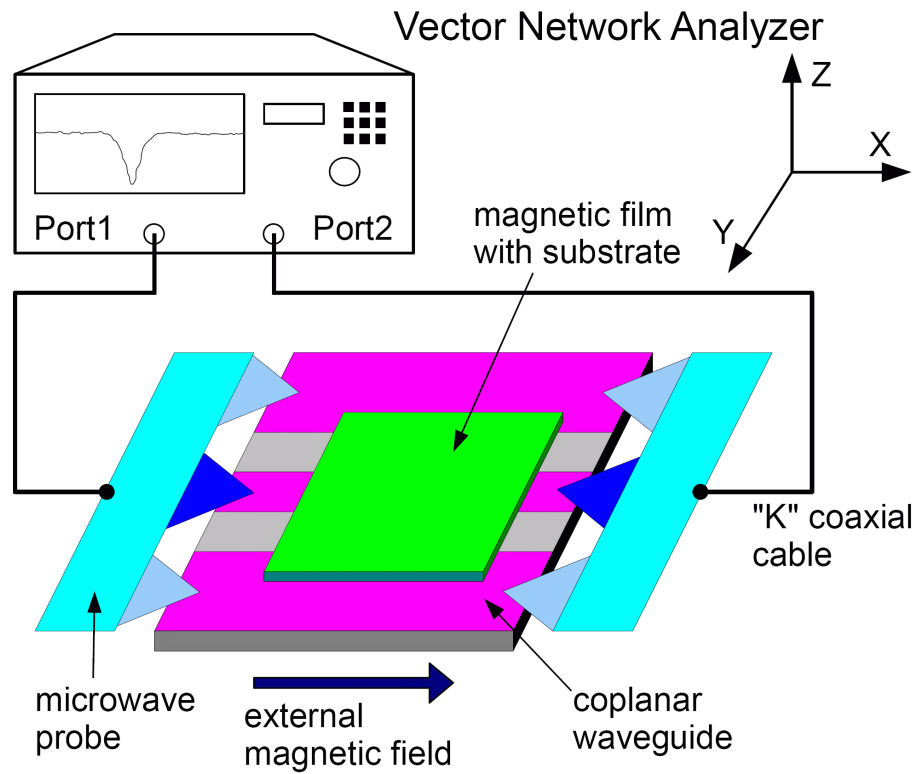


Figure 2.11: (Color online) Sketch of the experimental setup: The sample is placed magnetic film side downwards on the coplanar waveguide, in which photons are guided with their magnetic field strength in the y-direction, i.e. perpendicular to the external magnetic field following the x-axis.

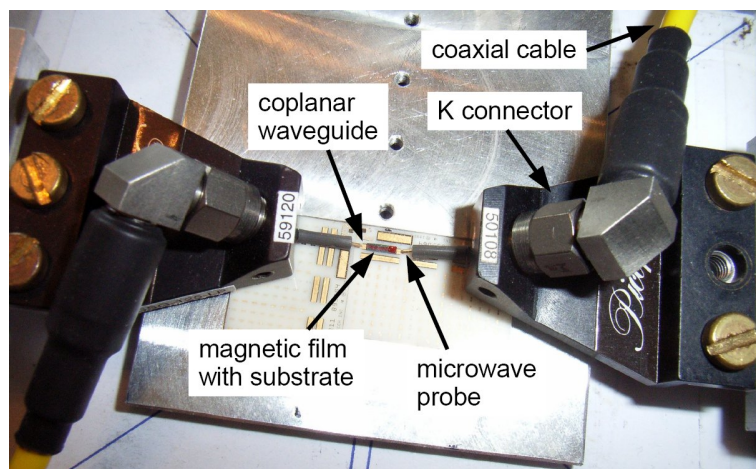


Figure 2.12: (Color online) Photograph of the experimental setup: The section between the two microwave cables in Fig. 2.11 is shown.

and therefore not suited for use in measurement conditions under the application of varying magnetic fields. The two probes were mounted on two opposing xyz manipulators, allowing a positioning of the tips with micrometer precision. As the movement of the probe tips leads to a movement of the microwave cables, the manipulators were fixed on the experimental table in such a way as to minimize the distance for every necessary connection. The calibration kit was indeed mounted on a third xyz manipulator fixed at  $90^\circ$  with respect to the microwave probes: In order to accomplish the connections necessary for the calibration, instead of moving the probes, the calibration kit was moved underneath. Thus, the displacement of the probes and consequently of the high-frequency cables was avoided. After having completed the calibration, the probes are connected to the coplanar waveguide. A good  $50\ \Omega$  matching of the CPW is achieved by proper selection of the waveguide substrate, the conductor material and their dimensions. Free design software can be found at [138] and [139]. We used either a  $5250\ \mu\text{m}$  or a  $3500\ \mu\text{m}$  long CPW present on the impedance standard substrate with excellent microwave characteristics.

The three manipulators with the microwave probes and the calibration substrate are fixed on an aluminum plate, together with a binocular microscope allowing the inspection of the established connections. Underneath the plate, an electromagnet is installed. The pole pieces of its yoke lie directly underneath the sample. The stray field penetrating through the plate creates a magnetic field at the sample position. The aluminum plate is thinned at the center allowing to approach the sample closer to the pole pieces and thereby increasing the field strength and improving the field homogeneity at the sample position. The magnetic field is monitored using a Hall probe between the pole pieces, which is calibrated using a commercial gaussmeter at the sample position. The Hall voltage showed a linear dependence on the magnetic field with an attainable maximum of  $170\ \text{mT}$  at the sample position. As the electromagnet is supported by a ball bearing, it can be turned  $360^\circ$  applying the magnetic field in an arbitrary in-plane direction. The high frequency cables have a length of  $1.5\ \text{m}$ , in order to keep the VNA at a certain distance from the electromagnet: The synthesized source uses a yttrium iron garnet (YIG) oscillator to provide the high frequency bands. The oscillator and thus the frequency precision could be influenced by the magnetic field.

In order to immunize the setup from vibrations, it is placed on a heavy marble plate decoupled from the foundations using rubber buffers. In addition, an air conditioning system is installed next to the setup stabilizing the temperature as mentioned in section 2.2.5. This helps prolong the validity of the error correction, as without a controlled climate the calibration has to be repeated several times per day.

### 2.3.2 Characterization without sample

The VNA provides a sinusoidal power wave which is guided by the coaxial cables to the microwave probes making the connection to the CPW (see Fig. 2.11). As we argued in the previous section, all components are well adapted to  $50\ \Omega$  and we shall consider them as without reflection, since any slight mismatch as well as imperfections of the VNA are corrected by the calibration. To give a practical example of the electromagnetic wave propagation, we analyze the employed CPW, where we introduce at the same time different representations of the raw measurement data as provided by the VNA.

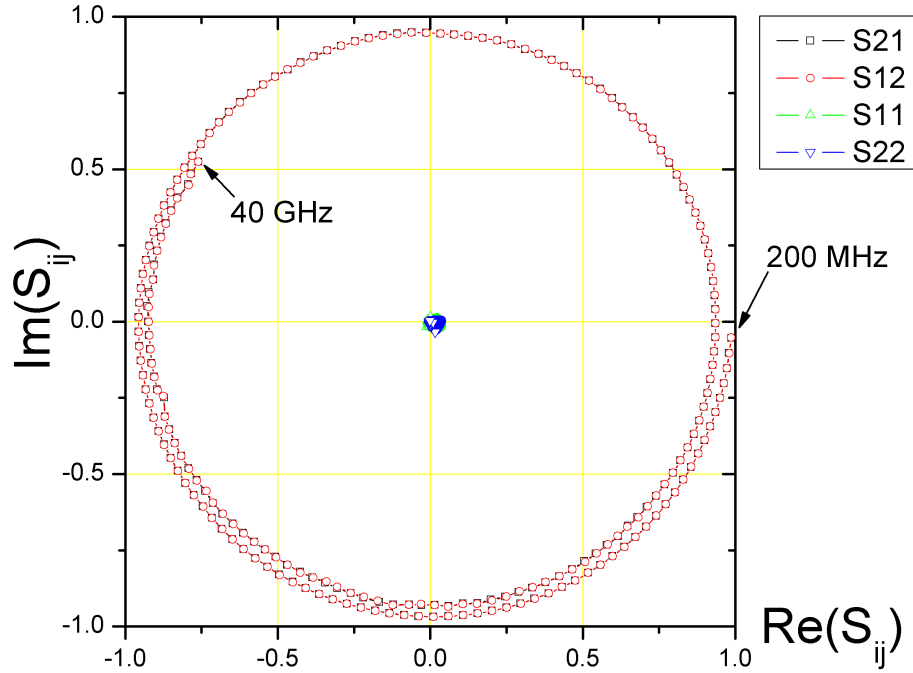


Figure 2.13: (Color online) Smith Chart/polar diagram of all four S-parameters characterizing the CPW between 200 MHz and 40 GHz.

According to Tab. 2.2, the complex S-parameters which we expect for a section of line are:  $S_{21} = S_{12} = e^{-\gamma l}$  and  $S_{11} = S_{22} = 0$ . A comprehensive representation of the measured data in the complex plane is shown in Fig. 2.13: For the transmission parameters ( $S_{21}$ ,  $S_{12}$ ) it is simply called polar diagram, but for the reflection parameters ( $S_{11}$ ,  $S_{22}$ ) it is usually termed Smith Chart. As expected, the two transmission parameters coincide. Following Eq. 2.14, we split the propagation constant  $\gamma$  in its real and imaginary part, leading to

$$\alpha = -\frac{\ln(|S_{21}|)}{l} \quad ; \quad \beta = -\frac{\arg(S_{21})}{l}. \quad (2.43)$$

The complex modulus  $|S_{ij}|$  and the complex argument  $\arg(S_{ij})$  of the transmission parameters as a function of frequency are plotted in Fig. 2.14. We saw in Eq. 2.19 that the phase constant  $\beta$  increases linearly with frequency. By fitting the slope of  $\arg(S_{ij})$ , we find a phase velocity of  $v = 128650$  km/s. According to Eq. 2.31 and 2.32, we determine the relative permittivity of the CPW substrate to  $\epsilon_r = 9.86$ , which agrees well with the value expected for Alumina given by the manufacturer (9.9).

The attenuation constant  $\alpha$  which is directly proportional to  $\ln(|S_{21}|)$  does not follow such a simple relation and is only approximately linear with frequency (when given in a logarithmic unit). However, it is low and the bandwidth, i.e. the frequency where  $|S_{ij}|$  would reach  $-3$  dB is much higher than the measured 40 GHz. We also observe that  $|S_{ij}|$  becomes more noisy for higher frequencies. This can be ascribed to the calibration which becomes more sensitive and more difficult to accomplish at high frequencies. While having higher noise, the characteristics are still good at 40 GHz, but anyway most measurements are taken at frequencies below 15 GHz, as the ferromagnetic resonance frequency is limited by the available magnetic field.



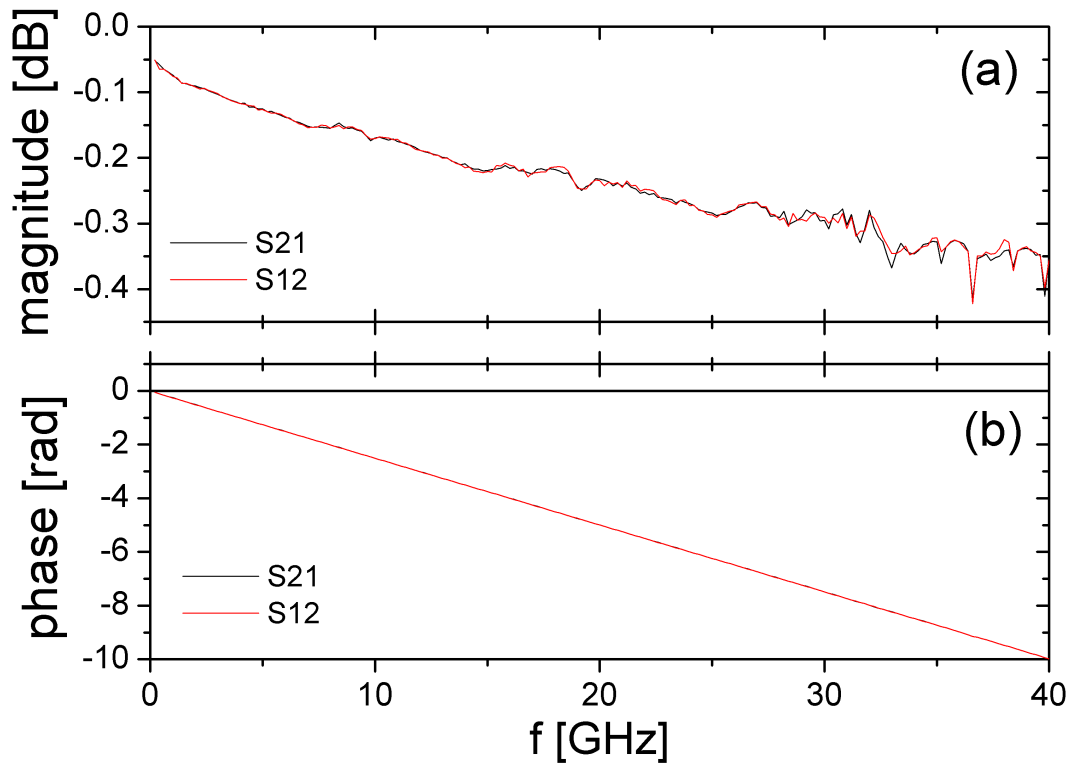


Figure 2.14: (Color online) (a) The magnitude of the transmission parameters ( $|S_{ij}|$ ) in decibel and (b) their phase ( $\arg(S_{ij})$ ) measured between 200 MHz and 40 GHz.

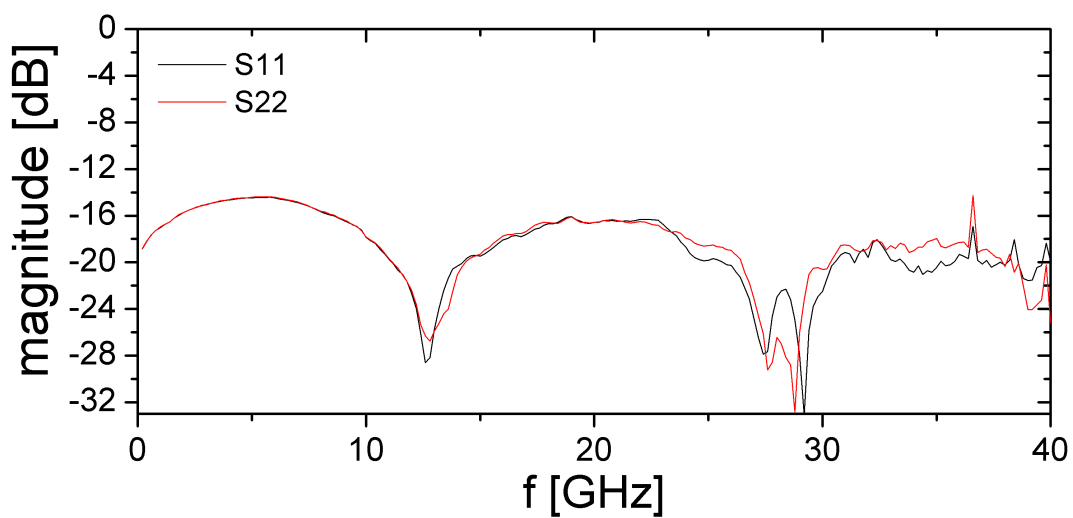


Figure 2.15: (Color online) The magnitude of the reflection parameters ( $|S_{ii}|$ ) in decibel measured between 200 MHz and 40 GHz.

The reflection parameters ( $S_{11}$ ,  $S_{22}$ ) are expected to be zero. Their magnitude in decibel is plotted in Fig. 2.15. Obviously, a perfect agreement cannot be achieved due to a finite calibration error, but they are sufficiently low to be perfectly negligible. However, one interesting feature can be seen: For frequencies which correspond to whole number multiples of the CPW length, a strong decrease in amplitude is observed. These dips appearing approximately at multiples of 13 GHz (including 0) are called dimensional resonances [140]. At these frequencies there is a large phase uncertainty due to the low amplitude, which we will need to take into account in the next chapter.

### 2.3.3 Measurement of a ferromagnetic thin film

As sketched in Fig. 2.11, we now place the magnetic thin film sample on top of the CPW, covering in particular its center conductor. The substrate of the sample is pointing away from the CPW. We found that the air gap separating the metallic thin film and the center conductor is sufficient in order to prevent a short between the ground and signal lines. The air gap is due to a curvature of the sample, which does not lie perfectly flat on the CPW. The magnetization of the thin film is aligned in parallel to the magnetic field applied by the electromagnet. We suppose that the static magnetic field is pointing along the x-axis. As we have seen in Fig. 2.7, the high-frequency current supplied by the VNA creates a small oscillating magnetic field on top of the center conductor. In its center and close to its surface, the generated high-frequency field can be considered as in-plane and aligned in the y-direction. This experimental situation corresponds to the calculation in section 1.3, where we saw that a magnetization precession is excited and maintained.

We need to make sure that the excitation angle remains small, i.e. that we can stay in the linear approximation. Therefore, we give an estimate for the exciting microwave field. The power applied by the VNA was chosen to 0 dBm corresponding to 1 mW. For a characteristic impedance  $Z_c$  of 50  $\Omega$  the current is then 4.5 mA. The high frequency field can be estimated using  $h = I/2w$  [96], where we find  $\mu_0 h = 56 \mu\text{T}$  (= 0.56 Oe). The real field value is lower, as this conservative estimation neglects the air gap. The correct value is still lower, as here we did not take into account the signal attenuation in the cables between the VNA and the CPW. A more precise estimation [141] using a commercial E-M software simulation correspondingly led to a smaller result. The field is sufficiently small such that we remain in the linear regime of excitation [142]. This is even valid at resonance, where we need to multiply the field with the maximum of the susceptibility having the order of magnitude  $10^2$ . The obtained high frequency magnetization is largely exceeded by the static magnetization  $\mu_0 M_s \geq 1$  T.

The oscillating magnetization leads to a magnetic flux variation, given by

$$d\phi \cong \mu_0 m_y(t) d dx, \quad (2.44)$$

where we consider an infinitesimal part of length  $dx$  of the sample of height  $d$  which is placed on top of the center conductor (see Fig. 2.16). This flux variation is detected by the CPW through the induction of an electromotive force, which is given by

$$dV = -\frac{d\phi}{dt} = -\mu_0 \frac{dm_y(t)}{dt} d dx. \quad (2.45)$$

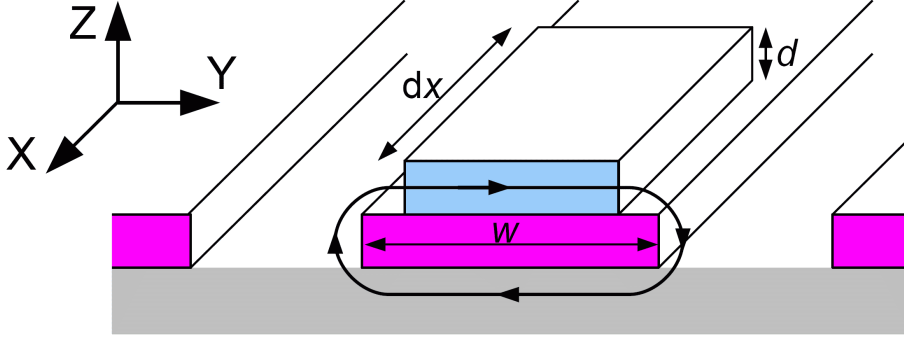


Figure 2.16: Magnetic thin film sample placed on top of the center conductor of the coplanar waveguide. The small excitation field is considered as approximately uniform and parallel to the surface of the conductor.

Still taking into account the oscillating motion of the magnetization, we can write  $dV$  as

$$dV = -\mu_0 i 2\pi f m_y(t) d dx. \quad (2.46)$$

After Eq. 1.33, we can express  $m_y(t)$  as  $m_y(t) = \chi_{yy} h_y$ , where  $h_y$  is expressed as  $h_y = I/2w$ , leading to

$$\frac{dV}{dx} = -i 2\pi f \chi_{yy} \frac{\mu_0 d}{2w} I. \quad (2.47)$$

Eq. 2.47 obviously leads to a similar relation between the voltage and the current as one of the Telegrapher's Equations (see Eq. 2.7), where we used the angular frequency  $\omega = 2\pi f$ . This allows to model the moving magnetization as an additional impedance as

$$\Delta L(\omega = 2\pi f) = \chi_{yy} \frac{\mu_0 d}{2w}. \quad (2.48)$$

We remind that  $\chi_{yy}$  is complex and therefore  $\Delta L$  is composed of both an inductance and an “imaginary” inductance. Obviously, the changed inductance influences the line characteristics, i.e. the propagation constant  $\gamma$  (see Eq. 2.10) and the characteristic impedance  $Z_c$  (see Eq. 2.13), leading to reflection and additional signal attenuation and delay, which is detected in the measured S-parameters. This is exemplified in Fig. 2.17 showing the complex norm and the phase of the transmission parameter  $S_{12}$  with and without a 40 nm CoFeB thin film sample placed on the CPW (under an applied magnetic field of 22 mT). The ferromagnetic resonance is clearly visible around 6 GHz.

The approach starting from the magnetic flux change shows how the oscillating magnetization leads to a change of the CPW characteristics. While this allows an intuitive understanding of the detection of the magnetization motion, it is easier to take the high frequency character of the wave propagation into account by developing a description directly starting from the S-parameters. The precise relation between the S-parameters and the susceptibility is complicated. Therefore, we will postpone the calculation of the scattering matrix to the next chapter, which is entirely dedicated to this subject.

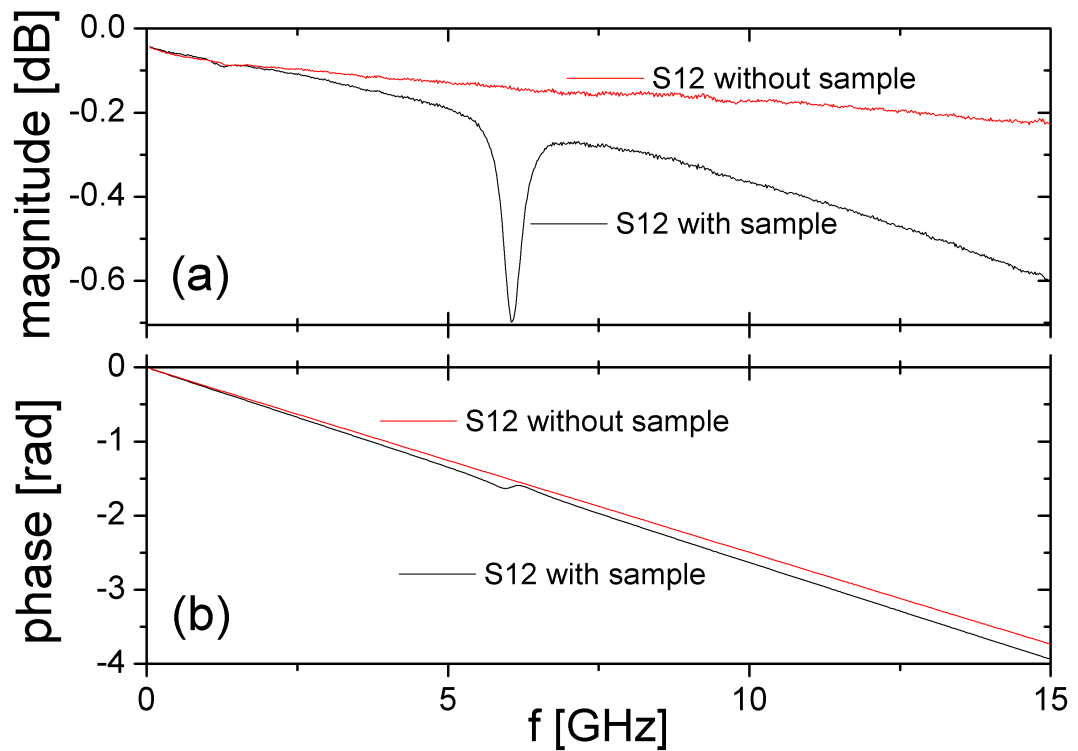


Figure 2.17: (Color online) The magnitude in decibel (a) and the phase (b) of the transmission parameter  $S_{12}$  with and without the 40 nm CoFeB film placed on the CPW.

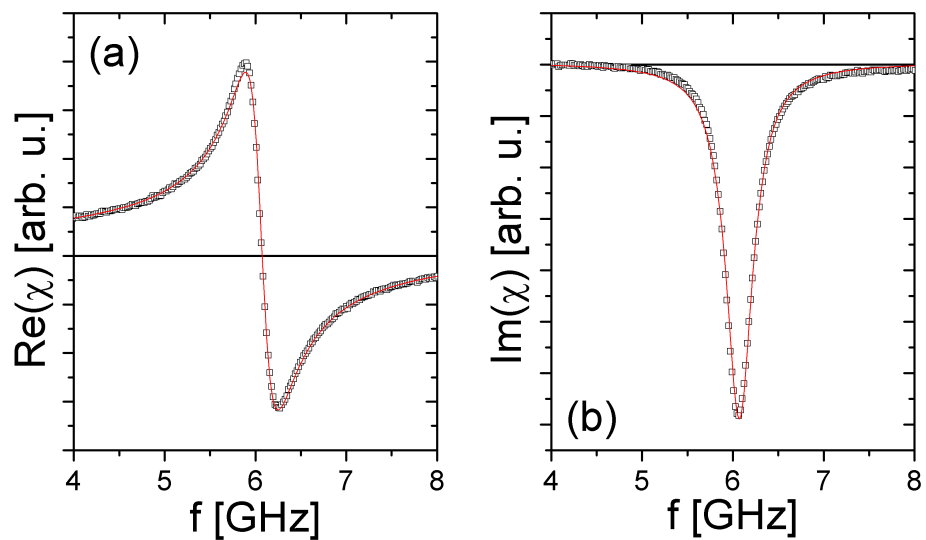


Figure 2.18: (Color online) The real (a) and imaginary (b) part of the susceptibility for the 40 nm CoFeB film with 22 mT applied field. The black open squares represent the measured susceptibility, while the plain red line is a fit.

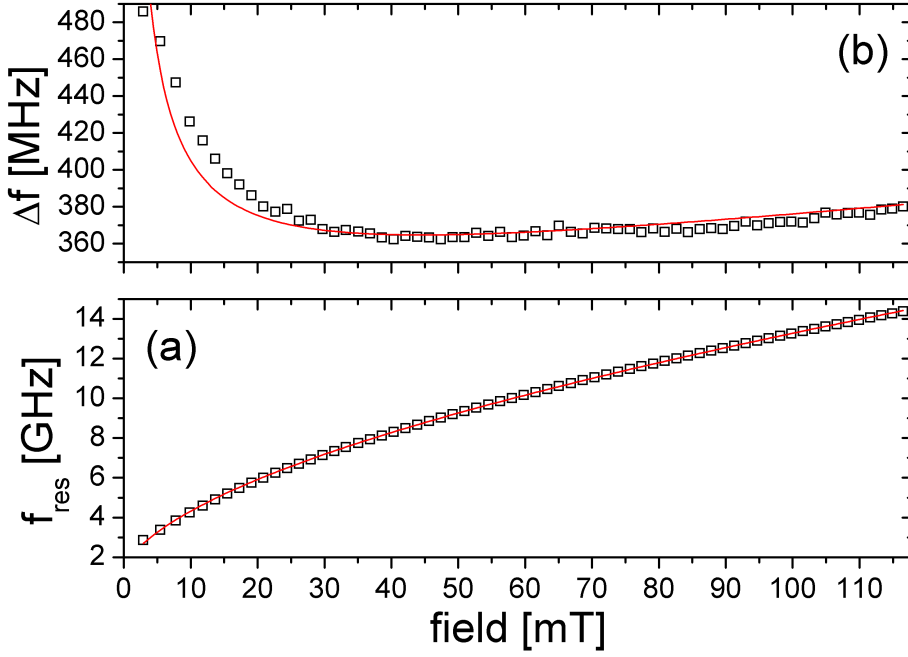


Figure 2.19: (Color online) (a) The resonance frequency  $f_{\text{res}}$  and (b) the linewidth  $\Delta f$  for the 40 nm CoFeB film as a function of the applied field. The measured data are represented by black open squares, the red line in part (a) is a fit using Eq. 2.50, in part (b) using Eq. 2.59.

### Resonance frequency and linewidth

Following the procedure that will be described in detail in section 3.2, the dynamic susceptibility  $\chi$  can then be calculated from the raw measurement data. An example is shown in Fig. 2.18: The susceptibility for the same sample and the same applied field as in Fig. 2.17. The measured susceptibility is represented by the black open squares. It corresponds well to the theoretically deduced formula which was discussed in section 1.3. This is illustrated by the fits marked by the plain red lines. The two most interesting data are the resonance frequency  $f_{\text{res}}$  and the linewidth  $\Delta f$ :  $f_{\text{res}}$  was determined from  $\text{Re}(\chi)$  to 6.068 GHz, from  $\text{Im}(\chi)$  to 6.070 GHz.  $\Delta f$  was fitted in  $\text{Re}(\chi)$  to 372 MHz, in  $\text{Im}(\chi)$  to 380 MHz. While the extracted data agree well, the fit is not perfect. This can be attributed to inhomogeneous broadening or extrinsic contributions to the damping (discussed in section 1.5). Both can distort the lineshape. Nevertheless, the linewidth can be used to calculate an apparent damping  $\alpha_{\text{app}}$  following Eq. 1.50:

$$\alpha_{\text{app}} = \frac{2\pi\Delta f}{\gamma\mu_0 [2(H_{\text{ext}} + H_{\text{uni}}) + M_{\text{eff}}]}, \quad (2.49)$$

where  $H_{\text{ext}}$  is the external magnetic field and  $H_{\text{uni}}$  the uniaxial in-plane anisotropy field.  $\alpha_{\text{app}}$  may differ from the intrinsic damping, but it always constitutes an upper boundary for  $\alpha_{\text{Gilb}}$ .

In Fig. 2.19  $f_{\text{res}}$  and  $\Delta f$  fitted from the susceptibility are plotted as a function of applied field. We calculated the resonance frequency in Eq. 1.37 and Eq. 1.76. Accordingly, the red line in Fig. 2.19(a) represents a fit with the function

$$f_{\text{res}} = \frac{\gamma\mu_0}{2\pi} \sqrt{[M_{\text{eff}} + H_{\text{ext}} + H_{\text{uni}}][H_{\text{ext}} + H_{\text{uni}}]}, \quad (2.50)$$

with the gyromagnetic ratio  $\gamma = g|e|/(2m_e)$ . Eq. 2.50 contains three unknowns, which can be determined: the g-factor  $g$ , the effective magnetization  $M_{\text{eff}}$  and the uniaxial anisotropy field  $H_{\text{uni}}$  (see Eq. 1.24).

However, as typically  $M_{\text{eff}} \gg (H_{\text{ext}} + H_{\text{uni}})$  the resonance frequency is approximately represented by

$$f_{\text{res}} = \frac{|e|\mu_0}{4\pi m_e} g \sqrt{M_{\text{eff}}} \sqrt{H_{\text{ext}} + H_{\text{uni}}}. \quad (2.51)$$

This illustrates why it is difficult to determine  $g$  and  $M_{\text{eff}}$  independently, as approximately the product  $g\sqrt{M_{\text{eff}}}$  is fit. In order to obtain a properly converging fit, we choose a fixed value for  $g$ . The g-factor for a free electron is equal to 2 (spin motion only). In the 3d transition elements we observe a slightly higher value due to a small contribution from the orbital magnetic moment. Tabular values can be found in [29], e.g.  $g(\text{Fe}) = 2.1$ ,  $g(\text{Co}) = 2.21$ ,  $g(\text{Ni}) = 2.21$  and  $g(\text{FeNi}) = 2.12$ .

Fig. 2.19(b) shows the linewidth as a function of applied field. As  $\alpha_{\text{Gillb}}$  is assumed independent of resonance frequency, we expect for  $\Delta f$  an almost constant value having only a very flat slope with applied field, according to Eq. 1.50 with  $2\omega_H \ll \omega_{\text{eff}}$ . In the plot this is observed only for higher applied fields. For low  $H_{\text{ext}}$  a steep increase is found, which can generally be attributed to several contributions:

(i) **Nonuniform spin wave excitation due to an inhomogeneous excitation field in VNA-FMR** was analyzed by Council et al. [142]. As shown in Fig. 2.16 we considered up till now a sample which only covered the middle of the center conductor of the CPW, where the high frequency field can be considered homogeneous. In practice the dimensions of the sample placed on the CPW exceed the center conductor. It is clear that the field at the border of the center conductor is spatially nonuniform and no longer directed solely in the y-direction, but having an out-of-plane component (see Fig. 2.7). This is confirmed by computer simulations displayed in [143, 90]. This inhomogeneous excitation field leads to the creation of magnetostatic modes [144]. They lead to a broadening of the resonance linewidth  $\Delta f$  at low frequency, where the observed linewidth is given by [142]

$$\Delta f_{\text{obs}} = \Delta f \sqrt{1 + \left( \frac{f(k_{\text{max}}, \phi) - f_{\text{res}}}{\Delta f} \right)^2}, \quad (2.52)$$

where  $f(k_{\text{max}}, \phi)$  is the spin wave frequency calculated using Eq. 1.90 without the exchange term. The highest wave vector which is excited by the excitation field inhomogeneity can be determined by  $k_{\text{max}} = \frac{\pi}{w}$ , where  $w$  is the width of the center conductor [100]. For our experimental situation we find  $k_{\text{max}} = 62800$  1/m and the external magnetic field is applied perpendicular to the excitation field:  $\phi = 90^\circ$ . Taking this into account, the observed linewidth is approximated to [142]

$$\Delta f_{\text{obs}}(k_{\text{max}}) \cong \Delta f \sqrt{1 + \frac{f_{\text{eff}}^4}{16\Delta f^2} \left( \frac{k_{\text{max}}d}{f_{\text{res}}} \right)^2} \approx \Delta f + \frac{f_{\text{eff}}^4}{32\Delta f} \left( \frac{k_{\text{max}}d}{f_{\text{res}}} \right)^2, \quad (2.53)$$

where  $\omega_{\text{eff}} = 2\pi f_{\text{eff}} = \gamma\mu_0 M_{\text{eff}}$ . While the last approximate equality illustrates the expected curve shape where the additional contribution to the linewidth decreases approximately proportional to  $1/f_{\text{res}}^2$ , this leads to an overestimation at low frequencies and should not be used for curve fitting.

While in principle all necessary quantities are known, the linewidth calculated according to Eq. 2.52 is significantly below the measured linewidth. A similar disagreement was found in [145] showing that the calculated linewidth increase at low frequencies is too small to explain the measured increase. We will give an explanation, when discussing another contribution (ii).

**(ii) Inhomogeneous broadening attributed to the dispersion of the magnetic material parameters** [10]. In field-swept FMR experiments this is generally modeled by introducing a finite zero-frequency field linewidth  $\Delta H_{\text{inhomo}}$  (see Eq. 1.79).  $\Delta H_{\text{inhomo}}$  models the spatial variation of the amplitude of the anisotropy. We will show in the following how  $\Delta H_{\text{inhomo}}$  is observed in the frequency linewidth.

We rewrite Eq. 2.50 as

$$f_{\text{res}} = \sqrt{\frac{\gamma^2 \mu_0^2}{4\pi^2} M_{\text{eff}} H_{\text{sum}} + \frac{\gamma^2 \mu_0^2}{4\pi^2} H_{\text{sum}}^2}, \quad (2.54)$$

where we introduced  $H_{\text{sum}} = H_{\text{ext}} + H_{\text{uni}}$ . The effect of a variation of  $H_{\text{sum}}$  on the frequency linewidth can then be modeled by

$$\Delta f_{\text{inhomo}} = \frac{\partial f_{\text{res}}}{\partial H_{\text{sum}}} \Delta H_{\text{sum}} \quad (2.55)$$

$$= \frac{1}{f_{\text{res}}} \frac{\gamma^2 \mu_0^2}{8\pi^2} [M_{\text{eff}} + 2H_{\text{sum}}] \Delta H_{\text{sum}} = \frac{\Delta f}{\alpha f_{\text{res}}} \frac{\gamma \mu_0}{4\pi} \Delta H_{\text{sum}}, \quad (2.56)$$

where  $\Delta H_{\text{sum}}$  is equal to the zero-frequency field linewidth  $\Delta H_{\text{inhomo}}$ . As we assume a spread of the magnetic anisotropy, the intrinsic linewidth and the additional linewidth due to inhomogeneous broadening add in quadrature (the total is the square root of the sum of the squares) [143], leading to an observed linewidth as follows:

$$\Delta f_{\text{obs}} = \sqrt{\Delta f^2 + \Delta f_{\text{inhomo}}^2} = \Delta f \sqrt{1 + \frac{1}{\alpha^2 f_{\text{res}}^2} \frac{\gamma^2 \mu_0^2}{16\pi^2} \Delta H_{\text{inhomo}}^2} \quad (2.57)$$

$$\approx \Delta f + \frac{\Delta f}{\alpha^2 f_{\text{res}}^2} \frac{\gamma^2 \mu_0^2}{32\pi^2} \Delta H_{\text{inhomo}}^2. \quad (2.58)$$

As for paragraph (i) the last approximate equality is added to give a simplified picture, illustrating the approximate  $1/f_{\text{res}}^2$  dependence of the additional linewidth, and should not be used for curve fitting. This additional linewidth is very similar in shape to the one caused by the excitation of magnetostatic modes (see Eq. 2.53). According to Eqs. 2.53 and 2.57, the dependence of the observed linewidth on the resonance frequency for both effects can be expressed as

$$\Delta f_{\text{obs}} \approx \Delta f \sqrt{1 + \frac{1}{f_{\text{res}}^2} C}, \quad (2.59)$$

where  $C$  is determined by one of the following two expressions:

$$C_{\text{spinwave}} = \frac{f_{\text{eff}}^4}{16\Delta f^2} (k_{\text{max}} d)^2 \quad ; \quad C_{\text{inhomo}} = \frac{\gamma^2 \mu_0^2}{16\pi^2} \frac{\Delta H_{\text{inhomo}}^2}{\alpha^2}. \quad (2.60)$$

The square root of  $C$  marks the resonance frequency for which the increased linewidth dropped to  $\sqrt{2}$  of the intrinsic value  $\Delta f$ . We remark that the observed linewidth dependence on resonance frequency is not exactly equal for both cases: While  $C_{\text{inhomo}}$

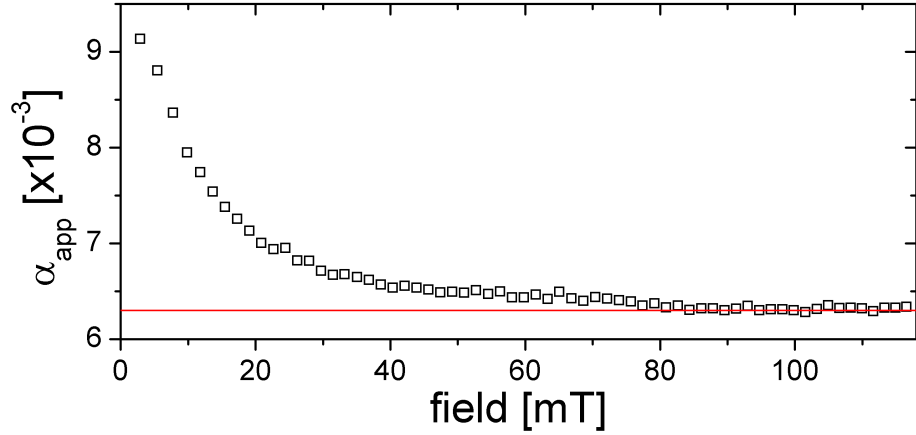


Figure 2.20: (Color online) The apparent damping calculated from the frequency linewidth using Eq.2.49. For increasing applied field  $\alpha_{\text{app}}$  approaches the intrinsic Gilbert damping.

is a true constant,  $C_{\text{spinwave}}$  shows a low variation with  $f_{\text{res}}$  due to the presence of  $\Delta f$ . However, this variation is not sufficiently high to distinguish between the two contributions of similar shape. Mosendz et al. suggested that the main part of the extrinsic frequency linewidth arises from variations of the anisotropy field for a 40 monolayer Fe layer examined in [143]. Scheck et al. attributed the low frequency increase of the frequency linewidth to inhomogeneous broadening only [146].

In Fig. 2.19(b) we present a fit of the measured frequency linewidth using Eq. 2.59 marked by the red plain line: the fit yields  $\sqrt{C} = 2.73$  GHz and  $\alpha = 0.0062$ . When assuming a purely inhomogeneous linewidth contribution, the fitted  $C$  corresponds to  $\mu_0 \Delta H_{\text{inhomo}} = 1.1$  mT. While here we considered spatial variations of the amplitude of the anisotropy, of course, other parameters as the anisotropy direction or the effective magnetization for very thin films can vary spatially, leading to similar contributions to the linewidth due to different local resonance frequencies [147, 148].

In Fig. 2.20 we plot the apparent damping calculated directly from the measured linewidth using Eq. 2.49. While it is difficult to quantitatively analyse the extrinsic linewidth contributions, we observe that for applied fields  $> 80$  mT the apparent damping approaches a constant value, as expected for Gilbert damping. We simply calculate the arithmetic mean of all  $\alpha_{\text{app}}$  above 80 mT yielding  $\bar{\alpha} = 0.0063$  in good agreement with the previously fitted value. The mean value is marked by a plain red line in Fig. 2.20.

In summary, we found that the increased low frequency linewidth can be attributed to two effects: nonuniform spin wave excitation (i) and inhomogeneous broadening (ii). In order to extract the intrinsic linewidth, the data can be fit using Eq. 2.59. Alternatively, it is sufficient to directly calculate  $\alpha$  for high applied fields, where the apparent damping converges to a constant value.

In chapter 7 we will give a full account of the results on the 40 nm CoFeB film employed here exemplarily to demonstrate the fitting of the data.





# Chapter 3

## Two port VNA-FMR data analysis

This chapter is dedicated exclusively to the evaluation of the raw data measured by two port vector network analyzer ferromagnetic resonance (VNA-FMR). First we give a short introduction motivating the need for a profound understanding of the relation between the raw data and the intended data of interest: the complex susceptibility (§3.1). Then, we describe in detail the calculation for the case of a full 2-port measurement on a coplanar waveguide (§3.2). In the subsequent section, we introduce other data evaluation methods (§3.3). As the latter methods are based on only one scattering parameter, we analyze the impact of this simplification in the following section (§3.4). We conclude this chapter by summarizing the outcome of the comparison (§3.5). Most of the content of this chapter has been published in [19].

### 3.1 Introduction

Already in the introductory chapter 1 we calculated theoretically the response of the magnetic sample on our experimental geometry: the dynamic susceptibility (see section 1.3). It describes the response of the magnetization, which is aligned along the coplanar waveguide (CPW) by a constant magnetic field, to a small perpendicular oscillating field: a small angle magnetization oscillation is excited, which is again picked up by the CPW. Thus, while we already have a description of the measurement result, we still need to clarify how to calculate the dynamic susceptibility from the raw measurement data.

As Vector Network Analyzer-FMR (VNA-FMR) of thin films on coplanar waveguides only appeared in recent years, the data evaluation is not yet standardized. Different approaches can be found in the literature: The simplest approach is a localized treatment [96, 142]. It allows to calculate the complex susceptibility (real and imaginary part). However, as it neglects the wave propagation, its validity is limited, especially with respect to the usable frequency range. A different approach is to analyze the absolute value of one of the measured transmission parameters [149]. As only the modulus is evaluated, it is consequently not possible to obtain the real and the imaginary part of the complex susceptibility. Another approach is also based on one of the transmission parameters, but takes into account both parts of the complex quantity: its phase and its modulus [97]. Therefore, it allows to calculate the complex susceptibility. But even the last approach neglects microwave reflection, as it is based on a single parameter.

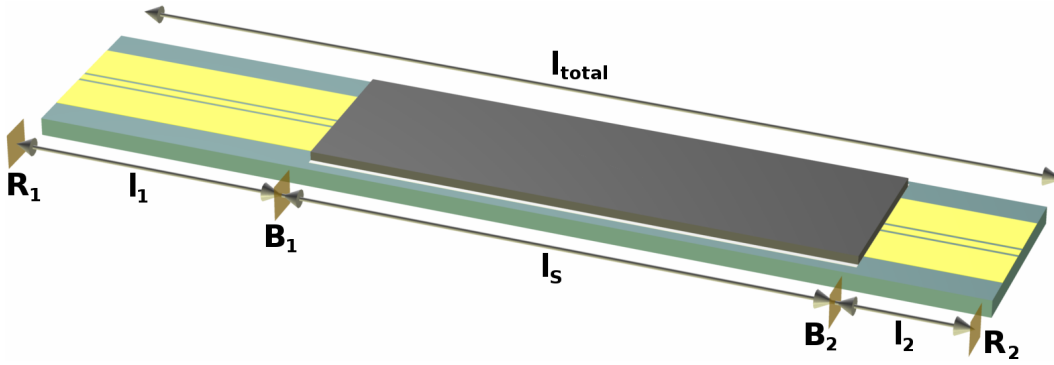


Figure 3.1: (Color online) Coplanar waveguide loaded with a magnetic film and its substrate on a length  $l_s$ , only separated by a small air gap. The sample placement is not necessarily centered ( $l_1 \neq l_2$ ). The high-frequency probes are connected at the planes  $R_1$  and  $R_2$ . During the calculation the reference planes will be shifted to  $B_1$  and  $B_2$ .

To emend this, we developed a complete description of the measurement, taking microwave reflection into account. We will sketch this accurate evaluation model using a complete set of S-parameters in detail in the following section. An application note found in appendix A of this manuscript describes the computerized version implemented in the course of this thesis work.

## 3.2 Full 2-Port data evaluation

In the following we develop step by step a model for our experimental geometry, as described in section 2.3. We will employ in particular the concepts concerning microwaves, introduced in section 2.2. The evaluation model is based on permeability measurement methods found in the literature [150, 140], which were adapted to our specific measurement geometry and our physical interest: To extract resonance frequency and linewidth.

### 3.2.1 Raw data: S-parameters

Our model situation is depicted in Fig. 3.1. The drawing corresponds to the area between the probe tips in Fig. 2.11. As shown there, the coplanar waveguide is connected with two high-frequency probes to the network analyzer (at the reference planes  $R_1$  and  $R_2$ ). The sample is placed on the CPW. As it is never perfectly flat, a small air gap separates it from the conductors. Correspondingly, we never observed a short-circuiting of the CPW.

A full 2-port calibration including the probes is performed. Thus, any contribution to the measured S-parameters from outside the waveguide is compensated (see section 2.2.5). The complex-valued S-matrix representing the section between the two probes is calculated analytically by multiplying several transmission matrices, followed by a transformation to the S-matrix (see section 2.2.3). We specify the 5 circuit components by their appearance in the drawing from the left side to the right, each being represented by a matrix listed in Tab. 2.2:

- The section of the CPW of length  $l_1$  between the left high-frequency probe and the sample border (propagation constant  $\gamma_0$ , impedance  $Z_0$ ).
- The change in impedance from  $Z_0$  to  $Z$  at the left border of the sample.
- The wave propagation in the region of length  $l_s$  loaded with the magnetic sample, having a modified propagation constant  $\gamma$ .
- The change in impedance from  $Z$  back to  $Z_0$  at the right border of the sample.
- The unloaded section of the waveguide of length  $l_2$  between the right border of the sample and the high frequency probe (propagation constant  $\gamma_0$ , impedance  $Z_0$ ).

When multiplying the 5 corresponding T-matrices, we find

$$\begin{aligned} \bar{\bar{T}} &= \begin{pmatrix} e^{-\gamma_0 l_1} & 0 \\ 0 & e^{\gamma_0 l_1} \end{pmatrix} \begin{pmatrix} \frac{1}{\sqrt{1-\Gamma^2}} & \frac{\Gamma}{\sqrt{1-\Gamma^2}} \\ \frac{\Gamma}{\sqrt{1-\Gamma^2}} & \frac{1}{\sqrt{1-\Gamma^2}} \end{pmatrix} \\ &\times \begin{pmatrix} e^{-\gamma l_s} & 0 \\ 0 & e^{\gamma l_s} \end{pmatrix} \begin{pmatrix} \frac{1}{\sqrt{1-\Gamma^2}} & \frac{-\Gamma}{\sqrt{1-\Gamma^2}} \\ \frac{-\Gamma}{\sqrt{1-\Gamma^2}} & \frac{1}{\sqrt{1-\Gamma^2}} \end{pmatrix} \begin{pmatrix} e^{-\gamma_0 l_2} & 0 \\ 0 & e^{\gamma_0 l_2} \end{pmatrix}. \end{aligned} \quad (3.1)$$

In order for this description to be valid, the impedance of the waveguide  $Z_0$  needs to be equal to the characteristic impedance of the measurement system, in our case  $50 \Omega$ . This is ensured because we buy coplanar waveguides realised on calibration kits certified to  $50 \Omega$ . The impedance  $Z$  of the waveguide loaded with the sample is related to the complex reflection coefficient  $\Gamma$  as follows:

$$\Gamma = \frac{Z - Z_0}{Z + Z_0} \quad \Leftrightarrow \quad \frac{Z}{Z_0} = \frac{1 + \Gamma}{1 - \Gamma}. \quad (3.2)$$

The transformation of  $\bar{\bar{T}}$  to the S-matrix, as described in Eq. 2.40, gives the desired description of our network

$$\bar{\bar{S}} = \begin{bmatrix} S_{11} & S_{12} \\ S_{21} & S_{22} \end{bmatrix} = \begin{bmatrix} e^{-\gamma_0 2l_1} \frac{\Gamma(1-P^2)}{1-P^2\Gamma^2} & e^{-\gamma_0(l_1+l_2)} \frac{P(1-\Gamma^2)}{1-P^2\Gamma^2} \\ e^{-\gamma_0(l_1+l_2)} \frac{P(1-\Gamma^2)}{1-P^2\Gamma^2} & e^{-\gamma_0 2l_2} \frac{\Gamma(1-P^2)}{1-P^2\Gamma^2} \end{bmatrix}, \quad (3.3)$$

where we have introduced for convenience the abbreviation

$$P = e^{-\gamma l_s}. \quad (3.4)$$

To illustrate the raw data obtained by the vector network analyzer, we plot in Fig. 3.2 the S-parameters measured for a 40 nm thick  $\text{Co}_{72}\text{Fe}_{18}\text{B}_{10}$  thin film: the figure shows a measurement under an applied field of 37 mT having the ferromagnetic resonance at 8.7 GHz. Additionally, the reference measurement is shown, where the resonance is suppressed by aligning the magnetization in the same direction as the exciting microwave field. The concept of representing the scattering parameters in the complex plane is called Smith Chart. It was introduced in section 2.3.2.

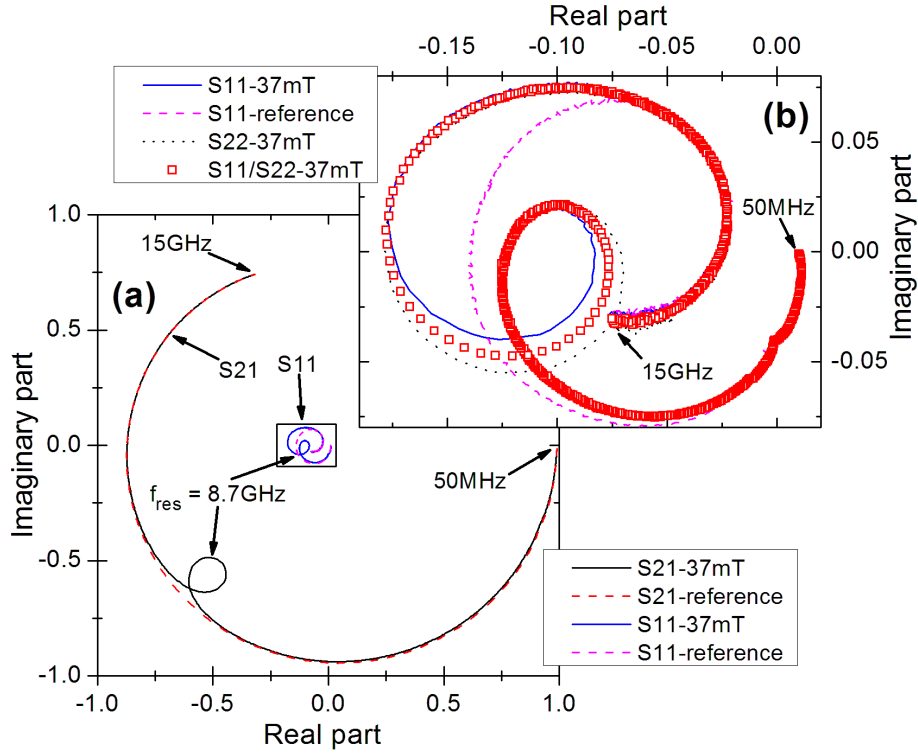


Figure 3.2: (Color online) Smith chart showing raw measurement (37 mT, magnetic resonance at 8.7 GHz) and reference data for the  $\text{Co}_{72}\text{Fe}_{18}\text{B}_{10}$  sample. (a)  $S_{21}$  and  $S_{11}$ ;  $S_{12}$  overlaps exactly with  $S_{21}$ , thus not shown;  $S_{22}$  not shown for clarity. (b) Zoom on S-parameters characterizing reflection.  $S_{22}$  of reference is not shown for clarity.  $S_{11/22}$  correcting off-centered sample position (see Eq. 3.5).

### 3.2.2 Correction of sample position

According to Eq. 3.3 the electrical network is reciprocal, i.e. the 2 matrix elements  $S_{12}$  and  $S_{21}$  are equal. Within measurement accuracy we verified that this condition is fulfilled and we will only use  $S_{21}$  in the following. However  $S_{11}$  and  $S_{22}$  are generally different. This comes from the fact that the sample is not precisely centered between the probes ( $l_1 \neq l_2$ ), leading to a different prefactor. This can be corrected mathematically by using the geometric mean of  $S_{11}$  and  $S_{22}$ :

$$S_{11/22} = \sqrt{S_{11}S_{22}} = e^{-\gamma_0(l_1+l_2)} \frac{\Gamma(1-P^2)}{1-P^2\Gamma^2}. \quad (3.5)$$

Now the prefactor is the same in  $S_{21}$  and  $S_{11/22}$ :  $e^{-\gamma_0(l_1+l_2)}$ . It only contains the sum of the lengths of the two empty sections of the CPW. This is obviously equal to the total distance between the two high-frequency probes minus the sample length:  $l_1 + l_2 = l_{\text{total}} - l_s$ . Therefore a potential miscentering of the sample is emended. The correction is illustrated in Fig. 3.2(b):  $S_{11}$  and  $S_{22}$  for the measurement under an applied field of 37 mT do not coincide due to the magnetic sample not being aligned in the exact center. This is corrected by calculating  $S_{11/22}$ .

### 3.2.3 Deembedding

The reference planes have to be shifted from the positions of the probes connecting to the CPW ( $R_1$  and  $R_2$ ) to the borders of the sample ( $B_1$  and  $B_2$ ). This deembedding procedure is achieved by multiplying  $S_{21}$  and  $S_{11/22}$  with the inverse prefactor. We still need to determine  $\gamma_0$ . It can be extracted by measuring the transmission parameter  $S_{21}^{\text{CPW}}$  of the CPW without the sample on top, not changing the position of the high-frequency probes at  $R_1$  and  $R_2$ . Without the magnetic sample, the CPW is simply a line section of length  $l_{\text{total}}$  with a matched characteristic impedance  $Z_0 = 50 \Omega$ . A plot of the magnitude and phase of  $S_{21}^{\text{CPW}}$  is shown in Fig. 2.14. We analyzed the propagation constant  $\gamma_0$  of the employed CPW of length 5.25 mm in section 2.3.2. However, we can avoid the explicit calculation of  $\gamma_0$ , as we find according to Tab. 2.2:

$$S_{21}^{\text{CPW}} = e^{-\gamma_0 l_{\text{total}}}. \quad (3.6)$$

The inverse prefactor is then calculated as

$$\left(e^{-\gamma_0(l_{\text{total}}-l_s)}\right)^{-1} = \exp\left[-\frac{l_{\text{total}}-l_s}{l_{\text{total}}}\ln\left(S_{21}^{\text{CPW}}\right)\right]. \quad (3.7)$$

We insist on the importance of correcting the empty sections of the waveguide. Failure to do so results in distortion of the measured spectra.

Finally, the two deembedded parameters are described by

$$S_{21}^{\text{B}} = e^{\gamma_0(l_{\text{total}}-l_s)}S_{21} = \frac{P(1-\Gamma^2)}{1-P^2\Gamma^2}, \quad (3.8)$$

$$S_{11/22}^{\text{B}} = e^{\gamma_0(l_{\text{total}}-l_s)}S_{11/22} = \frac{\Gamma(1-P^2)}{1-P^2\Gamma^2}. \quad (3.9)$$

### 3.2.4 Extraction of $\Gamma$ and $\gamma$

After Ref. [151], the complex reflection coefficient  $\Gamma$  can be obtained analytically from the measured S-parameters using

$$\Gamma = K \pm \sqrt{K^2 - 1} \quad (3.10)$$

with  $K$  defined as,

$$K = \frac{1 + (S_{11/22}^{\text{B}})^2 - (S_{21}^{\text{B}})^2}{2S_{11/22}^{\text{B}}}. \quad (3.11)$$

The plus or minus sign before the square root in Eq. 3.10 is chosen such that  $|\Gamma| < 1$ .  $P$  is calculated as follows:

$$P = \frac{S_{11/22}^{\text{B}} + S_{21}^{\text{B}} - \Gamma}{1 - (S_{11/22}^{\text{B}} + S_{21}^{\text{B}})\Gamma} \quad (3.12)$$

From  $P$  we can then calculate the propagation constant  $\gamma$  using Eq. 3.4:

$$\text{Re}(\gamma) = -\frac{\ln(|P|)}{l_s} \quad ; \quad \text{Im}(\gamma) = -\frac{\arg(P)}{l_s} \quad (3.13)$$

Care has to be taken when taking the logarithm, as  $P$  is a complex number and the logarithm of an imaginary number can be multivalued. This can be resolved by

calculating the real and imaginary part separately (see Eq. 3.13), and making sure that the discontinuities marked by jumps of  $2\pi$  appearing in the complex argument of  $P$  are corrected beforehand, i.e.  $\arg(P)$  has to decrease steadily with increasing frequency.

The validity of the solution presented in Eqs. 3.10, 3.11 and 3.12, can be easily verified by inserting them into Eqs. 3.8 and 3.9. We note for completeness that the same solution is presented in a slightly different form in [140] using trigonometric functions. We preferred the form presented here, avoiding trigonometric functions, as we found it easier to implement into the computer program automating the complex calculations.

### 3.2.5 Calculation of $\tilde{\epsilon}_r$ and $\tilde{\mu}_r$

We now introduce an effective relative permittivity  $\tilde{\epsilon}_r$  and an effective relative permeability  $\tilde{\mu}_r$ . These effective quantities (marked by a tilde) are used to link our complex geometry, where several materials contribute to  $\tilde{\epsilon}_r$  and  $\tilde{\mu}_r$ , to an effective medium model, where the waveguide is surrounded entirely by one single material with these effective electromagnetic properties.  $\tilde{\epsilon}_r$  and  $\tilde{\mu}_r$  are related to  $\Gamma$  and  $\gamma$  by:

$$\frac{\gamma}{\gamma_{fs}} = \frac{\gamma}{j2\pi f \sqrt{\mu_0 \epsilon_0}} = \sqrt{\tilde{\mu}_r \tilde{\epsilon}_r}, \quad (3.14)$$

$$\frac{1 + \Gamma}{1 - \Gamma} = \frac{Z}{Z_0} = G \sqrt{\frac{\tilde{\mu}_r}{\tilde{\epsilon}_r}} \propto \sqrt{\frac{\tilde{\mu}_r}{\tilde{\epsilon}_r}}. \quad (3.15)$$

Here  $\gamma_{fs}$  is the propagation constant of the CPW in vacuum, which is identical to the propagation constant of free space, and  $G$  is a frequency-independent constant depending on the geometry of the coplanar waveguide.  $G$  is not evaluated further, as it depends on the air gap remaining between the sample and the CPW, which is difficult to estimate. While thus the absolute values cannot be calculated accurately, we can easily calculate values proportional to the effective quantities:

$$\tilde{\mu}_r \propto \frac{\gamma}{\gamma_{fs}} \frac{1 + \Gamma}{1 - \Gamma} \quad ; \quad \tilde{\epsilon}_r \propto \frac{\gamma}{\gamma_{fs}} \frac{1 - \Gamma}{1 + \Gamma}. \quad (3.16)$$

While our main interest is in the permeability, it is still important to evaluate the effective relative permittivity:  $\tilde{\epsilon}_r$  is composed of several contributions. We are not able to separate the different ones from the relative permittivity  $\epsilon_r$  of the CPW substrate, of the substrate of the magnetic layer and of the small air gap between the CPW and the magnetic sample. However, we could observe that in our case using low-loss dielectrics,  $\text{Im}(\tilde{\epsilon}_r)$  is insignificantly small compared to  $\text{Re}(\tilde{\epsilon}_r)$  and can be neglected.

This is exemplarily demonstrated in Fig. 3.3(b), where we plot the real and imaginary part of  $\tilde{\epsilon}_r$  till 14.5 GHz. As  $\text{Re}(\tilde{\epsilon}_r)$  was found to be constant over the studied frequency range, we can more easily calculate  $\tilde{\mu}_r$ , the quantity in which we are primarily interested, like

$$\frac{\gamma}{\gamma_{fs}} \propto \tilde{\epsilon}_r \frac{1 + \Gamma}{1 - \Gamma} \quad \Rightarrow \quad \tilde{\mu}_r \propto \left( \frac{1 + \Gamma}{1 - \Gamma} \right)^2 \quad ; \quad \tilde{\mu}_r \propto \left( \frac{\gamma}{\gamma_{fs}} \right)^2. \quad (3.17)$$

Using Eq. 3.17 instead of Eq. 3.16 to calculate  $\tilde{\mu}_r$  from only one of the two extracted quantities ( $\Gamma$  or  $\gamma$ ), can be advantageous: depending on the specific measurement

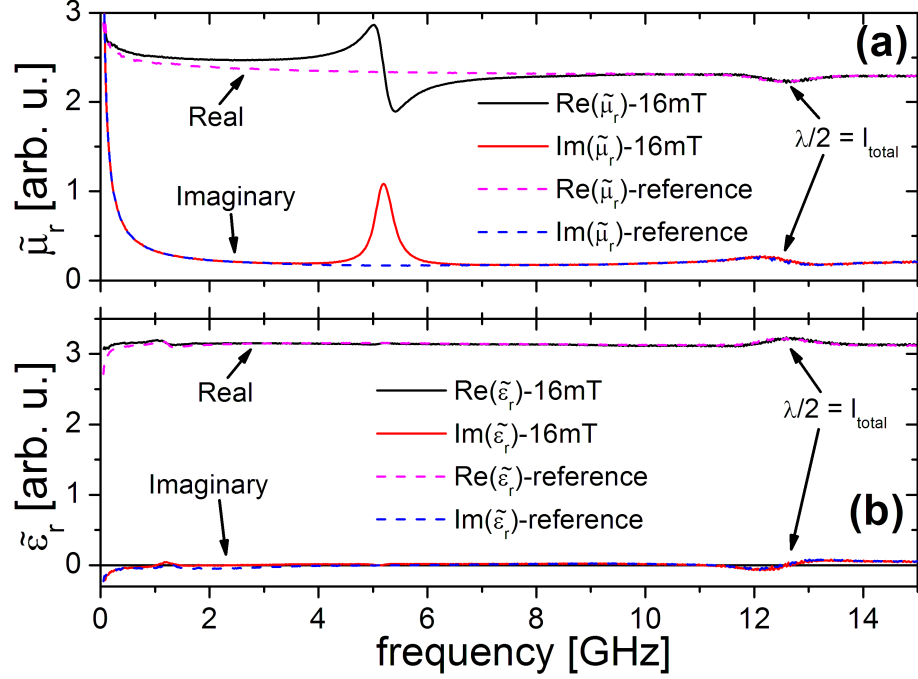


Figure 3.3: (Color online) Values proportional to  $\tilde{\mu}_r$  and  $\tilde{\epsilon}_r$  (see Eq. 3.16) for the  $\text{Co}_{72}\text{Fe}_{18}\text{B}_{10}$  deposited on glass (see section 7.2); the imaginary part is inverted according to accepted usage. (a) Real and imaginary part of the effective relative permeability for 16 mT applied field and reference measurement (no resonance). (b) Effective relative permittivity: 16 mT applied field and reference measurement coincide well; the imaginary part is negligibly small.

conditions, one of the quantities can be determined with a higher precision [152]. In our measurements we could observe low noise in  $\Gamma$  and  $\gamma$  at frequencies up to a few GHz. Above 10 GHz the noise in  $\Gamma$  increased significantly, while it stayed low in  $\gamma$ . Additionally, when calculating  $\tilde{\mu}_r$  according to Eq. 3.16, we observed distortions of the resonance at frequencies whose wavelength is a multiple of half the waveguide length. In Fig. 3.3 this is visible at 12.5 GHz. We already observed this feature, when measuring the CPW without the magnetic sample, as reported in section 2.3.2. There, it was clearly visible in the magnitude of the reflection parameters, plotted in Fig. 2.14. This observation is explained by a resonating electromagnetic wave, giving rise to a standing wave in the CPW [29]. These dimensional resonances [140] only appear in the reflection coefficient  $\Gamma$ , while the propagation constant  $\gamma$  is not affected. Therefore, we will limit further evaluation to calculating a value proportional to  $\tilde{\mu}_r$  from  $\gamma$ , when either accessing a frequency range where a dimensional resonance can lead to distortions or the noise in  $\Gamma$  is strongly increased.

Similar to the effective relative permittivity,  $\tilde{\mu}_r$  is a superposition of the relative permeability  $\mu_r$  of the magnetic layer and the relative permeability of the other surrounding materials, which is = 1 as they are nonmagnetic. As  $\tilde{\mu}_r$  is an unknown linear function of  $\mu_r$  of the magnetic material, a value directly proportional to the transverse susceptibility  $\chi$  can be calculated as follows:

$$\chi = \mu_r - 1 \propto \tilde{\mu}_r - \tilde{\mu}_r^{\text{ref}}, \quad (3.18)$$

where  $\tilde{\mu}_r$  is the measurement (magnetic field typically oriented along the CPW) and



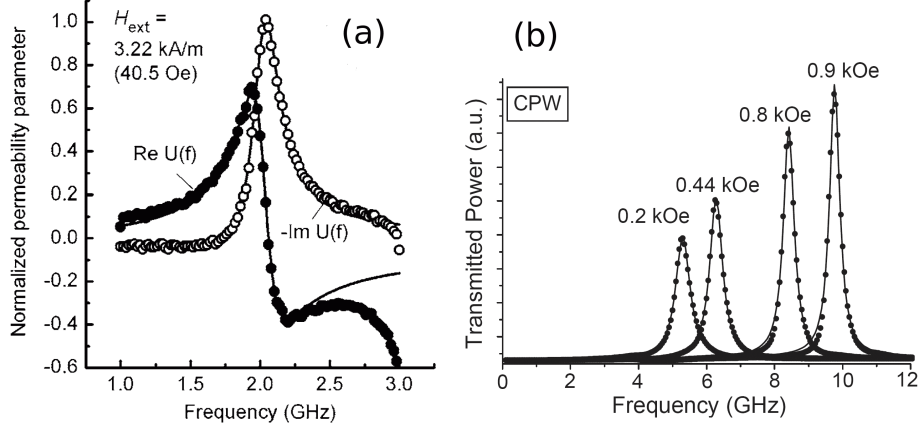


Figure 3.4: (a) Representative VNA-FMR data showing the normalized permeability parameter  $U$  of a 50 nm thick NiFe film, after [97]. (b) The transmitted amplitude ( $S_{21}$ ) spectra obtained from the CPW geometry for a 30 nm thick permalloy film, after [149].

$\tilde{\mu}_T^{\text{ref}}$  is a reference measurement. For the reference the magnetic field is oriented perpendicular to the CPW (thus parallel to the excitation field), and no FMR is excited. This can be observed in the raw data in Fig. 3.2, where the measurement shows a resonance at around 8.7 GHz, which is not excited in the reference measurement. The same is true for the calculated value proportional to  $\tilde{\mu}_T$ , as shown in Fig. 3.3, where the resonance fails to appear in the reference. Thus, by subtracting  $\tilde{\mu}_T^{\text{ref}}$  from  $\tilde{\mu}_T$ , a value proportional to the transverse dynamic susceptibility of the magnetic material alone is obtained.

### 3.2.6 Summary

In summary, the four S-parameters are measured for our 2-port network. They are described by Eq. 3.3.  $S_{11/22}$  is calculated using Eq. 3.5, which rectifies bad sample centering on the CPW. It is no longer necessary to know  $l_1$  and  $l_2$ , but sufficient to measure  $l_{\text{total}}$  and  $l_s$  (see Fig. 3.1).  $S_{11/22}$  and  $S_{21}$  are then deembedded using a measurement of the empty CPW, following Eqs. 3.7-3.9.  $\tilde{\mu}_T$  is then calculated from  $\gamma/\gamma_{\text{fs}}$  (see Eq. 3.17), which is calculated as an intermediate step (see Eqs. 3.10-3.15). This procedure is executed twice: once for the measurement and another time for the reference measurement, suppressing the magnetic resonance. Subtracting the two calculated  $\tilde{\mu}_T$  yields a value proportional to the transverse susceptibility (see Eq. 3.18).

## 3.3 Other evaluation models

Several different methods for the evaluation of the raw data are found in the literature. In this section, we present two approaches based on a single scattering parameter. While this simplifies the mathematical operations, which have to be performed on the raw data, the consequences on the precision of the calculated result need to be clarified. Hence, we will proceed with a comparison in the following section.

### 3.3.1 Neglecting reflections, using $S_{21}$ only

In Ref. [97] a 2-Port evaluation scheme is pointed out, neglecting reflections: Using only the  $S_{21}$ -parameter of the measurement and the reference measurement, an uncalibrated effective microwave permeability parameter is calculated according to Eq. 1 in Ref. [97], which is

$$U(f) = \pm \frac{i \ln [S_{21-H}(f)/S_{21-ref}(f)]}{\ln [S_{21-ref}(f)]}. \quad (3.19)$$

The sign is chosen such that  $\text{Im}[U(f)]$  is negative in the vicinity of the FMR peak.

It is emphasized in Ref. [97] that  $U(f)$  is related, but does not correspond strictly to the loss and dispersion profiles which are expected. One example of  $U(f)$  measured for a 50 nm thick NiFe film is shown in Fig. 3.4(a), after [97]. The additional offsets and distortions entailed by the simplification are corrected by introducing additional fitting parameters.

As Eq. 3.19 contains a logarithm, we found that using algebraic identities the expression can be easily simplified:

$$U(f) = \pm i \left( \frac{\ln [S_{21-H}(f)]}{\ln [S_{21-ref}(f)]} - 1 \right). \quad (3.20)$$

### 3.3.2 Absolute value of $S_{21}$

Ref. [149] presents resonance linewidth data from VNA-FMR on a CPW. Here, the linewidth is directly extracted from a fit to the amplitude of  $S_{21}$ , where the effects of the connections as well as the substrate were subtracted. This is exemplified in Fig. 3.4(b), showing the measurement result on a 30 nm permalloy film for several applied fields, after [149].

It is pointed out that the width of the peaks seen in  $|S_{21}|$  is not necessarily directly related to the linewidth seen in the permeability. Resonance data obtained with this evaluation method is presented in the following section.

## 3.4 Comparison of evaluation models

In order to compare the presented evaluation methods, we used the raw data, the 4 scattering parameters, measured for two different extended film samples: 40 nm  $\text{Co}_{72}\text{Fe}_{18}\text{B}_{10}$  and 40 nm  $\text{Co}_{80}\text{Fe}_{20}$ . Both were deposited on glass substrates and protected by 3 nm Ru layers. These two samples are among the films examined in the study presented in chapter 7. There we give a detailed description on the growth process and further characterization [153, 154, 155, 156].

Rather thick samples were chosen which provide a higher signal amplitude to minimize the influence of noise. Accordingly, the data was neither smoothed nor filtered. The two samples yield significantly different linewidth ( $\text{Co}_{72}\text{Fe}_{18}\text{B}_{10}$ :  $\approx 360$  MHz;  $\text{Co}_{80}\text{Fe}_{20}$ :  $\approx 900$  MHz), making the comparison more general.

As expected after Eq. 3.3,  $S_{21}$  and  $S_{12}$  coincide precisely.  $S_{21}$  was used to calculate  $U(f)$  (see section 3.3.1) and  $|S_{21}|$  (see section 3.3.2). Both these evaluation models neglect microwave reflections, which are primarily contained in  $S_{11}$  and  $S_{22}$ . As the full 2-port data evaluation described in section 3.2 is the only one including reflections, we will consider  $\chi$  calculated after this model as the best estimation for

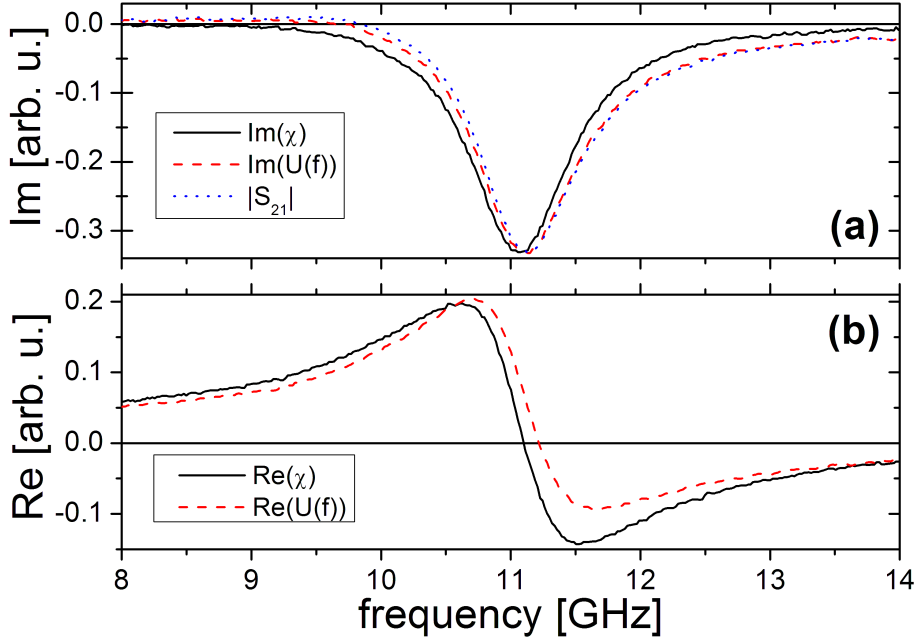


Figure 3.5: (Color online) Different evaluation methods demonstrated on the  $\text{Co}_{80}\text{Fe}_{20}$  sample at 62 mT applied field. 18.7 MHz spacing between data points. For easier comparison  $U(f)$  and  $|S_{21}|$  were scaled (no offset added) to have the same height as  $\chi$ . (a) Imaginary part (not inverted) of  $\chi$  and  $U(f)$ , and  $|S_{21}|$ ; (b) Real part of  $\chi$  and  $U(f)$ .

the sample susceptibility. Therefore, when comparing the different models we will give the relative error with respect to  $\chi$ .

Fig. 3.5 shows the real and imaginary part of  $U(f)$  and  $\chi$ , as well as  $|S_{21}|$ . All curves are calculated from the same raw measurement data of the  $\text{Co}_{80}\text{Fe}_{20}$  sample at 62 mT applied field. For  $|S_{21}|$  we observed some slight resonance frequency shift and a distorted curve shape with respect to a Lorentzian. For  $U(f)$  in particular the distortion of the real part which is asymmetric is eye-catching.

In the following, we will compare the resonance frequency  $f_{\text{res}}$  and the resonance linewidth  $\Delta f$  of the  $\text{Co}_{72}\text{Fe}_{18}\text{B}_{10}$  sample between the different models. Both quantities are extracted from Lorentzian profiles fit to the resonance using standard least squares curve fitting [157]. Fig. 3.6(a) shows  $f_{\text{res}}$  as a function of the static magnetic field applied along the CPW. The frequencies are well described by the Kittel FMR frequency. In the graph the data points from the different models overlap so closely that it is impossible to distinguish between them. Fig. 3.6(b) shows the relative error of  $f_{\text{res}}$  from  $U(f)$  and from  $|S_{21}|$  with respect to  $\chi$ . The deviation between the models stays below 1%. Even when taking  $f_{\text{res}}$  from the complex modulus of the raw data ( $|S_{21}|$ ), the error is small. This is no longer the case when  $\Delta f$  is examined.

Fig. 3.7(a) shows  $\Delta f$  as a function of the applied field. We will not give a precise interpretation of the line shape at this point. This is discussed in great detail in chapter 7. We just note that the observed line shape corresponds to the expected one, as analyzed in section 2.3.3.

In contrast to the resonance frequencies,  $\Delta f$  differs visibly between the evaluation models. Fig. 3.7(b) shows the relative error of  $\Delta f$  from  $U(f)$  and from  $|S_{21}|$  with respect to  $\chi$ : For both models the deviation is decreasing with increasing applied

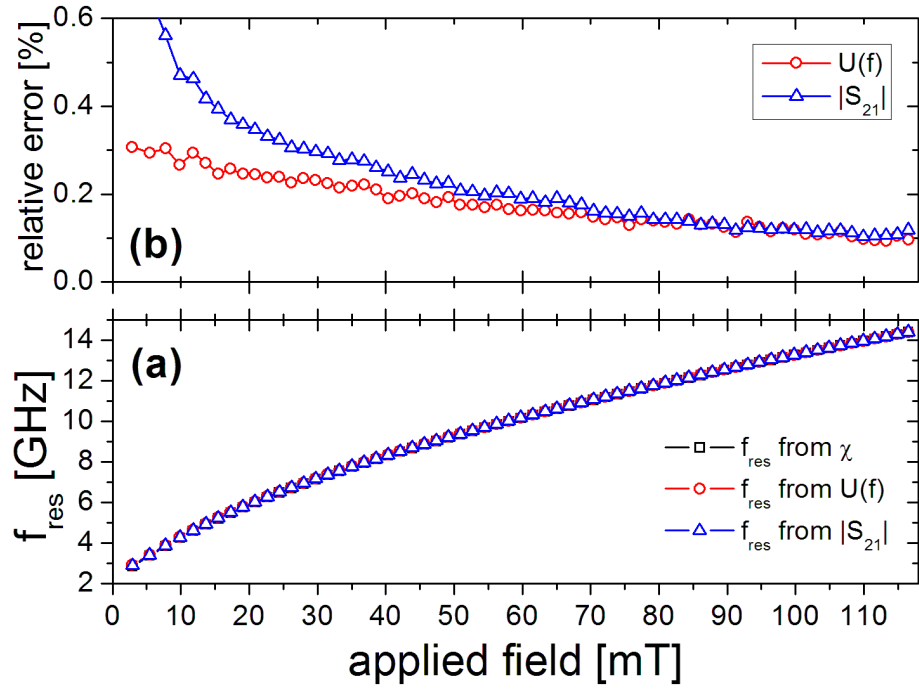


Figure 3.6: (Color online) (a) Resonance frequency  $f_{\text{res}}$  vs applied field extracted for the  $\text{Co}_{72}\text{Fe}_{18}\text{B}_{10}$  sample from  $\chi$ ,  $U(f)$  and  $|S_{21}|$ . (b) Relative error of  $f_{\text{res}}$  from  $U(f)$  and  $|S_{21}|$  with respect to  $\chi$ : The determined resonance frequencies deviate less than 1% between the different methods.

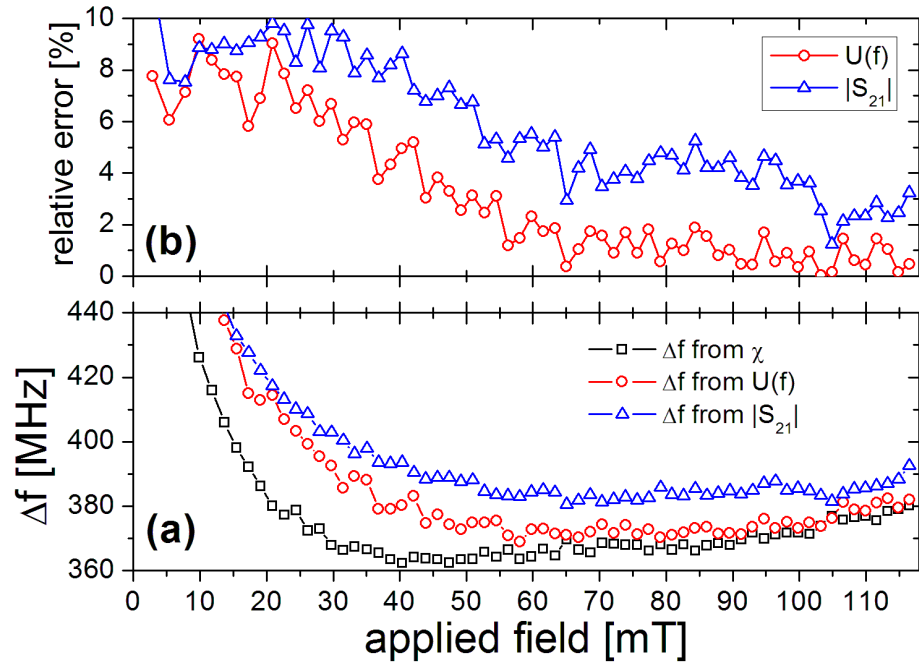


Figure 3.7: (Color online) (a) Resonance linewidth  $\Delta f$  vs applied field extracted for the  $\text{Co}_{72}\text{Fe}_{18}\text{B}_{10}$  sample from  $\chi$ ,  $U(f)$  and  $|S_{21}|$ . (b) Relative error of  $\Delta f$  from  $U(f)$  and  $|S_{21}|$  with respect to  $\chi$ .

field. The relative error was always higher for  $|S_{21}|$  than for  $U(f)$ . For the lowest applied field it reaches up to 10%.

For the  $\text{Co}_{80}\text{Fe}_{20}$  sample (not shown) yielding a broader resonance we found the same situation: There was a good agreement for  $f_{\text{res}}$  calculated with all 3 models. The relative error hardly exceeded 1%. The error was higher for  $|S_{21}|$  than for  $U(f)$ . The linewidths differed: the relative error was decreasing with increasing applied field. Similar to the  $\text{Co}_{72}\text{Fe}_{18}\text{B}_{10}$  sample, it reached up to 10% for low applied fields. The error was always higher for  $|S_{21}|$  than for  $U(f)$ .

Recapitulating, we compared the resonance frequencies and linewidths extracted from  $\chi$  with those extracted from  $|S_{21}|$  and from  $U(f)$  for two different thin film samples. If the focus of the data evaluation is on  $f_{\text{res}}$ , the differences are very small. All 3 evaluation methods agree within 1%. If on the other hand  $\Delta f$  is to be evaluated, it is indicated to employ the full 2-port data evaluation. The two other methods are approximate, as they ignore the information contained in the reflection parameters.  $|S_{21}|$  leads to a higher relative error than  $U(f)$ .

### 3.5 Summary

We presented a detailed description on how to calculate from the raw measurement data a value proportional to the complex susceptibility and permittivity of the ferromagnetic material. An easy way to correct an imprecise sample alignment in the center of the coplanar waveguide was introduced. This also renders unnecessary the measurement of the exact sample position on the waveguide. An application note explaining the automated implementation in a computer program is found in appendix A.

We have carried out 2-port network analyzer ferromagnetic resonance measurements on a coplanar waveguide up to 15 GHz on 2 model samples. Using these experimental data the presented full 2-port evaluation scheme based on all 4 scattering parameters is then compared to two commonly used approximate evaluation schemes. These approximate models only employ one transmission parameter ( $S_{21}$ ). The different evaluation models were applied to the same raw data, ensuring a good comparability.

We found close agreement between all methods for the ferromagnetic resonance frequencies (the relative error is below 1%). However, the resonance linewidths of the approximate models show a relative error that can reach up to 10% with respect to the presented full 2-port evaluation method.

Evaluation methods based on only one complex S-parameter necessarily provide a reduced set of information in comparison to a full two port measurement. Nevertheless, we will analyze another method based on a single scattering parameter in the following chapter. But, it can be distinguished from the approximate models presented in this chapter, as it only uses one high-frequency probe. Therefore, it is not by choice that only one reflection parameter is measured. The implications for the obtained scattering parameter will be described in detail.

# Chapter 4

## One port Open-reflection measurements

### 4.1 Motivation

In the previous chapter we treated in detail the data evaluation of a ferromagnetic resonance measurement on a coplanar waveguide from a complete set of scattering parameters. In order to measure the 4 S-parameters, the CPW was connected on both sides to a vector network analyzer using high-frequency probes.

While a full set of S-parameters allows the most complete characterization of the two-port network in-between, frequently FMR is measured in a one port geometry using a single scattering parameter [94, 95, 158, 159, 92]. A one port geometry has pros and cons: the most important advantage is the use of a single microwave probe. Experimentally it is not always feasible to install two probes and, in particular, two high-frequency cables, which need to be protected from contact and movement. This is considerably simplified by the restriction to only one high-frequency connector and, correspondingly, only one cable.

Another benefit in a one port measurement is the calibration, which is considerably simplified and sped up in comparison with a full two port calibration. The measurement itself is faster, too, i.e. a frequency sweep at one applied field takes less time, as only a single S-parameter has to be recorded. This corresponds to a reduced duration for the overall measurement, reducing drift during the data acquisition. The gained time can be used for a further noise reduction by a higher averaging. Measuring in a one port geometry, can also yield a higher signal in some cases, as we will demonstrate in the next section. This increases the signal to noise ratio, allowing for a higher measurement precision.

Among the disadvantages, we need to mention a more complicated system to take into account: in the two port measurement geometry, the only signal reflections appear at the sample borders, as the ports of the VNA are reflectionless. With only one microwave probe the reflections on the second side of the CPW need to be included in the calculation. Also, while the calibration is less time-consuming when using only one probe, it doesn't allow to correct imperfections of the measurement hardware in the same manner as a full two port calibration (see section 2.2.5). On the other hand, it is easier to obtain a precise calibration, as the number of connections, which need to be established with the calibration standards, is significantly smaller: therefore, it is less likely to accidentally have one bad connection during the calibration procedure deteriorating the whole calibration.

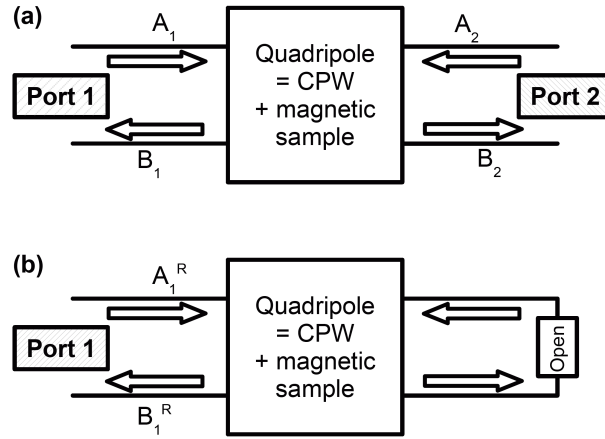


Figure 4.1: (a) Sketch of a two port network as employed in the last chapter. (b) The one port network when using only a single high-frequency probe. The opposite side acts as an open-circuit. This changes the incoming and outgoing wave and thus the scattering parameter measured at port 1.

We still want to mention the limitation of the one port geometry to the measurement of a single complex parameter: but, as we demonstrated in the last chapter, the sample is characterized by two complex quantities, the permittivity and the permeability. This issue is treated in the following section.

Most implementations of a one port geometry employ a short-circuited microstrip or CPW. In contrast, we analyze the possibility to simply use the same CPW as for the two port measurement, while not connecting one side (see Fig. 4.1). Thus, this side works as an open-circuit. This also has the added benefit, that it is easily possible to change between a one port and a two port measurement, for the purpose of comparison.

## 4.2 Open-circuit one port measurement

The description of the one port measurement setup is developed step-by-step in the following. This leads to an equation for the single measured scattering parameter and, through the application of an approximation, to a formula for the data evaluation. In the subsequent section, we will analyze the validity of the obtained data evaluation method.

### 4.2.1 The measurement geometry

The CPW loaded with the sample (magnetic film side down) was already sketched in Fig. 3.1. For conventional 2 port measurements, 2 high-frequency probes connect to the network analyzer at the planes  $R_1$  and  $R_2$ . Contributions from the cables and the probes are compensated by a full 2 port calibration procedure.

For the moment, we assume that the sample length  $l_s$  is equal to the total length of the CPW  $l_{\text{total}}$ . Otherwise the electromagnetic wave propagation over the lengths  $l_1$  and  $l_2$  adds a small phase contribution, which is more difficult to remove mathematically for the case of a one port measurement. Under the assumption  $l_1 = l_2 = 0$ , we find for the 4 S-parameters in the case of a 2 port measurement after

Eq. 3.3:

$$\begin{aligned} S_{11} = S_{22} &= \frac{\Gamma(1 - e^{-2\gamma l_s})}{1 - \Gamma^2 e^{-2\gamma l_s}}, \\ S_{12} = S_{21} &= \frac{e^{-\gamma l_s}(1 - \Gamma^2)}{1 - \Gamma^2 e^{-2\gamma l_s}}. \end{aligned} \quad (4.1)$$

$\gamma$  is the complex propagation constant of the CPW loaded with the sample,  $\Gamma$  is its complex reflection coefficient. In Fig. 3.1 this simplified situation would be described by coinciding B- and R-planes.

In order to avoid confusion, we want to stress that the complex reflection coefficient  $\Gamma$  is not directly equal to the complex reflection coefficients in the scattering matrix ( $S_{11}$  and  $S_{22}$ ). This equality is only fulfilled, if the S-matrix consists only of a sole impedance change (the third model matrix in Tab. 2.2). In this special case either  $S_{11}$  or  $S_{22}$  is equal to  $\Gamma$ , the other one equal to  $-\Gamma$ , depending on its definition.

#### 4.2.2 The single measured scattering parameter $S_{11}^R$

Now, the only modification necessary to perform the open-circuit one port measurement is to remove the high-frequency probe at port 2 and to measure  $S_{11}^R$ , the reflection coefficient of the whole network at port 1. It is important to notice that  $S_{11}^R$  is not simply equal to the reflection coefficient  $S_{11}$ . However,  $S_{11}^R$  measured in the one port geometry can be related to the 4 S-parameters measured in the two port geometry using Eq. 4.2 found in the microwave literature (e.g. Ref. [160, 134]):

$$S_{11}^R = S_{11} + \frac{S_{12}S_{21}}{e^{2\gamma_0 z} \frac{1}{R} - S_{22}}. \quad (4.2)$$

$R$  is the complex reflection coefficient of the open-circuit at port 2.  $e^{2\gamma_0 z}$  describes a small phase shift due to the electromagnetic wave propagation with the propagation constant  $\gamma_0$  of the empty CPW over the small length  $z$ . This small length is situated between the open at port 2 and the right border of the sample. This is sketched in Fig. 4.2, which shows the experimental situation in the one port geometry.

To make sure that we can model the unconnected end of the CPW as an open-circuit, we deembd it by solving Eq. 4.2 for the reflection coefficient at port 2:

$$R e^{-2\gamma_0 z} = \left( \frac{S_{12}S_{21}}{S_{11}^R - S_{11}} + S_{22} \right)^{-1}. \quad (4.3)$$

This equation is valid independently of the magnetic sample.

Using experimental data from corresponding one port and 2 port measurements, we found that  $R$  is equal to 1, and the small phase shift caused by  $e^{-2\gamma_0 z}$  increases linearly with frequency. Using  $\gamma_0$ , which we extracted for the empty CPW, we determined  $z$  to be 50  $\mu\text{m}$ . Indeed, when changing from the two port geometry to the one port geometry, a small part of the CPW is made free. Thus,  $z$  corresponds to the finite length taken up by the second high-frequency probe at port 2, which is commonly termed overdrive (illustrated exaggeratedly in Fig. 4.2).

We note that this small length  $z$  can not be compensated as it only appears in one of the summands in Eq. 4.2. This is not the case for an uncovered part of the



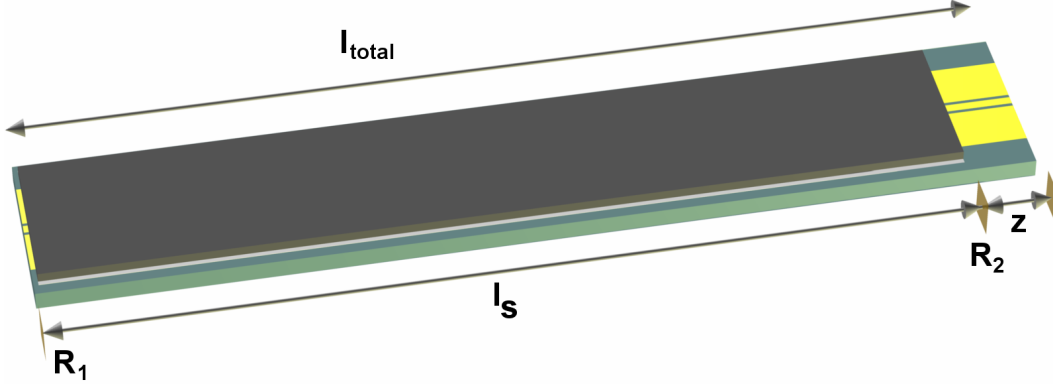


Figure 4.2: (Color online) Coplanar waveguide loaded with a magnetic film and its substrate on a length  $l_s$ , only separated by a small air gap. The high-frequency probe is connected at the plane  $R_1$ , the unconnected side at  $R_2$  acts as an open-circuit. A small uncovered part of the waveguide of length  $z$  is made free, when the second high-frequency probe is removed.

waveguide between the high-frequency probe and magnetic sample. If a length  $l_1$  is not covered (see Fig. 3.1), we obtain

$$e^{-\gamma_0 2l_1} S_{11} + \frac{e^{-\gamma_0 l_1} S_{12} e^{-\gamma_0 l_1} S_{21}}{e^{2\gamma_0 z} \frac{1}{R} - S_{22}} = e^{-\gamma_0 2l_1} S_{11}^R. \quad (4.4)$$

However, to correct this additional length, the precise position of the magnetic sample on the CPW would need to be determined. Therefore, we maintain the initial assumption  $l_1 = 0$ .

As we found  $R = 1$ , we will assume in the following a perfect open-circuit, and for all further one port measurements we will cover the CPW entirely ( $z \approx 0$ ), thereby avoiding the small phase shift. Introducing Eqs. 4.1 into Eq. 4.2 and simplifying, we find for  $S_{11}^R$ :

$$S_{11}^R = \frac{e^{-2\gamma l_s} + \Gamma}{1 + \Gamma e^{-2\gamma l_s}}. \quad (4.5)$$

### 4.2.3 Introducing an effective medium

In order to relate  $S_{11}^R$  to the permeability of the magnetic sample, we introduce again the effective medium model (see section 3.2.5): the CPW is assumed to be surrounded by a single material with the effective relative permittivity  $\tilde{\epsilon}_r$  and the effective relative permeability  $\tilde{\mu}_r$ .  $\tilde{\epsilon}_r$  and  $\tilde{\mu}_r$  are superpositions of the relative electromagnetic properties of the magnetic film, its substrate, the CPW and the air gap in-between. The effective quantities are marked by a tilde.  $\tilde{\epsilon}_r$  and  $\tilde{\mu}_r$  are related to  $\gamma$  as follows:

$$\gamma = \gamma_{fs} \sqrt{\tilde{\mu}_r \tilde{\epsilon}_r} = j\omega \sqrt{\mu_0 \epsilon_0} \sqrt{\tilde{\mu}_r \tilde{\epsilon}_r} = j \frac{\omega}{c} \sqrt{\tilde{\mu}_r \tilde{\epsilon}_r}. \quad (4.6)$$

$\gamma_{fs}$  is the propagation constant of free space. The relation for  $\Gamma$  is

$$\Gamma = \frac{\frac{Z}{Z_0} - 1}{\frac{Z}{Z_0} + 1}, \quad \text{where} \quad \frac{Z}{Z_0} = G \sqrt{\frac{\tilde{\mu}_r}{\tilde{\epsilon}_r}}. \quad (4.7)$$

$G$  is a frequency-independent constant depending on the geometry of the loaded CPW. For the empty CPW the geometry is designed such that the impedance of the waveguide  $Z$  is equal to the characteristic impedance of the network analyzer  $Z_0 = 50\Omega$ . We will not evaluate  $G$  further, as it depends on the air gap between the sample and the CPW, which is difficult to estimate. We note though that the order of magnitude of  $G$  is similar to  $\sqrt{\frac{\varepsilon_r+1}{2}}$ , where  $\varepsilon_r$  is the relative permittivity of the substrate (see section 2.2.2).

From the two port measurements in the last chapter, we concluded that, for the used low-loss dielectrics,  $\tilde{\varepsilon}_r$  can be considered as a real frequency-independent constant. This was demonstrated in Fig. 3.3. Using Eqs. 4.5 - 4.7 we should be able to determine the effective relative permeability  $\tilde{\mu}_r$  from  $S_{11}^R$ . However, due to the complexity of the relation, we could not invert the equation. We will therefore assess the possibility of an approximation.

#### 4.2.4 Simplifying $S_{11}^R$

We will look at the two components ( $e^{-2\gamma l_s}$  and  $\Gamma$ ) in Eq. 4.5 separately, in order to analyze the possibility of an approximate solution.

##### The exponential function in $S_{11}^R$

First we have a look at  $e^{-2\gamma l_s}$ , where we need to determine the relation of this term to the permeability. As  $\tilde{\mu}_r$  is a superposition of multiple relative permeabilities, which are all equal to 1 except the relative permeability of the magnetic film  $\mu_r$ , we model  $\tilde{\mu}_r$  as

$$\tilde{\mu}_r = x\mu_r + (1-x)1 = 1 + x\chi, \quad (4.8)$$

where  $\chi$  is the susceptibility of the magnetic film and  $x$  is the effective filling factor, representing the contribution of the relative permeability of the magnetic film to  $\tilde{\mu}_r$ . We can estimate that the filling factor is small, as we compare a magnetic film thickness of  $\approx 10$  nm to a substrate thickness of  $\approx 100$   $\mu\text{m}$ . As  $\tilde{\mu}_r$  always appears under a square root and  $x \ll 1$ , we find approximately:

$$\sqrt{\tilde{\mu}_r} = \sqrt{1 + x\chi} \approx 1 + \frac{1}{2}x\chi. \quad (4.9)$$

We can further justify this approximation by analyzing an explicit form of  $\chi$ , as we derived it in chapter 1: according to Eq. 1.45, the amplitude of  $\chi$  at the ferromagnetic resonance, where it reaches its maximum, is approximately proportional to the inverse of the resonance frequency. Therefore, the error, which we introduced by the approximation on the right-hand side of Eq. 4.9, is decreasing likewise. Using Eqs. 4.6 and 4.9 we find for the exponential function in Eq. 4.5:

$$e^{-2\gamma l_s} = e^{-j2l_s \frac{\omega}{c} \sqrt{\varepsilon_r} \sqrt{\tilde{\mu}_r}} \quad (4.10)$$

$$\approx e^{-j2l_s \frac{\omega}{c} \sqrt{\varepsilon_r}} e^{-j2l_s \frac{\omega}{c} \sqrt{\varepsilon_r} \frac{1}{2} x\chi}. \quad (4.11)$$

It decomposes into a product of 2 exponential functions: the first describes a path on a circle in the complex plane with modulus 1 and is independent of  $\chi$ . The second is a value in the complex plane with also modulus close to 1, except around the resonance frequency, where it describes a small loop in the complex plane. The overall modulus of  $e^{-2\gamma l_s}$  is therefore always close to 1, except around the resonance frequency.

### The reflection coefficient $\Gamma$ in $S_{11}^R$

Now, we analyze the reflection coefficient  $\Gamma$ : using Eqs. 4.7 and 4.9 we determine  $\Gamma$  to

$$\Gamma = \frac{\sqrt{\tilde{\mu}_r} - \frac{\sqrt{\tilde{\epsilon}_r}}{G}}{\sqrt{\tilde{\mu}_r} + \frac{\sqrt{\tilde{\epsilon}_r}}{G}} = \frac{\frac{1}{2}x\chi + 1 - \frac{\sqrt{\tilde{\epsilon}_r}}{G}}{\frac{1}{2}x\chi + 1 + \frac{\sqrt{\tilde{\epsilon}_r}}{G}}. \quad (4.12)$$

The modulus of  $\Gamma$  depends on  $G$  and  $x$ . These two quantities depend on the sample and its positioning and therefore on the exact experimental situation. As it is difficult to give a general estimation, we look at experimental values of  $\Gamma$ , which we extracted from two port measurements as described in the last chapter: we find that the modulus of  $\Gamma$  is on the order of 0.01.

Hence, we can neglect  $\Gamma$  in the denominator of Eq. 4.5, as  $|\Gamma e^{-2\gamma l_s}| \ll 1$ . The simplified equation is

$$S_{11}^R \approx e^{-2\gamma l_s} + \Gamma. \quad (4.13)$$

This equation allows an intuitive understanding of the measured scattering parameter:  $S_{11}^R$  mainly consists of a contribution due to the direct reflection at the sample border ( $\Gamma$ ) and a contribution due to the electromagnetic wave propagation over twice the length of the waveguide (the exponential function).

To see if we can also neglect the  $\Gamma$  remaining in the numerator, let us give estimations of the 2 terms at resonance.

For the exponential function, we already saw in Eq. 4.11 that it can be split into a product of two exponential functions, where only the second one contains  $\chi$ . To evaluate the modulus of the FMR-related contribution, we first need to analyze the value of  $\chi$  at the resonance frequency. At  $f_{\text{res}}$  the susceptibility is purely imaginary having the highest modulus. According to Eq. 1.45, we find

$$\text{Max}(|\chi|) = |\chi(\omega_{\text{res}})| = |-\chi''(\omega_{\text{res}})| \approx \left| -j \frac{\omega_M}{\alpha \omega_{\text{res}}} \right| = \frac{\omega_M}{\alpha \omega_{\text{res}}}. \quad (4.14)$$

When inserting  $\chi(\omega_{\text{res}})$  in the second exponential function in the product in Eq. 4.11, we obtain at resonance

$$e^{-j2l_s \frac{\omega_{\text{res}}}{c} \sqrt{\tilde{\epsilon}_r} \frac{1}{2} x (-j) \frac{\omega_M}{\alpha \omega_{\text{res}}}} = e^{-l_s \frac{1}{c} \sqrt{\tilde{\epsilon}_r} x \frac{\omega_M}{\alpha}}. \quad (4.15)$$

We note that the FMR-related contribution is independent of the resonance frequency.

We analyze in the same manner the modulus of  $\Gamma$  at the highest modulus of  $\chi$ , i.e. at resonance. Inserting  $\chi(\omega_{\text{res}})$  in Eq. 4.12 yields:

$$\Gamma(\omega_{\text{res}}) = \frac{-jx \frac{\omega_M}{\alpha \omega_{\text{res}}} + 2 - 2 \frac{\sqrt{\tilde{\epsilon}_r}}{G}}{-jx \frac{\omega_M}{\alpha \omega_{\text{res}}} + 2 + 2 \frac{\sqrt{\tilde{\epsilon}_r}}{G}}. \quad (4.16)$$

As  $x \ll 1$ , we deduce  $jx \frac{\omega_M}{\alpha \omega_{\text{res}}} \ll 1$ . We can thus neglect it in the denominator. As  $G \approx \sqrt{\tilde{\epsilon}_r}$ , we approximate  $2 + 2 \frac{\sqrt{\tilde{\epsilon}_r}}{G} \approx 4$  and  $2 - 2 \frac{\sqrt{\tilde{\epsilon}_r}}{G} = n$ , where  $n$  is a small frequency independent number. We find

$$\Gamma(\omega_{\text{res}}) \approx \frac{-jx \frac{\omega_M}{\alpha \omega_{\text{res}}} + n}{-jx \frac{\omega_M}{\alpha \omega_{\text{res}}} + 4} \approx \frac{-jx \frac{\omega_M}{\alpha \omega_{\text{res}}}}{4} + \frac{n}{4}. \quad (4.17)$$

In conclusion, we find that the contribution of  $\Gamma$ , which depends on the susceptibility, decreases approximately with the resonance frequency, apart from a constant offset term.

While we clarified the dependence of the two summands in Eq. 4.13 on the resonance frequency, we still need to do a numerical comparison in order to estimate if one is negligible. We will for example take values determined in chapter 7 for CoFeB:  $\alpha = 0.006$  and  $\mu_0 M_s = 1.79$  T. The length of the CPW is  $l_s = 5.25$  mm. By taking the measured susceptibility from a full two port measurement (see Eq. 3.18) and comparing to the susceptibility calculated from the theoretical formula (see Eq. 1.35 and 1.36) using the material parameters determined from the FMR measurement, we found  $x \approx 0.0002$ . A similar value was confirmed for several different samples. Also from the full two port measurement, we determined an approximate value for  $\tilde{\epsilon}_r = 6.25$ .

Using Eqs. 4.11 and 4.15, we determine the magnitude of the first summand (the exponential function) at resonance:

$$|e^{-2\gamma l_s}| \approx |e^{-j2l_s \frac{\omega}{c} \sqrt{\tilde{\epsilon}_r}}| |e^{-l_s \frac{1}{c} \sqrt{\tilde{\epsilon}_r} x \frac{\omega M}{\alpha}}| = 0.61. \quad (4.18)$$

When there is no magnetic susceptibility, we obtain  $|e^{-2\gamma l_s}| = 1$ . Therefore, we note a FMR-related contribution of 0.39 to the sum. This value compares to the magnitude of the second summand, which is after Eq. 4.17

$$|\Gamma(\omega_{\text{res}})| \approx \left| \frac{-jx \frac{\omega M}{\alpha \omega_{\text{res}}} + n}{4} \right| \approx \frac{447.5 \text{ MHz}}{f_{\text{res}}}. \quad (4.19)$$

In the last equality we neglected  $n$ , as it does not depend on frequency, and therefore its contribution does not influence the resonance. As discussed before, the value decreases with increasing resonance frequency. For  $f_{\text{res}} = 2$  GHz, we obtain  $|\Gamma(f_{\text{res}})| = 0.22$ . This value is not negligible before the exponential function. However, if we apply a higher field raising the resonance frequency to e.g. 10 GHz, we find  $|\Gamma(f_{\text{res}})| = 0.045$ . This is a only small FMR-related contribution in Eq. 4.13 and can therefore be neglected.

In summary, we found that Eq. 4.5 describing the single measured scattering parameter  $S_{11}^R$  can be approximated by

$$S_{11}^R \approx e^{-2\gamma l_s}. \quad (4.20)$$

We mentioned in the introduction that the measured signal can be higher in the one port geometry than in the two port geometry. This is easily understood, when comparing the measured exponential function in  $S_{11}^R$  to the exponential function constituting the main contribution to the transmission parameters in the two port measurement (see Eq. 3.4): for the one port measurement we have the same exponent multiplied by a factor of 2. As the real and imaginary parts of the resonance are twice as high in the complex plane, but still measured with the same precision, we have a higher signal to noise ratio.

However, the validity of the employed approximation is ensured only for higher resonance frequencies/higher applied fields, as otherwise  $\Gamma$  is not negligible. In order to better illustrate the quality of the approximation, we calculated the real and imaginary part of  $S_{11}^R$  with the mentioned material parameters for two different resonance frequencies: once following the exact formula (Eq. 4.5), once using the

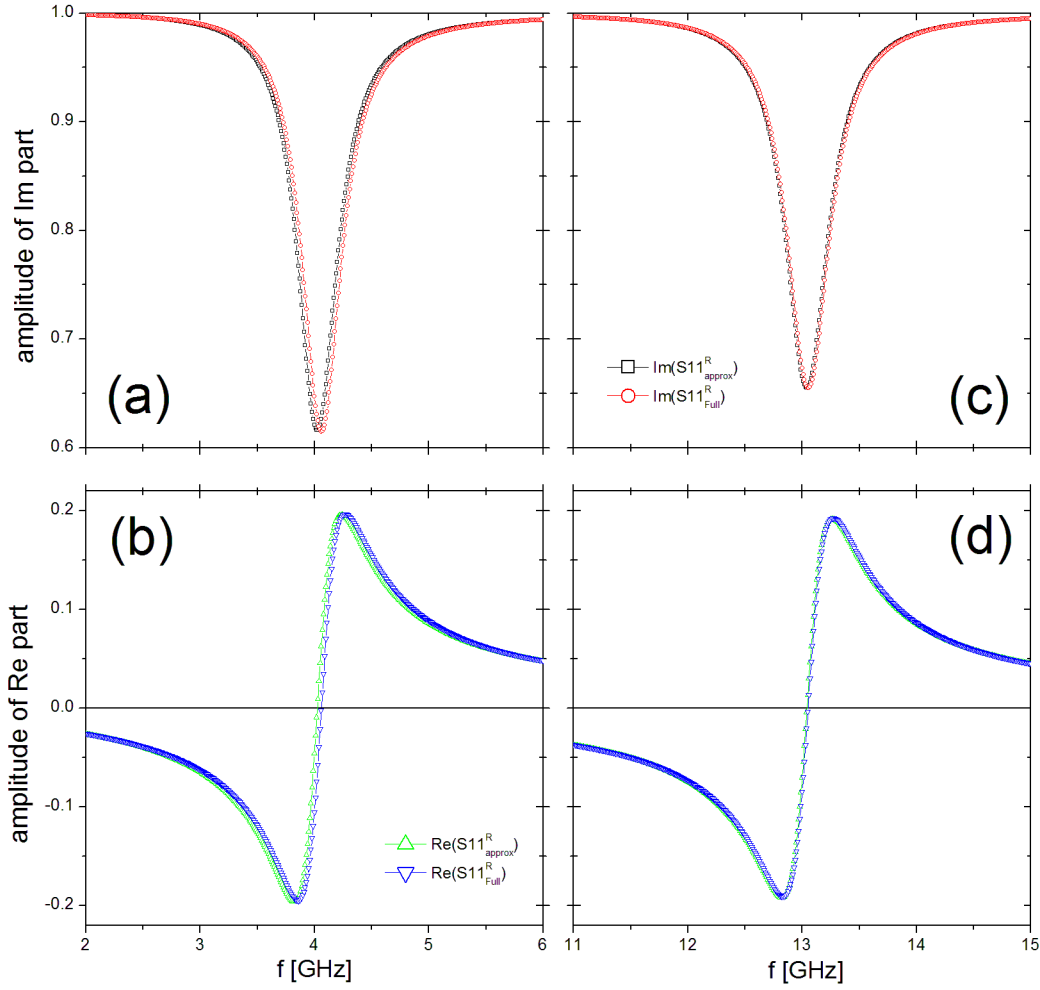


Figure 4.3: (Color online) The imaginary (a) and real (b) part of the full and the approximated formula for  $S_{11}^R$  for a resonance frequency of  $\approx 4$  GHz. The imaginary (c) and real (d) part for  $f_{\text{res}} \approx 13$  GHz.

approximation (Eq. 4.20). The simulation is shown in Fig. 4.3. The applied field is chosen such as to obtain a lower resonance frequency of  $\approx 4$  GHz and a higher resonance frequency of  $\approx 13$  GHz.

While the shape of  $S_{11}^R$  is almost conserved by the approximate formula, we observe a small shift for the lower frequency resonance (Fig. 4.3(a) and (b)) with respect to the full formula. For the higher frequency resonance, the shift disappeared:  $\Gamma$  became completely negligible.

We conclude that Eq. 4.20 is a correct description of the single scattering parameter measured in the one port geometry at high resonance frequencies.

#### 4.2.5 Open one port data evaluation

We will thus base the evaluation of the raw measurement data on Eq. 4.20. In order to obtain the susceptibility of the magnetic sample, it is necessary to do a measurement and a reference measurement. This is similar to the full two port geometry: during the measurement the magnetic field is applied in parallel to the CPW, al-

lowing for a high pumping efficiency. For the reference measurement, the magnetic field is aligned perpendicular to the CPW, thus parallel to the small excitation field. Hence, no FMR is excited.

After Eqs. 4.20 and 4.11, we find for the measured reflection coefficient in both cases:

$$S_{11,\text{mea}}^R \approx e^{-j2l_s \frac{\omega}{c} \sqrt{\tilde{\epsilon}_r}} e^{-j2l_s \frac{\omega}{c} \sqrt{\tilde{\epsilon}_r} \frac{1}{2} x \chi}, \quad (4.21)$$

$$S_{11,\text{ref}}^R \approx e^{-j2l_s \frac{\omega}{c} \sqrt{\tilde{\epsilon}_r}}. \quad (4.22)$$

We simply divide

$$\frac{\ln(S_{11,\text{mea}}^R)}{\ln(S_{11,\text{ref}}^R)} \approx 1 + \frac{-j2l_s \frac{\omega}{c} \sqrt{\tilde{\epsilon}_r} \frac{1}{2} x \chi}{-j2l_s \frac{\omega}{c} \sqrt{\tilde{\epsilon}_r}} = 1 + \frac{1}{2} x \chi. \quad (4.23)$$

We obtain a value proportional to the susceptibility  $\chi$  of the ferromagnetic film. In order to emphasize that the calculated expression is an approximation, we use in the following the notation:

$$X = \frac{\ln(S_{11,\text{mea}}^R)}{\ln(S_{11,\text{ref}}^R)} - 1. \quad (4.24)$$

In the next section, we compare  $X$  calculated following the described procedure for a one port measurement with the sample susceptibility  $\chi$  obtained from a full two port measurement, as described in section 3.2.

### 4.3 Comparison with two port measurement

The same two model samples as in section 3.4 were chosen for the comparison between the results of a measurement in the one port and the two port geometries: 40 nm  $\text{Co}_{72}\text{Fe}_{18}\text{B}_{10}$  and 40 nm  $\text{Co}_{80}\text{Fe}_{20}$ . The two thin films have different effective magnetizations and significantly different linewidths, ensuring a more general validity of the comparison. Thick samples were chosen deliberately, to minimize the influence of measurement noise on the results. More details on the samples are provided in chapter 7, which is dedicated to a study of CoFeB thin films.

Two independent measurements of each sample are performed: first, the full two port measurement after section 3.2 is executed. Here, the recorded raw data consists of the full S-matrix. A reference measurement with the magnetic field applied perpendicular to the CPW is performed, followed by a series of measurements with different applied fields parallel to the CPW.

Then, without moving the sample, the same measurements and the reference are repeated, but without the second high-frequency probe connected. Only a single S-parameter is recorded,  $S_{11,\text{mea}}^R$  and  $S_{11,\text{ref}}^R$  respectively for the reference.  $X$  is calculated after Eq. 4.24.

Fig. 4.4 plots the evaluated raw data for the  $\text{Co}_{80}\text{Fe}_{20}$  sample at an applied field of 40 mT as an example. While a slight misalignment can be observed, the shape of both curves show approximate agreement. To better quantify the differences, we proceed to a systematic comparison.

Both  $\chi$  from the two port measurement and  $X$  from the one port measurement are fit using Lorentzian profiles. The ferromagnetic resonance frequency  $f_{\text{res}}$  and

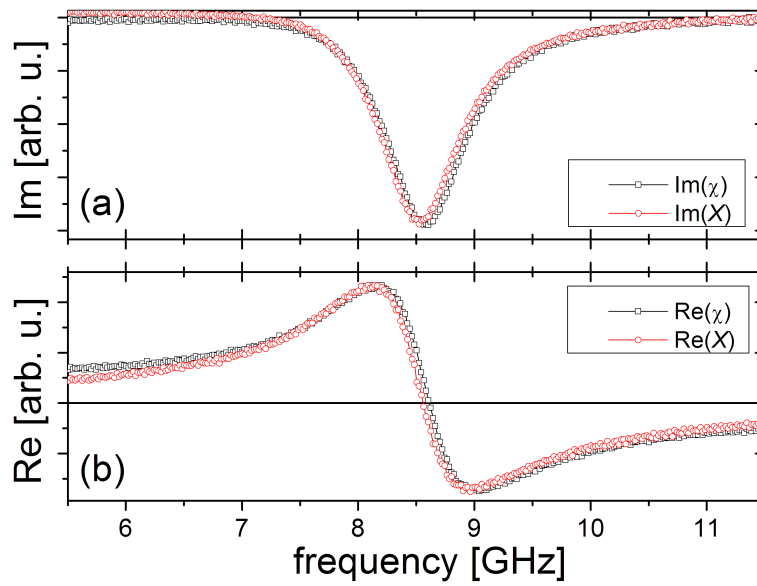


Figure 4.4: (Color online) Evaluated raw data for the  $\text{Co}_{80}\text{Fe}_{20}$  sample at 40 mT applied field: the imaginary (a) and real parts (b) of  $X$  calculated after Eq.4.24 and  $\chi$  for the full two port measurement. The y-axis were scaled to the same height of the resonance for easier comparison.

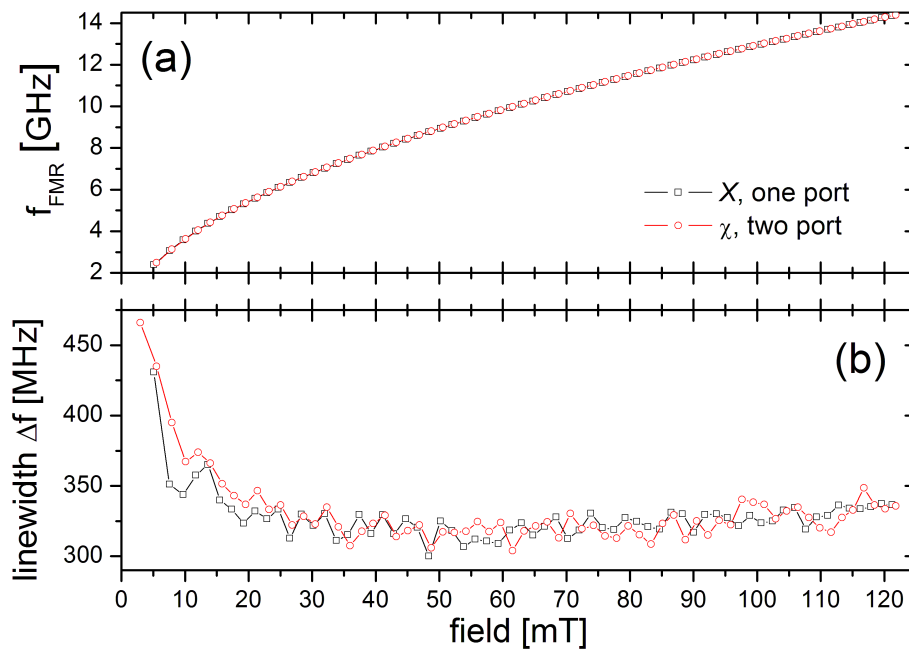


Figure 4.5: (Color online) The ferromagnetic resonance frequency (a) and the linewidth (b) as a function of applied field. The measurements are performed twice: Once in the described one port geometry, evaluating  $X$  (black square), once in the two port geometry, calculating  $\chi$  (red circle).

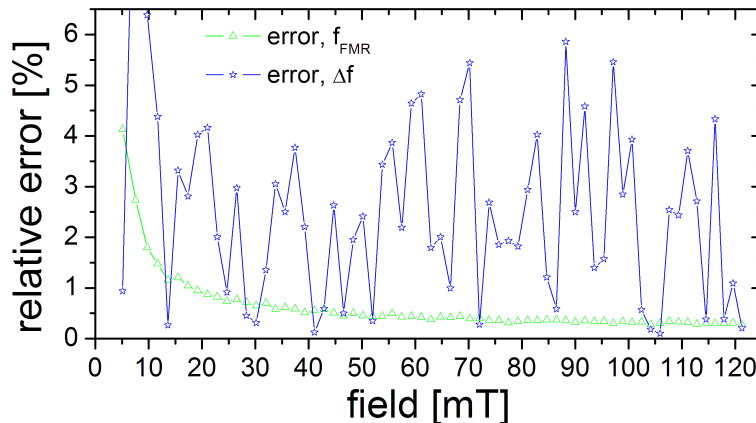


Figure 4.6: (Color online) The relative error of the data extracted from  $X$  with respect to  $\chi$  as a function of applied field: for  $f_{\text{res}}$  it is represented by green triangles, for the linewidth  $\Delta f$  by blue stars.

the resonance linewidth  $\Delta f$  are extracted. Both quantities are plotted for both measurement geometries in Fig. 4.5. An overall excellent agreement is observed.

To quantify the difference, we calculated the relative error of  $X$  with respect to  $\chi$ , which we consider as the correct value for the susceptibility, due to the approximations employed in the calculation of  $X$ . The relative errors for  $f_{\text{res}}$  and the resonance linewidth  $\Delta f$  are plotted in Fig. 4.6. For the resonance frequency, the error decreases for higher resonance frequencies, going quickly below 1%. The relative error of the resonance linewidth stays below 6%. In particular this low value for  $\Delta f$  is well comparable to the error obtained by an approximate two port measurement, where all 4 S-parameters are measured, but only one exploited (see section 3.4). This is well visible in Fig. 4.5(b): the difference between the values extracted for the two measurement geometries can be mainly attributed to arbitrary noise.

The relative error for  $f_{\text{res}}$  is slightly higher than for the approximate two port measurements. To quantify the impact, we fit both curves in Fig. 4.5(a) with the appropriate Kittel-equation (see Eq. 7.1). For the effective magnetization, the difference between the value fitted for the two different measurement geometries is  $\mu_0 \Delta M_{\text{eff}} = 0.01$  T. For the anisotropy field, the resulting values differ by  $\mu_0 \Delta H_{\text{uni}} = 0.1$  mT. These differences can be neglected.

For the 40 nm  $\text{Co}_{80}\text{Fe}_{20}$  thin film, the findings were similar (not shown): The relative error of the resonance frequency quickly goes below 1%. It is comparable to the error obtained from an approximate two port measurement, where the raw data is only evaluated using a single S-parameter. The error of the resonance linewidth was even lower than for the  $\text{Co}_{72}\text{Fe}_{18}\text{B}_{10}$  sample: for the  $\text{Co}_{80}\text{Fe}_{20}$  sample yielding a broad linewidth ( $\approx 900$  MHz), it never exceeded 4% with respect to the full two port measurement.

## 4.4 Conclusion

Vector network analyzer ferromagnetic resonance on a coplanar waveguide is typically carried out in a two port network. We analyse the possibility to carry out measurements using only a single high-frequency probe. Using the same coplanar



waveguide as for the two port measurement, the second unconnected port is described as an open-circuit. The theory connecting the single measured scattering parameter  $S_{11}^R$  and the sample susceptibility is developed. A data evaluation procedure is presented, which yields the complex parameter  $X$ , which is related to the susceptibility. In order to assess a potential deviation from the sample susceptibility due to the employed approximations, actual measurement data is used for a comparison.

Measurements are carried out on two model samples, once in the full two port geometry, once in the open-circuit one port geometry. The ferromagnetic resonance frequency and the linewidth is extracted from  $X$  obtained for the one port measurement and from  $\chi$  obtained for the two port measurement. Only a small deviation is found between the resonance frequencies, which leads to entirely negligible differences, when fitting their dependence on the applied field with the Kittel-equation. Similarly, the observed difference for the linewidths is small. In conclusion, one port open circuit measurements represent an alternative to full two port measurements, which can be advantageous under certain conditions, e.g. when the available space is constrained. While we obtained correct results, nevertheless, the validity of the employed approximations needs to be ensured for the specific measurement implementation.

# Chapter 5

## Fe/Au multilayers - Smoothing by irradiation

This chapter analyzes different possibilities to improve the interface roughness in a Fe/Au multilayer sample. Essentially, two different treatments were examined: Decreasing the surface roughness of the substrate and its contamination with carbon by exposing it to low energy oxygen ions, improves the interfaces of the layers subsequently grown on top (§5.1). The second possibility lies in a post-growth treatment: Irradiation with He<sup>+</sup> ions leads to further improvement of the interface characteristics (§5.2). We finish this chapter by concluding on the efficiency of the employed treatments (§5.3). Part of this chapter has been submitted and is accepted for publication in the Journal of Applied Physics, as proceedings of the 52nd Magnetism and Materials Conference [161].

### 5.1 Pre-growth substrate cleaning

#### 5.1.1 Removing substrate carbon contamination

Magnesium oxide (MgO) is today a widely used substrate for the epitaxial growth of Fe films. It is insulating, has a high temperature stability and is comparatively affordable. MgO(001) is well suited for the growth of fcc Au(001) or bcc Fe(001), as the in-plane mismatch is below 4% [162]. However, often the MgO surface is contaminated by carbon, degrading the morphology of the grown films due to the formation of several reconstructions and inhibiting layer-by-layer growth [163].

Ion beam oxidation was found to be an efficient technique for the preparation of MgO surfaces free of carbon contamination [162]: The surfaces are treated with a low energy atomic oxygen ion beam at room temperature, which is generated by a high frequency, low pressure plasma source with an inductive excitation, type COPRA 160 (see [164]). The charged oxygen ion beam is neutralized and the dissociation degree is up to 80%. The process time was 2 minutes, providing an atomic oxygen ion dose of  $6 \times 10^{16}$  ions/cm<sup>2</sup> with the nominal energy of 60 eV under a pressure of  $10^{-4}$  mbar. The dissociated low energy oxygen ions were found to clean the surface due to a chemical reaction with carbon atoms. This was clearly demonstrated by Auger spectroscopy: As shown in Fig. 5.1(c) the described ion treatment leads to the disappearance of the carbon peak in the Auger electron spectrum.

Apart from the chemical cleanness of the ion beam treated surface, an atomic force microscopy (AFM) study confirmed additionally a reduced root mean square

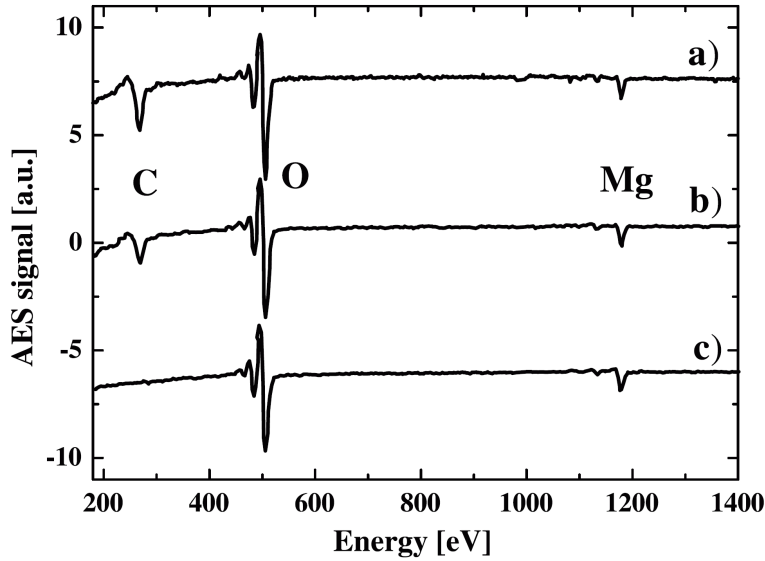


Figure 5.1: Auger electron spectra of MgO surfaces, after [162]. Curve (a) shows a substrate pre-heated at  $150^{\circ}\text{C}$ , (b) annealed for 3 h at  $600^{\circ}\text{C}$  and (c) a substrate treated with the oxygen ion plasma. While (b) shows a reduced carbon peak, it vanishes entirely in (c). All spectra are normalized for comparison and shifted for clarity.

(RMS) roughness of the MgO substrates [162].

The ion beam substrate treatment for the samples examined within this thesis was carried out in the Magnetism group lead by Prof. Dr. B. Hillebrands at the Department of Physics at the University of Kaiserslautern participating in the European Research Training Network (RTN) Ultrasmooth.

The interested reader can find further information on surface smoothing using low energy ions from the same plasma source in [165]: under an argon ion bombardment with energies between 30 and 70 eV the RMS roughness of a permalloy film could be reduced by 40% allowing to reduce the Néel “orange peel” coupling when employing it in magnetic tunnel junctions. Also, Fourier power spectra of scanning tunneling microscopy images revealed that the smoothing is particularly pronounced for short length scales (5 – 40 nm), while being present on all length scales. This relates to the detected increase in the lateral correlation length corresponding to the roughness reduction.

### 5.1.2 Studied samples

The nominal structure of the grown Fe/Au multilayer samples is

$$\text{MgO}(100)/\text{Fe}(3\text{nm})/\text{Au}(19\text{nm})/[\text{Fe}(1\text{nm})/\text{Au}(0.9\text{nm})]_{20}. \quad (5.1)$$

The actual multilayer consists of 20 repetitions of  $[\text{Fe}(1\text{nm})/\text{Au}(0.9\text{nm})]$ , while the underlying layers act as a buffer. The MgO-substrates were prepared by Crystal GmbH [166] exhibiting a RMS roughness of 0.53 nm on their polished side. The samples were grown using molecular beam epitaxy (MBE) in order to obtain epitaxial layers. To improve homogeneity the substrate was situated on a rotating molybdenum plate. The growth pressure was  $6.9 \times 10^{-9}$  Torr ( $= 9.2 \times 10^{-9}$  mbar).

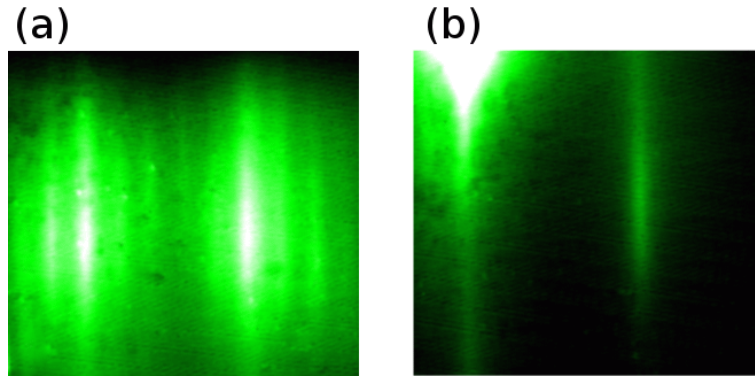


Figure 5.2: (Color online) In-situ Reflection High Energy Electron Diffraction (RHEED) images of the samples A-non (a) and B-non (b) taken directly after deposition. For the sample B-non only one Rheed stripe was found.

The substrate was annealed for one hour at 500°C removing water and hydrogen from the surface. Then the 3 nm Fe seed layer was deposited at the same temperature, while the 19 nm Au buffer was deposited at 200°C. The Fe seed layer helps to shift the Au growth from three-dimensional island growth (due to the high mobility of Au atoms on MgO) to layer-by-layer growth [167]. Growing the buffer layer at an elevated temperature results in an improved crystal structure due to the enhanced surface diffusion length [168]. The subsequent Fe/Au multilayer was grown at a lower temperature of 70°C with the aim of avoiding interdiffusion of the nanometer thick layers. Fe(001) grows in the bcc phase in a 45° rotation of its lattice on fcc Au(001) with a corresponding in-plane lattice mismatch of less than 1% [169].

Two samples of size 1 × 1 cm<sup>2</sup> were grown in the same manner following precisely the above mentioned steps, the only difference being the used substrate: while the sample referred to in the following as **B-non** was grown on a MgO-substrate not subject to any preparing treatment apart from annealing, the sample **A-non** was grown on an additionally oxygen ion-beam treated MgO-substrate, removing the carbon contamination (according to the procedure in the previous section).

The sample deposition was conducted by Ania Suszka in the Condensed Matter group of Prof. Bryan Hickey at the University of Leeds being a partner in the RTN Ultrasmooth.

### Initial characterization

Different techniques were employed in order to achieve an initial characterization of the samples immediately after deposition: In-situ Reflection High Energy Electron Diffraction (RHEED) [170] was used to monitor the growth process. Fig. 5.2 showing the RHEED images after finished deposition gives a hint on a difference between the two samples: While the sample B-non only shows one broad RHEED stripe, on the image for the sample A-non several distinct stripes can be distinguished. The decreased width of the streaks is a qualitative indication of the increased in-plane correlation length [168].

To accomplish a quantitative measure of the surface roughness, Atomic Force Microscopy (AFM) measurements were performed immediately after removing the samples from vacuum. Fig. 5.3 shows typical images of the surface of both samples,

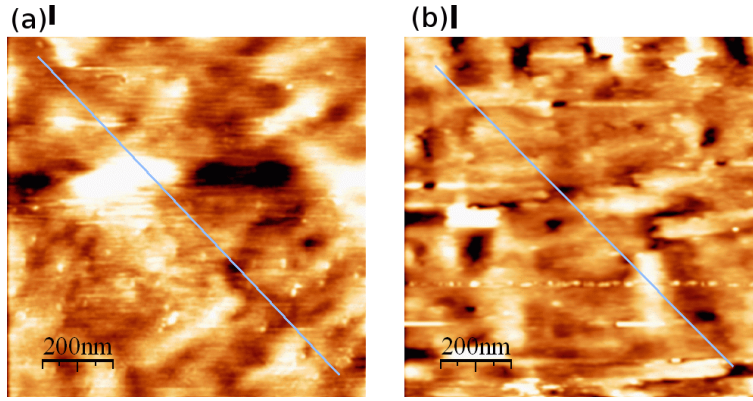


Figure 5.3: (Color online) Ex-situ atomic force microscopy (AFM) surface scans of the sample A-non ((a), smoother) and the sample B-non ((b), rougher). The diagonal lines correspond to the depth profiles shown in Fig. 5.4.

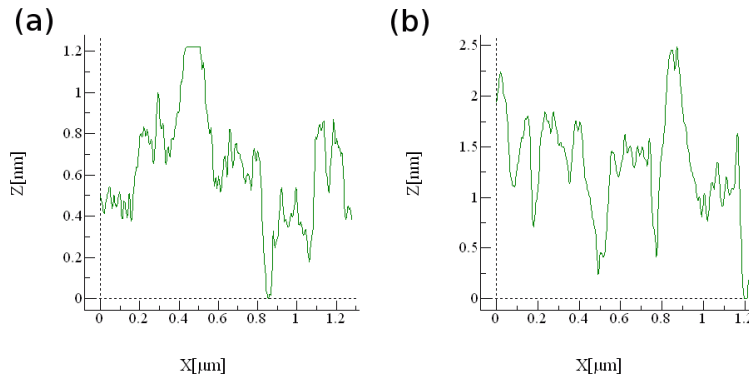


Figure 5.4: The depth profiles of the sample A-non (a) and the sample B-non (b) extracted from the AFM images shown in Fig. 5.3. We point out the different scale of the y-axis.

while Fig. 5.4 shows plots of the depth profiles marked in the AFM images as diagonal lines. A higher variation is observed for the profile of the sample B-non (plotted in (b)). The root mean square (RMS) roughness is determined to 0.27 nm for the sample A-non and 0.44 nm for B-non.

Both samples were also subject to magnetization measurements using a Vibrating Sample Magnetometer (VSM) at 127 K. The measured hysteresis loops are plotted in Fig. 5.5. Antiferromagnetic coupling between the Fe layers mediated by the intermediate Au layers is ruled out, as evidenced by the saturation of the magnetization at low fields. The coercitivity is lower for the sample A-non than for the sample B-non. This is most probably related to a better spatial homogeneity which favors domain wall motion.

### 5.1.3 Ferromagnetic resonance measurements

The samples A-non and B-non were measured using VNA-FMR following the full two-port data evaluation described in chapter 3. Fig. 5.6 shows exemplarily the imaginary part of the complex susceptibility of both samples for an applied field

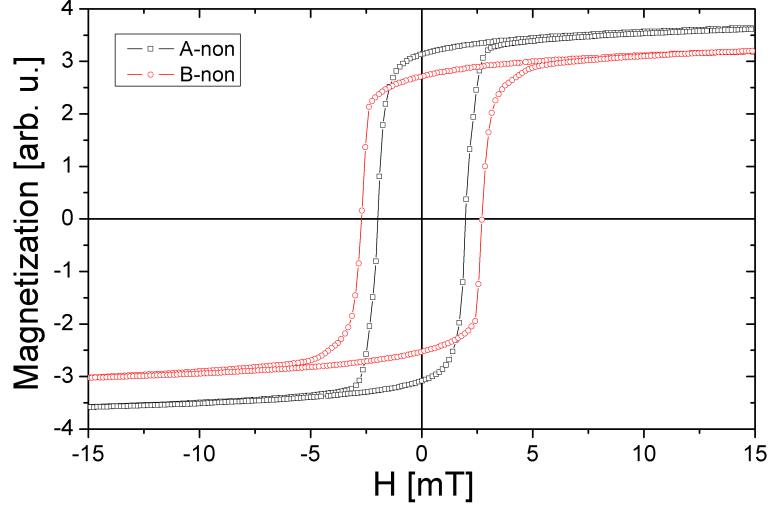


Figure 5.5: (Color online) Vibrating Sample Magnetometer measurement: the two samples show clearly different coercivity fields. The magnetization is not calibrated.

of 45 mT (the real part is omitted to clarify the figure). The two main resonance frequencies coincide closely. We will shortly discuss the second small resonance, which was only observed for the sample A-non. While the intrinsic linewidth  $\Delta f$  expected for bulk Fe is rather low ( $\approx 250$  MHz, see e.g. publications of Bretislav Heinrich et al. [143]), we found very broad resonances ( $\Delta f > 1$  GHz). This is not surprising when considering that we deal with particularly thin layers (1 nm), coupled ferromagnetically to each other. Their magnetic properties and the effective fields acting on each of them may differ slightly. For example, as each Fe layer consists of very few monolayers only, a slightly varied thickness can have a strong effect. Or the outermost layers have a different magnetic environment than the inner ones [171].

Hence, the observed resonance is likely to be a superposition of shifted resonances and therefore the measured spectrum is not corresponding precisely to a Lorentzian lineshape [172]. Indeed, there is a visible asymmetry. While we will still evaluate the resonance frequency  $f_{\text{res}}$  and the linewidth  $\Delta f$ , it has to be kept in mind that they cannot be directly related to the magnetic properties of a single Fe layer, but only to the ensemble of layers.

### Resonance frequency $f_{\text{res}}$

The resonance frequency is extracted from the maximum of the imaginary part of the complex susceptibility for a series of measurements at different applied fields. The square of  $f_{\text{res}}$  is plotted in Fig. 5.15. As pointed out in section 2.3.3, we expect a linear dependence on the applied field when squaring Eq. 2.51. We remark that while we treated the case of a uniaxial anisotropy, this is also valid for a cubic anisotropy. Here, the resonance frequency is given by [173]

$$f_{\text{res}}^2 = \left( \frac{\gamma \mu_0}{2\pi} \right)^2 [H_{\text{ext}} + H_1 \cos(4\beta)] \left[ M_{\text{eff}} + H_{\text{ext}} + \frac{H_1}{4} (3 + \cos(4\beta)) \right], \quad (5.2)$$

where  $H_1 = \frac{2K_1}{\mu_0 M_s}$  is the cubic anisotropy field and  $\beta$  is the angle of an easy axis with respect to the magnetization direction. We use a g-factor of  $g = 2.1$  [174].

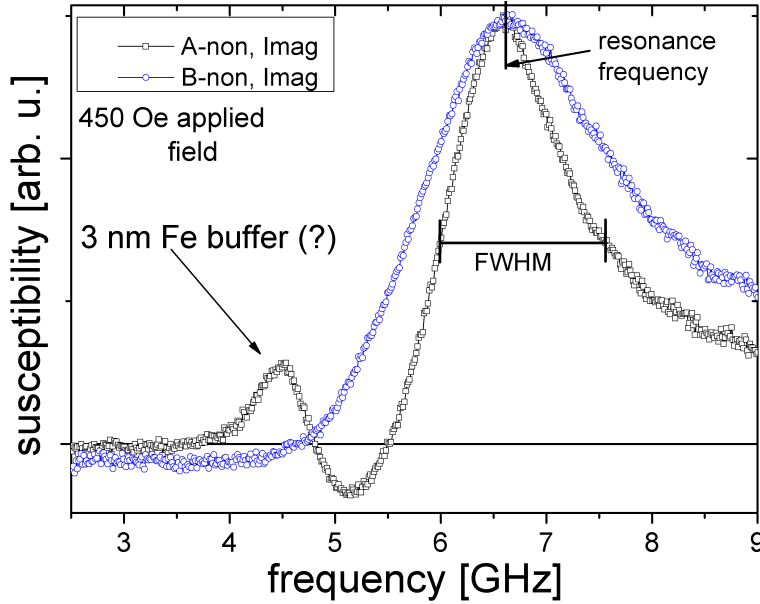


Figure 5.6: (Color online) The imaginary part of the complex susceptibility of the samples A-non and B-non for the same applied field of 45 mT. The linewidth is broader for the sample B-non. The small second resonance is only visible for the sample A-non.

However, high angle X-ray diffraction measurements revealed the presence of a (111) texture in the multilayer growth direction. As demonstrated in [174], contrary to the behavior in (100) and (110), the first-order cubic anisotropy energy does not vary in the (111) plane. While we did not conduct angle dependent measurements, the samples were placed on the setup without choosing a particular orientation of the magnetic symmetry axes. The intersection points of the curves with the x-axis in Fig. 5.15 all lie within 4 mT from the origin, i.e. the anisotropy field does not exceed 4 mT. This is compatible with a Fe (111) texture.

Fitting the data, we find an effective magnetization of  $\mu_0 M_{\text{eff}} = 0.97$  T for the sample A-non and 0.99 T for B-non. These values coincide with the expectations according to the study of Fe/Au multilayers with FMR and SQUID magnetometry in [35]: while the saturation magnetization remains high independent of the layer thickness, the uniaxial out-of-plane anisotropy field increases with decreasing thickness due to a surface anisotropy contribution. This leads to an effective magnetization which is decreasing with decreasing layer thickness. We found further support for these values using Moke (see section 5.1.4).

One remarkable difference between the susceptibility spectrum of sample A-non and B-non is the presence of a small second magnetic resonance, which is only observed for the sample A-non. Since the two samples were grown following precisely the same scheme, the only difference being the cleaning of the substrate, we identify the lowermost 3 nm Fe nucleation layer as at the origin of the additional resonance. We suppose that for the sample B-non the lowest Fe layer is a (partially) magnetic dead layer yielding no signal or a signal too low to detect it. An alternative explanation is that the 3 nm Fe seed layer grew differently on the carbon contaminated substrate of the sample B-non, showing similar magnetic properties as the Fe layers in the multilayer, and therefore the small resonance is hidden by the main reso-

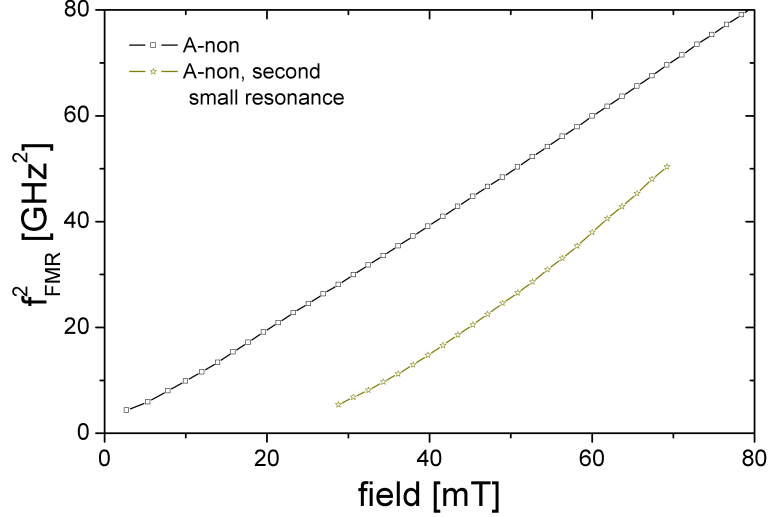


Figure 5.7: (Color online) The squared resonance frequency as a function of the applied field for the main resonance (black squares) and the small resonance (green stars) of the sample A-non.

nance for the sample B-non. The resonance frequencies of both resonances of the sample A-non are plotted as a function of the applied field in Fig. 5.7. In contrast to the multilayer resonance, the small resonance shows a much higher anisotropy field, which is found by extrapolating the curve towards the intersection point with the x-axis. According to Eq. 5.2, here the applied field is

$$H_{\text{ext}} = -H_1 \cos(4\beta) \quad \Rightarrow \quad f_{\text{res}}^2 = 0. \quad (5.3)$$

We can deduce that the magnetic field was applied following or close to a hard axis of the cubic anisotropy ( $\beta = 45^\circ$ ), as the axis crossing is at a positive applied field. Fitting the curve yields  $\mu_0 M_{\text{eff}} = 1.5$  T and  $\mu_0 H_1 = 31$  mT, under the assumption  $\beta = 45^\circ$ . As expected the effective magnetization is higher than for the only 1 nm thick Fe layers in the multilayer (higher slope in the graph), as the out-of-plane surface anisotropy is decreasing with thickness (see Eq. 1.12) [35]. The obtained fourfold anisotropy is of the expected magnitude for bcc (001) Fe (see [143]).

### Resonance linewidth $\Delta f$

While the resonance frequencies of both samples almost coincide, we observe in contrast a strong difference in the linewidth. The resonance of the sample B-non is considerably broader than for the sample A-non (see Fig. 5.6). In Fig. 5.17  $\Delta f$  is plotted as a function of the applied field: It is always higher for the sample B-non, until at high applied fields the linewidths of both the sample A-non and B-non converge towards  $\approx 1100$  MHz. Indeed, the observed curve shape of both samples corresponds to the one depicted in Fig. 2.19(b) illustrating the effect of inhomogeneous broadening, where the inhomogeneity can be anticipated much higher for the sample B-non than for the sample A-non. While it is impossible to explicitly determine the origin of the inhomogeneity (defects, spread in anisotropy or in effective magnetization), it can be related to the higher roughness of the carbon contaminated substrate of the sample B-non. As has been mentioned before, AFM measurements



confirmed that the higher roughness can still be detected at the surface of the uppermost layer of the whole structure. The lower inhomogeneity contribution to the linewidth for the sample A-non, can therefore be attributed to the substrate cleaning procedure reducing the interface roughness of subsequently grown layers.

At high applied field (100 mT) the linewidth is approximately the same for both samples. The inhomogeneous broadening contributes no longer. Still the linewidth is higher than expected from the intrinsic linewidth of bulk iron. Several studies comparing the resonance linewidth versus the film thickness for single layer samples of different materials observed very broad linewidths for the thinnest films [175, 176, 177]. While the interpretations are not in agreement, this is generally attributed either to spin-pumping or to two-magnon scattering. Additionally, as noted before, the broad linewidth can be explained by 20 layers contributing to the resonance which are subject to slightly different effective fields.

#### 5.1.4 Measurements using Perpendicular Magneto-Optical Kerr Effect (PMOKE)

The perpendicular Moke measurement is based on the polar magneto-optical Kerr effect. Its microscopic origin is for example explained in [115] and is based on the spin-orbit coupling which couples the spin components of the electron wavefunctions to the spatial components which govern the electric dipole matrix elements and optical selection rules. In the polar configuration the magneto-optical Kerr effect leads to a change in the elliptical polarization of the reflected beam, which is proportional to the magnetization projected on the propagation direction of the photons [29], i.e. here the out-of-plane direction. In our measurement setup linearly polarized light from a laser diode (wavelength  $\lambda = 682$  nm) is shone on the magnetic sample at normal incidence. After the reflection the polarization is generally elliptic. The Kerr effect is characterized by the rotation, which is the angle of rotation of the major axis of the polarization with respect to the incident polarization, and the ellipticity, which is the ratio between the major axis and the minor axis of the reflected polarization.

For a sample having an easy axis normal to the film plane, a perpendicular Moke measurement would show a hysteretic curve. All samples examined in this study have the preferential magnetization direction in the film plane. With increasing magnetic field applied normal to the film plane, the magnetization will be gradually rotated out of the plane being counterbalanced by the demagnetizing field. In the simple case of an infinite thin film, which is approximately realized, the demag field depends linearly on the out-of-plane component of the magnetization (see Eq. 1.9). Therefore, when the magnetization is aligned completely normal to the film plane, the highest Kerr rotation is detected and the applied magnetic field corresponds to the saturation magnetization of the sample. More precisely, the effective magnetization is measured, as a potential surface anisotropy can favor an out-of-plane orientation of the magnetization and hence facilitate the rotation out-of-plane. Therefore, the perpendicular Moke measurement yields the effective magnetization (see Eq. 1.24) as measured by VNA-FMR.

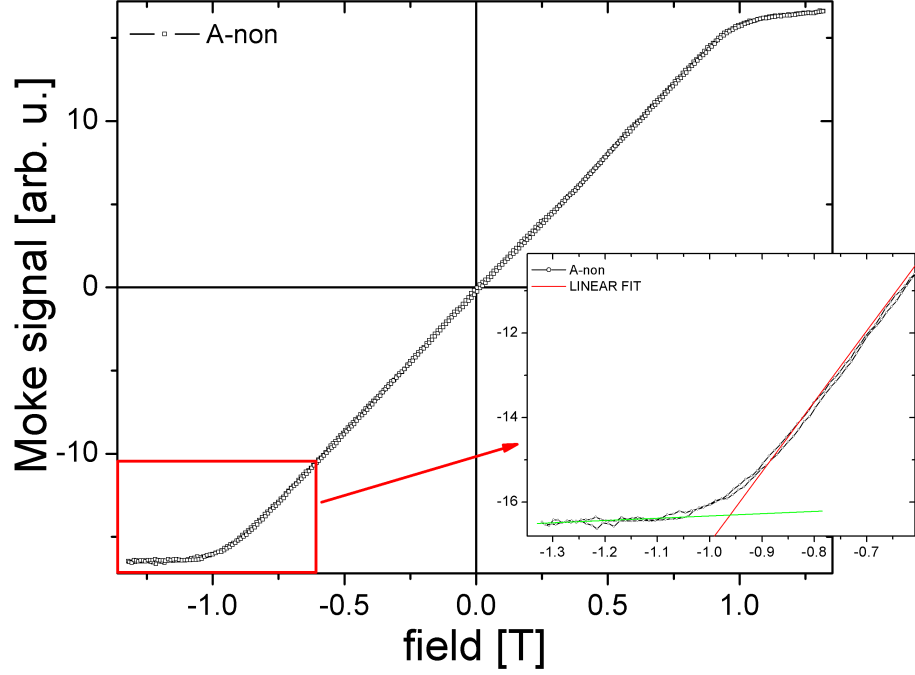


Figure 5.8: (Color online) The perpendicular Moke measurement of the sample A-non. The inset shows the determination of the effective magnetization.

## Results

The perpendicular Moke measurement curve for the sample A-non is displayed in Fig. 5.8, the inset showing the determination of the effective magnetization:  $M_{\text{eff}}$  is equal to the applied magnetic field at the intersection point of a straight line having the slope at origin with a second line conformed to the paramagnetic contribution of the substrate visible after having saturated the magnetization out of the plane. The effective magnetization was determined for the sample A-non to  $\mu_0 M_{\text{eff}} = 0.96$  T and for the sample B-non to 0.97 T. These values agree well with the FMR measurements.

The slightly lower  $M_{\text{eff}}$  for the sample A-non in comparison to the sample B-non might be attributed to smoother interfaces for the multilayer on the cleaned substrate, leading to an enhanced surface anisotropy, which in turn leads to a stronger reduction of the effective magnetization [162].

### 5.1.5 X-Ray characterization

The FMR measurements showed clear qualitative evidence that the interface roughness in the multilayer depends on the substrate treatment. Grazing incidence x-ray measurements allow to obtain quantitative data backing up the findings.

The samples were subject to x-ray measurements relying on charge scattering (magnetic scattering was not used). We present in the following data from x-ray specular reflectivity. The measurement geometry is shown in Fig. 5.9(a).

The incoming x-ray beam is at the grazing angle of incidence  $\theta_i$ , while the scattered beam reflects off the interfaces at the angle  $\theta_f = \theta_i$ . The scattering vector is determined to  $\vec{q} = \vec{k}_f - \vec{k}_i$ . It is normal to the surface and its magnitude is  $q = q_z = 4\pi \sin(\theta_i)/\lambda$ , with  $\lambda$  being the x-ray wavelength. The specular reflectivity is obtained in a so-called “ $\theta - 2\theta$ ” scan, where  $\theta_f = \theta_i$  are kept equal and scanned,

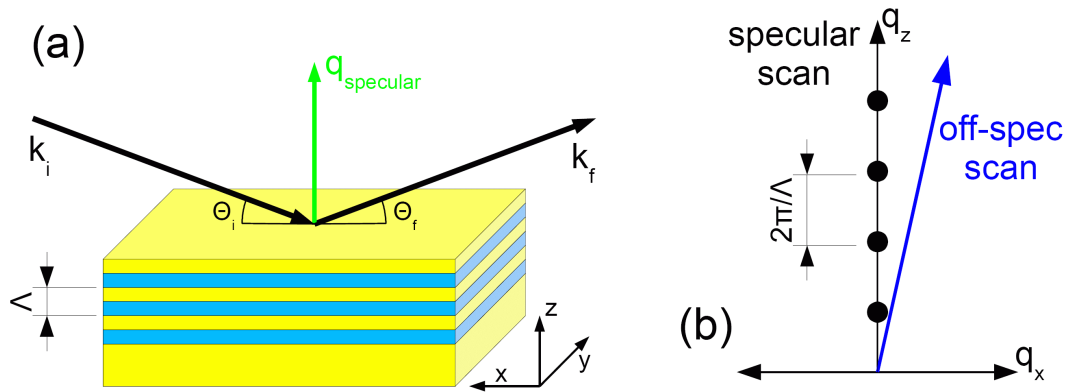


Figure 5.9: (Color online) (a) Sketch of the X-ray specular reflectivity geometry on a multilayer sample with period  $\Lambda$ . (b) The scattering geometry in reciprocal space with the Bragg peaks marked by filled dots for specular scattering. An off-spec scan probing the diffuse scattering is also indicated.

while the scattering intensity is monitored. The total scattering angle sums up to  $2\theta$ . The intensity contains information on the structure normal to the surface: the layer thicknesses and the root-mean-square interfacial width. As illustrated in the figure, the scattering vector  $q$  only has a component normal to the interfaces. As its in-plane components are zero, the values obtained from the measured intensity provide information on the laterally averaged structure.

As we examine a multilayer sample with the period  $\Lambda$ , Bragg peaks due to constructive interference are observed for  $q_z = 2\pi n/\Lambda$ , where  $n$  is an integer (see Fig. 5.9(b)). As the angle of incidence is related to  $q_z$ , the angles, at which the Bragg peaks are measured, allow to determine the multilayer period.

For rough interfaces, also diffuse scattering occurs into a cone around the specular beam. Some diffuse scattering occurs along the specular scattering direction. It has to be subtracted from the specular scattering in order to obtain the true specular scattering (see Fig. 5.10). Diffuse scattering is measured in a so-called “off-specular scan”, which is similar to a specular reflectivity scan except that the film normal is offset by a small angle  $\delta$  (in our measurements:  $\delta = -0.1^\circ$ ). Fig. 5.9(b) shows the probed wave vectors having a small  $q_x$  component, which can be neglected compared to  $q_z$  as the diffuse scattering usually depends only weakly on  $q_x$  near the specular condition [178]. Data presented in the following is always true specular scattering data with the diffuse scattering already subtracted.

A detailed review on thin film characterization by specular x-ray reflectivity is given in [179], a shorter one also for superlattices in [180]. The x-ray characterization was carried out by Dr. Alessio Lamperti in the group of Prof. Brian Tanner at the University of Durham, additional measurements were performed in the facilities of Prof. Dr. Hartmut Zabel at the Ruhr-Universität Bochum, both groups participating in the RTN Ultrasmooth.

## Results

The specular scattering measurements for the sample A-non and B-non are plotted in Fig. 5.18. In extended measurements up to a higher angle ( $7^\circ$ ) Bragg peaks up to the third order are visible (not shown).

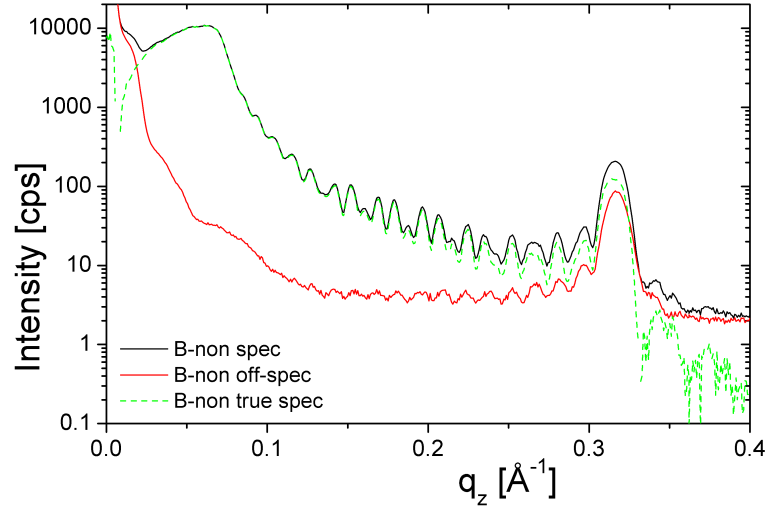


Figure 5.10: (Color online) The specular, longitudinal diffuse (off-specular) and true specular measurement of the sample B-non. The true specular is the point-to-point difference between the intensity of the specular and off-specular measurements.

The positions of the Bragg peaks of both samples are slightly shifted, giving a hint on a difference in the multilayer period  $\Lambda$ . The higher intensity of the first Bragg peak for the sample A-non is a clear indication on sharper interfaces.

Quantitative data was obtained by evaluating the measurement data with the Bede REFS software [181]. This program uses a genetic algorithm to find the global minimum in the difference between the log absolute deviation between a simulation and the measurement [168]. The extracted thicknesses are slightly higher than the nominal values: for the sample A-non we found Fe(0.968 nm)/Au(1.086 nm) = 2.054 nm, for B-non Fe(0.983 nm)/Au(1.153 nm) = 2.136 nm. These values represent the average over the 20 repetitions.

The roughness averaged over all interfaces confirms previous results: while the RMS roughness of the sample B-non was determined to 0.56 nm, a smaller value is found for A-non 0.47 nm. While the trend is clearly the same, a reduction of the interface roughness, the data don't coincide with the RMS roughness measured by atomic force microscopy (see section 5.1.2). The AFM data only takes into account the surface roughness of the uppermost Au layer, while x-ray reflectivity averages over the interfaces, justifying the discrepancy. We also emphasize that from specular scattering data it is impossible to distinguish between a graded interface (due to interdiffusion) and the roughness of an abrupt interface [178, 180].

## 5.2 Post-growth irradiation

### 5.2.1 Phase diagram of Fe-Au

The type of phase diagram plotting temperature against the relative concentrations of two substances in a binary mixture is called a binary phase diagram. The one for iron and gold is shown in Fig. 5.11 (see [182, 183]). For temperatures below 868°C it shows three different phases: for a low iron content the equilibrium phase is the fcc terminal solid solution of the Fe solute in the Au solvent, for a high iron content

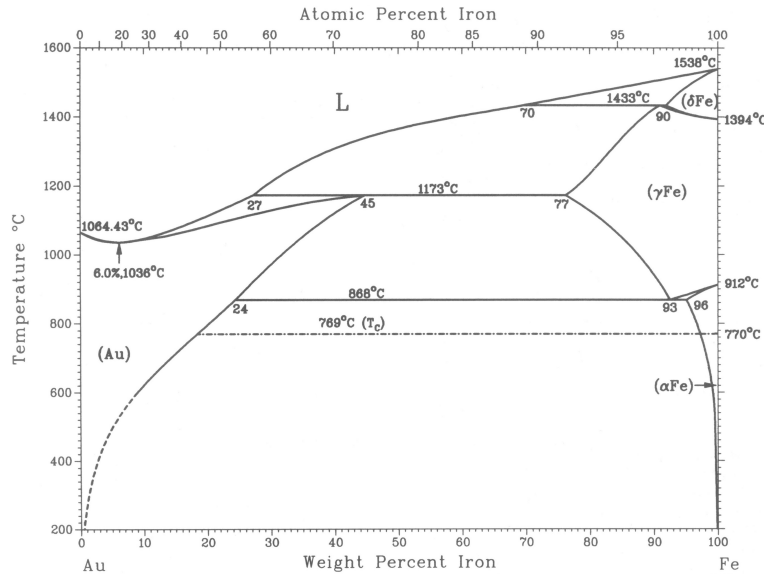


Figure 5.11: The phase diagram of binary Fe-Au alloys plotting the different phases depending on temperature and concentration, after [182].

the equilibrium phase is the terminal solid solution based on the low-temperature bcc phase of Fe ( $\alpha$ Fe). A solid solution is a mixture having the crystal structure of the solvent which remains unchanged by the addition of the solute. The solute is either replacing solvent atoms in the crystal lattice or is interstitial.

A rather broad range of concentrations between the two solid solutions is not in a single homogeneous phase: the mixture consists of the two separate phases, the solid solution Fe-in-Au and the solid solution Au-in-Fe, and this range is called their miscibility gap.

Attempts to exploit the immiscibility of iron and gold to improve the interface smoothness in a multilayer structure by annealing are reported in [184]. However, heating of the Fe/Au multilayers resulted in a complete destruction of the multilayer structure (for a sufficiently high temperature). The whole sample is at high temperature and therefore the interface energy is minimized by the formation of spherical Au clusters destroying the layered structure. Instead of annealing, we analyze in the next section the possibility of planar smoothing by resorting to ion irradiation: ion collisions provide the atom mobility necessary to overcome the kinetic limit and lead to demixing of the Fe/Au interface.

### 5.2.2 Low-energy ion irradiation

A different approach than heating the entire sample in order to reduce the surface roughness by exploiting the immiscibility is found in ion irradiation. To find guidelines to choose a suitable element for the irradiation, we used the free SRIM (Stopping and Range of Ions in Matter) software package [185, 186], which is a commonly employed simulation tool based on Monte Carlo algorithms. While being a powerful tool, the software still has some limitations, e.g. neglecting the crystal structure of the target which is always assumed amorphous. It also neglects cumulative effects, since it makes a statistical evaluation of the mean effect of the first ion impinging the surface. The different assumptions and limitations are analyzed

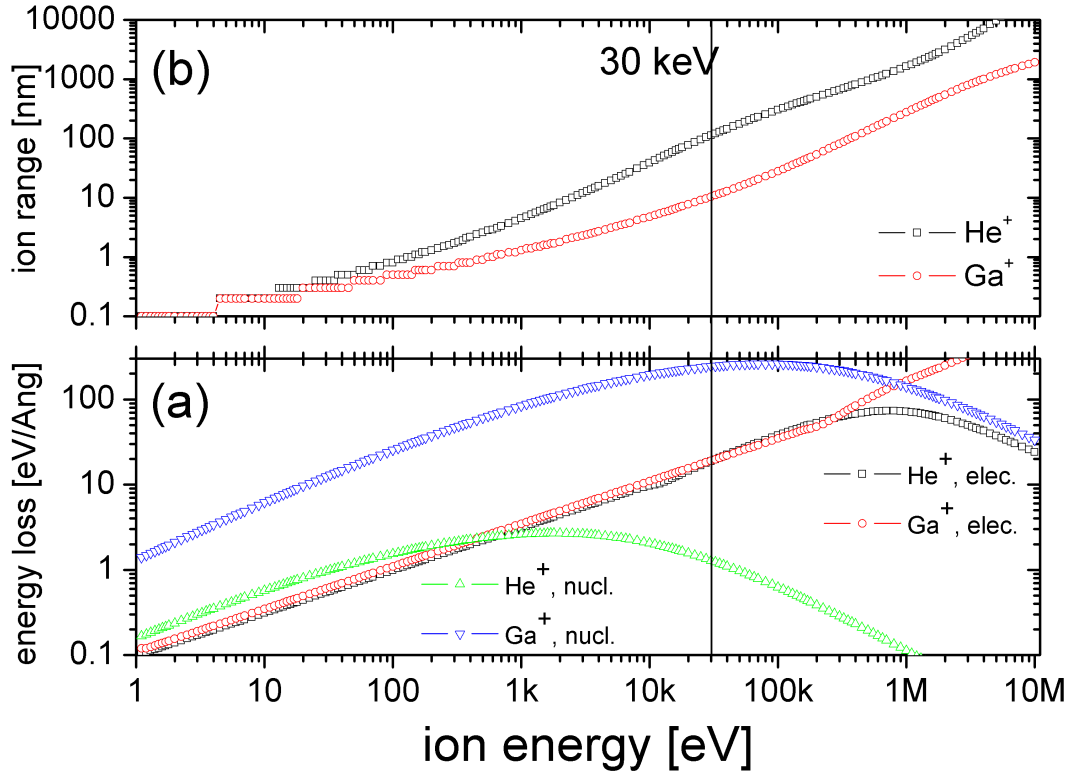


Figure 5.12: (Color online) Electronic and nuclear energy loss (a) as well as an estimation for the penetration depth (b) for He<sup>+</sup> and Ga<sup>+</sup> ions in a Fe target as a function of ion energy. The actually used energy of 30 keV is marked.

in [187], concluding that for ions and ion energies similar to the ones used here, the estimations calculated by SRIM are rather accurate.

The interaction between the incident ion and the target is an interaction between charged particles. It can be split up into nuclear collisions, where the incident ion is colliding with the nucleus, and electronic collisions, respectively with electrons in the target. Thus, the charged incident particles gradually lose their energy, which is quantified by the stopping power. This is the average energy loss of the particle per unit path length. It can be expressed as a sum of the electronic stopping power and the nuclear stopping power [188]:  $S(E) = S_{\text{elec}}(E) + S_{\text{nucl}}(E)$ . Fig. 5.12(a) shows calculated values for both types of energy loss for two different cases: He<sup>+</sup> or Ga<sup>+</sup> incident ions into an iron target. While for higher ion energies the electronic energy loss becomes relatively more important, it does not effect the target's structure: as the target is metallic (Fe/Au), the relaxation time of the conduction electrons is short and the dissipated energy is virtually instantly shared between all electrons. Hence, it does not contribute to a displacement of the atoms in the sample.

Considering the nuclear energy loss, we observe that it is always higher for Ga<sup>+</sup> ions which are commonly used in ion beam lithography than for He<sup>+</sup> ions. This can be easily understood as we are considering elastic collisions: The highest transferred energy is reached when both target and incident atom have similar mass. The atomic number and consequently the mass of Ga is much closer to the one of Fe than it is the case for He: at 30 keV we find a nuclear stopping power of 1.28 eV/Å for incident He<sup>+</sup> ions, while the energy loss is estimated much higher for Ga<sup>+</sup> ions to 243.4 eV/Å. The atom scattered by the incident particle is called primary knocked-

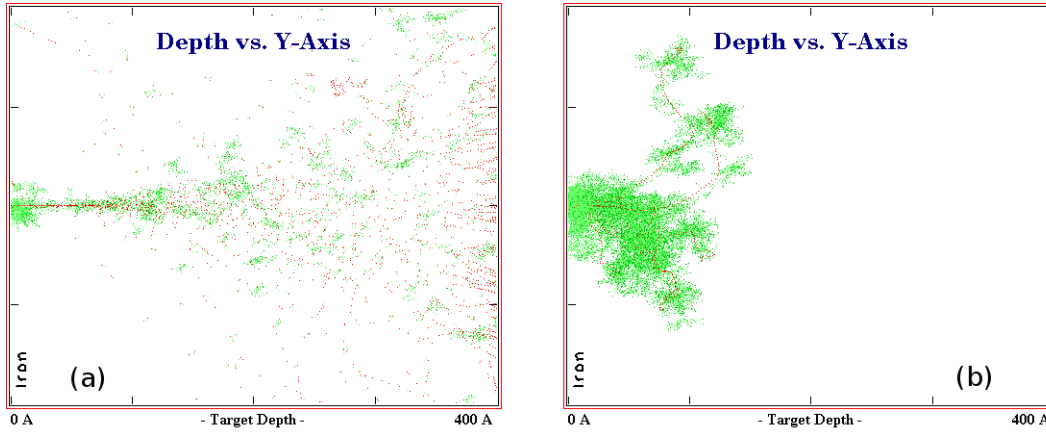


Figure 5.13: (Color online) SRIM (Stopping and Range of Ions in Matter) simulation [186] of the collisions of 100  $\text{He}^+$  ions (a) or 10  $\text{Kr}^+$  ions (b) having an energy of 30 keV incident into 40 nm of Au. Red dots mark primary, green dots secondary collisions. The most striking features are the collision cascades provoked by the heavier  $\text{Kr}^+$  ions and the  $\text{He}^+$  ions entirely traversing the layer, while the  $\text{Kr}^+$  ions are implanted.

on atom (pka). If the transferred energy is higher than the displacement energy, which is the minimum energy necessary to knock it far enough away from its lattice site so that it does not return immediately, a Frenkel pair is created. This most fundamental type of damage caused by an ion is a single vacancy and a nearby interstitial atom [185]. If the energy of the pka is very high, it can create on its own a large number of Frenkel pairs, especially as the efficiency of the secondary scattering processes is very high, as the pka has the same mass as the other target atoms, i.e. the energy transfer is at its maximum. If a large number of these so-called secondary knocked-on atoms (ska) is created, we speak about a collision cascade. For very high energies transferred to the pka, the effect is termed thermal spike. Here, the collisions occur very close to each other and the collisional process has to be understood as a many-body process. The dense collisions essentially lead to a local melting of the crystal followed by a fast quench, which can result in amorphization.

Fig. 5.13 gives a simulated example of the collisions taking place in 40 nm Au for (a) 100 incident  $\text{He}^+$  ions and (b) only 10 incident  $\text{Kr}^+$  ions. The red dots mark primary collisions, while the green dots represent secondary collisions of the primary knocked-on atoms. The y-axis represents the lateral position and all ions are incident in the center. Obviously, collision cascades take place for the heavier element (b), while for the  $\text{He}^+$  ions fewer ska are visible and the collisions are more homogeneously distributed over the entire depth of the film, taking into account that in the actual irradiation experiment the sample is exposed to a broad parallel beam. It is worth to remind that in (a) 10 times more incident ions are present than in (b).

Collision cascades can lead to damage to the crystal structure [189] and are not desirable. Therefore, we chose the light  $\text{He}^+$  ions for the irradiations, as extensive collision cascades are absent and structural modifications are confined to the vicinity of the ion path in the metal [187]. Another important criterion is a possible implantation: As seen for the heavy ions, they are stopped inside the sample. Fig. 5.12(b)

Table 5.1: Listing of the examined Fe/Au multilayer samples having the structure following Eq. 5.1, which are distinguished by the substrate treatment and the post-growth irradiation.

Sample	MgO-substrate used	Post-growth irradiation
A-non	plasma treated	no post-growth irradiation
B-non	carbon contaminated	no post-growth irradiation
A-low	plasma treated	He <sup>+</sup> ion, fluence $1 \times 10^{15}$ ion/cm <sup>2</sup>
B-low	carbon contaminated	He <sup>+</sup> ion, fluence $1 \times 10^{15}$ ion/cm <sup>2</sup>
A-high	plasma treated	He <sup>+</sup> ion, fluence $3 \times 10^{15}$ ion/cm <sup>2</sup>
B-high	carbon contaminated	He <sup>+</sup> ion, fluence $3 \times 10^{15}$ ion/cm <sup>2</sup>

shows estimated penetration depths: While for He<sup>+</sup> at 30 keV in Fe most ions remain at around 113 nm, for Ga<sup>+</sup> they only penetrate 10 nm. In the latter case they are implanted, while for He<sup>+</sup> they stop in the substrate. The same simulation for He<sup>+</sup> ions in gold yields a lower value of 67 nm. The ion energy can not be chosen much lower as otherwise the penetration depth is reduced and implantation in the magnetic material cannot be avoided.

A more detailed analysis of 30 keV He<sup>+</sup> ion irradiation of magnetic targets can be found in [190], a topical review on light-ion irradiation is given in [187].

### 5.2.3 Irradiated samples

A listing of the irradiated samples can be found in Tab. 5.1: the two initial samples **A-non** and **B-non** were cut in several pieces using a dicing saw. The samples **A-low** and **B-low** represent each a sample piece irradiated with a low fluence of  $1 \times 10^{15}$  ion/cm<sup>2</sup> of 30 keV He<sup>+</sup> ions. The intensity of the ion current was kept at a low value of  $0.25 \mu\text{A}/\text{cm}^2$  (irradiation time of 10.6 min for the fluence of  $1 \times 10^{15}$  ion/cm<sup>2</sup>). This prevents a heating of the sample [191]. The samples **A-high** and **B-high** were treated likewise except with a three times higher fluence. All irradiations were carried out by Olivier Plantevin on the Irma implanter at the *Centre de Spectrométrie Nucléaire et de Spectrométrie de Masse* (CSNSM) at the University Paris-Sud 11 [192].

Following the arguments given in the previous section, the samples are irradiated with 30 keV He<sup>+</sup> ions. This “soft” irradiation process using light ions maintains the crystallographic structure [187]. The target atom is typically displaced only a few interatomic distances [193]. When occurring at an interface, this can lead to demixing: Though Fe and Au are immiscible (see section 5.2.1), demixing is kinetically quenched in a FeAu alloy at room temperature. The atom mobility provided by the ion collisions allows to overcome this kinetic limit and to achieve demixing of the Fe/Au interface by means of substitutions between neighbouring atoms [187]. Due to the immiscibility it is thermodynamically favourable to reduce the interfacial area and the corresponding interfacial energy [184]. This is favoured in comparison to clustering reducing the surface-to-volume ratio (caused by annealing [184]) because large scale transport of matter cannot occur, and the rate of evolution of the grain boundaries and of the insides of the grains are equal upon irradiation. The substitutional demixing is limited by the spontaneous recombination volume. Therefore, an interface smoothing effect is expected.



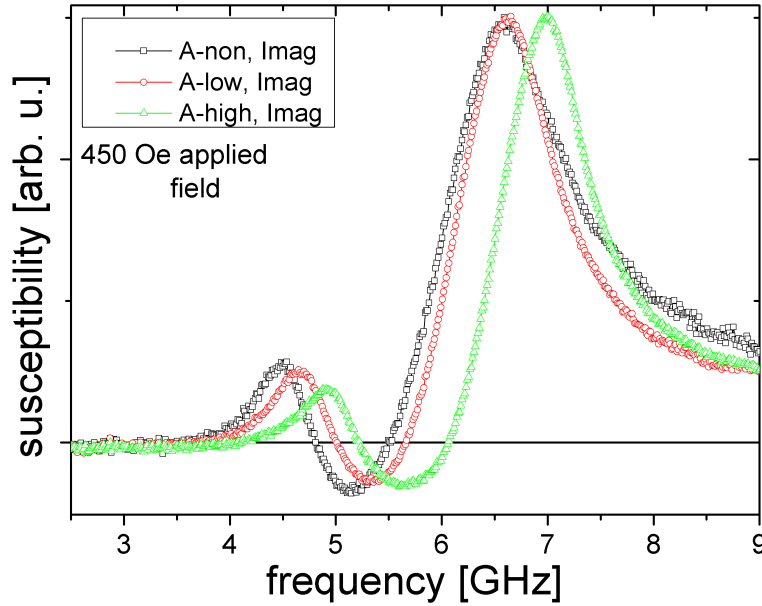


Figure 5.14: (Color online) The imaginary part of the complex susceptibility of the 3 A-samples for the same applied field of 45 mT. The resonance frequency is shifted to a higher frequency for a higher irradiation dose.

#### 5.2.4 Ferromagnetic resonance measurements

The 4 irradiated samples were measured similar to the two non-irradiated samples using VNA-FMR. The general characteristics of the measured frequency spectra correspond to the ones of the non-irradiated samples already analyzed in section 5.1.3. We emphasize in the following the differences between the 3 A-samples A-non, A-low and A-high, and between the 3 B-samples B-non, B-low and B-high, respectively, triggered by irradiation.

##### Resonance frequency $f_{\text{res}}$

Fig. 5.14 shows the imaginary part of the complex susceptibility of all 3 A-samples for one applied field (45 mT). The irradiation with the lower fluence (sample A-low) resulted only in a small shift of the resonance peak to higher frequencies. The shift is much more pronounced for the sample A-high having been subjected to a three times higher fluence. The resonance frequency behaves likewise for the B-samples (not shown): a small shift to a higher frequency is observed for the sample B-low with respect to the sample B-non. The shift is more pronounced for the sample B-high.

In Fig. 5.15 we plot the square of the resonance frequency  $f_{\text{res}}$  as a function of the applied field for all samples. All curves obey the expected linear relation on the applied field. For each pair of A- and B-samples irradiated with the same fluence the curves almost coincide. In agreement with the analysis of the susceptibility spectra, the slope increases with the applied fluence: an increase is observed for the sample A-low with respect to A-non (B-low vs B-non), an even higher increase for the sample A-high with respect to A-non (B-high vs B-non). The extracted values for the effective magnetization are summarized in Tab. 5.2: as estimated from the graph, the  $M_{\text{eff}}$  of each pair of samples (A and B) agree within the error.

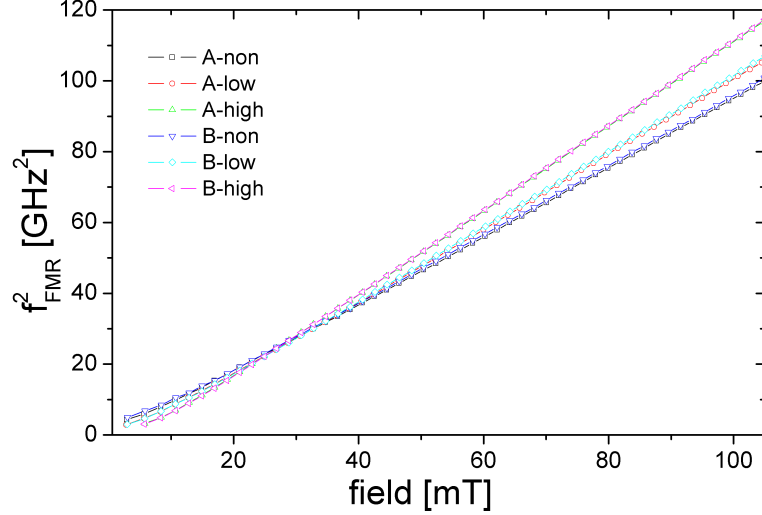


Figure 5.15: (Color online) The squared resonance frequency as a function of the applied field for all examined samples. Each pair of samples irradiated with the same fluence matches closely (A-non and B-non, ...).

At first glance, the increase of the effective magnetization with the irradiation is counterintuitive: if we suppose that the saturation magnetization stays constant, the observed increase would correspond to a decreased surface anisotropy. However, as we estimated from the structural studies that the irradiation leads to smoother interfaces, we expect thus an increase of the surface anisotropy [162], i.e. a decrease of  $M_{\text{eff}}$ . We remark that similar to the surface anisotropy on the uppermost layer interface anisotropies exist at the interfaces between the ferromagnetic and the non-magnetic media [28].

Several possible explanations can be imagined: we observe an increase of  $M_{\text{eff}}$  after irradiation, while we don't expect the interface anisotropy to decrease. But the increased effective magnetization could also be attributed to an increased saturation magnetization  $M_s$ . However, in comparable Fe/Au multilayer stacks  $M_s$  was measured by Squid magnetometry and was found to be constant for different Fe layer thicknesses ranging from 7.2 nm down to 0.7 nm [35]. To entirely rule out this explanation, Squid measurements on the studied samples would be required.

Apart from the surface anisotropy, another effect can influence the preferential magnetization direction: stress anisotropy. It can be caused by deposition stresses, which gradually relax beyond a critical thickness, thus even imitating the same thickness dependence as surface anisotropy [28]. The magnetoelastic anisotropy is the reverse of magnetostriction which describes an influence of a change of the magnetization direction on the sample dimensions. Detailed information on this type of anisotropy can be found in [194, 28].

We give an estimation of the expected stress relaxation: According to Tab. 5.2, we found  $\mu_0 M_{\text{eff}}(\text{A-non}) = 0.96$  T and  $\mu_0 M_{\text{eff}}(\text{A-high}) = 1.18$  T. After [35], we assume  $\mu_0 M_s = 2.1$  T for all samples. Representing the perpendicular anisotropy as a uniaxial anisotropy using  $\mu_0 M_{\text{eff}} = \mu_0 M_s - 2K_{\text{uni}}/M_s$ , we find  $K_{\text{uni}}(\text{A-non}) = 953$  kJ/m<sup>3</sup> and  $K_{\text{uni}}(\text{A-high}) = 769$  kJ/m<sup>3</sup>. We attribute their difference of  $\Delta K_{\text{uni}} = 184$  kJ/m<sup>3</sup> to the stress relaxation. The magnetoelastic anisotropy creates a uniaxial anisotropy along the stress axis, which is described by  $K_{\text{uni}} = \lambda\sigma/2$  [28], where

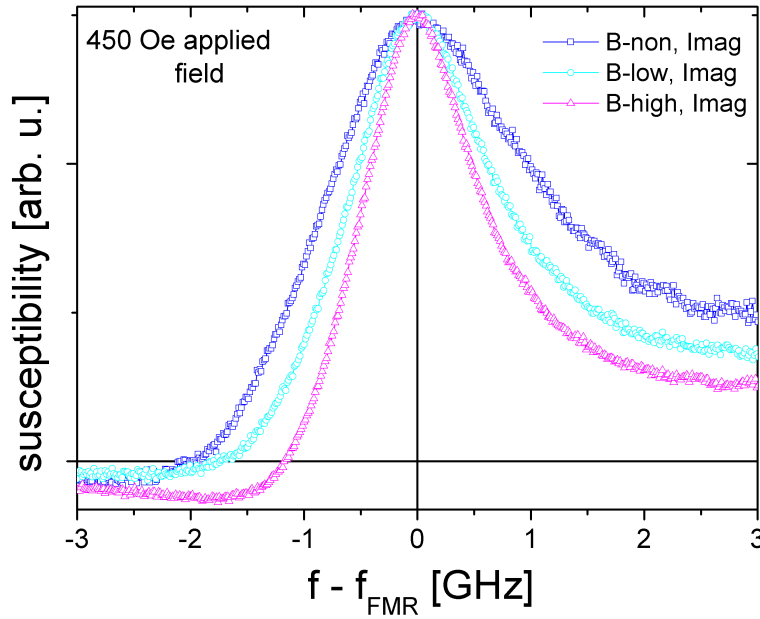


Figure 5.16: (Color online) The imaginary part of the complex susceptibility of the 3 B-samples for the same applied field of 45 mT centered around 0 (shifted by their respective resonance frequency). The linewidth is clearly smaller for a higher irradiation dose.

we assume the magnetostriction constant  $\lambda = 20.7 \times 10^{-6}$  [29]. We find a stress reduction of  $\sigma = 6.1$  GPa. With the elastic modulus of iron  $E \approx 200$  GPa, we can calculate the corresponding strain using  $\sigma = E\varepsilon$ : we find  $\varepsilon = 0.031$ . This relative strain is related to the absolute strain by  $\varepsilon = \delta l/l_0$ , where  $l_0$  is the original length and  $\delta l$  is the length change. We use the multilayer period  $l_0 = 2.0$  nm to obtain  $\delta l = 0.06$  nm.

A thickness change of the multilayer period of this order of magnitude is in fair correlation with the x-ray measurements (see Fig. 5.19). It cannot be confirmed unambiguously due to the large error bars. Additional magneto-elastic measurements would be required to confirm unequivocally the origin of the increased effective magnetization in stress relaxation. Previous work under similar irradiation conditions already established the connection between the irradiation and stress relaxation [189], which results in the lowering of the magnetic anisotropy [191].

### Resonance linewidth $\Delta f$

Fig. 5.16 shows the imaginary part of the complex susceptibility of all 3 B-samples for an applied field of 45 mT. To simplify the comparison of the linewidth, the resonance peaks were centered around 0, i.e. the susceptibility spectra were shifted by their respective resonance frequency. The linewidth is smaller after the irradiation with the lower fluence (B-low in comparison to B-non). It is further decreased for the higher fluence (sample B-high). A qualitatively similar linewidth evolution is found for the 3 A-samples (not shown). The numerical values of the linewidth for all samples at this applied field are summarized in Tab. 5.2 for comparison: It is interesting to note that the measured linewidth of any A-sample is smaller than the one of any B-sample.

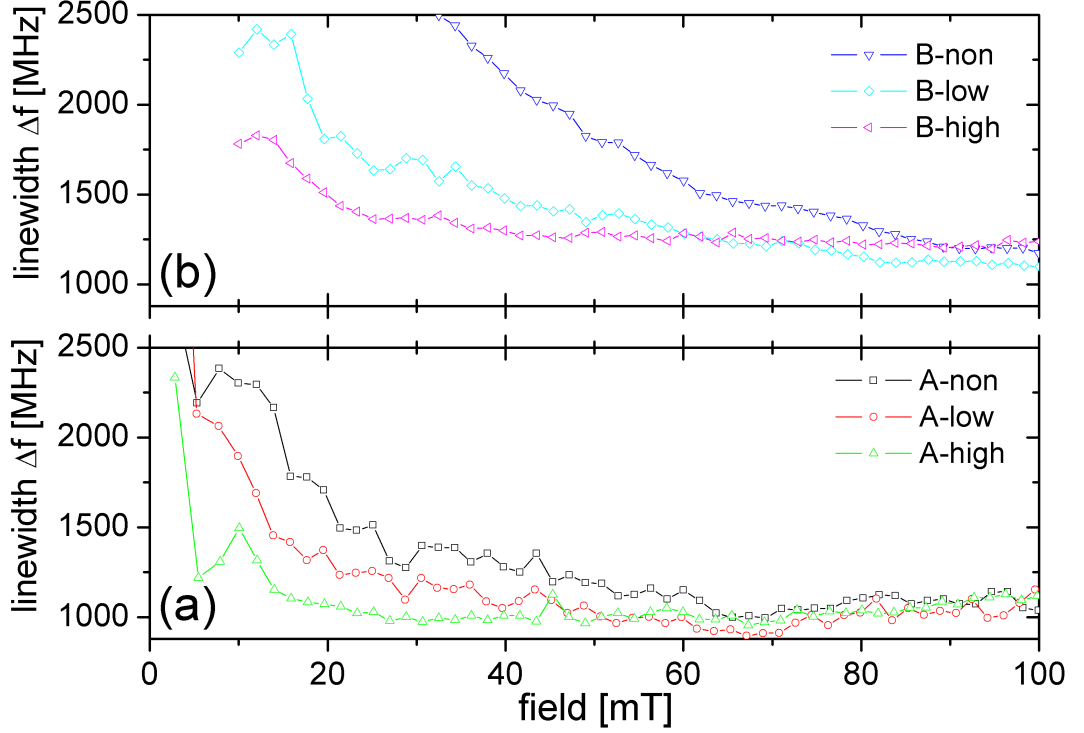


Figure 5.17: (Color online) Resonance linewidth as a function of the applied magnetic field for the 3 A-samples (a) and for the 3 B-samples (b). At lower fields the linewidths are clearly larger for the B-samples compared to the A-samples.

Table 5.2: Overview of different properties for all examined samples: The effective magnetization measured by FMR and by perpendicular Moke as well as the resonance linewidth at an applied field of 45 mT (see Fig. 5.17).

Sample	A-non	A-low	A-high	B-non	B-low	B-high
FMR: $\mu_0 M_{\text{eff}}$ [T]	0.97	1.08	1.24	0.99	1.10	1.25
Moke: $\mu_0 M_{\text{eff}}$ [T]	0.96	1.00	1.18	0.97	1.03	1.17
$\Delta f$ at 45 mT [MHz]	1245	1069	1012	2001	1415	1265

The linewidth as a function of the applied field is plotted in Fig. 5.17. The data are interpreted in a similar way as for the comparison between A-non and B-non: for a high applied field the resonance linewidths of all samples coincide approximately. Thus, the differently pronounced increase of the linewidth at low applied fields is not related to the intrinsic damping, but is due to inhomogeneous broadening. We find that the inhomogeneous broadening is lower for a higher fluence. This is valid for the A-samples as well as for the B-samples. Following the reasoning on the expected effect of the ion irradiation, we attribute the inhomogeneity reduction to an actual smoothing effect of the Fe/Au interfaces due to demixing. We still point out that the effect combines with the previously analyzed substrate treatment, as also for each pair of irradiated samples (A-low and B-low, A-high and B-high) the inhomogeneous broadening is smaller for the A-sample.

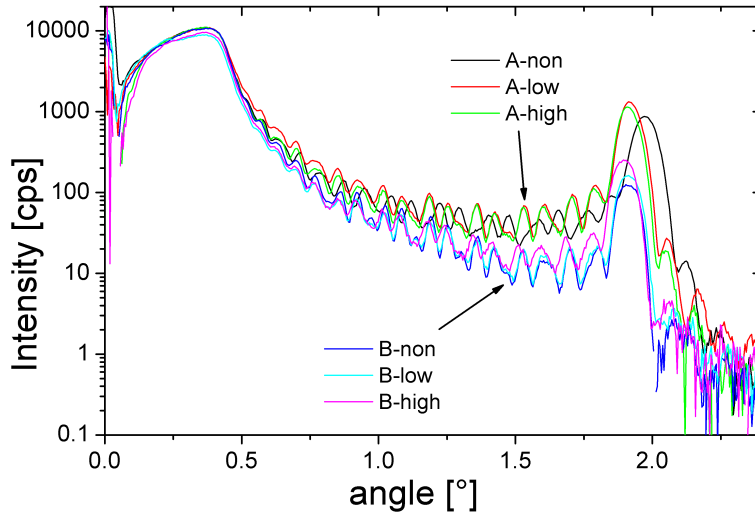


Figure 5.18: (Color online) The true specular measurements of all six samples (see section 5.1.5). The comparison of the heights of the first Bragg Peak gives a first indication of the relative interface roughness. The overall intensity of the curves is clearly lower for all 3 B-samples in comparison with the A-samples.

### 5.2.5 Perpendicular Magneto-Optical Kerr Effect

The effective magnetization measured by PMOKE is tabulated in Tab. 5.2 for all samples. An overall good agreement with the FMR measurements is found. A slight discrepancy of the absolute values is attributed to the measurement error. The changes caused by the ion irradiation are clearly similar: for the A-samples as well as for the B-samples  $M_{\text{eff}}$  is increased for the low fluence irradiation, a higher increase is found for the high fluence irradiation.  $M_{\text{eff}}$  coincides closely for each pair of A- and B-samples.

### 5.2.6 X-Ray characterization

Fig. 5.18 shows the true specular scattering measurements of all samples in comparison. One eye-catching criteria is the different amplitude of the first Bragg peak: a higher intensity hints on a sharper interface in a first approximation. But a full comparison is only possible using data obtained by simulating the whole reflected intensity spectrum. The simulation results are plotted in Fig. 5.19: the thickness of one multilayer period, i.e. one double layer of Fe and Au, and the average rms roughness of its both interfaces, i.e. the roughness of the two interfaces Au/Fe and Fe/Au averaged. As the multilayer consists of 20 repetitions, it was treated as an overall in the simulation, i.e. all double layers shared the same 6 parameters: The density, thickness and roughness of the Fe layer and the same 3 parameters for the Au layer, where the densities were constrained to within 10% of the nominal values. The introduction of average parameters is justified, as the diffuse scans show that the roughness is correlated between different interfaces.

For the thicknesses of the 3 B-samples we observe a slight reduction with increasing fluence. This can be explained by ion induced stress relaxation [184, 189]. A qualitatively similar evolution under ion irradiation is observed for the A-samples, except for the too high value of the sample A-low. The clearly visible shift in the

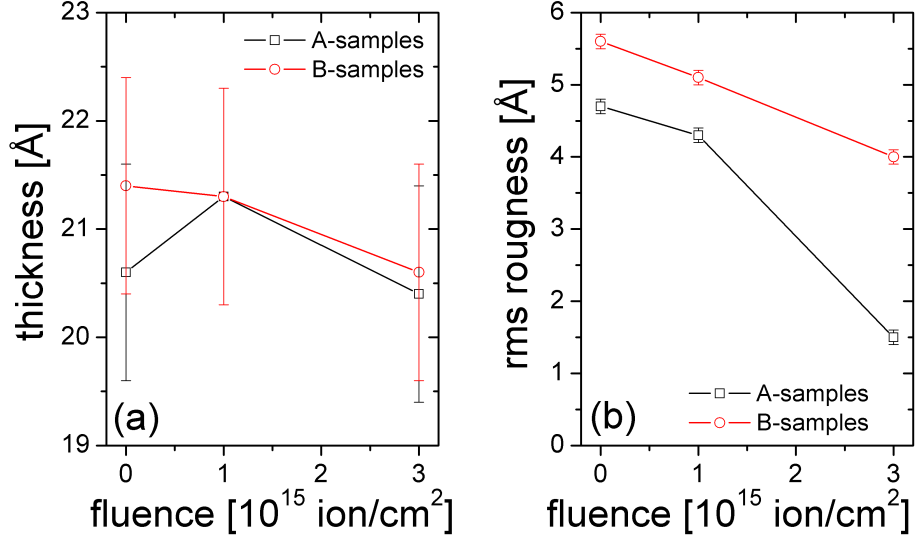


Figure 5.19: (Color online) The thickness of one multilayer period (a) and the average rms roughness of its Au/Fe and Fe/Au interface (b), for the A- and B-samples and for all fluences. The plotted values are averages over all 20 multilayer periods.

position of the first Bragg peak between the samples A-non and B-non hints on the difference in layer thickness between the two unirradiated samples.

The error on the spatial period of the multilayers is fairly high, as only the first Bragg Peak was included in the fit. The error on the rms roughnesses can be estimated as lower, as more information in the data contributes to their determination (the critical angle shape, the overall intensity drop and the decay of the fringe contrast with increasing diffusion vector).

Regarding the roughness, the conclusions conjectured from the FMR measurements are confirmed: for each pair of A- and B-samples, the observed roughness is lower for the A-sample, grown on the ion-beam treated substrate. For the post-growth irradiation, we observe a decreasing roughness with increasing fluence: The smoothing is clearly visible for each irradiation dose.

This was further confirmed by performing transverse diffuse scans: Fig. 5.20 shows the corresponding measurement curves for the samples A-non and A-low and the respective B-samples. To obtain these data, the angles  $\theta_i$  and  $\theta_f$  are chosen in the specular condition on the first Bragg Peak (see Fig. 5.9). Then the sample is rocked, i.e. it is turned while keeping the incoming beam and the detector fixed. This introduces a finite x-component of the scattering vector  $q_x$ , allowing to measure the diffuse intensity due to in-plane interface roughness.

Comparing the intensities  $I$  at  $q_x = 0 \text{ \AA}^{-1}$ , we observe that  $I(\text{A-samples}) > I(\text{B-samples})$ , consistent with the specular scans. Comparing the diffuse intensities, e.g. at  $q_x = 0.002 \text{ \AA}^{-1}$ , we observe that  $I(\text{A-samples}) < I(\text{B-samples})$ . For the samples irradiated with the same fluence, we find  $I(\text{A-low}) < I(\text{A-non})$  and  $I(\text{B-low}) < I(\text{B-non})$ . In each comparison the lower diffuse intensity indicates a lower interface roughness, in agreement with the quantitative data from the specular reflectivity scans.

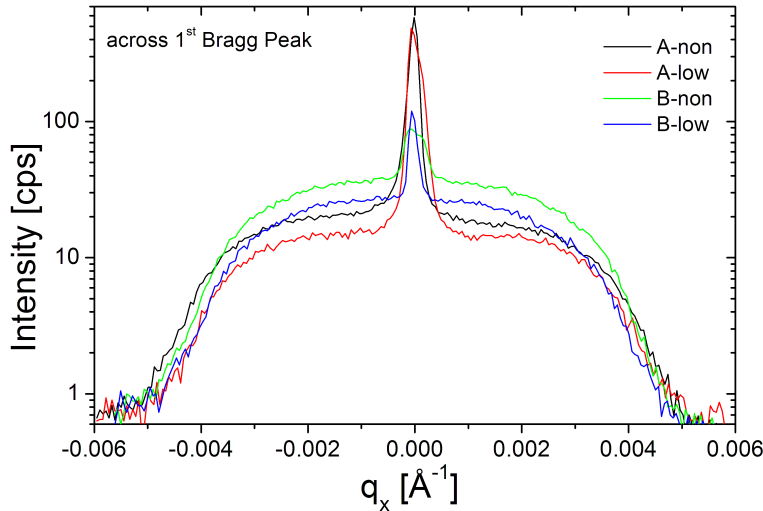


Figure 5.20: (Color online) The transverse diffuse scattered intensity of the unirradiated A- and B-samples and the ones irradiated with the lower fluence, across the first Bragg Peak. The intensities at  $q_x = 0$  correspond to the specular scan condition. The diffuse intensity at  $q_x = 0$  relates to the interface roughness.

### 5.3 Conclusion on smoothing

In this chapter we analyzed the possibility to reduce the surface and interface roughness using pre-growth and post-growth ion-beam treatments. The efficiency was tested on Fe/Au multilayer samples grown on single crystal MgO substrates. Adding an additional preparation step to the substrate cleaning resulted in reduced roughness. The additional step consists of a 2 minute exposition of the substrate to a 60 eV oxygen ion beam. This removes entirely the carbon contamination commonly observed on commercially available MgO substrates and additionally improved their smoothness. The reduced roughness was confirmed by a reduced inhomogeneous broadening in the FMR linewidth of the ion-beam treated sample. In addition, AFM measurements of the uppermost Au surface and grazing incidence x-ray scattering yielded quantitative data validating the observations.

The post-growth irradiations with 30 keV  $\text{He}^+$  ions led to a further smoothing. This can be attributed to the thermodynamically favored demixing of the two immiscible elements, activated by the atom mobility provided by ion collisions. The smoothing effect is well evidenced by the decrease of the inhomogeneous linewidth contribution for samples treated with an increasing fluence. A higher irradiation dose leads to a more pronounced smoothing effect. Additional confirmation is provided by x-ray specular reflectivity measurements.

In conclusion, we establish the efficiency of both smoothing procedures and the possibility to combine their effects.

# Chapter 6

## Dynamics of exchange biased films

In this chapter we analyze the influence of coupling an antiferromagnetic layer to a soft ferromagnetic thin film, where we characterize in particular the changes in its dynamical behavior. We begin by introducing briefly the exchange bias effect (§6.1). Then we describe the deposition and basic characterization of all samples we studied (§6.2). We proceed by evaluating the hysteretic dynamic susceptibility of the ferromagnetic single layer samples (§6.3), before presenting the FMR measurements on the exchange-biased samples (§6.4).

### 6.1 Brief overview of exchange bias

Exchange bias is an interface effect caused by the interaction between a ferromagnet and a neighbouring antiferromagnet in contact. It was discovered in 1956 by Meiklejohn and Bean in experiments on Co particles [195, 196]: The observed phenomenon was characterized by a displacement of the hysteresis loop. This is sketched in Fig. 6.1: the part (a) shows an unbiased ferromagnetic hysteresis loop with the two coercive fields  $H_{c1}$  and  $H_{c2}$  of equal magnitude. The part (b) shows the biased hysteresis loop displaced from the origin along the field axis by  $H_{\text{eb}} \equiv \frac{1}{2}(H_{c1} + H_{c2})$ . This loop shift was attributed to the presence of cobaltous oxide (CoO) on the surface of the fine particles. The interaction between the spins of the ferromagnetic cobalt and the antiferromagnetic oxide are responsible for the exchange bias effect [195].

This effect is also referred to as exchange anisotropy. This is motivated by its correspondance to a unidirectional anisotropy: in the absence of an applied field, the magnetization aligns in the direction opposite to the hysteresis loop displacement, being the only stable position (if the exchange bias field exceeds the coercive field).

Following its discovery, exchange bias has been observed in a variety of material systems (small particles, inhomogeneous materials, antiferromagnetic single crystals/polycrystals [197]). In this study, we will examine samples in one particular geometry: thin films. This is also the most widely used geometry in magneto-electronic applications, where the exchange bias effect has become a key ingredient: it is nowadays routinely employed to pin the direction of the fixed layer in GMR and TMR field sensors [198], which are for example integrated in hard disk drive heads. The magnetization of the fixed layer thus becomes almost insensitive to small external magnetic fields. This allows to use its direction as a reference with respect to the free layer, which is sensitive to the external field.



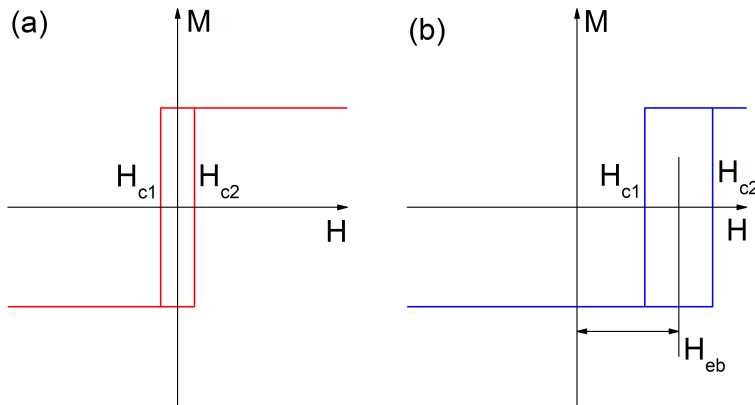


Figure 6.1: Sketch of the exchange bias effect: (a) Hysteresis loop of an unbiased ferromagnet. The two coercive fields are equal in magnitude. (b) The exchange bias effect shifts the hysteresis loop away from the origin by the so-called bias field  $H_{\text{eb}}$ .

In the following section, we will present hysteresis loops of our thin film samples, showing an exchange bias as illustrated in Fig.6.1. However, a second characteristic is observed, which is already hinted at in the drawing: Exchange bias often leads to an increased coercivity. For soft ferromagnets brought in contact with an antiferromagnet, this increase is sometimes larger than one order of magnitude.

A first simple model to explain the experimental observations was already proposed by Meiklejohn [199]. It provides intuitive explanations for the bias field  $H_{\text{eb}}$  as well as for the coercivity increase, starting from a coherent rotation approach. It considers a perfectly flat interface between a ferromagnetic thin film (FM) and an antiferromagnetic thin film (AFM). The magnetic structure of both films does not vary laterally, i.e. the films are homogenous in the  $x$ - $y$  plane. The FM is assumed to be single domain. All spins in each layer of the AFM are aligned in the plane in one of two opposite directions. This direction alternates between consecutive layers, i.e. the spins of one layer point for example along  $y$ , then the spins of the neighbouring layers point along  $-y$ , and so forth. The interface is called uncompensated, as the AFM layer in contact with the FM has a non-zero net magnetization.

While this alignment makes the AFM insensitive to an applied magnetic field in principle, this is changed by the presence of the FM: the spins in the layer of the FM at the interface are exchange coupled to the neighbouring layer of the AFM. According to Meiklejohn [199], the energy per unit surface is expressed as [198]

$$\frac{E}{S} = -HM_{\text{FM}}t_{\text{FM}}\cos(\theta - \beta) + K_{\text{FM}}t_{\text{FM}}\sin^2(\beta) + K_{\text{AFM}}t_{\text{AFM}}\sin^2(\alpha) - J_{\text{INT}}\cos(\beta - \alpha), \quad (6.1)$$

where  $H$  is the applied magnetic field,  $M_{\text{FM}}$  is the saturation magnetization of the FM,  $t_{\text{FM}}$  and  $t_{\text{AFM}}$  are the thicknesses of the FM and the AFM,  $K_{\text{FM}}$  and  $K_{\text{AFM}}$  are the magnetic anisotropy constants of the FM and the AFM (both are assumed uniaxial and aligned along the same in-plane axis) and  $J_{\text{INT}}$  is the exchange coupling constant at the interface. The angles are chosen as in the original work of Meiklejohn, illustrated in Fig. 6.2. The angles  $\beta$  and  $\alpha$  are the angles between the common anisotropy direction and the spins of the FM and respectively the spins of the AFM layer next to the interface. The opposite direction of the spins of the second sublattice of the AFM is shown in the drawing.  $\theta$  is the angle between the

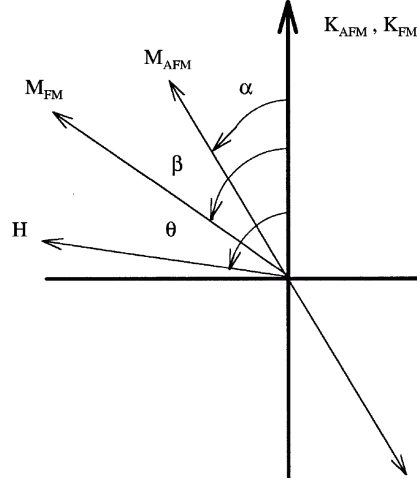


Figure 6.2: Schematic diagram of the in-plane angles introduced in Eq. 6.1, after [197]. The anisotropy axes of the FM and the AFM are considered to be collinear. The AFM has two sublattices with opposite magnetization directions.

anisotropy direction and the applied field.

The four terms contributing to Eq. 6.1 represent (in order of appearance): the Zeeman energy of the FM, the uniaxial anisotropy of the FM, the uniaxial anisotropy of the AFM and the ferromagnetic coupling at the interface between the FM and the AFM. The model can be further simplified by neglecting the FM anisotropy [199]. This is justified for soft ferromagnetic films.

To observe a loop shift,  $K_{\text{AFM}}t_{\text{AFM}} \geq J_{\text{INT}}$  is found as a necessary condition. If the anisotropy of the AFM is very high, its spins remain aligned along its easy axis ( $\alpha \approx 0^\circ$ ), in order to minimize the total energy. If the magnetic field is applied in the opposite direction ( $\theta = 180^\circ$ ), the amplitude required to align the FM in that direction is equal to the bias field:  $H_{\text{eb}} = J_{\text{INT}}/(M_{\text{FM}}t_{\text{FM}})$ .

If, on the other hand,  $J_{\text{INT}} \gg K_{\text{AFM}}t_{\text{AFM}}$ , the energy is minimized by a common rotation of the FM and the AFM, i.e.  $(\beta - \alpha) \approx 0^\circ$ . While no biasing is observed in this case, the magnetic anisotropy of the FM adds with the anisotropy of the AFM. This also leads to an enhancement of the coercivity [198].

If the exchange coupling constant is taken to be similar to the ferromagnetic exchange, the given theoretical formula overestimates the experimentally observed exchange bias field, often by several orders of magnitude [197]. Up until here, we only considered perfectly flat interfaces. An explanation for the overestimation can be found by introducing a random interface roughness, which gives rise to a random field acting on the interface spins [200, 201]. This causes the antiferromagnet to break up into domains, depending on the ratio between the interface energy and the domain wall energy in the AFM. The domains result in a more realistic unidirectional anisotropy than in the idealized case.

Also for perfectly flat interfaces with no lateral variation of the spin orientation, the creation of domain walls has been considered [202]: for an infinitely thick antiferromagnet, the domain wall builds up perpendicular to the interface, when the magnetization of the FM is turned. This is based on a competition between the exchange energy at the interface, favoring generally a parallel alignment of the FM and AFM interface spins, and the exchange energy in the AFM, stiffening its

Table 6.1: Structures of the magnetron sputtered samples studied with/without exchange biasing IrMn layer (labeled by I8). The thicknesses in brackets are given in nanometers.

Single layer sample	Structure
N8	SiO <sub>2</sub> /Ru(15)/NiFe(8.3)/Ru(7.5)
N11	SiO <sub>2</sub> /Ru(15)/NiFe(11)/Ru(7.5)
B8	SiO <sub>2</sub> /Ru(15)/CoFeB(8.3)/Ru(7.5)
B11	SiO <sub>2</sub> /Ru(15)/CoFeB(11)/Ru(7.5)
Exchange biased sample	Structure
I8N8	SiO <sub>2</sub> /Ru(15)/IrMn(8)/NiFe(8.3)/Ru(7.5)
I8N11	SiO <sub>2</sub> /Ru(15)/IrMn(8)/NiFe(11)/Ru(7.5)
I8B8	SiO <sub>2</sub> /Ru(15)/IrMn(8)/CoFeB(8.3)/Ru(7.5)
I8B11	SiO <sub>2</sub> /Ru(15)/IrMn(8)/CoFeB(11)/Ru(7.5)

spin structure. This model has the consequence, that the reversing of the FM spins influences the AFM spins, as they are not entirely rigid.

For a sufficiently thick antiferromagnetic biasing film, the two effects, the loop shift and the coercivity enhancement, are observed simultaneously. For polycrystalline AFM, this is explained by Stiles and McMichael in a model considering independent antiferromagnetic grains coupled to the FM [203, 204]. In this model, the stability of the AFM grains relative to FM rotation determines whether they contribute to loop shift or coercivity enhancement.

This model allows a basic understanding of the exchange bias effect. When it is adequate later in this chapter, we will discuss some modifications allowing to achieve a better interpretation of the experimental findings. The reader interested in further details can find reviews of the exchange bias phenomena in [197] and [205]. A short, but more recent overview is given in the first introductory section of [206]. The application of exchange bias in nanostructures is highlighted in [198].

## 6.2 Sample fabrication

All samples were deposited on thermally oxidized Si wafers [207] (75 mm diameter) covered by 500 nm SiO<sub>2</sub>. Prior to deposition the wafers were etched for 5 min inside the vacuum chamber by an Argon plasma. For all samples a 15 nm Ru buffer was deposited first and they were covered by a 7.5 nm Ru layer for protection against oxidation. Ru and Ir<sub>20</sub>Mn<sub>80</sub> were deposited using DC magnetron sputtering, while permalloy (Ni<sub>80</sub>Fe<sub>20</sub>) and Co<sub>60</sub>Fe<sub>20</sub>B<sub>20</sub> were deposited using RF magnetron sputtering. Prior optimization guided the choice for a Ru buffer [208, 209]. A thickness of 8 nm was selected for the IrMn layer, guaranteeing a high exchange bias and temperature stability [210]. Tab. 6.1 summarizes all deposited samples, and the abbreviations that we shall use in the following. After deposition, all samples were annealed at 270°C for 30 minutes under an applied field of 0.5 T in an Argon atmosphere. This ensured a well defined easy axis of the ferromagnetic layer, and the subsequent field cooling resulted in a corresponding orientation of the unidirectional exchange bias of the IrMn.

Table 6.2: Characterization of the samples listed in Tab. 6.1 by AGM: saturation magnetization  $M_s$ , coercivity  $H_c$  and anisotropy field  $H_{\text{uni}}$ . For samples showing a unidirectional anisotropy, the exchange bias field  $H_{\text{eb}}$  is listed.

Single layer sample	$\mu_0 M_s$ [T]	$\mu_0 H_c$ [mT]	$\mu_0 H_{\text{uni}}$ [mT]
N8	0.7	< 0.1	0.35
N11	0.6	< 0.1	0.4
B8	1.1	0.75	2.7
B11	1.2	0.59	2.8
Exchange biased sample	$\mu_0 M_s$ [T]	$\mu_0 H_c$ [mT]	$\mu_0 H_{\text{eb}}$ [mT]
I8N8	0.6	2.3	21.9
I8N11	0.7	2.0	11.6
I8B8	1.3	4.5	36.6
I8B11	1.4	6.1	33.6

Table 6.3: The effective magnetization  $M_{\text{eff}}$  and the anisotropy field  $H_{\text{uni}}$  of the ferromagnetic single layer samples (see Tab. 6.1) extracted from the field-dependent FMR frequencies.

Single layer sample	$\mu_0 M_{\text{eff}}$ [T]	$\mu_0 H_{\text{uni}}$ [mT]
N8	0.99	0.39
N11	0.97	0.43
B8	1.32	2.6
B11	1.40	2.6

### 6.2.1 Basic characterization

To achieve a first characterization, all samples were measured using a MicroMag Model 2900 Alternating Gradient Magnetometer (AGM) [211]. The samples were measured with a field sweep in the sample plane along the annealing direction and perpendicular to it. Fig. 6.3 shows loops for the sample N11 consisting of a single NiFe layer and the sample I8N11, where an exchange biasing layer was inserted underneath. The substrate contribution to the signal was already subtracted. In order to reduce noise the averaging time was increased to 1 sec, and to improve the field precision the smallest available field gradient between the gradient coils was selected.

In Tab. 6.2 we summarize the extracted magnetic properties: The saturation magnetization  $M_s$  was extracted from a very broad field sweep ( $[-200 \text{ mT}; +200 \text{ mT}]$ , not shown). For the single layer ferromagnetic samples the coercivity  $H_c$  was extracted from the easy axis loops as the intersection points with the x-axis, the anisotropy field  $H_{\text{uni}}$  was taken from the hard axis loops. For the exchange biased samples, the coercivity  $H_c$  is half the field between the two intersection points with the x-axis in the easy axis loop, the unidirectional exchange bias  $H_{\text{eb}}$  is defined as the field at the center position in the hysteresis. It is worth noting that the direction of the hysteresis loop shift is opposite of the direction of the field applied during field cooling.

We postpone the discussion of the extracted values to the two subsequent sections, where we compare them to FMR measurements.

The sample deposition and the AGM characterization were carried out by myself in the laboratories of the Materials & Microsystems Division of the Corporate

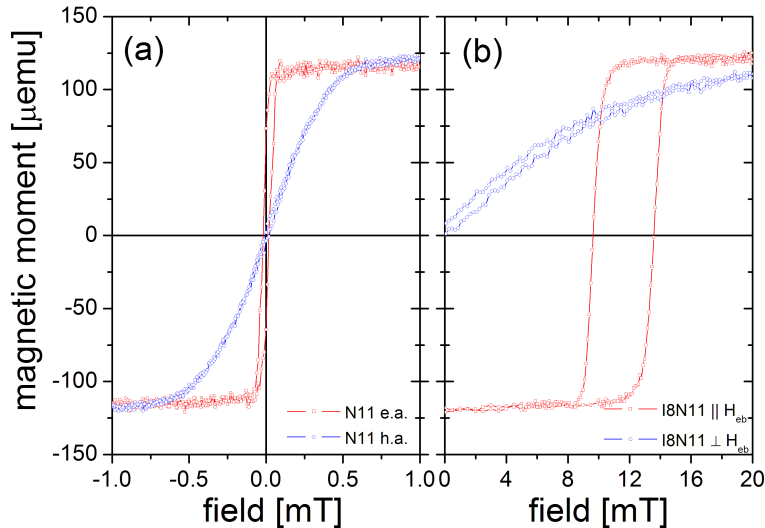


Figure 6.3: (Color online) AGM measurements: (a) The easy and hard axis loops of the sample N11 and (b) the field sweep parallel and perpendicular to the exchange bias direction for the sample I8N11. The contribution of the substrate was subtracted.

Technology department of Siemens AG (Erlangen, Germany).

## 6.3 Hysteretic dynamics of ferromagnetic single layers

### 6.3.1 The effective magnetization and anisotropy

The single layer samples were aligned on the VNA-FMR measurement setup with their easy axis along the direction of the coplanar waveguide (see section 2.3). The measurements were carried out following the full two-port data evaluation, as described in chapter 3. To give an example, the FMR frequencies extracted from the susceptibility spectra of the sample N8 are plotted in Fig. 6.4.

The data corresponds well to the curve shape expected from the Kittel-formula. For a uniaxial anisotropy with an applied field along the easy axis, we find after Eq. 1.76:

$$f_{\text{res}} = \frac{\gamma\mu_0}{2\pi} \sqrt{[M_{\text{eff}} + H_{\text{uni}} + H_{\text{ext}}][H_{\text{uni}} + H_{\text{ext}}]}. \quad (6.2)$$

A fit using this formula is shown in Fig. 6.4 by the red plain line. We assumed the g-factor, which is contained in  $\gamma$ , to be  $g = 2.14$  [29, 212]. The evaluated two free parameters, the effective magnetization  $M_{\text{eff}}$  and the uniaxial anisotropy field  $H_{\text{uni}}$ , are summarized in Tab. 6.3 for all single layer samples.

When comparing with  $M_s$  determined by AGM measurements in Tab. 6.2, we find a discrepancy for  $M_{\text{eff}}$ . While the trends are similar, the absolute values measured by FMR are systematically higher. This cannot be explained by the small uncertainty introduced due to the fixed g-factor (2%). We attribute the different values to the inaccuracy of the AGM, when measuring the saturation magnetization. To test this, we measured the same sample a second time after having repeated the calibration procedure of the AGM with the precise nickel standard. Despite a most careful

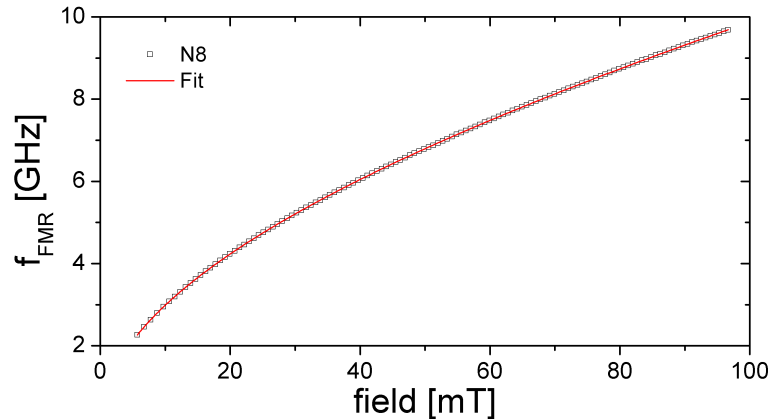


Figure 6.4: (Color online) The resonance frequency  $f_{\text{res}}$  for the sample N8 as a function of the applied external field. The measured data are represented by black open squares, the red line is a fit using Eq. 6.2.

calibration and sample alignment, the resulting values for the saturation magnetization were differing by 13% from the first AGM measurement. Furthermore, the  $M_{\text{eff}}$  measured by FMR agree better with values expected for the considered materials and film thicknesses (see [212] and [156]). We remark that both methods confirm a higher magnetization for the nominally thinner permalloy sample (N8) than for the thicker one (N11). This is most likely related to a problem during sample growth, as the permalloy target was only recently reinstalled in the sputtering system.

The anisotropy fields determined by both methods agree well. We remind that the small gradient field employed in the AGM can influence the precision of this measurement. For example, the hysteresis of the permalloy can be observed only when choosing the smallest available field gradient, as the gradient field otherwise exceeds the coercivity over the sample dimensions.

While we can extract  $M_{\text{eff}}$  and  $H_{\text{uni}}$  from the FMR frequencies plotted in Fig. 6.4, they do not allow the coercivity to be determined. Below we show that  $H_c$  can be measured by FMR nevertheless.

### 6.3.2 Dynamic bistability

In classical FMR the resonance frequency is fixed by the microwave cavity and the applied field is swept through the resonance field. Typically, only a few different cavities are used and therefore there are only few data to fit the effective magnetization. This presents itself differently in VNA-FMR, where the microwave frequency is swept and the applied field can be chosen arbitrarily. This allows the acquisition of many data points to improve the precision of the fitted values (see Fig. 6.4).

In addition, this also has the added benefit of allowing “stepped” field sweeps (as e.g. in an AGM measurement), where the applied field is first increased in one direction going through 0 applied field, using a discrete field step. Then the field is swept similarly in the opposite direction. For each field step the resonance frequency is determined, while the magnetization configuration remains unchanged (neglecting magnetic viscosity), as  $H_{\text{ext}}$  is kept constant during the measurement. While for applied fields higher than the coercivity no dependence of the magnetization configuration on the history of applied fields is expected, for  $|H_{\text{ext}}| < H_c$  the remanent

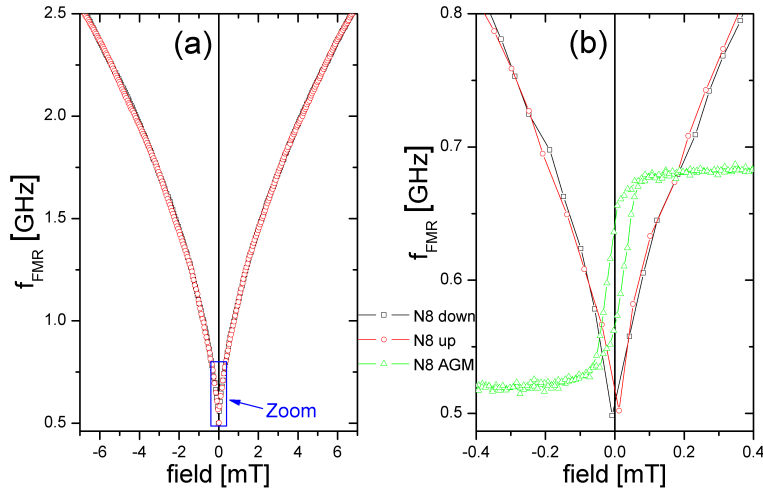


Figure 6.5: (Color online) (a) The resonance frequency  $f_{\text{res}}$  for the sample N8 as a function of the applied external field, when decreasing the field (N8 down, black squares) and increasing again (N8 up, red circles). (b) Zoom on the hysteretic region in (a), additionally the AGM measurement is shown, where the measured magnetic moment is in arbitrary units.

magnetization and the field applied along the easy axis are not necessarily pointing in the same direction. Indeed, it is well evidenced in the AGM measurements by the hysteresis loop that two stable magnetization configurations exist in this field range.

The part of this hysteretic behavior on  $f_{\text{res}}$  is shown in Fig. 6.5 for the sample N8. (a) shows the FMR frequencies for which the field is decreased starting from 8 mT down to  $-8$  mT, with a field step of 0.05 mT (N8 down, black squares). Then the field sweep is reversed (N8 up, red circles). Part (b) shows a zoom on the area marked by a blue square in (a), which comprises the field range showing a bistability of the magnetization orientation. To emphasize the bistability, the AGM measurement is additionally shown in (b), where the y-axis is given in arbitrary units.

The hysteresis is observable in the FMR frequencies around zero applied field. However, it is only visible across two adjacent data points, as the very low coercivity of the permalloy samples (see Tab. 6.2) limits the detection with the smallest available field step of 0.05 mT. The observation of hysteresis is made easier for the CoFeB samples which have a higher coercivity: Fig. 6.6 shows the same data for the sample B8, as Fig. 6.5 for the sample N8. Due to the higher coercivity, the hysteresis in frequency is already clearly visible in Fig. 6.6(a). Within  $|H_{\text{ext}}| < H_c$  two different resonance frequencies are observed, depending on the field history. The good agreement between the coercivity and the AGM measurement is clear in panel (b).

In its present form, Eq. 6.2 does not take the hysteretic behavior into account. In the bistable region, the resonance frequencies can be lower than the zero field resonance. This occurs in small negative fields,  $-H_c < H_{\text{ext}} < 0$ , in which the magnetization remains aligned along the positive field axis but is in a local energy minimum, rather than a global one. We can account for this behavior with a modified

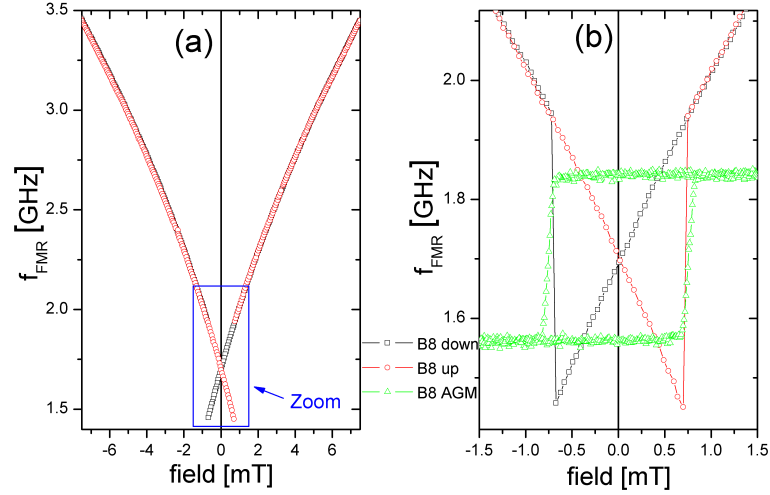


Figure 6.6: (Color online) (a) The resonance frequency  $f_{\text{res}}$  for the sample B8 as a function of the applied external field. (b) Zoom on the hysteretic region in (a) with the AGM measurement in arbitrary units.

form of the Kittel equation,

$$f_{\text{res}} = \frac{\gamma\mu_0}{2\pi} \sqrt{[M_{\text{eff}} + H_{\text{uni}} \pm |H_{\text{ext}}|][H_{\text{uni}} \pm |H_{\text{ext}}|]}, \quad (6.3)$$

where in the bistable region the second resonance frequency is calculated by choosing twice the minus sign in the equation. For  $|H_{\text{ext}}| \geq H_c$ , only the positive sign is required. We remind that this equation is only applicable if the field is applied in parallel to the easy axis.

The coercivity corresponds to the applied fields at which the FMR frequency makes a discontinuous jump. We do not list here the coercivities determined from FMR, as for all samples they correspond to the ones measured by AGM within the precision of the field steps (0.05 mT).

## 6.4 Hysteretic dynamics of exchange biased samples

### 6.4.1 Effective magnetization, anisotropy and exchange bias

The samples exchange biased by IrMn were measured using VNA-FMR in the same manner as the ferromagnetic single layer samples. They were aligned on the setup with the direction of the hysteresis loop shift oriented in the direction of a positive applied field. From the full two-port measurement the susceptibility was calculated. Fig. 6.7 shows the complex susceptibility for the sample I8N11, measured for an applied field of 45.5 mT along the negative field direction. For comparison, the susceptibility of the sample N11 measured under the same applied field is also shown. The main difference is the shift to a higher resonance frequency for the sample I8N11 with respect to N11. To further clarify the influence of the exchange bias on the resonance condition, we extracted the FMR frequencies from a series of measurements with different applied fields.



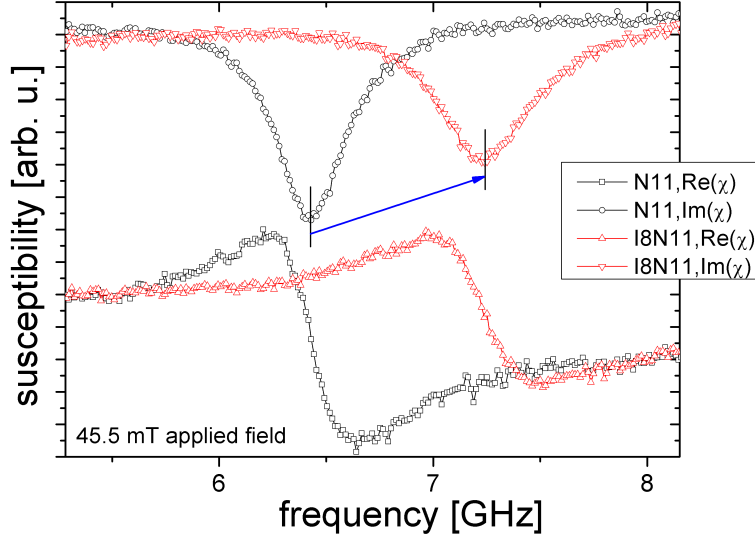


Figure 6.7: (Color online) The complex susceptibility spectra of the samples N11 and I8N11 under an applied field of 45.5 mT. The real and imaginary parts are shifted for clarity. The field is applied along the easy axis, opposite to the direction of the hysteresis shift in the exchange biased sample.

For the ferromagnetic single layers, we found  $f_{\text{res}}$  to be symmetric for positive and negative applied fields, due to the uniaxial anisotropy as expected. As the exchange bias introduces a unidirectional anisotropy, it is necessary to measure at applied fields along the entire axis to observe the entire excitation spectrum, in particular, across the bistable region. In accordance with the AGM measurements, we don't expect a symmetric behavior around zero applied field. This is indeed observed in Fig. 6.8 in which the resonance frequency is shown as a function of the applied field for the same two samples as in Fig 6.7 (N11 and I8N11).

While the curve for the N11 sample is well described by Eq. 6.2, the formula in its present form does not take into account the exchange bias effect. The most prominent feature is the shift of the center of the uniaxial symmetry from zero to the exchange bias field  $H_{\text{eb}}$ . In the simplest model, this is introduced as an additional fixed field  $H_{\text{eb}}$  added to the applied field, which can be easily integrated in the Kittel-formula as follows,

$$f_{\text{res}} = \frac{\gamma\mu_0}{2\pi} \sqrt{[M_{\text{eff}} + H_{\text{uni}} + |H_{\text{ext}} - H_{\text{eb}}|] [H_{\text{uni}} + |H_{\text{ext}} - H_{\text{eb}}|]}. \quad (6.4)$$

An additional feature observed is an increase of the uniaxial anisotropy field  $H_{\text{uni}}$ . It can be seen when comparing the smallest resonance frequencies, at zero applied field for the sample N11 and at  $(H_{\text{ext}} - H_{\text{eb}}) = 0$  for the sample I8N11. At these fields we find

$$f_{\text{res}} = \frac{\gamma\mu_0}{2\pi} \sqrt{[M_{\text{eff}} + H_{\text{uni}}] [H_{\text{uni}}]}. \quad (6.5)$$

Fitting the curve of I8N11 with Eq. 6.4, we find  $\mu_0 M_{\text{eff}} = 0.91$  T,  $\mu_0 H_{\text{uni}} = 3.65$  mT and  $\mu_0 H_{\text{eb}} = 11.1$  mT. The uniaxial anisotropy measured for I8N11 is considerably higher than the one found for the sample N11 without exchange bias (0.43 mT). This increase in  $H_{\text{uni}}$  is in agreement with the measured coercivity increase. It can be attributed to the exchange interaction with those grains in the AFM, whose

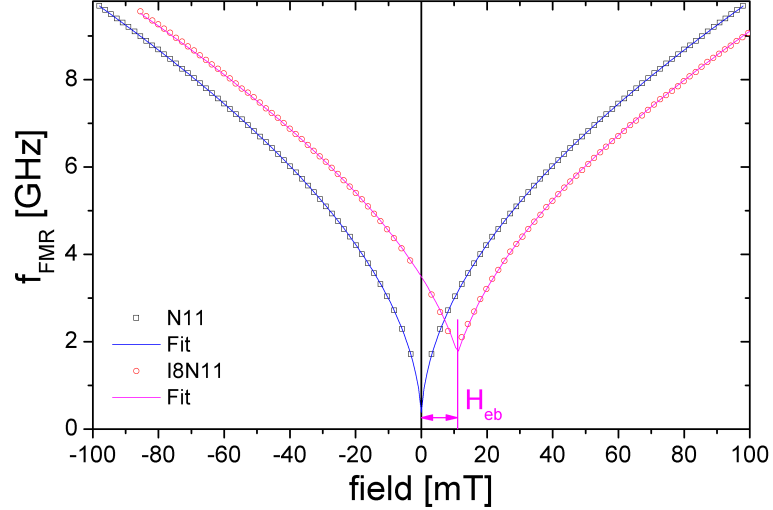


Figure 6.8: (Color online) The resonance frequency  $f_{\text{res}}$  for the sample N11 (squares) and I8N11 (circles) as a function of the applied external field. The fits of the data are represented by plain lines. The extracted exchange bias field of 11.1 mT is marked.

magnetization follows the magnetization of the FM (when considering the model introduced in section 6.1).

The effective magnetization deviates slightly from the sample N11 (see Tab. 6.3). This can be explained by the effect of the different underlying layer on the growth. For the measurement of  $M_s$  in the exchange biased samples, we find a similar difference between the FMR and AGM measurements as that found for the single ferromagnet films. We again attribute this discrepancy to the inaccuracy of the AGM, when used to determine the saturation magnetization.

The extracted exchange bias field agrees well with the AGM measurement. However, we still miss direct evidence for the increased coercivity from the FMR measurements. To emend this, we performed increasing and decreasing field sweeps, as for the single layer samples.

### 6.4.2 Dynamic bistability with exchange bias

In order to study the dynamic bistability in our exchange biased samples, we measured the field-dependent susceptibility as in the case of single ferromagnetic films (see section 6.3.2). In contrast to the single layer samples, a larger field range was required for the exchange bias samples because of the loop shift and larger coercivity. The exchange bias field measured by the AGM was taken to be the origin for the field-swept susceptibility measurements.

Earlier, we presented a modified Kittel-formula for the single ferromagnetic films to include the bistability (from Eq. 6.2 to Eq. 6.3). We likewise include this modification in Eq. 6.4, to find

$$f_{\text{res}} = \frac{\gamma\mu_0}{2\pi} \sqrt{[M_{\text{eff}} + H_{\text{uni}} \pm |H_{\text{ext}} - H_{\text{eb}}|][H_{\text{uni}} \pm |H_{\text{ext}} - H_{\text{eb}}|]}. \quad (6.6)$$

As observed before, we expect only a single resonance frequency for  $|H_{\text{ext}} - H_{\text{eb}}| \geq H_c$ , which is calculated by choosing the plus sign in Eq. 6.6. Between the two coercive fields a second resonance frequency is expected, which should be observed, when the

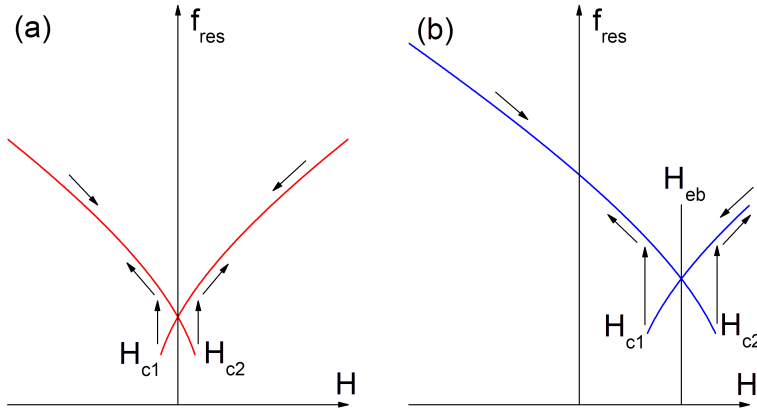


Figure 6.9: Sketch of the exchange bias effect on the resonance frequencies:  $f_{\text{res}}$  as a function of applied field for an unbiased ferromagnet (a) and for a ferromagnet-antiferromagnet bilayer (b). This can be compared to Fig. 6.1 showing the effect on an AGM measurement.

magnetization of the FM and  $(\vec{H}_{\text{ext}} - \vec{H}_{\text{eb}})$  are pointing in opposite directions. It is obtained by choosing the minus signs in the formula. In reference to Fig. 6.1, which illustrates the effect of the exchange bias on an AGM measurement, we plot the expected effect on the FMR measurement as described by Eq. 6.6 in Fig. 6.9.

The corresponding measurement of the sample I8N11 is plotted in Fig. 6.10. To facilitate comparison, the AGM measurement is included in the same figure. Several unexpected features are identified: The crossing of the two upper branches corresponds approximately, but not precisely, to  $H_{\text{eb}}$  determined by AGM. It coincides with the bias field determined from the rough FMR measurement in Fig. 6.8,  $H_{\text{eb}} = 11.1$  mT. The two coercivities show approximate agreement with the AGM measurement. However, it is difficult to determine a precise field value for the switching of the FM, as the frequency does not change very abruptly at the lower coercivity. The strongly visible asymmetry between the resonance frequency values at the two coercivities is unexpected.

Another important feature is the opening between the resonance frequency branches outside the coercivity ( $|H_{\text{ext}} - H_{\text{eb}}| \geq H_c$ ): While only one single resonance frequency should exist for these applied fields, two slightly different ones are clearly distinguished. They slowly converge as the difference between the applied field and the bias field increases, i.e. as  $|H_{\text{ext}} - H_{\text{eb}}|$  increases.

The possibility of a measurement artifact can be excluded, as a qualitatively similar behavior is observed for the other samples containing an IrMn layer. As a second example, Fig. 6.11 shows the measurement of the sample I8B11.

While being qualitatively similar, the shape of the frequency minima does not coincide precisely. Similar differences in shape are found when comparing between the sample I8N8 and the sample I8B8. The frequency changes are more abrupt for the CoFeB samples than for the permalloy samples. This can be attributed to a more coherent switching of the amorphous ferromagnetic layers under the influence of the exchange bias. This can be already deduced from the AGM measurements, where the slopes of the hysteresis loop are steeper for the exchange biased samples with CoFeB than with NiFe.

For the I8B11 sample, there is a clearer disagreement between the crossing point

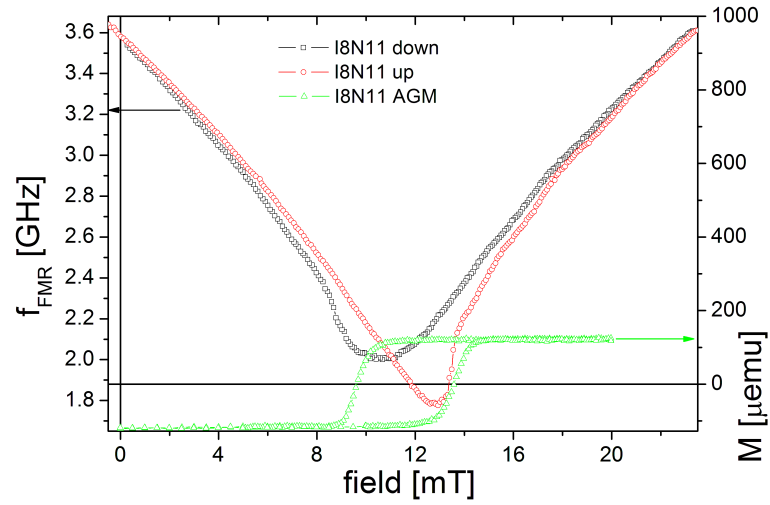


Figure 6.10: (Color online) The resonance frequency  $f_{\text{res}}$  for the sample I8N11 as a function of the applied external field, when increasing the field (I8N11 up, red circles) and decreasing again (I8N11 down, black squares). Additionally the AGM measurement is shown, for easy comparison of the coercivities. The measured magnetic moment is marked on the right.

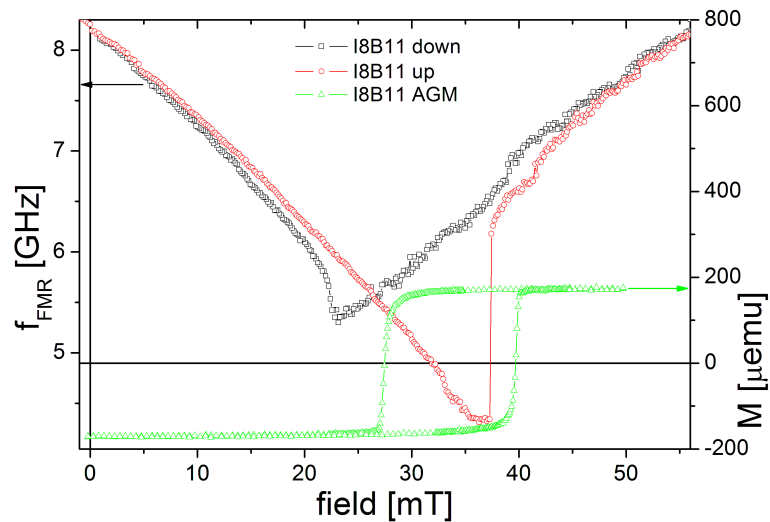


Figure 6.11: (Color online) The resonance frequency  $f_{\text{res}}$  for the sample I8B11 as a function of the applied external field. Additionally the AGM measurement is shown.

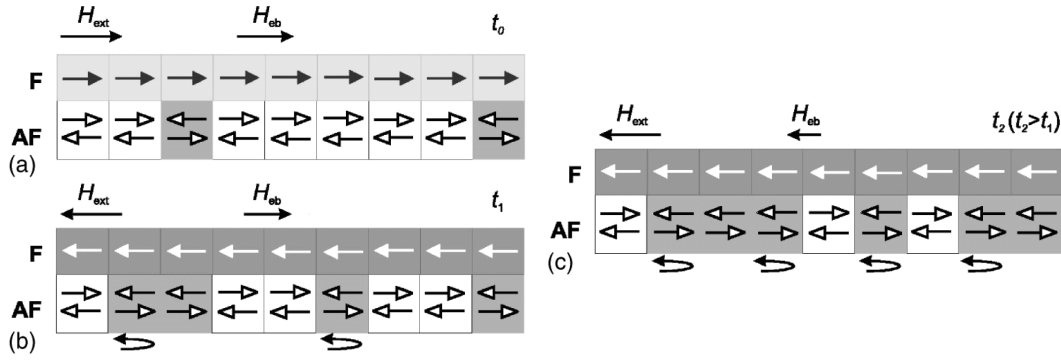


Figure 6.12: (a) Schematic of the initial spin configuration. (b) Magnetization configuration after reversing the FM magnetization. (c) With increasing measurement time more AFM grains reverse magnetization, the exchange bias field changes sign, after [21].

of the two upper branches and the bias field determined by AGM. Also, while the range between the two coercivities is approximately equal for FMR and AGM, both coercive fields are at higher applied fields in the AGM measurement. Again, outside the coercive fields, still two resonance frequencies exist, which approach one another with increasing distance from the exchange bias field.

## Discussion

Clearly, the simple model introduced in section 6.1 is not suited to explain the observations. There, we considered independent grains of a polycrystalline AFM, contributing either to the unidirectional anisotropy (AFM anisotropy > interface coupling, grain magnetization unchanged) or to the coercivity increase (grain magnetization rotates with FM). However, we were not able to fit the measurement data of any biased sample with Eq. 6.6, under the assumption of a unique and fixed bias field.

A suitable explanation can be found in another experiment: Xi et al. determined the bias field of NiFe/IrMn bilayer samples by magneto-optic Kerr effect (Moke) magnetometry [20]. The bias field was extracted as the center field of the hysteresis loops. The extracted exchange bias field as well as the coercivity were observed to depend on the measurement speed: Increasing the sweep rate led to an increase in the extracted bias field.

In the model applied to explain the observation, several grains form domains in the AFM. When the magnetic field is swept during the measurement of the hysteresis loop, the magnetization of the FM is reversed. In order to minimize the coupling energy at the interface, which is enhanced after the reversal of the FM, some of the domains contributing to the unidirectional exchange bias relax by reversing, too. The bias field becomes smaller. As this is a thermally activated process, it is consequently time-dependent. Increasing the sweep rate, a lesser number of AFM domains changes their orientation, due to the shorter time, that the FM stays in the reversed position during the loop measurement. Hence, relatively more AFM domains still contribute to the exchange bias, and a higher bias field is measured for a faster loop. With decreasing sweep rate on the other hand, an increasing amount of grains can relax.

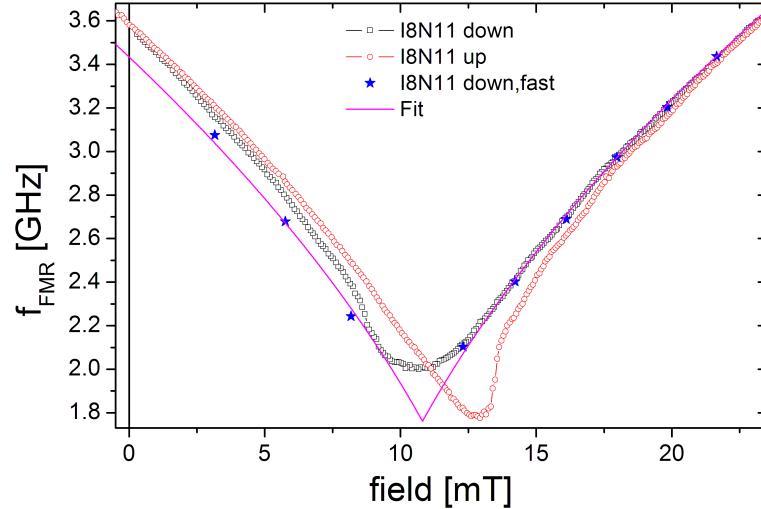


Figure 6.13: (Color online) The ascending (up) and descending (down) branches of the resonance frequency for the sample I8N11. Additionally the descending branch (down) of the quick measurement in Fig. 6.8 is shown, together with a fit.

A time dependence of the observed exchange bias was also found by McCord et al. by AGM magnetometry [21]. By applying a field greater than the exchange bias and in the opposite direction for several hours, they even managed to inverse the exchange bias direction. This process is usually termed field annealing and is illustrated in Fig. 6.12, after [21]. In the initial situation the exchange bias field and the external field were aligned in the same direction (a). As the FM was aligned in the opposite direction of the AF spins at the interface (b), the time span was sufficient to allow them to reverse, be activated thermally, thereby leading to a decrease in the interface energy. After several hours a sufficiently high fraction of the AFM domains had reversed, so that the subsequent hysteresis loop measurement showed an exchange bias in the opposite direction (c). We remark that a complete reversal of the exchange bias direction was surely only possible due to the low IrMn layer thickness used ( $t_{\text{IrMn}} = 3.0$  nm). The small thickness limits the size of the AFM grains and hence their thermal stability.

As we cannot fit our data with a single fixed exchange bias field, we hypothesize a changing bias field during the measurement: One single FMR measurement takes between 9 and 40 seconds, depending on the number of frequencies scanned. This yields one data point, i.e. one resonance frequency, at one applied field. Due to the closely spaced data points required to reconstruct the whole hysteresis (see Fig. 6.10 and Fig. 6.11), the measurement duration is up to 8 hours. This allows the domains in the AFM to adapt to the reversal of the FM and to minimize the interface energy by reversing likewise.

The time dependence can be shown, by simply comparing the “slow” FMR hysteresis measurement of the sample I8N11 presented in Fig. 6.10 and the “fast” one already presented in Fig. 6.8. The latter took 1.5 h to measure, but the few data points in the field range between 0 and 25 mT were measured in less than 5 min. Both measurements are plotted in Fig. 6.13. The fast measurement (blue stars) has to be compared to the branch ‘I8N11 down’ of the slow hysteresis measurement (black squares), as the field was decreased starting from high positive values. The

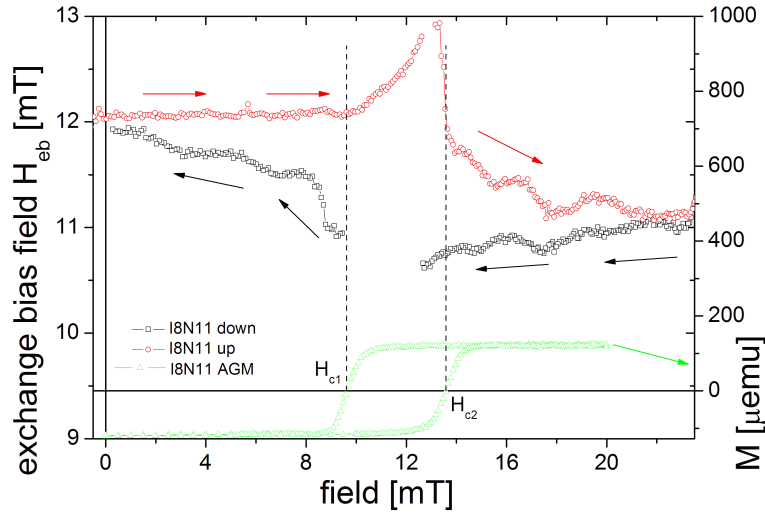


Figure 6.14: (Color online) The exchange bias field calculated from the data in Fig. 6.10 using Eq. 6.6. Additionally, the AGM measurement is shown. Between the coercivities,  $H_{\text{eb}}$  could not be determined reliably.

data points coincide, as long as the applied field is higher than the bias field. As the applied field decreases further after having passed below  $H_{\text{eb}}$ ,  $f_{\text{res}}$  is higher for the slow measurement.

As the measurement lasts longer, AFM domains reverse back through thermal activation to accommodate to the reversed FM magnetization. The exchange bias field increases again.  $|H_{\text{ext}} - H_{\text{eb}}|$  in Eq. 6.6 increases with the bias field which leads to increased resonance frequencies.

If we assume the bias field extracted from the AGM measurement to be correct, we can resolve the absolute value in Eq. 6.6:  $|H_{\text{ext}} - H_{\text{eb}}|$ . We resolve additionally the  $\pm$  signs in Eq. 6.6, depending on the upper and lower frequency branch inside the coercive fields. This permits us to evaluate  $H_{\text{eb}}$  from  $f_{\text{res}}$ , assuming  $\mu_0 M_{\text{eff}} = 0.91$  T and a constant anisotropy field  $\mu_0 H_{\text{uni}} = 3.65$  mT. These are the data extracted from Fig. 6.8.

The bias field as a function of applied field is plotted in Fig. 6.14. Additionally, the AGM measurement is included, where the coercive fields are marked. Between the two coercivities, the bias field could not be determined reliably. This is attributed to the assumption that  $H_{\text{uni}}$  is a constant, which becomes invalid as some AFM domains contributing to the unidirectional anisotropy for low applied fields follow the magnetization of the FM. In addition, the magnetization of the FM is likely non-uniform at these applied fields.

The curve in Fig. 6.14 agrees well with the presented model. Increasing the applied field starting from 0 T,  $H_{\text{eb}}$  stays constant. At  $H_{\text{c2}}$ , the bias field starts to decrease, after the reversal of the FM magnetization. When the applied field is decreased again, we still observe a slight, but less pronounced decrease. At  $H_{\text{c1}}$ , the tendency is inverted and  $H_{\text{eb}}$  increases again, after the second reversal of the FM magnetization. When reaching 0 T applied field, the bias field almost reached again its initial value. Thus, the bias field varied in the range of [10.8 mT; 12.1 mT] during the measurement, explaining why we observe two different resonance frequencies outside the coercive fields.

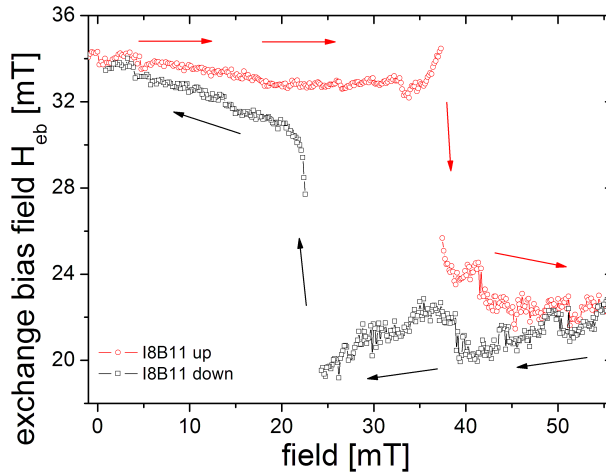


Figure 6.15: (Color online) The exchange bias field calculated for the sample I8B11 from the data in Fig. 6.11 using Eq. 6.6.  $H_{\text{eb}}$  could be better resolved between the coercivities than for the sample I8N11 (see Fig. 6.14).

Similar results (as plotted in Fig. 6.14 for the sample I8N11) were obtained for all samples containing an IrMn layer. As a second example, the exchange bias calculated for the I8B11 sample is plotted in Fig. 6.15, where we assumed  $\mu_0 M_{\text{eff}} = 1.48$  T and a constant anisotropy field  $\mu_0 H_{\text{uni}} = 17$  mT. During the measurement the bias field varied in the range of [19.3 mT; 34.3 mT]. We had already noticed the better defined coercivities in the resonance frequencies in Fig. 6.11. This was mainly attributed to a more coherent rotation of the FM than in the sample I8N11. This also allowed the exchange bias field to be resolved for applied fields between the coercivities, except at fields very close to them. In contrast to the sample I8N11, we find that the shape between the coercive fields coincides well with the shape observed outside. Abrupt changes only take place directly at the coercivities. The observed behavior is in agreement with the suggested model.

In summary, we found that the effective exchange bias changes depending on measurement time and field history. The values for  $H_{\text{eb}}$  in Tab. 6.2 extracted from the AGM hysteresis loops can thus be considered “correct” in a sense. However, it is always necessary to provide the exact measurement conditions together with the values.

### 6.4.3 Conclusion

In conclusion, we found that it is difficult to give a precise value for the exchange bias field, following the commonly employed definition in which  $H_{\text{eb}}$  is defined as the field in the center between the coercive fields in a hysteresis loop measurement. This is restricted by some of the AFM domains, which normally contribute to the magnitude of the bias field, but which can be reversed through thermal activation, once the FM magnetization is reversed by the externally applied field. Therefore, the effectively exerted bias field decreases, when the magnetization of the FM is inversed with respect to the exchange bias direction, for a sufficiently long time.

The same is true for the coercive fields. It is also difficult to give precise values for  $H_c$ , as, e.g., an AGM hysteresis loop does not provide information on the magnitude of the  $H_{\text{eb}}$ , when sweeping past one coercive field or the other. For a low



measurement speed, the coercive fields will be necessarily influenced by a changing value of the bias field.

We can therefore conclude that any extracted value of the bias field or of the coercivities of an exchange biased sample should always be accompanied by a precise description of the measurement conditions at the same time.

We still add that the observed phenomenon is independent of the measurement technique. However, it cannot always be observed directly: AGM and Moke hysteresis loops only reveal information about the magnetic moments of the FM. There is no evidence if the exchange bias field leading to one coercivity is the same one, as the one acting on the FM during the measurement of the other coercivity. Under well-chosen measurement conditions, it is still possible to gain insight on the underlying processes, as demonstrated in [20] and [21].

On the contrary, the VNA-FMR measurements also allowed to draw direct conclusions: they do not only depend on the alignment of the magnetic moments in the FM, but on the total energy of the examined system. Therefore, it is possible to extract some information on the state of the AFM, even when the FM is already saturated.  $H_{\text{eb}}$  can be calculated from each FMR resonance frequency, and it becomes possible to give a range of values that the exchange bias field adopts.

# Chapter 7

## High-frequency magnetization dynamics of CoFeB alloys

In the first section of this chapter we motivate the increasing interest in CoFeB alloys, which has recently become one of the hottest materials in nanospintronics (§7.1). Then we describe the thin film samples prepared for this study (§7.2). We continue by detailing the results of the performed FMR measurements, in particular on the effective magnetization and the damping parameter (§7.3). The subsequent section analyzes possible consequences of our findings, providing e.g. plausible explanations for an unresolved observation concerning current induced magnetization switching in CoFeB systems (§7.4). Apart from the FMR resonance, a perpendicular standing spinwave resonance is observed, allowing to calculate the exchange stiffness constants of the samples (§7.5). The chapter is concluded by a short summary (§7.6).

### 7.1 Interest in CoFeB alloys

Magnetic tunnel junctions (MTJs) constitute the primary application of the tunnel magnetoresistance (TMR) effect. Obtaining high TMR facilitates the operation of MTJs as field sensors or in magnetic memory cells. High TMR ratios exceeding largely the ones observed using amorphous aluminium oxide tunnel barriers were predicted from first-principles electronic structure calculations as early as 2001 for a fully epitaxial MgO tunnel barrier [213]. Indeed, for an epitaxial Fe/MgO/Fe junction it was estimated that the TMR ratio could be higher than 1000% [214]. First experimental realizations of these systems achieved TMR ratios exceeding the previous limits, e.g. up to 180% was reached in 2004 with MgO tunnel barriers and highly ordered MBE-grown Fe electrodes [215].

A later theoretical prediction foresaw even several times larger magnetoresistance, by replacing the Fe layers with Co or CoFe [216]. In the following, CoFeB was discovered as the material of choice: in 2005 CoFeB/MgO/CoFeB MTJs allowed to achieve a TMR of 355% at room temperature [217]. Also in the subsequent years, the “record” in TMR ratio was attained by MTJs employing CoFeB: 472% were achieved in 2006 [218], still surpassed with 500% at room temperature and 1010% at 5 K in 2007. While permitting a high TMR, CoFeB offers several other favorable properties: It is magnetically softer than Fe or CoFe, being better suited for most applications. It also favorably substitutes soft NiFe alloys: For these permalloys, an ultrathin CoFe layer is generally inserted at the oxide interface to achieve a

higher tunnelling spin polarization. This is no longer necessary, when replacing the permalloy/CoFe combination with CoFeB alloys, as it already shows a high spin polarization [219]. Additionally, its magnetization is higher than for permalloy, which results in an improved thermal stability.

Both transport and hysteresis properties benefit from the amorphous nature of CoFeB: being amorphous, CoFeB is usually free from pinning centers, having thus quite soft magnetic properties [220]. In addition, the amorphous structure can lead to very smooth CoFeB interfaces, which are ideal for the subsequent growth of ultrathin tunnel barriers [209], which makes CoFeB an ideal electrode material when MTJs with low resistance area (RA) products are targeted. Besides, the accessible low RA in combination with the high spin polarization makes these CoFeB/MgO combinations promising candidates for current-driven magnetization switching at low current densities [219].

Due to the strong interest, over the past years an intense research activity has been directed on characterizing CoFeB materials. Data on structural characterization can be found easily [221, 156, 222, 223]. However, little is known about their dynamic magnetic properties, e.g. Gilbert damping and exchange stiffness, which are of great importance to assess the technological potential of CoFeB alloys. They are also needed for reliable micromagnetic descriptions of CoFeB-based devices and the damping is needed to estimate the suitability for high speed switching applications.

In this chapter we investigate the magnetic properties of CoFeB, including effective magnetization, Gilbert damping and exchange stiffness and the thickness dependence thereof. We also report on the evolution of these magnetic properties with post-growth thermal treatments. The results presented in this chapter were published in [153].

## 7.2 Examined samples

The INESC MN research institute is well-known for its expertise in magnetic device fabrication. In an effort to improve the structure of magnetic tunnel junctions, the integration of smooth CoFeB layers was explored. Thus, all sample fabrication for this study was carried out by Susana Cardoso de Freitas and Ricardo Ferreira at the INESC Microsystems and Nanotechnologies institute directed by Paulo Freitas, being a partner in the RTN Ultrasmooth.

The examined CoFeB samples are grown by ion beam deposition (Nordiko 3000 system) from a target with 10 at. % boron content and a Co:Fe ratio of 80:20 [154]. The composition is maintained to  $9.9 \pm 1$  % of boron [155] in the deposited films. All samples were deposited on 1x1 inch glass substrates and covered by 3 nm Ru capping layers, as a protection against oxidation. Samples with four different thicknesses of the Co<sub>72</sub>Fe<sub>18</sub>B<sub>10</sub> layer were prepared: 5 nm, 10 nm, 25 nm and 40 nm. Additionally, a Co<sub>80</sub>Fe<sub>20</sub> sample without boron content having a thickness of 40 nm was deposited as a reference sample.

The as-deposited Co<sub>72</sub>Fe<sub>18</sub>B<sub>10</sub> films are amorphous. A study on magnetic tunnel junctions containing similar Co<sub>72</sub>Fe<sub>18</sub>B<sub>10</sub> films with a thickness of 20 nm showed, that annealing leads to a strong (111) fcc texture. This is illustrated in the high angle X-ray diffraction measurement shown in Fig. 7.1(a), after [220]: for the as-deposited Co<sub>72</sub>Fe<sub>18</sub>B<sub>10</sub> no signal is observed, confirming the amorphous state. A 20 nm Co<sub>80</sub>Fe<sub>20</sub> reference sample shows a peak at 45.3°, corresponding to its tex-

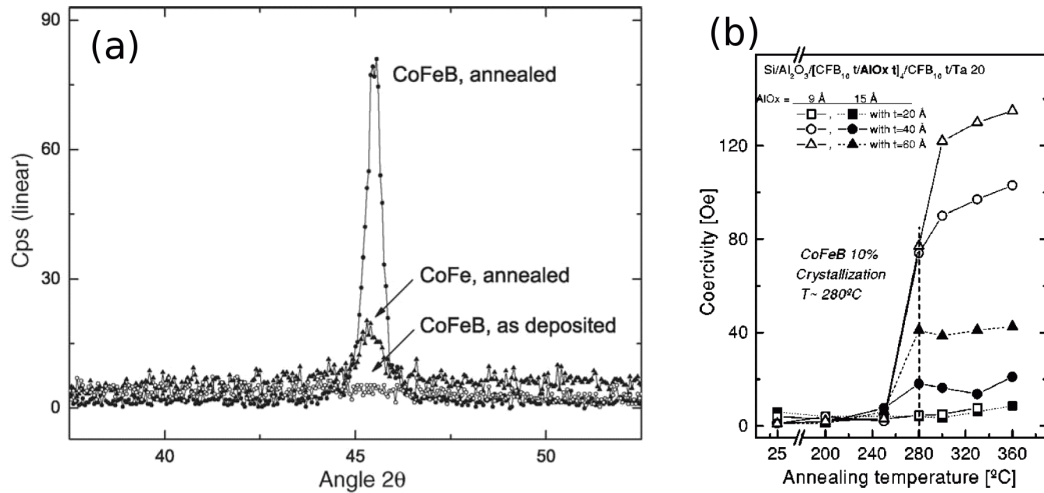


Figure 7.1: (a) X-rays measurements of Si/SiO<sub>2</sub>/CoFe or CoFeB 20 nm thick films, after [220]. Only after annealing at 280°C, the CoFeB with 10 at. % boron content shows a signal. (b) The coercivity of Co<sub>72</sub>Fe<sub>18</sub>B<sub>10</sub> multilayer samples as a function of annealing temperature, after [156]. The multilayers have the structure Si/Al<sub>2</sub>O<sub>3</sub>(100)/[CoFeB<sub>10</sub>(t)/AlOx(0.9,1.5)]<sub>4</sub>/CoFeB<sub>10</sub>(t)/Ta(3), where  $t = 2, 4, 6$  nm.

ture. The peak obtained from the annealed Co<sub>72</sub>Fe<sub>18</sub>B<sub>10</sub> sample is even higher. The annealing temperature was 280°C. At this temperature, the structure of the Co<sub>72</sub>Fe<sub>18</sub>B<sub>10</sub> evolves in a fcc polycrystal [156]. High-resolution electron microscopy of both Co<sub>80</sub>Fe<sub>20</sub> layers and annealed Co<sub>72</sub>Fe<sub>18</sub>B<sub>10</sub> layers suggested crystals with similar grain sizes of  $\approx 10$  nm [155].

The annealing temperature necessary to trigger the phase change was determined in another study shown in Fig. 7.1(b), after [156]: the plot shows the coercivity of a Co<sub>72</sub>Fe<sub>18</sub>B<sub>10</sub> multilayer sample extracted from vibrating sample magnetometer measurements, as a function of annealing temperature. The onset of crystallization is clearly indicated at 280°C by a strong coercivity increase.

To study the effect of this annealing induced phase change on the magnetic properties, the samples were diced after deposition. An as-deposited piece of each sample was conserved, a second piece was annealed for 30 minutes in vacuum ( $10^{-6}$  Torr), under a magnetic field of 0.5 T, also applied during heating and cooling down.

## 7.3 Ferromagnetic resonance measurements

All as-deposited and annealed samples were characterized with the Vector Network Analyzer FerroMagnetic Resonance (VNA-FMR) technique described in section 2.3. Exemplarily, the real and imaginary part of the complex susceptibility measured for the 40 nm thick Co<sub>72</sub>Fe<sub>18</sub>B<sub>10</sub> film under an applied field of 41.5 mT is plotted in Fig. 7.2(a). Susceptibility spectra were recorded for in-plane applied fields from 0 up to 110 mT. Each spectrum measured for one applied field contains two quantities characterizing the uniform precession: the ferromagnetic resonance frequency and the linewidth. We describe in the following the information we can deduce from these two quantities.

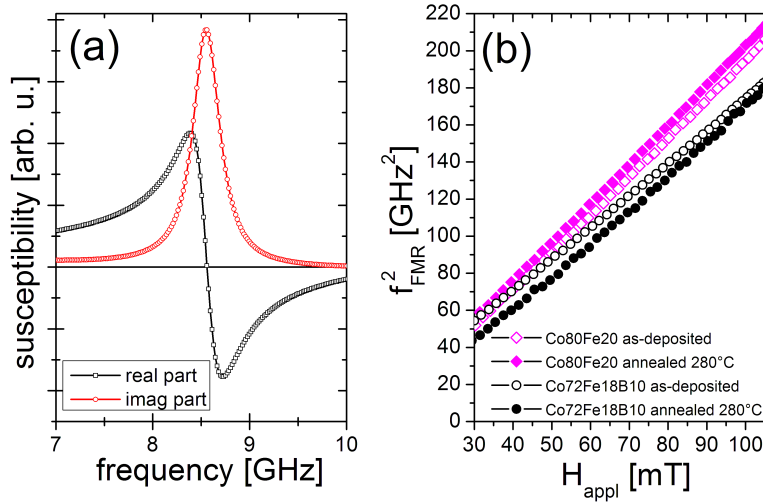


Figure 7.2: (Color online) (a) Representative measurement of the complex susceptibility of the 40 nm thick as-deposited Co<sub>72</sub>Fe<sub>18</sub>B<sub>10</sub> sample at 41.5 mT applied field showing the uniform precession mode. (b) Squared resonance frequency of the uniform precession mode versus applied field for the 40 nm Co<sub>80</sub>Fe<sub>20</sub> and Co<sub>72</sub>Fe<sub>18</sub>B<sub>10</sub> layers, as-deposited and annealed at 280°C.

### 7.3.1 Results on the resonance frequency $f_{\text{res}}$

The square of the FMR frequency as a function of the applied field is shown for all samples having a thickness of 40 nm in Fig. 7.2(b). All samples examined in this study exhibit a uniaxial in-plane anisotropy. The applied field dependence of the resonance frequency was reported in Eq. 2.50, when the easy axis is aligned with the external field. Squaring the equation, we find

$$f_{\text{FMR}}^2 = \left( \frac{\gamma\mu_0}{2\pi} \right)^2 [M_{\text{eff}} + H_{\text{ext}} + H_{\text{uni}}] [H_{\text{ext}} + H_{\text{uni}}], \quad (7.1)$$

where  $H_{\text{ext}}$  is the applied field and  $H_{\text{uni}}$  is the contribution due to the crystalline anisotropy.  $M_{\text{eff}}$  is the effective magnetization, i.e. the saturation magnetization reduced by surface perpendicular anisotropy field terms.  $\gamma$  is the gyromagnetic factor, proportional to the spectroscopic splitting Lande factor  $g$ , which we assumed to be 2.14 (determined for CoFe in [55]). Note that this assumption of fixed  $g$  factor due to the unavailability of a precise value is the main source of error ( $\pm 2\%$ ) in our reported values of the magnetic properties.

We consider the square of  $f_{\text{FMR}}$ , as it is approximately linear with  $H_{\text{ext}}$  (see section 2.3.3). Fitting the data in Fig. 7.2(b) with Eq. 7.1, we obtain the effective magnetization as a function of layer thickness, composition and annealing state. For all studied thicknesses and thermal treatments, the anisotropy field  $H_{\text{uni}}$  was found to be negligibly small compared to  $H_{\text{ext}}$ , confirming previous studies dedicated specifically to anisotropy [209].

For an easy comparison, all  $M_{\text{eff}}$  values are also collected in Tab. 7.1. As other authors have already concluded [155], we confirm that the addition of boron reduces the effective magnetization, for instance from 2.14 T (Co<sub>80</sub>Fe<sub>20</sub>) to 1.77 T (Co<sub>72</sub>Fe<sub>18</sub>B<sub>10</sub>) for the as-deposited 40 nm thick layers. Annealing only marginally affects the effective magnetization of the 40 nm Co<sub>80</sub>Fe<sub>20</sub> film, increasing it to  $\mu_0 M_{\text{eff}} = 2.22$  T. In contrast the annealing at 280°C triggered a larger change in the 40 nm Co<sub>72</sub>Fe<sub>18</sub>B<sub>10</sub>

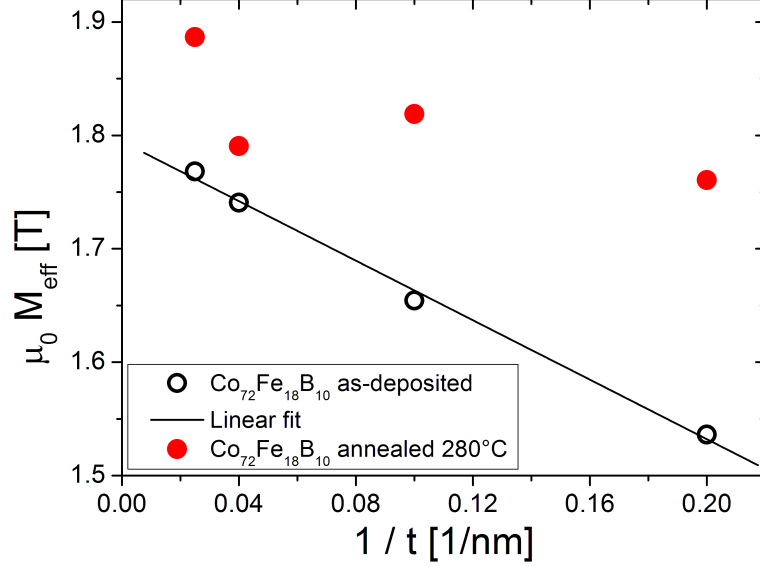


Figure 7.3: The effective magnetization as a function of the inverse layer thickness for the as-deposited (open symbols) and annealed (filled)  $\text{Co}_{72}\text{Fe}_{18}\text{B}_{10}$  samples. A linear dependence is found for the as-deposited samples (marked by the straight line).  $M_{\text{eff}}$  is obtained by fitting the field-dependence of the uniform resonance frequency.

layer, increasing  $\mu_0 M_{\text{eff}}$  to 1.9 T. A similar annealing induced magnetization increase was ascertained for all examined thicknesses of the  $\text{Co}_{72}\text{Fe}_{18}\text{B}_{10}$  layers.

In Fig. 7.3 the effective magnetization is plotted as a function of the inverse layer thickness, resolving the thickness dependence of the  $\text{Co}_{72}\text{Fe}_{18}\text{B}_{10}$  layers: In the as-grown state,  $M_{\text{eff}}$  scales linearly with the inverse layer thickness ( $1/t$ ). This is well described by Eq. 1.24, which gives

$$\mu_0 M_{\text{eff}} = \mu_0 M_s - \frac{2K_{\perp}}{M_s} \left( \frac{1}{t} \right). \quad (7.2)$$

This indicates the presence of a significant surface anisotropy term, which is determined by the fit to  $K_{\perp} = 9.4 \times 10^{-4} \text{ J/m}^2$ . The fit also yields the saturation magnetization of bulk  $\text{Co}_{72}\text{Fe}_{18}\text{B}_{10}$ :  $\mu_0 M_s = 1.79 \text{ T}$ . While  $M_{\text{eff}}$  is still thickness dependent after annealing, the interface anisotropy could not be observed unambiguously. However, the increase of the effective magnetization, observed after annealing for all  $\text{Co}_{72}\text{Fe}_{18}\text{B}_{10}$  samples, is a clear indication for a structural change. This corresponds to the expected crystallization at 280°C.

### 7.3.2 Results on the linewidth $\Delta f$

The frequency linewidth allows to draw conclusions on the Gilbert damping parameter  $\alpha_{\text{Gil}}$  of the samples. As calculated in Eq. 1.50, the two are related as

$$\Delta f_{\text{Gil}} = \alpha_{\text{Gil}} \frac{\gamma \mu_0}{2\pi} [M_{\text{eff}} + 2(H_{\text{ext}} + H_{\text{uni}})]. \quad (7.3)$$

However,  $\Delta f_{\text{Gil}}$  and the measured linewidth  $\Delta f_{\text{mea}}$  do not necessarily coincide. This was already analyzed in section 2.3.3, where we found a strongly increased linewidth

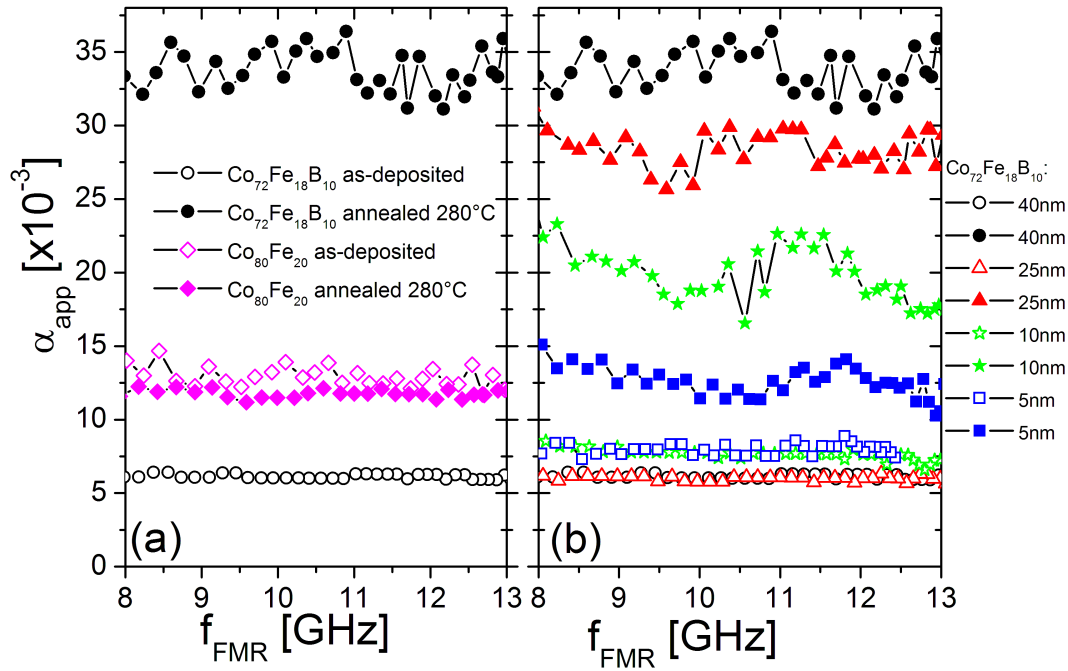


Figure 7.4: (Color online) The apparent damping parameter  $\alpha_{\text{app}}$  versus the FMR frequency. Open symbols represent as-deposited layers, filled symbols represent layers annealed at  $280^\circ\text{C}$ . (a) 40 nm  $\text{Co}_{80}\text{Fe}_{20}$  (diamond) and 40 nm  $\text{Co}_{72}\text{Fe}_{18}\text{B}_{10}$  (circle) layers; to note: the particularly low  $\alpha_{\text{app}}$  of as-deposited  $\text{Co}_{72}\text{Fe}_{18}\text{B}_{10}$  (o) and the increase by a factor of 5 (●) after annealing (leading to crystallization). (b) 5 (square), 10 (star), 25 (triangle) and 40 nm (circle)  $\text{Co}_{72}\text{Fe}_{18}\text{B}_{10}$ , as-deposited and annealed.

at low resonance frequencies. Indeed, this was demonstrated on the data of one of the samples examined in this study: in Fig. 2.19(b) we showed that the linewidth increase at low frequency can be well fit using Eq. 2.59. The presented data belongs to the 40 nm thick  $\text{Co}_{72}\text{Fe}_{18}\text{B}_{10}$  sample. The increased linewidth is not related to the intrinsic Gilbert damping, but to nonuniform spin wave excitation [142] and inhomogeneous broadening [10]. Both the linewidth contributions due to the excitation of finite wave vector spin waves and due to the non-uniformities of the magnetic properties in the measured volume decrease approximately with the square of the inverse resonance frequency (see Eqs. 2.53 and 2.57). Therefore, we simply avoid these contributions by extracting the damping from the linewidth data only at high resonance frequencies ( $> 8$  GHz). This corresponds to higher applied fields ( $> 60$  mT), where they become negligibly small (see Fig. 2.20).

For these frequencies, our measured resonance linewidths  $\Delta f_{\text{mea}}$  seem to be mostly governed by the phenomenological Gilbert damping. For the sake of brevity and to denote the difference to the ideal  $\Delta f_{\text{Gil}}$ , we will speak below about the “apparent” damping parameter  $\alpha_{\text{app}}$ , as calculated according to the inverse of Eq. 7.3:

$$\alpha_{\text{app}} = \frac{2\pi\Delta f_{\text{mea}}}{\gamma\mu_0 [M_{\text{eff}} + 2(H_{\text{ext}} + H_{\text{uni}})]}. \quad (7.4)$$

We have collected in Fig. 7.4 the apparent damping parameters measured between 60 and 100 mT applied field: 7.4(a) compares  $\alpha_{\text{app}}$  of the as-deposited (open symbols) and annealed (filled symbols) 40 nm  $\text{Co}_{80}\text{Fe}_{20}$  (diamond) and 40 nm

Table 7.1: Overview of the apparent damping parameter  $\alpha_{\text{app}}$  and the effective magnetization  $M_{\text{eff}}$  for the as-deposited and annealed  $\text{Co}_{72}\text{Fe}_{18}\text{B}_{10}$  layers of different thicknesses, and 40 nm of  $\text{Co}_{80}\text{Fe}_{20}$ .

$\text{Co}_{72}\text{Fe}_{18}\text{B}_{10}$ as-deposited	5 nm	10 nm	25 nm	40 nm
$\mu_0 M_{\text{eff}}$ [T]	1.54	1.65	1.74	1.77
$\alpha_{\text{app}}$	0.008	0.008	0.006	0.006
$\text{Co}_{72}\text{Fe}_{18}\text{B}_{10}$ annealed	5 nm	10 nm	25 nm	40 nm
$\mu_0 M_{\text{eff}}$ [T]	1.76	1.82	1.79	1.89
$\alpha_{\text{app}}$	0.012	0.019	0.028	0.032
40 nm $\text{Co}_{80}\text{Fe}_{20}$	as-deposited		annealed	
$\mu_0 M_{\text{eff}}$ [T]	2.14		2.22	
$\alpha_{\text{app}}$	0.013		0.012	

$\text{Co}_{72}\text{Fe}_{18}\text{B}_{10}$  (circle) films, while 7.4(b) only shows  $\text{Co}_{72}\text{Fe}_{18}\text{B}_{10}$ , but all examined thicknesses (5 (square), 10 (star), 25 (triangle) and 40 nm (circle)). In order to reduce the influence of measurement noise, the values of the apparent damping parameters  $\alpha_{\text{app}}$  (summarized in Table 7.1) are extracted by averaging between 60 mT and 100 mT. The standard deviation never exceeded 0.002. Within this experimental accuracy, the damping of the 40 nm  $\text{Co}_{80}\text{Fe}_{20}$  films was not affected by the annealing and remained  $\alpha_{\text{app}} = 0.013$ ; This is expected, as  $\text{Co}_{80}\text{Fe}_{20}$  is already crystalline before thermal annealing, and stays so upon annealing. For the amorphous 40 nm  $\text{Co}_{72}\text{Fe}_{18}\text{B}_{10}$  film a strikingly low value of  $\alpha_{\text{app}} = 0.006$  was measured. This  $\alpha_{\text{app}}$  compares well with that of high quality permalloy [224]. Another important conclusion is that the apparent damping parameter  $\alpha_{\text{app}}$  of the as-deposited  $\text{Co}_{72}\text{Fe}_{18}\text{B}_{10}$  layers is not thickness dependent, remaining equally low within our experimental accuracy.

Conversely, annealing the  $\text{Co}_{72}\text{Fe}_{18}\text{B}_{10}$  films, inducing crystallization, resulted in a strong increase of the apparent damping parameters  $\alpha_{\text{app}}$ . For instance, the damping of the 40 nm film undergoes an increase from 0.006 before annealing (= amorphous) to 0.032 after annealing (= polycrystalline). More generally the annealing procedure resulted in an increase of damping for all  $\text{Co}_{72}\text{Fe}_{18}\text{B}_{10}$  samples. This increase in  $\alpha_{\text{app}}$  is less pronounced at low film thicknesses. However, even for the thinnest layer (5 nm), a significant 50% increase is still measured.

Surface contributions would give an inverse thickness dependence of damping, for example 2-magnon scattering mediated by surface roughness [11] or spin-pumping (see Eq. 1.81 in section 1.5.4). As such a dependence is not observed, correspondingly contributions due to the surface/interface can be estimated as low. Therefore, we can clearly relate the increase observed in the apparent damping to the phase change taking place in the volume of the  $\text{Co}_{72}\text{Fe}_{18}\text{B}_{10}$  layer upon thermal annealing.

For further explanations on the thickness dependence of the apparent damping parameter after annealing, we refer to a recent study giving evidence on the crystal structure in CoFeB pseudo-spinvalves upon thermal annealing [110]: using high resolution transmission electron microscopy CoFeB<sub>20</sub> layers with different Co to Fe ratios and different thicknesses were examined. Thin layers (3 nm) always crystallized fully after annealing at 450°C for 1 h, independent of the Co-Fe ratio. Thicker layers (10 nm) in contrast showed only partial crystallization: the sample with a higher Co content, which is closer to our material, was  $(\text{Co}_{75}\text{Fe}_{25})_{80}\text{B}_{20}$ . For



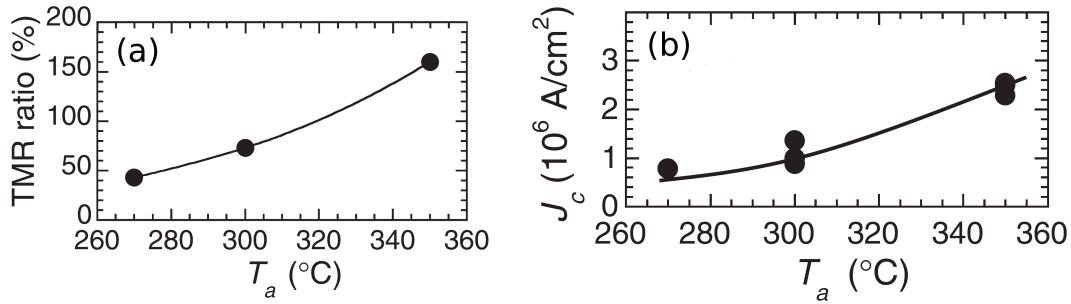


Figure 7.5: (a) The TMR ratio observed for a CoFeB/MgO/CoFeB magnetic tunnel junction (MTJ) as a function of annealing temperature  $T_a$ . (b) The critical current  $J_c$  of the same MTJ sample as a function of  $T_a$ . Both plots after [219].

this sample, a granular structure embedded in an amorphous matrix was observed after annealing, with additionally a large spacing between the individual crystallites (50 nm). Such an increasingly non-uniform crystallization with increasing layer thickness could explain the increasing apparent damping, which we measured with increasing thickness. However, the proposed interpretation is based on the presence of an MgO barrier layer in contact to the CoFeB layers. In [110], the MgO layer is assumed to act as a sink for B and therefore to promote crystallization. For our samples, no such layer is present. In order to prove unambiguously the transferability of the presented interpretations on our results, the examination of the microstructural evolution of our samples is desirable.

## 7.4 Expected consequences of our results on spin-torque magnetization switching

In the previous section, we found a very low value of  $\alpha_{\text{app}} = 0.006$  for the magnetization damping in the as-deposited  $\text{Co}_{72}\text{Fe}_{18}\text{B}_{10}$  films. Upon annealing at  $280^\circ\text{C}$ , the apparent damping increased (see Fig. 7.4(b)).

In the following, we discuss conclusions drawn from these results, by applying them to a study of magnetic tunnel junctions (MTJs): Hayakawa et al. [219] published values as low as  $7.8 \times 10^5$  A/cm<sup>2</sup> for the critical current  $J_c$  in current-driven magnetization switching. This very low value was obtained in a MTJ with layers composed of  $\text{Co}_{40}\text{Fe}_{40}\text{B}_{20}$  (we studied  $\text{Co}_{72}\text{Fe}_{18}\text{B}_{10}$ ). The sample was annealed at  $270^\circ\text{C}$ . Annealing the same sample at  $350^\circ\text{C}$  caused  $J_c$  to increase to a less favorable value of  $2.5 \times 10^6$  A/cm<sup>2</sup>. The critical current values are shown as a function of annealing temperature in Fig. 7.5(b). At the same time, the TMR ratio increased upon annealing at higher temperatures. It is plotted as a function of annealing temperature in Fig. 7.5(a).

While the low  $J_c$  was well justified using a formula after Slonczewski [225], the explanation for the increased  $J_c$  was not satisfactory. The employed formula includes the proportionality

$$J_c \propto \alpha M_s M_{\text{eff}} \frac{1}{G}, \quad (7.5)$$

where  $M_s$  is the saturation magnetization and  $G$  a parameter depending roughly linearly on spin polarization. The reported TMR ratios (49% after annealing at

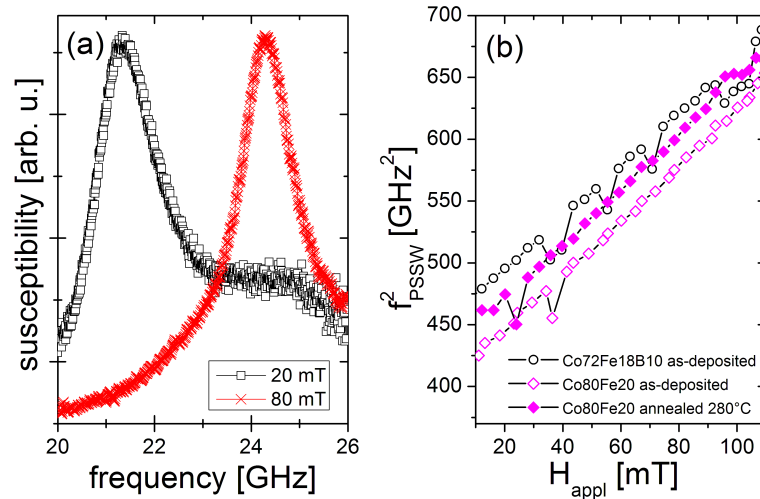


Figure 7.6: (Color online) (a) Imaginary part of the susceptibility of the 40 nm as-deposited Co<sub>80</sub>Fe<sub>20</sub> sample for 20 mT and 80 mT applied fields, for frequencies near the perpendicular standing spinwave (PSSW) resonances. (b) Squared resonance frequency of the PSSW versus applied field for the 40 nm Co<sub>80</sub>Fe<sub>20</sub> and Co<sub>72</sub>Fe<sub>18</sub>B<sub>10</sub> layers, as-deposited and annealed at 280°C.

270°C, 160% for 350°C) indicated higher spin polarization for the highest annealing temperature. As  $G$  increases with spin polarization, Eq. 7.5 would suggest a decrease in critical current for higher annealing temperature. This was not observed [219], and could not be explained so far.

The samples studied by Hayakawa cannot be compared quantitatively to our samples due to the differing CoFeB composition: Co<sub>40</sub>Fe<sub>40</sub>B<sub>20</sub>. Nevertheless, the low  $J_c$  was measured on their sample being in amorphous state, while the increased  $J_c$  was measured in crystalline state. For the different CoFeB composition employed in their sample, the crystallization temperature was determined to around 325°C [226]. In our study, we observed an increase in damping for the Co<sub>72</sub>Fe<sub>18</sub>B<sub>10</sub> samples upon phase change triggered by thermal annealing at 280°C. A similar increase after the phase change can be presumed for the Co<sub>40</sub>Fe<sub>40</sub>B<sub>20</sub> samples. As Eq. 7.5 states a direct proportionality to the Gilbert damping parameter  $\alpha$ , an increase in  $\alpha$  due to phase change justifies the  $J_c$  enhancement. On top of this, the proportionality to  $M_{\text{eff}}$  and to  $M_s$  also justifies the increase in  $J_c$ , as after annealing above crystallization temperature both quantities were increased as well.

In conclusion, the unfavorably increased critical current can be attributed to the evolution of the magnetization and the damping upon thermal treatment.

## 7.5 Exchange stiffness constant of CoFeB

All data presented so far were extracted from the uniform precession (FMR) mode, in which the dynamic magnetization is uniform across the thickness of the film. However, higher-order exchange-dominated thickness modes exist and they are excited in our experiment by the small gradient of the RF field across the layer thickness. We already introduced these so-called perpendicular standing spinwaves (PSSW) in section 1.6.3. We observed only the lowest index ( $p = 1$ ) PSSW, as illustrated in

Table 7.2: Calculated exchange stiffness constants  $A$  and literature values [30, 32].

Sample	$A_{\text{exchange}}$
Co <sub>80</sub> Fe <sub>20</sub> as-deposited 40nm	$26.1 \cdot 10^{-12}$ J/m
Co <sub>80</sub> Fe <sub>20</sub> annealed 40nm	$27.5 \cdot 10^{-12}$ J/m
Co <sub>72</sub> Fe <sub>18</sub> B <sub>10</sub> as-deposited 40nm	$28.4 \cdot 10^{-12}$ J/m
Literature Co	$28.5 \cdot 10^{-12}$ J/m
Literature Fe	$20.0 \cdot 10^{-12}$ J/m

Fig. 1.11. According to Eq. 1.92, we find for the square of their resonance frequencies

$$f_{\text{PSSW}}^2 = \left(\frac{\gamma\mu_0}{2\pi}\right)^2 \left[ M_{\text{eff}} + H_{\text{ext}} + \frac{2A}{\mu_0 M_s} \left(\frac{\pi}{t}\right)^2 \right] \left[ H_{\text{ext}} + \frac{2A}{\mu_0 M_s} \left(\frac{\pi}{t}\right)^2 \right], \quad (7.6)$$

where  $t$  is the film thickness and  $A$  is the exchange stiffness constant (introduced in section 1.1 with the exchange energy). Typical PSSW resonances are plotted in Fig. 7.6(a) for the 40 nm as-deposited Co<sub>80</sub>Fe<sub>20</sub> sample, for two distinct applied fields.

The square of the PSSW resonance frequencies is plotted in Fig. 7.6(b). We note that the corresponding resonance frequencies are considerably higher than for the uniform precession mode (see Fig. 7.2(b)). Additionally, the tiny field gradient-induced excitation of this mode leads to a poor pumping efficiency, resulting in a strongly reduced signal intensity compared to the FMR mode. Higher index PSSW modes than first ( $p > 1$ ) are probably even more weakly excited, and would anyway require to access frequencies higher than our current capability. The same is valid for the samples of thickness 25 nm and below, as the thickness dependence in Eq. 7.6 leads to frequencies exceeding the range of our finite bandwidth instrument (0 – 26.5 GHz). Thus, we could observe only the lowest index ( $p = 1$ ) PSSW for the thickest (40 nm) films.

From the PSSW mode frequency, we could extract the exchange stiffness constants  $A$  of the as-deposited and annealed 40 nm Co<sub>80</sub>Fe<sub>20</sub> films, and that of the 40 nm Co<sub>72</sub>Fe<sub>18</sub>B<sub>10</sub> as-deposited film. They are summarized in Tab. 7.2. They differ only slightly from literature values for Co [30]. As expected from its high damping deduced from the FMR mode, the resonance of the annealed 40 nm Co<sub>72</sub>Fe<sub>18</sub>B<sub>10</sub> film is large, which prevents any reliable estimate of its exchange constant.

## 7.6 Summary

In summary, I have studied the magnetization, damping, and exchange stiffness constant as a function of film thickness and crystalline state in ion-beam deposited Co<sub>72</sub>Fe<sub>18</sub>B<sub>10</sub> films, by means of ferromagnetic resonance. As-deposited amorphous layers showed low damping ( $\alpha_{\text{app}} = 0.006$ ), with negligible thickness dependence in the examined range (5 - 40 nm). A crystalline Co<sub>80</sub>Fe<sub>20</sub> reference sample with no boron content exhibited a value twice higher ( $\alpha_{\text{app}} = 0.013$ ). The value for CoFeB is even below the one usually observed for high quality permalloy. Thus, this also qualifies CoFeB alloys as suitable materials for high speed applications. As no literature data was available for the magnetization damping in CoFeB before our contribution, our measured value was already exploited to explain experimental observations [22, 23].

Thermal annealing at 280°C triggered a structural phase change in the amorphous  $\text{Co}_{72}\text{Fe}_{18}\text{B}_{10}$ . This crystallization process resulted in an increased effective magnetization as well as a dramatic increase in damping, for instance by a factor of 5 for 40 nm films. For lower thicknesses the damping increase upon annealing was less pronounced. The annealing dependence of damping can account for the recently published surprising evolutions upon annealing of the spin-transfer switching thresholds in CoFeB/MgO/CoFeB magnetic tunnel junctions: here, the critical current  $J_c$ , necessary to set off a magnetization switching event, was increased after annealing, in spite of an enhanced spin polarization determined from the TMR ratio. This can be explained by our findings, as  $J_c$  is both proportional to  $\alpha$  and to the effective magnetization, which were both increased after annealing.

Additionally, I deduced the exchange stiffness constant from perpendicular standing spin waves for the amorphous 40 nm  $\text{Co}_{72}\text{Fe}_{18}\text{B}_{10}$  sample to  $A = 28.4 \cdot 10^{-12}$  J/m. The determined value is close to the literature value of Co. As no literature data existed for  $\text{Co}_{72}\text{Fe}_{18}\text{B}_{10}$ , this can prove useful e.g. for micromagnetic simulations, depending on the exchange stiffness as an input parameter.



# Conclusion

## Summary

In the course of this thesis vector network analyzer ferromagnetic resonance was used to gain insight into several topics in modern nanomagnetism. The technique itself being a novelty, efforts were directed to improve its mode of operation. For two port measurements on a coplanar waveguide structure, which is the most common realization of this type of measurement for thin film samples, a better understanding of the obtained raw data was achieved. For this purpose, a precise analytical representation of the measured scattering parameters was developed using elements from microwave circuit theory. This analysis resulted in a data evaluation procedure allowing to calculate a value directly proportional to the dynamic susceptibility of the sample under test. We compared this new procedure with approximate ones found in the literature. While for some aspects (determination of the resonance frequency) results of the approximate methods agree rather well, for other aspects (linewidth) there is a bigger difference between the results. We therefore recommend the use of the two port data evaluation presented in this thesis for this kind of measurements, as it is the only one among the examined methods taking into account the reflection parameters in the scattering matrix.

While we obtained a solid description of the measurement in the two port geometry, several research groups perform their measurements using only one high-frequency probe in a one port geometry. This can offer several benefits as simplified calibration, faster measurement speed and higher signal. Usually, the second end of the waveguide is shorted. Here, we examined an alternative realization leaving the second end simply unconnected and unchanged with respect to the two port geometry, working as an open-circuit. Although this allows an easy change between a two port measurement and the one port geometry by simply disconnecting the second high-frequency probe, the use of an open instead of a short was not addressed up to now. In a similar fashion to the two port geometry, we established an analytical model as far as possible. Due to the additional complexity added by the reflection at the open end, we analyzed the possibility to simplify the description. Using an appropriate approximation, we developed a data analysis allowing to calculate the sample susceptibility. Using actual raw data, we confirm a good agreement with respect to two port measurements.

The resonance linewidth, which is extracted from the susceptibility measured by VNA-FMR contains a contribution due to the inhomogeneity of the magnetic sample properties. This inhomogeneous broadening can be separated from the intrinsic linewidth, when the frequency linewidth is measured as a function of applied field. We exploited this criterion to qualify the changes inflicted on Fe/Au multilayer samples by ion-beam irradiation. A cleaning of the MgO-substrate by a bombardment

with chemically active oxygen atoms prior to the sample deposition yielded a reduced inhomogeneous broadening with respect to a nominally equivalent sample grown on an uncleaned substrate. This treatment removes the carbon contamination on the substrate leading to better growth conditions for the deposited layers. Structural characterization correlated the lesser inhomogeneity with a roughness reduction at the interfaces of the multilayer. A post-growth irradiation with  $\text{He}^+$  ions was applied on the samples with different fluences. Fe and Au are immiscible, but the demixing at the multilayer interfaces is kinetically quenched at room temperature. Using simulations, 30 keV  $\text{He}^+$  ions were singled out as the ideal candidates for an ion-beam treatment, where the ion collisions provide the necessary atom mobility to achieve demixing. Indeed, the inhomogeneous broadening in the linewidth reduced increasingly with higher irradiation fluence. X-ray reflectivity confirmed a coinciding reduction of the layer roughness. The effects of both irradiation treatments were found to cumulate.

FMR measurements are renowned for the precise determination of the magnetic properties of ferromagnetic materials. We examined the information obtainable by FMR on an antiferromagnetic layer coupled to a ferromagnetic one. Conventional magnetometry is only sensitive to the magnetization of the ferromagnetic layer and the properties of the antiferromagnet are derived indirectly, e.g. the exchange bias field is defined as the arithmetic mean of the two coercivities marking the switching of the ferromagnet. In contrast, FMR also allows to directly draw conclusions on the state of the antiferromagnet, as it is sensitive to the total energy of the system. In particular, the frequency domain measurements permitted to obtain the instantaneous exchange bias at each applied field when performing a hysteresis loop. During the field sweeps the value of the bias field was observed to change. This can be explained by the thermally activated flipping of the order parameter of the grains in the polycrystalline antiferromagnet. While in principle this field annealing is expected at finite temperature, it is difficult to analyze using standard techniques. Due to the exposed dependence of the exchange bias on the applied field history and the measurement time, we recommend to always accompany results characterizing an antiferromagnet with a precise description of the measurement conditions. Otherwise, the unambiguity of the results is not guaranteed.

Due to their advantageous properties CoFeB alloys have become widely used materials in magnetic tunnel junctions. While static characterization was published in the literature, no data on ferromagnetic resonance measurements was available. We measured a series of  $\text{Co}_{72}\text{Fe}_{18}\text{B}_{10}$  samples of different thicknesses and in the as-deposited as well as a thermally annealed state. The effective magnetization of the as-deposited layers showed an expected thickness dependence with a surface anisotropy. The thermal annealing is known to provoke a crystallization of the otherwise amorphous layers. This was evidenced by increased values of the effective magnetization for all thicknesses. The magnetization damping, which was not characterized previously, was found to be very low for the as-deposited films. The obtained values are well comparable to high quality permalloy. An unexpected strong increase of damping was observed after thermal annealing, which can be attributed to the triggered phase transition. The thickness dependence of the damping of the annealed samples can be associated with an only partial crystallization of the layers. Additionally, perpendicular standing spinwave resonances were observed, which permit a quantitative determination of the exchange stiffness constant. Its value for  $\text{Co}_{72}\text{Fe}_{18}\text{B}_{10}$  was found to be close to the literature value of Co.

## Outlook

We presented results on the exchange bias mediated by an antiferromagnetic IrMn layer on different ferromagnetic layers (chapter 6). These pinned layers can form a part of a spin-valve structure, when adding a metallic non-magnetic layer on top followed by a ferromagnetic “free” layer, which reacts to the applied magnetic field. Indeed, this type of sample was also elaborated during my stay at Siemens and they behave as field sensors, showing a giant magneto resistance under the application of a magnetic field. These samples can be used for further investigations of spin pumping, as up-to-date only few studies were concerned with this effect. The precessing magnetization in the FMR measurements leads to a spin current which can be subject to non-local damping in the second ferromagnetic layer. A quantitative analysis of this effect in different systems as well as the suppression of this effect under particular measurement conditions, still represent interesting fields of research. In particular the impact on applications, which use very different structures than the model systems examined up to now, could be assessed. VNA-FMR measurements are ideally suited for this study, as both field and frequency can be varied independently, giving a more flexible approach to bring the resonance conditions of two different layers to match. This is the prerequisite to annihilate the added damping due to spin pumping [79].

In applications, as for example magnetic memories, usually patterned samples are employed instead of extended thin films. The influence of the patterning and consequently of the lateral confinement on the dynamic sample parameters is still in need of further characterization. Due to its high sensitivity, VNA-FMR was already used in first studies on arrays of disk and ring shaped structures [227, 116, 123]. Other shapes, as e.g. ellipses or diamonds, or further reduced sizes influence the magnetization configurations in a different manner and are still to be studied. To obtain ideal conditions, up to now the structures were directly created in the same lithography process together with the coplanar waveguide. In an on-going study we assess the feasibility of measuring independently created structures, which are simply placed on the transmission line, as in the case of the extended thin films. This greatly improves the flexibility due to the easy interchangeability of the samples and the separation of the deposition of the sample and the waveguide.

Recently, patterned samples with sizes below 100 nm were studied using a network analyzer following a different approach: instead of exciting a magnetization precession using an oscillating magnetic field generated by a transmission line, the excitation is mediated by spin-transfer torque in nanopillar shaped samples. The detection of the ferromagnetic resonance is either achieved using the tunnel magnetoresistance [228] or giant magnetoresistance effect [229, 230]. This approach allows in particular to access the properties of individual patterned structures, being also of great interest for applications. Several new scenarios can be envisioned, as for example a comparison between the damping in spatially confined samples and extended thin films or an evaluation of the spin torque related noise in sensor elements as e.g. read heads.

FMR measurements are particularly suited for the characterization of magnetization damping. While damping has been a subject of long-standing study, a universal theory of the fundamental contributions is still missing and it remains a phenomenological parameter. Due to the revealed temperature dependence of different contributions, cryogenic measurements are promising to provide further insight



into the mechanisms behind magnetization damping. While previous work [100] provided first results, the used cryostat was limited in particular with respect to the applied magnetic field. A new cryostat allowing FMR studies is about to be built, which also enables the application of higher in-plane fields. It will permit measurements of the damping parameter as a function of temperature. In combination with conductivity measurements, conclusions can be drawn on the contributing processes involving conduction electrons.

In the near future, measurements of novel magnetic systems, namely diluted magnetic semiconductors, are planned. The study of these systems is made difficult by the fact that their Curie temperature is considerably below room temperature. The new cryogenic facility will also permit precise characterization of the (dynamic) properties of these systems using ferromagnetic resonance.

# Appendix A

## Application Note

This chapter explains the different steps during the execution of the measurement, when using the LabVIEW programs [231] realized in the course of this thesis.

### A.1 Full two port measurement

Two programs are used for a full two port measurement: the first program is used during the measurement to obtain the scattering parameters from the vector network analyzer, the second one is executed after the measurement to calculate the susceptibility according to the data evaluation procedure in section 3.2.

The first program is called

“MAIN-Inductive\_measurement-decrease\_field-ALL-S.vi” in the directory “1Make\_measurement”. Fig. A.1 shows a screenshot of the main window. Several parameters need to be entered manually on the left side of the vertical bar, before starting the measurement: the name of the directory, where the files containing the scattering parameters recovered from the network analyzer are to be saved. This directory needs to be created beforehand by the user. The sample name, which is also used as the basis of the file names. One file is created for each applied field in the given directory, where the command voltage applied to the electromagnet and the magnetic field measured by the Hall probe are attached to the sample name. The number of frequency points as well as the lowest and highest measurement frequency need to be entered. The measured magnetic fields are determined by entering the initial and final command voltage, together with the voltage step.

Usually, a reference measurement is performed, where the magnetic field is applied perpendicular to the coplanar waveguide. If this option is chosen in the program, the electromagnet has to be turned to the 90° position before launching the program. When started, the command voltage of the magnet is increased to the given reference voltage value, the S-parameters are measured and a dialog box appears, informing of the finished reference measurement. The electromagnet has to be turned back on its ball bearing to the standard position and, upon confirmation by a key press, the measurements are executed: The initial voltage value is applied to the electromagnet, the S-parameters are measured, the voltage is changed by the given voltage step, and so forth.

On the bottom left side, a second voltage step can be entered. This voltage step is used to sub-divide strong changes in the magnetic field in smaller ones, improving the stability of the experimental setup. Additionally, two waiting times can be input:

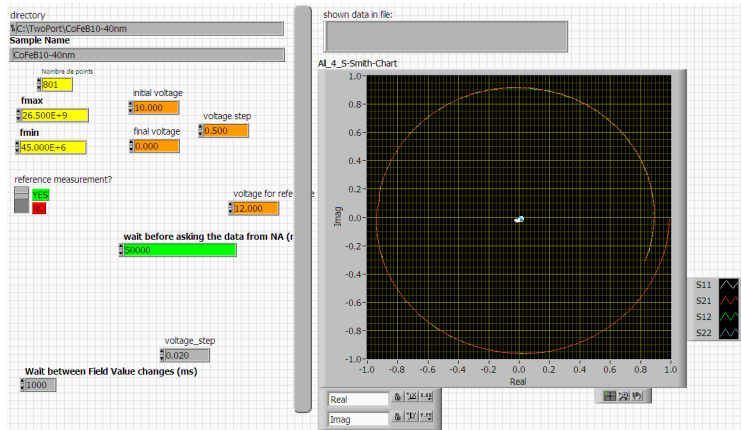


Figure A.1: (Color online) The LabVIEW program for the data acquisition in the two port geometry.

the waiting time after a magnetic field change (usually 1 s), which serves to stabilize the electromagnet. And the waiting time between the beginning of the S-parameter measurement by the network analyzer and their inquiry by a GPIB-command (for a 801 point measurement with  $32\times$  averaging: 50 s).

The created file names end either with “-measure.txt” for the actual measurement files or with “-reference.txt” for the reference measurement. In order to deembed the measurement (see section 3.2.3), a measurement of the coplanar waveguide without the magnetic sample on top still needs to be performed. This can be easily done by removing the magnetic sample, changing the file name accordingly and choosing 0 as the reference voltage. Instead of turning the electromagnet to the  $90^\circ$  position, it remains in the standard position parallel to the waveguide. The program is started and, as soon as the reference measurement is saved to a file, aborted. The end of the file name needs to be changed from “-reference.txt” to “-empty.txt” and it needs to be in the same directory as the other measured files.

The second program is called “2Port\_data\_analysis.vi” in the directory “2Data\_analysis”. Few inputs are necessary: The name of the directory containing the measured scattering parameters. The name of an empty directory for the evaluated data, previously created by the user. The total length of the coplanar waveguide and the length of the measured sample. When started, one file containing the susceptibility is created in the given directory for each measured field. Each file consists of three columns: the frequency, the real part and the imaginary part of the susceptibility.

## A.2 One port Open reflection measurement

As in the case of the two port geometry, two programs are used for the measurements in the one port geometry: the first program retrieves the scattering parameters from the vector network analyzer during the measurement, the second one evaluates the data, calculating  $X$  according to section 4.2.5. As the use of these programs is very similar to the instructions in the previous section for the two port geometry, we limit the description to the occurring differences.

The first program is called

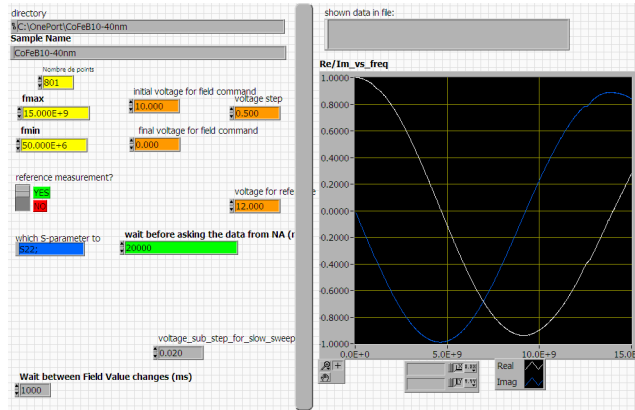


Figure A.2: (Color online) The LabVIEW program for the data acquisition in the one port geometry.

“MAIN-Inductive\_measurement-decrease\_field-one-S.vi” in the directory “1Make\_measurement”. The waiting time between the start of the S-parameter measurement and the data recovery is considerably shorter than in the two port case (for a 801 point measurement with  $32\times$  averaging: 20 s). Additionally to the other inputs, the scattering parameter asked from the network analyzer needs to be entered. It is entered using a string terminated by a semicolon, which is directly sent on the GPIB-bus. For the reflection parameters, this is either “S11;” or “S22;”. No measurement of the coplanar waveguide without the magnetic sample needs to be performed. Apart from these differences, the procedure in section A.1 applies.

The second program is called “1Port\_data\_analysis.vi” in the directory “2Data\_analysis”. The two directories are as before: the directory containing the measurement files and a second, empty directory for the evaluated data, created by the user. An input of the waveguide or sample length is not necessary.



# Bibliography

- [1] G. Reiss and D. Meyners. Logic based on magnetic tunnel junctions. *J. Phys.-Condes. Matter*, 19(16):165220, 2007.
- [2] B. N. Engel, J. Akerman, B. Butcher, R. W. Dave, M. DeHerrera, M. Durlam, G. Grynkewich, J. Janesky, S. V. Pietambaram, N. D. Rizzo, J. M. Slaughter, K. Smith, J. J. Sun, and S. Tehrani. A 4-mb toggle mram based on a novel bit and switching method. *IEEE Trans. Magn.*, 41(1-1):132, 2005.
- [3] I. L. Prejbeanu, M. Kerekes, R. C. Sousa, H. Sibuet, O. Redon, B. Dieny, and J. P. Nozières. Thermally assisted mram. *J. Phys.-Condes. Matter*, 19(16):165218, 2007.
- [4] M. Hosomi, H. Yamagishi, T. Yamamoto, K. Bessho, Y. Higo, K. Yamane, H. Yamada M. Shoji, H. Hachino, C. Fukumoto, H. Nagao, and H. Kano. A novel nonvolatile memory with spin torque transfer magnetization switching: spin-ram. *Electron Devices Meeting, 2005*, (5-7):459, 2005.
- [5] P. Grünberg, R. Schreiber, Y. Pang, M. B. Brodsky, and H. Sowers. Layered magnetic structures: Evidence for antiferromagnetic coupling of fe layers across cr interlayers. *Phys. Rev. Lett.*, 57(19):2442–2445, Nov 1986.
- [6] W. H. Butler and X.-G. Zhang. Electron transport in magnetic multilayers. In J. A. C. Bland and B. Heinrich, editors, *Ultrathin Magnetic Structures III*, pages 5–50, Berlin, 2005. Springer.
- [7] P. LeClair, J. S. Moodera, and H. J. M. Swagten. Spin polarized electron tunneling. In J. A. C. Bland and B. Heinrich, editors, *Ultrathin Magnetic Structures III*, pages 51–97, Berlin, 2005. Springer.
- [8] Charles Kittel. On the theory of ferromagnetic resonance absorption. *Phys. Rev.*, 73(2):155–161, Jan 1948.
- [9] B. Heinrich. Ferromagnetic resonance in ultrathin film structures. In B. Heinrich and J. A. C. Bland, editors, *Ultrathin Magnetic Structures II*, pages 195–222, Berlin, 1994. Springer.
- [10] Michael Farle. Ferromagnetic resonance of ultrathin metallic layers. *Rep. Prog. Phys.*, 61(7):755–826, 1998.
- [11] Rodrigo Arias and D. L. Mills. Extrinsic contributions to the ferromagnetic resonance response of ultrathin films. *Phys. Rev. B*, 60(10):7395, 1999.

- [12] K. Lenz, H. Wende, W. Kuch, K. Baberschke, K. Nagy, and A. Janossy. Two-magnon scattering and viscous gilbert damping in ultrathin ferromagnets. *Phys. Rev. B*, 73(14):144424, 2006.
- [13] J. C. Slonczewski. Current-driven excitation of magnetic multilayers. *J. Magn. Magn. Mater.*, 159(1-2):L1–L7, June 1996.
- [14] L. Berger. Emission of spin waves by a magnetic multilayer traversed by current. *Phys. Rev. B*, 54(13):9353, 1996.
- [15] J. A. Katine, F. J. Albert, R. A. Buhrmann, E. B. Myers, and D. C. Ralph. Current-driven magnetization reversal and spin-wave excitations in co/cu/co pillars. *Phys. Rev. Lett.*, 84(14):3149, 2000.
- [16] Hirofumi Morise and Shiho Nakamura. Stable magnetization states under a spin-polarized current and a magnetic field. *Phys. Rev. B*, 71(1):014439, 2005.
- [17] J. Grollier, V. Cros, H. Jaffres, A. Hamzic, J. M. George, G. Faini, J. Ben Youssef, H. Le Gall, and A. Fert. Field dependence of magnetization reversal by spin transfer. *Phys. Rev. B*, 67(17):174402, 2003.
- [18] Q. Mistral, A. Deac, J. Grollier, O. Redon, Y. Liu, M. Li, P. Wang, B. Dieny, and T. Devolder. High frequency magnetic eigen excitations in a spin valve submitted to cpp dc current. *Mater. Sci. Eng. B*, 126(2-3):267–270, January 2006.
- [19] C. Bilzer, T. Devolder, P. Crozat, C. Chappert, S. Cardoso, and P. P. Freitas. Vector network analyzer ferromagnetic resonance of thin films on coplanar waveguides: Comparison of different evaluation methods. *J. Appl. Phys.*, 101(7):074505, 2007.
- [20] Haiwen Xi, James Rantschler, Sining Mao, Mark T Kief, and Robert M White. Interface coupling and magnetic properties of exchange-coupled  $\text{ni}_{81}\text{fe}_{19}/\text{ir}_{22}\text{mn}_{78}$  bilayers. *J. Phys. D-Appl. Phys.*, 36(13):1464–1468, 2003.
- [21] Jeffrey McCord, Roland Mattheis, and Dieter Elefant. Dynamic magnetic anisotropy at the onset of exchange bias: The nife/irmn ferromagnet/antiferromagnet system. *Phys. Rev. B*, 70(9):094420, 2004.
- [22] S. Laribi, V. Cros, M. Munoz, J. Grollier, A. Hamzic, C. Deranlot, A. Fert, E. Martinez, L. Lopez-Diaz, L. Vila, G. Faini, S. Zoll, and R. Fournel. Reversible and irreversible current induced domain wall motion in cofeb based spin valves stripes. *Appl. Phys. Lett.*, 90(23):232505, 2007.
- [23] G. D. Fuchs, J. C. Sankey, V. S. Pribiag, L. Qian, P. M. Braganca, A. G. F. Garcia, E. M. Ryan, Zhi-Pan Li, O. Ozatay, D. C. Ralph, and R. A. Buhrman. Spin-torque ferromagnetic resonance measurements of damping in nanomagnets. <http://arxiv.org/abs/cond-mat/0703577v1>, 2007.
- [24] J. F. Gregg, I. Petej, E. Jouguelet, and C. Dennis. Spin electronics - a review. *J. Phys. D-Appl. Phys.*, 35(18):R121–R155, 2002.
- [25] A. Aharoni. *Introduction to the Theory of Ferromagnetism*. Oxford University Press, New York, second edition, 2000.

- [26] C. Kittel. *Introduction to Solid State Physics*. Wiley, New York, third edition, 1966.
- [27] J. Stoehr and H. C. Siegmann. *Magnetism - From Fundamentals to Nanoscale Dynamics*. Springer, Berlin, 2006.
- [28] A. Hubert and R. Schaefer. *Magnetic Domains - The Analysis of Magnetic Microstructures*. Springer, Berlin, 1998.
- [29] S. Chikazumi. *Magnetism - From Fundamentals to Nanoscale Dynamics*. Oxford University Press, New York, second edition, 1999.
- [30] B. Hillebrands and G. Guentherodt. In B. Heinrich and J. A. C. Bland, editors, *Ultrathin Magnetic Structures II*, page 266, Berlin, 2005. Springer.
- [31] C. Bayer, J. Jorzick, S. O. Demokritov, A. N. Slavin, K. Y. Guslienko, D. V. Berkov, N. L. Gorn, M. P. Kostylev, and B. Hillebrands. Spin-wave excitations in finite rectangular elements. In B. Hillebrands and A. Thiaville, editors, *Spin Dynamics in Confined Magnetic Structures III*, pages 57–103, Berlin, 2006. Springer.
- [32] J. F. Cochran. Light scattering from ultrathin magnetic layers and bilayers. In B. Heinrich and J. A. C. Bland, editors, *Ultrathin Magnetic Structures II*, pages 222–257, Berlin, 1994. Springer.
- [33] A. G. Gurevich and G. A. Melkov. *Magnetization Oscillations and Waves*. CRC Press, London, 1996.
- [34] R. Urban, B. Heinrich, G. Woltersdorf, K. Ajdari, K. Myrtle, J. F. Cochran, and E. Rozenberg. Nanosecond magnetic relaxation processes in ultrathin metallic films prepared by mbe. *Phys. Rev. B*, 65(2):020402, 2002.
- [35] S. Visnovsky, R. Lopusnik, M. Nyvlt, A. Das, R. Krishnan, M. Tessier, Z. Frait, P. Aitchison, and J. N. Chapman. Magneto-optic studies of fe/au multilayers. *J. Magn. Magn. Mater.*, 198-199:480–482, June 1999.
- [36] T. L. Gilbert. A phenomenological theory of damping in ferromagnetic materials. *IEEE Trans. Magn.*, 40(6):3443, 2004.
- [37] D. L. Landau and E. Lifshitz. On the theory of the dispersion of magnetic permeability in ferromagnetic bodies. *Phys. Z. Sowjetunion*, 8:153, 1935.
- [38] T. L. Gilbert. A lagrangian formulation of the gyromagnetic equation of the magnetization field. *Phys. Rev.*, 100:1243, 1955.
- [39] N. Bloembergen and S. Wang. Relaxation effects in para- and ferromagnetic resonance. *Phys. Rev.*, 93(1):72–83, Jan 1954.
- [40] J. Miltat, G. Albuquerque, and A. Thiaville. An introduction to micromagnetics in the dynamic regime. In B. Hillebrands and K. Ounadjela, editors, *Spin Dynamics in Confined Magnetic Structures I*, pages 1–33, Berlin, 2002. Springer.



- [41] D. Polder. On the quantum theory of ferromagnetic resonance. *Phys. Rev.*, 73(9):1116, May 1948.
- [42] O. Acher and A. L. Adenot. Bounds on the dynamic properties of magnetic materials. *Phys. Rev. B*, 62(17):11324–11327, Nov 2000.
- [43] S. Queste. *Elaboration de couches minces ferromagnétiques à forte perméabilité pour applications hyperfréquences*. PhD thesis, Université François Rabelais Tours, Tours, France, 2004.
- [44] B. Heinrich. Spin relaxation in magnetic metallic layers and multilayers. In J. A. C. Bland and B. Heinrich, editors, *Ultrathin Magnetic Structures III*, pages 143–210, Berlin, 2005. Springer.
- [45] D. L. Mills and S. M. Rezende. Spin damping in ultrathin magnetic films. In B. Hillebrands and K. Ounadjela, editors, *Spin Dynamics in Confined Magnetic Structures II*, pages 27–58, Berlin, 2003. Springer.
- [46] J-M. L. Beaujour, J. H. Lee, A. D. Kent, K. Krycka, and C-C. Kao. Magnetization damping in ultrathin polycrystalline co films: Evidence for nonlocal effects. *Phys. Rev. B*, 74(21):214405, 2006.
- [47] J. Smit and H. G. Beljers. *Philips Res. Rep.*, 10:113, 1955.
- [48] H. Suhl. Ferromagnetic resonance in nickel ferrite between one and two kilomegacycles. *Phys. Rev.*, 97(2):555–557, Jan 1955.
- [49] L. Baselgia, M. Warden, F. Waldner, Stuart L. Hutton, John E. Drumheller, Y. Q. He, P. E. Wigen, and M. Maryško. Derivation of the resonance frequency from the free energy of ferromagnets. *Phys. Rev. B*, 38(4):2237–2242, Aug 1988.
- [50] M. Sparks. *Ferromagnetic-Relaxation Theory*. McGraw-Hill, New York, 1964.
- [51] C. Kittel and A. H. Mitchell. Ferromagnetic relaxation and gyromagnetic anomalies in metals. *Phys. Rev.*, 101(5):1611–1612, Mar 1956.
- [52] B. Heinrich, R. Urban, and G. Woltersdorf. Magnetic relaxation in metallic films: Single and multilayer structures. *J. Appl. Phys.*, 91(10):7523–7525, 2002.
- [53] V. Kambersky. On the landau-lifshitz relaxation in ferromagnetic metals. *Can. J. Phys.*, 48(24):2906, 1970.
- [54] R. J. Elliott. Theory of the effect of spin-orbit coupling on magnetic resonance in some semiconductors. *Phys. Rev.*, 96(2):266–279, Oct 1954.
- [55] F. Schreiber, J. Pflaum, Z. Frait, Th. Muhge, and J. Pelzl. Gilbert damping and g-factor in fexco1-x alloy films. *Solid State Commun.*, 93(12):965–968, March 1995.
- [56] S. M. Bhagat and P. Lubitz. Temperature variation of ferromagnetic relaxation in the 3d transition metals. *Phys. Rev. B*, 10(1):179–185, Jul 1974.

- [57] J. Kuneš and V. Kamberský. First-principles investigation of the damping of fast magnetization precession in ferromagnetic 3d metals. *Phys. Rev. B*, 65(21):212411, Jun 2002.
- [58] V. Korenman and R. E. Prange. Anomalous damping of spin waves in magnetic metals. *Phys. Rev. B*, 6(7):2769–2777, Oct 1972.
- [59] E. R. Cohen, D. R. Lide, and G. L. Trigg. *AIP Physics Desk Reference*. Springer, New York, third edition, 2003.
- [60] J. Ben Youssef, N. Vukadinovic, D. Billet, and M. Labrune. Thickness-dependent magnetic excitations in permalloy films with nonuniform magnetization. *Phys. Rev. B*, 69(17):174402, 2004.
- [61] E. van de Riet and F. Roozeboom. Ferromagnetic resonance and eddy currents in high-permeable thin films. *J. Appl. Phys.*, 81(1):350–354, 1997.
- [62] W. S. Ament and G. T. Rado. Electromagnetic effects of spin wave resonance in ferromagnetic metals. *Phys. Rev.*, 97(6):1558–1566, Mar 1955.
- [63] K. Seemann, H. Leiste, and V. Bekker. New theoretical approach to the rf-dynamics of soft magnetic fetan films for cmos components. *J. Magn. Magn. Mater.*, 278(1-2):200–207, July 2004.
- [64] G. Woltersdorf and B. Heinrich. Two-magnon scattering in a self-assembled nanoscale network of misfit dislocations. *Phys. Rev. B*, 69(18):184417, 2004.
- [65] C. B. Craus, G. Palasantzas, A. R. Chezan, J. Th. M. De Hosson, D. O. Boerma, and L. Niesen. The influence of the surface topography on the magnetization dynamics in soft magnetic thin films. *J. Appl. Phys.*, 97(1):013904, 2005.
- [66] B. Heinrich and J.F. Cochran. Ultrathin metallic magnetic films: magnetic anisotropies and exchange interactions. *Adv. Phys.*, 42(5):523–639, October 1993.
- [67] S. Mizukami, Y. Ando, and T. Miyazaki. Ferromagnetic resonance linewidth for nm/80nife/nm films (nm=cu, ta, pd and pt). *J. Magn. Magn. Mater.*, 226-230(Part 2):1640–1642, May 2001.
- [68] S. Mizukami, Y. Ando, and T. Miyazaki. Magnetic relaxation of normal-metal (nm)/80nife/nm films. *J. Magn. Magn. Mater.*, 239(1-3):42–44, February 2002.
- [69] S. Mizukami, Y. Ando, and T. Miyazaki. Effect of spin diffusion on gilbert damping for a very thin permalloy layer in cu/permalloy/cu/pt films. *Phys. Rev. B*, 66(10):104413, 2002.
- [70] M. D. Stiles and J. Miltat. Spin-transfer torque and dynamics. In B. Hillebrands and A. Thiaville, editors, *Spin Dynamics in Confined Magnetic Structures III*, pages 225–308, Berlin, 2006. Springer.

- [71] Arne Brataas, Yaroslav Tserkovnyak, Gerrit E. W. Bauer, and Bertrand I. Halperin. Spin battery operated by ferromagnetic resonance. *Phys. Rev. B*, 66(6):060404, Aug 2002.
- [72] Yaroslav Tserkovnyak, Arne Brataas, and Gerrit E. W. Bauer. Enhanced gilbert damping in thin ferromagnetic films. *Phys. Rev. Lett.*, 88(11):117601, Feb 2002.
- [73] Yaroslav Tserkovnyak, Arne Brataas, Gerrit E. W. Bauer, and Bertrand I. Halperin. Nonlocal magnetization dynamics in ferromagnetic heterostructures. *Rev. Mod. Phys.*, 77(4):1375, 2005.
- [74] B. Heinrich and G. Woltersdorf. Intrinsic spin relaxation processes in metallic magnetic multilayers. *J. Supercond.*, 20(2):83–89, February 2007.
- [75] Th. Gerrits, M. L. Schneider, and T. J. Silva. Enhanced ferromagnetic damping in permalloy/cu bilayers. *J. Appl. Phys.*, 99(2):023901, 2006.
- [76] R. Urban, G. Woltersdorf, and B. Heinrich. Gilbert damping in single and multilayer ultrathin films: Role of interfaces in nonlocal spin dynamics. *Phys. Rev. Lett.*, 87:217204, 2001.
- [77] D. L. Mills. Ferromagnetic resonance relaxation in ultrathin metal films: The role of the conduction electrons. *Phys. Rev. B*, 68(1):014419, Jul 2003.
- [78] B. Heinrich, G. Woltersdorf, R. Urban, and E. Simanek. Role of dynamic exchange coupling in magnetic relaxations of metallic multilayer films (invited). *J. Appl. Phys.*, 93(10):7545–7550, 2003.
- [79] Bret Heinrich, Yaroslav Tserkovnyak, Georg Woltersdorf, Arne Brataas, Radovan Urban, and Gerrit E. W. Bauer. Dynamic exchange coupling in magnetic bilayers. *Phys. Rev. Lett.*, 90(18):187601, 2003.
- [80] P. C. Fletcher and C. Kittel. Considerations on the propagation and generation of magnetostatic waves and spin waves. *Phys. Rev.*, 120(6):2004–2006, Dec 1960.
- [81] D. D. Stancil. *Theory of Magnetostatic Waves*. Springer, New York, 1993.
- [82] L. R. Walker. Magnetostatic modes in ferromagnetic resonance. *Phys. Rev.*, 105(2):390–399, Jan 1957.
- [83] R. W. Damon and J. R. Eshbach. Magnetostatic modes of a ferromagnetic slab. *Journal of Applied Physics*, 31(5):S104–S105, 1960.
- [84] R. W. Damon and J. R. Eshbach. Magnetostatic modes of a ferromagnet slab. *J. Phys. Chem. Solids*, 19(3-4):308–320, May 1961.
- [85] B A Kalinikos and A N Slavin. Theory of dipole-exchange spin wave spectrum for ferromagnetic films with mixed exchange boundary conditions. *J. Phys. C: Solid State Phys.*, 19(35):7013–7033, 1986.

- [86] S. O. Demokritov and B. Hillebrands. In B. Hillebrands and K. Ounadjela, editors, *Spin Dynamics in Confined Magnetic Structures I*, page 70, Berlin, 2002. Springer.
- [87] S O Demokritov. Dynamic eigen-modes in magnetic stripes and dots. *J. Phys.-Condes. Matter*, 15(34):S2575–S2598, 2003.
- [88] C. Kittel. Excitation of spin waves in a ferromagnet by a uniform rf field. *Phys. Rev.*, 110(6):1295–1297, Jun 1958.
- [89] U. Ebels, L. D. Buda, K. Ounadjela, and P. E. Wigen. Small amplitude dynamics of nonhomogeneous magnetization distributions: The excitation spectrum of stripe domains. In B. Hillebrands and K. Ounadjela, editors, *Spin Dynamics in Confined Magnetic Structures I*, pages 167–216, Berlin, 2002. Springer.
- [90] I. Neudecker, G. Woltersdorf, B. Heinrich, T. Okuno, G. Gubbiotti, and C.H. Back. Comparison of frequency, field, and time domain ferromagnetic resonance methods. *J. Magn. Magn. Mater.*, 307(1):148–156, December 2006.
- [91] Bucknell C. Webb, Mark E. Re, Christopher V. Jahnes, and Michael A. Rusak. High-frequency permeability of laminated and unlaminated, narrow, thin-film magnetic stripes. *J. Appl. Phys.*, 69(8):5611–5615, 1991.
- [92] V. Bekker, K. Seemann, and H. Leiste. A new strip line broad-band measurement evaluation for determining the complex permeability of thin ferromagnetic films. *J. Magn. Magn. Mater.*, 270(3):327–332, April 2004.
- [93] A.-L. Adenot, O. Acher, D. Pain, F. Duverger, M.-J. Malliavin, D. Damiani, and T. Taffary. Broadband permeability measurement of ferromagnetic thin films or microwires by a coaxial line perturbation method. *J. Appl. Phys.*, 87(9):5965–5967, 2000.
- [94] D. Pain, M. Ledieu, O. Acher, A. L. Adenot, and F. Duverger. An improved permeameter for thin film measurements up to 6 ghz. *J. Appl. Phys.*, 85(8):5151–5153, 1999.
- [95] E. Moraitakis, L. Kompotiatis, M. Pissas, and D. Niarchos. Permeability measurements of permalloy films with a broad band stripline technique. *J. Magn. Magn. Mater.*, 222(1-2):168–174, December 2000.
- [96] G. Counil, J-V. Kim, K. Shigeto, Y. Otani, T. Devolder, P. Crozat, H. Hurdquint, and C. Chappert. Inductive measurement of the high frequency permeability of a permalloy thin film. *J. Magn. Magn. Mater.*, 272-276(Part 1):290–292, May 2004.
- [97] Sangita S. Kalarickal, Pavol Krivosik, Mingzhong Wu, Carl E. Patton, Michael L. Schneider, Pavel Kabos, T. J. Silva, and John P. Nibarger. Ferromagnetic resonance linewidth in metallic thin films: Comparison of measurement methods. *J. Appl. Phys.*, 99(9):093909, 2006.
- [98] T. J. Silva, C. S. Lee, T. M. Crawford, and C. T. Rogers. Inductive measurement of ultrafast magnetization dynamics in thin-film permalloy. *J. Appl. Phys.*, 85(11):7849–7862, 1999.

- [99] G. M. Sandler, H. N. Bertram, T. J. Silva, and T. M. Crawford. Determination of the magnetic damping constant in nife films. *J. Appl. Phys.*, 85(8):5080–5082, 1999.
- [100] G. Council. *Perméamétrie hyperfréquence de couches minces magnétiques*. PhD thesis, Université Paris-Sud, Paris, France, 2005.
- [101] Anthony B. Kos, Thomas J. Silva, and Pavel Kabos. Pulsed inductive microwave magnetometer. *Rev. Sci. Instrum.*, 73(10):3563–3569, 2002.
- [102] Matthieu Bailleul, Dominik Olligs, and Claude Fermon. Propagating spin wave spectroscopy in a permalloy film: A quantitative analysis. *Appl. Phys. Lett.*, 83(5):972–974, 2003.
- [103] L.K. Brundle and N.J. Freedman. Magnetostatic surface waves on a y.i.g. slab. *Electronics Letters*, 4(7):132–134, 1968.
- [104] M. Bailleul, D. Olligs, C. Fermon, and S. O. Demokritov. Spin waves propagation and confinement in conducting films at the micrometer scale. *Europhysics Letters (EPL)*, 56(5):741–747, 2001.
- [105] M. Bailleul. *Propagation et confinement d’ondes de spin dans les microstructures magnétiques*. PhD thesis, Ecole Polytechnique, CEA Saclay, France, 2002.
- [106] E. Nicolle. *Caractérisations et fiabilité de mémoires magnétiques à accès aléatoire (titre provisoire)*. PhD thesis, Université Paris-Sud, Paris, France, 2007.
- [107] C. Maunoury, C. Bilzer, C.K. Lim, T. Devolder, J. Wecker, L. Bar, and C. Chappert. Quasi-static and dynamic switching of exchange biased micron-sized tmr junctions. *Mater. Sci. Eng. B*, 126(2-3):202–206, January 2006.
- [108] T. Devolder, H. W. Schumacher, and C. Chappert. Precessional switching of thin nanomagnets with uniaxial anisotropy. In B. Hillebrands and A. Thiaville, editors, *Spin Dynamics in Confined Magnetic Structures III*, pages 1–55, Berlin, 2006. Springer.
- [109] S. E. Russek, R. D. McMichael, M. J. Donahue, and S. Kaka. High speed switching and rotational dynamics in small magnetic thin film devices. In B. Hillebrands and K. Ounadjela, editors, *Spin Dynamics in Confined Magnetic Structures II*, pages 94–154, Berlin, 2003. Springer.
- [110] Y. M. Lee, J. Hayakawa, S. Ikeda, F. Matsukura, and H. Ohno. Effect of electrode composition on the tunnel magnetoresistance of pseudo-spin-valve magnetic tunnel junction with a mgo tunnel barrier. *Appl. Phys. Lett.*, 90(21):212507, 2007.
- [111] S. O. Demokritov and B. Hillebrands. Spinwaves in laterally confined magnetic structures. In B. Hillebrands and K. Ounadjela, editors, *Spin Dynamics in Confined Magnetic Structures I*, pages 65–92, Berlin, 2002. Springer.

- [112] J. Jorzick. *Brillouin-Lichtstreu-Spektroskopie an dipolar-gekoppelten magnetischen Mikrostrukturen*. PhD thesis, Universität Kaiserslautern, Kaiserslautern, Germany, 2001.
- [113] M. Binder, A. Weber, O. Mosendz, G. Woltersdorf, M. Izquierdo, I. Neudecker, J. R. Dahn, T. D. Hatchard, J.-U. Thiele, C. H. Back, and M. R. Scheinfein. Magnetization dynamics of the ferrimagnet cogd near the compensation of magnetization and angular momentum. *Phys. Rev. B*, 74(13):134404, 2006.
- [114] M. Buess. *Pulsed Precessional Motion*. PhD thesis, Swiss Federal Institute of Technology Zürich, Zürich, Switzerland, 2005.
- [115] S. D. Bader and J. L. Erskine. Magneto-optical effects in ultrathin magnetic structures. In B. Heinrich and J. A. C. Bland, editors, *Ultrathin Magnetic Structures II*, pages 297–325, Berlin, 1994. Springer.
- [116] I. Neudecker, K. Perzlmaier, F. Hoffmann, G. Woltersdorf, M. Buess, D. Weiss, and C. H. Back. Modal spectrum of permalloy disks excited by in-plane magnetic fields. *Phys. Rev. B*, 73(13):134426, 2006.
- [117] B. C. Choi and M. R. Freeman. Nonequilibrium spin dynamics in laterally defined magnetic structures. In J. A. C. Bland and B. Heinrich, editors, *Ultrathin Magnetic Structures III*, pages 211–232, Berlin, 2005. Springer.
- [118] M. R. Freeman and W. K. Hiebert. Stroboscopic microscopy of magnetic dynamics. In B. Hillebrands and K. Ounadjela, editors, *Spin Dynamics in Confined Magnetic Structures I*, pages 93–126, Berlin, 2002. Springer.
- [119] V. Charbois, V. V. Naletov, J. Ben Youssef, and O. Klein. Mechanical detection of ferromagnetic resonance spectrum in a normally magnetized yttrium–iron–garnet disk. *J. Appl. Phys.*, 91(10):7337–7339, 2002.
- [120] V. Charbois. *Détection mécanique de la résonance ferromagnétique*. PhD thesis, Université Paris 7 - Denis Diderot, Paris, France, 2003.
- [121] A. Volodin, D. Buntinx, S. Brems, and C. Van Haesendonck. Piezoresistive detection-based ferromagnetic resonance force microscopy of microfabricated exchange bias systems. *Appl. Phys. Lett.*, 85(24):5935–5937, 2004.
- [122] P. E. Wigen, M. L. Roukes, and P. C. Hammel. Ferromagnetic resonance force microscopy. In B. Hillebrands and A. Thiaville, editors, *Spin Dynamics in Confined Magnetic Structures III*, pages 105–136, Berlin, 2006. Springer.
- [123] F. Giesen, J. Podbielski, T. Korn, M. Steiner, A. van Staa, and D. Grundler. Hysteresis and control of ferromagnetic resonances in rings. *Appl. Phys. Lett.*, 86(11):112510, 2005.
- [124] M. Buess, T. Haug, M. R. Scheinfein, and C. H. Back. Micromagnetic dissipation, dispersion, and mode conversion in thin permalloy platelets. *Phys. Rev. Lett.*, 94(12):127205, 2005.
- [125] R. I. Sarbacher and W. A. Edson. *Hyper and Ultrahigh Frequency Engineering*. Wiley, New York, 1943.

- [126] P. F. Combes. *Micro-ondes 1.Lignes, guides et cavités*. Dunod, Paris, 1996.
- [127] F. Gardiol. *Microstrip Circuits*. Wiley, New York, 1994.
- [128] K.C. Gupta, R. Garg, I. Bahl, and P. Bhartia. *Microstrip Lines and Slotlines*. Artech House, Boston, second edition, 1996.
- [129] G. Ghione and C. Naldi. Analytical formulas for coplanar lines in hybrid and monolithic mics. *Electronics Letters*, 20(4):179–181, 1984.
- [130] Charles A. Lee and G. Conrad Dalman. *Microwave Devices, Circuits and their Interaction*. Wiley, New York, 1994.
- [131] Agilent Technologies. *Application Note 1287-1: Understanding the Fundamental Principles of Vector Network Analysis*. Agilent, U.S.A., 2000.
- [132] Agilent Technologies. *Application Note 1364-1: De-embedding and Embedding S-Parameter Networks Using a Vector Network Analyzer*. Agilent, U.S.A., 2004.
- [133] M. H. W. Hoffmann. *Hochfrequenztechnik*. Springer, Berlin, 1997.
- [134] P. F. Combes. *Micro-ondes 2.Circuits passifs, propagation, antennes*. Dunod, Paris, 1997.
- [135] Agilent Technologies. *Back to Basics*. Agilent, U.S.A., 2000.
- [136] Agilent Technologies. *Application Note 1287-3: Applying Error Correction to Network Analyzer Measurements*. Agilent, U.S.A., 2002.
- [137] Picoprobe Home Page. <http://www.picoprobe.com/>.
- [138] TX-Line Transmission Line Calculator. <http://web.appwave.com/>. Applied Wave Research.
- [139] Trace Impedance Calculator for Microwave Designs. <http://www.eecircle.com/applets/traceanalyzerapplet/traceanalyzerapplet.html>. Electrical Engineers Circle.
- [140] Walter Barry. A broad-band, automated, stripline technique for the simultaneous measurement of complex permittivity and permeability. *IEEE Trans. Microw. Theory Tech.*, 34(1):80, 1986.
- [141] I. Neudecker. *Magnetization Dynamics of Confined Ferromagnetic Systems*. PhD thesis, Universität Regensburg, Regensburg, Germany, 2006.
- [142] G. Counil, Joo-Von Kim, T. Devolder, C. Chappert, K. Shigeto, and Y. Otani. Spin wave contributions to the high-frequency magnetic response of thin films obtained with inductive methods. *J. Appl. Phys.*, 95(10):5646–5652, 2004.
- [143] O. Mosendz, B. Kardasz, D.S. Schmool, and B. Heinrich. Spin dynamics at low microwave frequencies in crystalline fe ultrathin film double layers using co-planar transmission lines. *J. Magn. Magn. Mater.*, 300(1):174–178, May 2006.

- [144] M. L. Schneider, A. B. Kos, and T. J. Silva. Finite coplanar waveguide width effects in pulsed inductive microwave magnetometry. *Appl. Phys. Lett.*, 85(2):254–256, 2004.
- [145] M. L. Schneider, Th. Gerrits, A. B. Kos, and T. J. Silva. Gyromagnetic damping and the role of spin-wave generation in pulsed inductive microwave magnetometry. *Appl. Phys. Lett.*, 87(7):072509, 2005.
- [146] C. Scheck, L. Cheng, and W. E. Bailey. Low damping in epitaxial sputtered iron films. *Appl. Phys. Lett.*, 88(25):252510, 2006.
- [147] C. Chappert, K. Le Dang, P. Beauvillain, H. Hurdequint, and D. Renard. Ferromagnetic resonance studies of very thin cobalt films on a gold substrate. *Phys. Rev. B*, 34(5):3192–3197, Sep 1986.
- [148] James O. Rantschler and Jr. Chester Alexander. Ripple field effect on high-frequency measurements of fetin films. *J. Appl. Phys.*, 93(10):6665–6667, 2003.
- [149] Bijoy K. Kuanr, R.E. Camley, and Z. Celinski. Extrinsic contribution to gilbert damping in sputtered nife films by ferromagnetic resonance. *J. Magn. Magn. Mater.*, 286:276–281, February 2005.
- [150] W.B. Weir. Automatic measurement of complex dielectric constant and permeability at microwave frequencies. *Proc. IEEE*, 62(1):33–36, 1974.
- [151] D.K. Ghodgaonkar, V.V. Varadan, and V.K. Varadan. Free-space measurement of complex permittivity and complex permeability of magnetic materials at microwave frequencies. *IEEE Trans. Instrum. Meas.*, 39(2):387–394, 1990.
- [152] H. Nemeč, F. Kadlec, P. Kuzel, L. Duvillaret, and J.-L. Coutaz. Independent determination of the complex refractive index and wave impedance by time-domain terahertz spectroscopy. *Opt. Commun.*, 260(1):175–183, April 2006.
- [153] C. Bilzer, T. Devolder, Joo-Von Kim, G. Counil, C. Chappert, S. Cardoso, and P. P. Freitas. Study of the dynamic magnetic properties of soft cofeb films. *J. Appl. Phys.*, 100(5):053903, 2006.
- [154] S. Cardoso, V. Gehanno, R. Ferreira, and P. P. Freitas. Ion beam deposition and oxidation of spin-dependent tunnel junctions. *IEEE Trans. Magn.*, 35(5-1):2952, 1999.
- [155] S. Cardoso, R. Ferreira, P. P. Freitas, M. MacKenzie, J. Chapman and J. O. Ventura, J. B. Sousa, and U. Kreissig. Ferromagnetic coupling field reduction in cofeb tunnel junctions deposited by ion beam. *IEEE Trans. Magn.*, 40(4-2):2272, 2004.
- [156] S. Cardoso, C. Cavaco, R. Ferreira, L. Pereira, M. Rickart, P. P. Freitas, N. Franco, J. Gouveia, and N. P. Barradas. Characterization of cofeb electrodes for tunnel junctions. *J. Appl. Phys.*, 97(10):10C916, 2005.
- [157] W. H. Press, S. A. Teukolsky, W. T. Vetterling, and B. P. Flannery. *Numerical Recipes in C: The Art of Scientific Computing*, page 683. Cambridge University Press, Cambridge, second edition, 2002.



- [158] M. Ledieu, F. Schoenstein, J.-H. Le Gallou, O. Valls, S. Queste, F. Duverger, and O. Acher. Microwave permeability spectra of ferromagnetic thin films over a wide range of temperatures. *J. Appl. Phys.*, 93(10):7202–7204, 2003.
- [159] P. M. Jacquart and L. Roux. Influence of the electrical resistivity of a ferromagnetic thin film on its permeability measurement performed with a permeameter. *J. Magn. Magn. Mater.*, 281(1):82–91, October 2004.
- [160] Charles A. Lee and G. Conrad Dalman. *Microwave Devices, Circuits and their Interaction*. Wiley, New York, 1994. p. 35.
- [161] C. Bilzer, T. Devolder, C. Chappert, O. Plantevin, A. K. Suszka, B. J. Hickey, A. Lamperti, B. K. Tanner, B. Mahrov, and S. O. Demokritov. Ferromagnetic resonance linewidth reduction in fe/au multilayers using ion beams. *submitted to J. Appl. Phys.*, 2007.
- [162] M. Rickart, B. F. P. Roos, T. Mewes, J. Jorzick, S. O. Demokritov, and B. Hillebrands. Morphology of epitaxial metallic layers on mgo substrates: influence of submonolayer carbon contamination. *Surf. Sci.*, 495(1-2):68–76, December 2001.
- [163] Fabrice Didier and Jacques Jupille. Layer-by-layer growth mode of silver on magnesium oxide (100). *Surf. Sci.*, 307-309(Part 1):587–590, April 1994.
- [164] CCR GmbH Beschichtungstechnologie Home Page. <http://www.ccrtechnology.de/>.
- [165] P.A. Beck, B.F.P. Roos, S.O. Demokritov, and B. Hillebrands. Ion beam smoothing with low-energy argon ions and reduction of neel "orange peel" coupling in magnetic tunnel junctions. *J. Magn. Magn. Mater.*, 290-291(Part 2):1108–1111, April 2005.
- [166] Crystal GmbH Home Page. <http://www.crystal-gmbh.com/>.
- [167] P. Etienne, J. Massies, S. Lequien, R. Cabanel, and F. Petroff. Molecular beam epitaxial growth of cr/fe, ag/fe, ag/cr and ag/co superlattices on mgo (001) substrates. *J. Cryst. Growth*, 111(1-4):1003–1010, May 1991.
- [168] A Cole, B J Hickey, T P A Hase, J D R Buchanan, and B K Tanner. Influence of the interfacial roughness on electron channelling in fe/au(001) multilayers. *J. Phys.-Condes. Matter*, 16(8):1197–1209, 2004.
- [169] P. Grunberg, S. Demokritov, A. Fuss, R. Schreiber, J. A. Wolf, and S. T. Purcell. Interlayer exchange, magnetotransport and magnetic domains in fe/cr layered structures. *J. Magn. Magn. Mater.*, 104-107(Part 3):1734–1738, February 1992.
- [170] A. S. Arrott. Introduction to reflection high energy electron diffraction (rheed). In J. A. C. Bland and B. Heinrich, editors, *Ultrathin Magnetic Structures I*, pages 177–220, Berlin, 1994. Springer.
- [171] G. V. Sudhakar Rao, A. K. Bhatnagar, and F. S. Razavi. Investigation of fe/al multilayers. *J. Magn. Magn. Mater.*, 247(2):159–170, June 2002.

- [172] B. L. Ramakrishna, C. H. Lee, Y. Cheng, and M. B. Stearns. Ferromagnetic resonance in co-cr multilayer films. *J. Appl. Phys.*, 61(8):4290–4292, 1987.
- [173] G. Counil, Joo-Von Kim, T. Devolder, P. Crozat, C. Chappert, and A. Cebollada. Magnetic anisotropy of epitaxial mgo/fe/mgo films studied by network analyzer ferromagnetic resonance. *J. Appl. Phys.*, 98(2):023901, 2005.
- [174] S. M. Rezende, J. A. S. Moura, F. M. de Aguiar, and W. H. Schreiner. Ferromagnetic resonance of fe(111) thin films and fe(111)/cu(111) multilayers. *Phys. Rev. B*, 49(21):15105–15109, Jun 1994.
- [175] J.-M. L. Beaujour, W. Chen, A. D. Kent, and J. Z. Sun. Ferromagnetic resonance study of polycrystalline cobalt ultrathin films. *J. Appl. Phys.*, 99(8):08N503, 2006.
- [176] R. C. Oliveira, R. L. Rodriguez-Suarez, F.M.D.F. M. de Aguiar, S. M. Rezende, J. R. Fermin, and A. Azevedo. Magnetization relaxation in sputtered thin permalloy films. *J. Magn. Magn. Mater.*, 272-276(Supplement 1):E795–E796, May 2004.
- [177] B. K. Kuanr, A. V. Kuanr, R. E. Camley, and Z. Celinsky. Magnetization relaxation in sputtered thin fe films: An fmr study. *IEEE Trans. Magn.*, 42(10):2930, 2006.
- [178] E. E. Fullerton and S. K. Sinha. X-ray scattering studies of ultrathin metallic structures. In J. A. C. Bland and B. Heinrich, editors, *Ultrathin Magnetic Structures III*, pages 285–313, Berlin, 2005. Springer.
- [179] E. Chason and T. M. Mayer. Thin film and surface characterization by specular x-ray reflectivity. *Crit. Rev. Solid State Mat. Sci.*, 22(1):1–67, 1997.
- [180] H. Zabel. X-ray and neutron reflectivity analysis of thin films and superlattices. *Applied Physics A: Materials Science & Processing*, 58(3):159–168, March 1994.
- [181] bede X-ray metrology. <http://www.bede.co.uk/>. Bede Analysis Suite.
- [182] T. B. Massalski, H. Okamoto, P. R. Subramanian, and L. Kacprzak, editors. *Binary alloy phase diagrams, Volume 1 Ac-Ag to Ca-Zn*. ASM international, second edition, 1990.
- [183] H. Okamoto, T. B. Massalski, L. J. Swartzendruber, and P. A. Beck. Au-fe (gold-iron). United States of America, 1990. William W. Scott, Jr.
- [184] C. Rumbolz, W. Bolse, S. Kumar, R.S. Chauhan, D. Kabiraj, and D.K. Avasthi. Smoothing of fe/au and fe/ag multilayers by swift heavy ion bombardment. *Nucl. Instrum. Meth. B*, 245(1):145–149, April 2006.
- [185] J. F. Ziegler, J. P. Biersack, and U. Littmark. *The Stopping and Range of Ions in Matter*, volume 1. Pergamon, New York, 1985.
- [186] Stopping and Range of Ions in Matter-Home page. <http://www.srim.org/>.

- [187] J Fassbender, D Ravelosona, and Y Samson. Tailoring magnetism by light-ion irradiation. *J. Phys. D-Appl. Phys.*, 37(16):R179–R196, 2004.
- [188] P.-N. Favennec. *L'implantation ionique pour la microélectronique et l'optique*. Masson, Paris, 1993.
- [189] J. Pacaud, C. Jaouen, and G. Gladyszewski. Irradiation effects in cu/w multilayers: Ion beam mixing and structural evolution. *J. Appl. Phys.*, 86(9):4847–4854, 1999.
- [190] T. Devolder. *Structuration et nanostructuration de couches magnétiques Co/Pt par irradiation ionique*. PhD thesis, Université Paris-Sud, Paris, France, 2000.
- [191] T. Devolder. Light ion irradiation of co/pt systems: Structural origin of the decrease in magnetic anisotropy. *Phys. Rev. B*, 62(9):5794–5802, Sep 2000.
- [192] IRMA ion implanter Home page. <http://www-csasm.in2p3.fr/groupes/semirami/>.
- [193] C. Chappert, H. Bernas, J. Ferre, V. Kottler, J.-P. Jamet, Y. Chen, E. Cambril, T. Devolder, F. Rousseaux, V. Mathet, and H. Launois. Planar patterned magnetic media obtained by ion irradiation. *Science*, 280(5371):1919–1922, 1998.
- [194] W. J. M. de Jonge, P. J. H. Bloemen, and F. J. A. den Broeder. Experimental investigations of magnetic anisotropy. In J. A. C. Bland and B. Heinrich, editors, *Ultrathin Magnetic Structures I*, pages 65–90, Berlin, 1994. Springer.
- [195] W. H. Meiklejohn and C. P. Bean. New magnetic anisotropy. *Phys. Rev.*, 102(5):1413–1414, Jun 1956.
- [196] W. H. Meiklejohn and C. P. Bean. New magnetic anisotropy. *Phys. Rev.*, 105(3):904–913, Feb 1957.
- [197] J. Nogues and I. K. Schuller. Exchange bias. *J. Magn. Magn. Mater.*, 192(2):203–232, February 1999.
- [198] J. Nogues, J. Sort, V. Langlais, V. Skumryev, S. Surinach, J.S. Munoz, and M.D. Baro. Exchange bias in nanostructures. *Phys. Rep.*, 422(3):65–117, December 2005.
- [199] W. H. Meiklejohn. Exchange anisotropy—a review. *J. Appl. Phys.*, 33(3):1328–1335, 1962.
- [200] A. P. Malozemoff. Random-field model of exchange anisotropy at rough ferromagnetic-antiferromagnetic interfaces. *Phys. Rev. B*, 35(7):3679–3682, Mar 1987.
- [201] A. P. Malozemoff. Mechanisms of exchange anisotropy (invited). *J. Appl. Phys.*, 63(8):3874–3879, 1988.

- [202] D. Mauri, H. C. Siegmann, P. S. Bagus, and E. Kay. Simple model for thin ferromagnetic films exchange coupled to an antiferromagnetic substrate. *J. Appl. Phys.*, 62(7):3047–3049, 1987.
- [203] M. D. Stiles and R. D. McMichael. Model for exchange bias in polycrystalline ferromagnet-antiferromagnet bilayers. *Phys. Rev. B*, 59(5):3722–3733, Feb 1999.
- [204] M. D. Stiles and R. D. McMichael. Coercivity in exchange-bias bilayers. *Phys. Rev. B*, 63(6):064405, Jan 2001.
- [205] R L Stamps. Mechanisms for exchange bias. *J. Phys. D-Appl. Phys.*, 33(23):R247–R268, 2000.
- [206] Joo-Von Kim. *Microscopic disorder, finite temperatures and spin waves in domain-wall driven exchange bias*. PhD thesis, University of Western Australia, Perth, Australia, 2002.
- [207] Si-Mat Silicon Materials. <http://www.si-mat.com/>.
- [208] T. Dimopoulos, G. Gieres, J. Wecker, N. Wiese, Y. Luo, and K. Samwer. Large tunnel magnetoresistance with plasma oxidized mgo barrier. *J. Appl. Phys.*, 98(7):073705, 2005.
- [209] T. Dimopoulos, G. Gieres, J. Wecker, N. Wiese, and M. D. Sacher. Thermal annealing of junctions with amorphous and polycrystalline ferromagnetic electrodes. *J. Appl. Phys.*, 96(11):6382–6386, 2004.
- [210] M. Ali, C. H. Marrows, M. Al-Jawad, B. J. Hickey, A. Misra, U. Nowak, and K. D. Usadel. Antiferromagnetic layer thickness dependence of the irnm/co exchange-bias system. *Phys. Rev. B*, 68(21):214420, Dec 2003.
- [211] Princeton Measurements Corporation. <http://www.princetonmeasurements.com/>. MicroMag AGM.
- [212] J. P. Nibarger, R. Lopusnik, Z. Celinski, and T. J. Silva. Variation of magnetization and the Landé g factor with thickness in ni-fe films. *Appl. Phys. Lett.*, 83(1):93–95, 2003.
- [213] W. H. Butler, X.-G. Zhang, T. C. Schulthess, and J. M. MacLaren. Spin-dependent tunneling conductance of  $fe|mgo|fe$  sandwiches. *Phys. Rev. B*, 63(5):054416, Jan 2001.
- [214] J. Mathon and A. Umerski. Theory of tunneling magnetoresistance of an epitaxial  $fe/mgo/fe(001)$  junction. *Phys. Rev. B*, 63(22):220403, May 2001.
- [215] Shinji Yuasa, Taro Nagahama, Akio Fukushima, Yoshishige Suzuki, and Koji Ando. Giant room-temperature magnetoresistance in single-crystal  $fe/mgo/fe$  magnetic tunnel junctions. *Nat. Mater.*, 3(12):868, 2004.
- [216] X.-G. Zhang and W. H. Butler. Large magnetoresistance in bcc  $co/mgo/co$  and  $feco/mgo/feco$  tunnel junctions. *Phys. Rev. B*, 70(17):172407, 2004.

- [217] Shoji Ikeda, Jun Hayakawa, Young Min Lee, Ryutaro Sasaki, Toshiyasu Meguro, Fumihiro Matsukura, and Hideo Ohno. Dependence of tunnel magnetoresistance in mgo based magnetic tunnel junctions on ar pressure during mgo sputtering. *Japanese J. Appl. Phys.*, 44(48):L1442, 2005.
- [218] J. Hayakawa, S. Ikeda, Y. M. Lee, F. Matsukura, and H. Ohno. Effect of high annealing temperature on giant tunnel magnetoresistance ratio of cofeb/mgo/cofeb magnetic tunnel junctions. *Appl. Phys. Lett.*, 89(23):232510, 2006.
- [219] Jun Hayakawa, Shoji Ikeda, Young Min Lee, Ryutaro Sasaki, Toshiyasu Meguro, Fumihiro Matsukura, Hiromasa Takahashi, and Hideo Ohno. Current-driven magnetization switching in cofeb/mgo/cofeb magnetic tunnel junctions. *Japanese J. Appl. Phys.*, 44(41):L1267, 2005.
- [220] J.M. Teixeira, R.F. A. Silva, J. Ventura, A.M. Pereira, F. Carpinteiro, J.P. Araujo, J.B. Sousa, S. Cardoso, R. Ferreira, and P.P. Freitas. Domain imaging, moke and magnetoresistance studies of cofeb films for mram applications. *Mater. Sci. Eng. B*, 126(2-3):180–186, January 2006.
- [221] Shinji Yuasa, Yoshishige Suzuki, Toshikazu Katayama, and Koji Ando. Characterization of growth and crystallization processes in cofeb/mgo/cofeb magnetic tunnel junction structure by reflective high-energy electron diffraction. *Appl. Phys. Lett.*, 87(24):242503, 2005.
- [222] David D. Djayaprawira, Koji Tsunekawa, Motonobu Nagai, Hiroki Maehara, Shinji Yamagata, Naoki Watanabe, Shinji Yuasa, Yoshishige Suzuki, and Koji Ando. 230tunnel junctions. *Appl. Phys. Lett.*, 86(9):092502, 2005.
- [223] Stuart S. P. Parkin, Christian Kaiser, Alex Panchula, Philip M. Rice, Brian Hughes, Mahesh Samant, and See-Hun Yang. Giant tunnelling magnetoresistance at room temperature with mgo (100) tunnel barriers. *Nat. Mater.*, 3(12):862, 2004.
- [224] D. J. Twisselmann and R. D. McMichael. Intrinsic damping and intentional ferromagnetic resonance broadening in thin permalloy films. *J. Appl. Phys.*, 93(10):6903–6905, 2003.
- [225] D. Lacour, J. A. Katine, N. Smith, M. J. Carey, and J. R. Childress. Thermal effects on the magnetic-field dependence of spin-transfer-induced magnetization reversal. *Appl. Phys. Lett.*, 85(20):4681–4683, 2004.
- [226] Jun Hayakawa, Shoji Ikeda, Fumihiro Matsukura, Hiromasa Takahashi, and Hideo Ohno. Dependence of giant tunnel magnetoresistance of sputtered cofeb/mgo/cofeb magnetic tunnel junctions on mgo barrier thickness and annealing temperature. *Japanese J. Appl. Phys.*, 44(19):L587, 2005.
- [227] I. Neudecker, M. Klaui, K. Perzlmaier, D. Backes, L. J. Heyderman, C. A. F. Vaz, J. A. C. Bland, U. Rudiger, and C. H. Back. Spatially resolved dynamic eigenmode spectrum of co rings. *Phys. Rev. Lett.*, 96(5):057207, 2006.

- [228] A. A. Tulapurkar, Y. Suzuki, A. Fukushima, H. Kubota, H. Maehara, K. Tsunekawa, D. D. Djayaprawira, N. Watanabe, and S. Yuasa. Spin-torque diode effect in magnetic tunnel junctions. *Nature*, 438(7066):339–342, November 2005.
- [229] G. D. Fuchs, J. C. Sankey, V. S. Pribiag, L. Qian, P. M. Braganca, A. G. F. Garcia, E. M. Ryan, Zhi-Pan Li, O. Ozatay, D. C. Ralph, and R. A. Buhrman. Spin-torque ferromagnetic resonance measurements of damping in nanomagnets. *Appl. Phys. Lett.*, 91(6):062507, 2007.
- [230] J. C. Sankey, P. M. Braganca, A. G. F. Garcia, I. N. Krivorotov, R. A. Buhrman, and D. C. Ralph. Spin-transfer-driven ferromagnetic resonance of individual nanomagnets. *Phys. Rev. Lett.*, 96(22):227601, 2006.
- [231] NI LabVIEW graphical development. <http://www.ni.com/labview/>. National Instruments.



# Publications

## Articles

- **Study of the dynamic magnetic properties of soft CoFeB films**  
C. Bilzer, T. Devolder, J.-V. Kim, G. Council, C. Chappert, S. Cardoso, and P. P. Freitas  
J. Appl. Phys., **100**(5):053903, 2006.
- **Vector network analyzer ferromagnetic resonance of thin films on coplanar waveguides: Comparison of different evaluation methods**  
C. Bilzer, T. Devolder, P. Crozat, C. Chappert, S. Cardoso, and P. P. Freitas  
J. Appl. Phys., **101**(7):074505, 2007.
- **Quasi-static and dynamic switching of exchange biased micron-sized TMR junctions**  
C. Maunoury, C. Bilzer, C. K. Lim, T. Devolder, J. Wecker, L. Bär, and C. Chappert  
Mater. Sci. Eng. B, **126**(2-3):202, 2006.
- **Ferromagnetic resonance linewidth reduction in Fe/Au multilayers using ion beams**  
C. Bilzer, T. Devolder, C. Chappert, O. Plantevin, A. K. Suszka, B. J. Hickey, A. Lamperti, B. K. Tanner, B. Mahrov, and S. O. Demokritov  
Accepted for publication in J. Appl. Phys. (2007).

## Presentations

- **Caractérisation haute fréquence du comportement amorti de l'aimantation dans des couches minces magnétiques**  
C. Bilzer, T. Devolder, and C. Chappert  
Institut d'Electronique Fondamentale - Internal Seminar (Orsay, France, 2006).

## Posters

- **Surface and Interface Smoothing on Fe/Au multilayers using Ion Beams**  
C. Bilzer, A. K. Suszka, A. Lamperti, B. Mahrov, O. Plantevin, B. J. Hickey, S. O. Demokritov, B. K. Tanner, C. Chappert, and T. Devolder  
52nd Conference on Magnetism and Magnetic Materials (Tampa, USA, 2007).
- **Evolution of the high-frequency permeability of CoFeB thin films under thermal treatment**



C. Bilzer, T. Devolder, J-V. Kim, G. Counil, P. Crozat, C. Chappert, S. Cardoso, and P.P. Freitas  
19th International Colloquium on Magnetic Films and Surfaces - ICMFS (Sendai, Japan, 2006).

- **Quasi-static and dynamic switching of exchange biased micron-sized TMR junctions**

C. Maunoury, C. Bilzer, C. K. Lim, T. Devolder, J. Wecker, L. Bär, and C. Chappert  
EMRS - European Materials Research Society: Spring Meeting (Strasbourg, France, 2005).

- **Magnetization dynamics of thin films studied by network analyzer ferromagnetic resonance**

C. Bilzer, T. Devolder, and C. Chappert  
Heraeus Summer school: Spinelectronics (Wittenberg, Germany, 2005).

- **Magnetisation dynamics in (multi)layers characterised at microwave frequencies**

C. Bilzer, P. Crozat, J-V. Kim, T. Devolder, and C. Chappert  
Summer school of the Ultrasmooth Research Training Network (Durham, England, 2006).

- **Méthodologies d'évaluation des données de la résonance ferromagnétique sur guide d'onde coplanaire**

C. Bilzer, T. Devolder, P. Crozat, C. Chappert, S. Cardoso, and P.P. Freitas  
11ème Colloque Louis Néel - Couches minces et nanostructures magnétiques (Lyon, France, 2007).

- **Caractérisation du comportement hyperfréquence de couches minces CoFeB**

C. Bilzer, T. Devolder, Joo-Von Kim, G. Counil, C. Chappert, S. Cardoso, and P.P. Freitas  
11ème Colloque Louis Néel - Couches minces et nanostructures magnétiques (Lyon, France, 2007).

- **Reduced interface roughness in Fe/Au multilayers**

C. Bilzer, A.K. Suszka, A. Lamperti, B. Mahrov, O. Plantevin, M. Ali, M.J. Walker, C.H. Marrows, B.J. Hickey, S.O. Demokritov, B.K. Tanner, T. Devolder, and C. Chappert  
Workshop on Smoothing & Characterization of Magnetic Films for Advanced Devices (Krakow, Poland, 2007).

## In Collaboration

- **Instrumentation pour la perméamétrie hyperfréquence de couches minces (presentation)**

G. Counil, C. Bilzer, J-V. Kim, P. Crozat, T. Devolder, and C. Chappert  
10ème Colloque Louis Néel - Couches minces et nanostructures magnétiques (Dourdan, France, 2005).

- **Longitudinal and Lateral finite size effects in Network Analyzer FMR** (presentation)  
G. Counil, C. Bilzer, P. Crozat, T. Devolder, S. Zoll, R. Fournel and C. Chappert  
IEEE International Magnetism Conference (San Diego, USA, 2006).
- **Semi-epitaxial magnetic tunnel transistor: Effect of electron energy and temperature** (presentation)  
T. Hagler, C. Bilzer, M. Dumm, W. Kipferl, and G. Bayreuther  
49th Conference on Magnetism and Magnetic Materials (Jacksonville, USA, 2004).
- **Semi-epitaxial magnetic tunnel transistor: Effect of electron energy and temperature**  
T. Hagler, C. Bilzer, M. Dumm, W. Kipferl, and G. Bayreuther  
J. Appl. Phys., **97**(10):10D505, 2005.



# Acknowledgements

First, I would like to thank my supervisor Dr. Thibaut Devolder for sharing with me his immense knowledge on magnetism, electronics and many other subjects not necessarily related to the natural sciences. Apart from the scientific guidance, I am also particularly thankful for the warm welcome when arriving in France and for the help with my ‘integration’ in general.

I am equally grateful to Dr. Claude Chappert, the head of the NanoSpinTronics department, for giving me the opportunity to learn and work in his world-renowned group.

Special thanks also goes to Dr. Joo-Von Kim, who is able to effortlessly provide easy-to-understand explanations for complicated facts, for his ever present advice. Personally, I also appreciated a lot his enthusiasm for the german, ähm, culture.

I also wish to extend my warmest thanks to the following people who contributed in some manner to the successful conclusion of this thesis:

- Dr. Paul Crozat and Dr. Nicolas Zerounian for their invaluable help on the high-frequency measurements.
- Dr. Olivier Plantevin for the irradiation of the Fe/Au multilayer samples.
- The PhD students and PostDocs being members of the work group at some point in time: Dr. Mohamed Belmeguenäi, Capucine Burrowes, Dr. Guillaume Council, Dr. Robert Drese, Maryam Golmaï, Dr. Julie Grollier, Michel He, Annerose Helmer, Yann LeMaho, Quentin Mistral, Dr. Dana Stanescu, Weisheng Zhao.
- Sylvain Eimer, Virginie Auger and the other staff members for a pleasant working atmosphere.
- All the other people from the NST work group and from the Institut d’Electronique Fondamentale, who did not appear in this list, but should have.
- Ania Suszka, Dr. Ricardo Ferreira and Dr. Susana Cardoso de Freitas for providing many interesting samples and characterizations and Dr. Boriss Mahrov for participating in the sample preparation by carrying out the ion beam substrate cleaning.
- Dr. Alessio Lamperti for performing the X-ray scattering measurements.
- Miriana Vadala for providing very rapidly necessary magnetometer measurements.

- Prof. Dr. Günther Bayreuther, Prof. Dr. Sergej Demokritov, Prof. Dr. Paulo Freitas, Prof. Dr. Bryan Hickey, Prof. Dr. Brian Tanner, Prof. Dr. Dr. Hartmut Zabel for the excellent network meetings.
- Prof. Dr. Günther Bayreuther for fulfilling the role of being my mentor in the network.
- Prof. Dr. Bryan Hickey for his friendly invitation to visit his laboratory and for his hospitality.
- The industrial partners in the european network, in particular, Dr. Rolf Al-lenspach, Dr. Wolfram Maass and Dr. Berthold Ocker, for the possibility to visit their laboratories.
- Dr. Manfred Rührig for giving me the possibility to spend my secondment in his work group and Dr. Ludwig Bär for his help with stubborn machinery and for taking care of my accommodation. Dr. Günther Gieres, Dr. Joachim Bangert, Dr. Michael Vieth and Herbert Mai for the interesting discussions.
- Thibaut Devolder and Joo-Von Kim for the proofreading of this manuscript.
- Priv.-Doz. Dr. Jürgen Fassbender and Dr. Jan Vogel for acting as reviewers for my manuscript.
- Dr. Matthieu Bailleul, Priv.-Doz. Dr. Jürgen Fassbender, Dr. André Thiaville and Dr. Jan Vogel for accepting to participate in my thesis defense.

The financial support provided through the European Community's Marie Curie actions (Research Training Networks) under contract MRTN-CT-2003-504462, UL-TRASMOOTH is gratefully acknowledged.

Finally, I want to express my deepest thanks to my parents, my brother and my wider family for being unwavering in their support, and  
... to Elsa for everything.